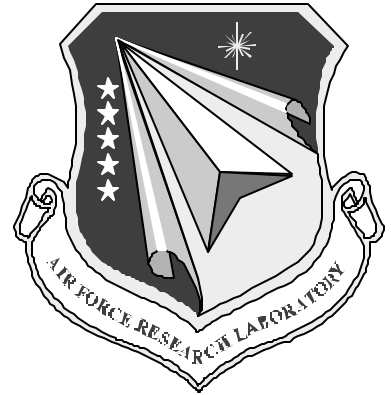


AFRL-ML-WP-TR-2001-4020



**LIFE PREDICTION METHODOLOGIES FOR
AEROSPACE MATERIALS**

**N.E. ASHBAUGH, R.A. BROCKMAN, D.J. BUCHANAN, G.A. HARTMAN, A.L.
HUTSON, K. LI, W.J. PORTER, AND D.A. STUBBS**

**UNIVERSITY OF DAYTON RESEARCH INSTITUTE
STRUCTURAL INTEGRITY DIVISION
300 COLLEGE PARK
DAYTON, OHIO 45469-0128**

JANUARY 2001

INTERIM REPORT FOR PERIOD 25 MAY 1999 - 24 MAY 2000

Approved for public release; distribution unlimited.

**MATERIALS AND MANUFACTURING DIRECTORATE
AIR FORCE RESEARCH LABORATORY
AIR FORCE MATERIEL COMMAND
WRIGHT-PATTERSON AFB, OHIO 45433-7750**

Form SF298 Citation Data

Report Date ("DD MON YYYY") 01012001	Report Type N/A	Dates Covered (from... to) ("DD MON YYYY") 25051999 24052000
Title and Subtitle Life Prediction Methodologies for Aerospace Materials		Contract or Grant Number
		Program Element Number
Authors Ashbaugh, N. E.; Brockman, R. A.; Buchanan, D. J.; Hartman, G. A.; Hutson, A. L.; Li, K.; Porter, W. J.; Stubbs, D. A.		Project Number
		Task Number
		Work Unit Number
Performing Organization Name(s) and Address(es) UNIVERSITY OF DAYTON RESEARCH INSTITUTE STRUCTURAL INTEGRITY DIVISION 300 COLLEGE PARK DAYTON, OHIO 45469-0128		Performing Organization Number(s)
Sponsoring/Monitoring Agency Name(s) and Address(es) Materials and Manufacturing Directorate Air Force Research Laboratory Airforce Materiel Command Wright-Patterson AFB, OH 45433-7750		Monitoring Agency Acronym
		Monitoring Agency Report Number(s)
Distribution/Availability Statement Approved for public release, distribution unlimited		
Supplementary Notes		

Abstract

The understanding of the effect of material defects, i.e., inclusions and grain size variances, on tensile and fatigue behavior, specifically initiation, in wrought gamma titanium aluminides was improved. Orientation imaging microscopy (OIM) aided in determining microstructural situations favorable for initiation of fatigue cracks. Finite element models were refined to predict elastic and plastic behavior of fully lamellar microstructures under static loading. An effective ligament model that successfully correlated crack growth rate behaviors parallel to the fibers in fiber titanium-matrix composite (TMC) was developed. Acoustic emission signals were obtained from the specimens during tensile, creep, and fatigue tests to assess damage evolution in a unidirectional TMC. A phenomenological model for the constitutive behavior of the matrix was developed to predict the time-dependent response of a TMC under tensile, creep, and fatigue conditions. Fracture behavior and damage progression in Nextel720/AS and Nextel610/AS ceramic matrix composites were studied using middle hole, single edge hole, semicircular double-notched, and double-notched geometries. In addition to the elasticity models of Nextel720/AS, creep and damage models were developed. Initial room temperature tensile tests on melt infiltrated Sylramic/BN/SiC composite exhibited poor ultimate strength results and provided evidence of oxidized fibers and of large regions of matrix porosity. Fretting fatigue investigations focussed on the effects of applied clamping stress, time required for detrimental fretting fatigue damage, and applied shear stress. Extensive characterizations of laboratory simulated fretting fatigue and FOD damage were conducted on an SEM. An investigation of the effect of compressive mean stress on fatigue behavior was conducted within the elastic compressive regime to identify damage mechanisms related to compressive mean stress loading. A fractographic technique to investigate the effect of stress ratio on small crack growth rates using fatigue striations was developed. Newly developed technologies include infrared damage detection and ultra-precise calibration equipment.

Subject Terms

Titanium aluminides; titanium matrix composites; SiC fibers; ceramic matrix composites; nickle-base superalloys; turbine blade materials; high cycle fatigue; fatigue crack growth; elevated temperatures; creep; thermal fatigue; thermomechanical fatigue; fretting fatigue; load interactions; mixed-mode; stress intensity factors; finite element analysis; nondestructive evaluation

Document Classification unclassified	Classification of SF298 unclassified
Classification of Abstract unclassified	Limitation of Abstract unlimited
Number of Pages 162	

NOTICE

Using government drawings, specifications, or other data included in this document for any purpose other than government procurement does not in any way obligate the U.S. Government. The fact that the government formulated or supplied the drawings, specifications, or other data does not license the holder or any other person or corporation; or convey and rights or permission to manufacture, use, or sell any patented invention that may relate to them.

This report has been reviewed by the Office of Public Affairs (ASC/PA) and is releasable to the National Technical Information Service (NTIS). At NTIS, it will be available to the general public, including foreign nations.

This technical report has been reviewed and is approved for publication.



LT. BRITT P. CUNNINGHAM, Project Engineer
Behavior/Life Prediction Section
Metals Branch
Metals, Ceramics & NDE Division



Katherine A. Stevens, Chair
Metals Branch
Metals, Ceramics & NDE Division
Materials and Manufacturing Directorate



GERALD J. PERIAK, Asst. Chair
Metals, Ceramics, and Nondestructive
Evaluation Division
Materials and Manufacturing Directorate

Copies of this report should not be returned unless return is required by security considerations, contractual obligations, or notice on a specific document.

REPORT DOCUMENTATION PAGE			Form Approved OMB No. 0704-0188
Public reporting burden for this collection of information is estimated to average 1 hour per response, including the time for reviewing instructions, searching existing data sources, gathering and maintaining the data needed, and completing and reviewing the collection of information. Send comments regarding this burden estimate or any other aspect of the collection of information, including suggestions for reducing this burden, to Washington Headquarters Services, Directorate for Information Operations and Reports, 1215 Jefferson Davis Highway, Suite 1204, Arlington, VA 22202-4302, and to the Office of Management and Budget, Paperwork Reduction Project (0704-0188), Washington, DC 20503.			
1. AGENCY USE ONLY (LEAVE BLANK)	2. REPORT DATE	3. REPORT TYPE AND DATES COVERED	
	January 2001	Interim, 25 May 1999 – 24 May 2000	
4. TITLE AND SUBTITLE			5. FUNDING NUMBERS
Life Prediction Methodologies for Aerospace Materials			C: F33615-98-C-5214 PE: 62102F PR: 4347 TA: 52 WU: 01
6. AUTHOR(S) N.E. Ashbaugh, R.A. Brockman, D.J. Buchanan, G.A. Hartman, A.L. Hutson, K. Li, W.J. Porter, and D.A. Stubbs			
7. PERFORMING ORGANIZATION NAME(S) AND ADDRESS(ES) UNIVERSITY OF DAYTON RESEARCH INSTITUTE STRUCTURAL INTEGRITY DIVISION 300 COLLEGE PARK DAYTON, OHIO 45469-0128			8. PERFORMING ORGANIZATION REPORT NUMBER
9. SPONSORING/MONITORING AGENCY NAME(S) AND ADDRESS(ES) Materials and Manufacturing Directorate Air Force Research Laboratory Airforce Materiel Command Wright-Patterson AFB, OH 45433-7750 POC: Lt. Brett Conner, AFRL/MLLMN (937) 255-1348			10. SPONSORING/MONITORING AGENCY REPORT NUMBER AFRL-ML-WP-TR-2001-4020
11. SUPPLEMENTARY NOTES			
12a. DISTRIBUTION AVAILABILITY STATEMENT Approved for public release; distribution unlimited.		12b. DISTRIBUTION CODE	
13. ABSTRACT (Maximum 200 words) The understanding of the effect of material defects, i.e., inclusions and grain size variances, on tensile and fatigue behavior, specifically initiation, in wrought gamma titanium aluminides was improved. Orientation imaging microscopy (OIM) aided in determining microstructural situations favorable for initiation of fatigue cracks. Finite element models were refined to predict elastic and plastic behavior of fully lamellar microstructures under static loading.			
An effective ligament model that successfully correlated crack growth rate behaviors parallel to the fibers in fiber titanium-matrix composite (TMC) was developed. Acoustic emission signals were obtained from the specimens during tensile, creep, and fatigue tests to assess damage evolution in a unidirectional TMC. A phenomenological model for the constitutive behavior of the matrix was developed to predict the time-dependent response of a TMC under tensile, creep, and fatigue conditions. Fracture behavior and damage progression in Nextel™720/AS and Nextel™610/AS ceramic matrix composites were studied using middle hole, single edge hole, semicircular double-notched, and double-notched geometries. In addition to the elasticity models of Nextel™720/AS, creep and damage models were developed. Initial room temperature tensile tests on melt infiltrated Sylramic/BN/SiC composite exhibited poor ultimate strength results and provided evidence of oxidized fibers and of large regions of matrix porosity.			
Fretting fatigue investigations focussed on the effects of applied clamping stress, time required for detrimental fretting fatigue damage, and applied shear stress. Extensive characterizations of laboratory simulated fretting fatigue and FOD damage were conducted on an SEM. An investigation of the effect of compressive mean stress on fatigue behavior was conducted within the elastic compressive regime to identify damage mechanisms related to compressive mean stress loading. A fractographic technique to investigate the effect of stress ratio on small crack growth rates using fatigue striations was developed. Newly developed technologies include infrared damage detection and ultra-precise calibration equipment.			
14. SUBJECT TERMS Titanium aluminides, titanium matrix composites, SiC fibers, ceramic matrix composites, nickel-base superalloys, turbine blade materials, high cycle fatigue, fatigue crack growth, elevated temperatures, creep, thermal fatigue, thermomechanical fatigue, fretting fatigue, load interactions, mixed-mode, stress intensity factors, finite element analysis, nondestructive evaluation			15. NUMBER OF PAGES 166
			16. PRICE CODE
17. SECURITY CLASSIFICATION OF REPORT Unclassified	18. SECURITY CLASSIFICATION OF THIS PAGE Unclassified	19. SECURITY CLASSIFICATION OF ABSTRACT Unclassified	20. LIMITATION OF ABSTRACT SAR

TABLE OF CONTENTS

SECTION	PAGE
Foreword	vi
1.0 EXECUTIVE SUMMARY	1
1.1 γ TiAl-BASE ALUMINIDES	1
1.2 Ti-MATRIX COMPOSITES.....	1
1.3 CERAMIC MATRIX COMPOSITES	1
1.4 OTHER AEROSPACE MATERIALS	2
1.5 DEVELOPMENT OF EXPERIMENTAL PROCEDURES, METHODOLOGIES AND LABORATORY ENHANCEMENTS	3
2.0 INTRODUCTION	4
2.1 BACKGROUND.....	4
2.2 PROGRAM OBJECTIVES	4
2.3 REPORT ORGANIZATION.....	4
3.0 DAMAGE TOLERANCE STUDIES OF γ TiAl-BASE TITANIUM ALUMINIDE	6
3.1 MECHANISMS OF FATIGUE CRACK INITIATION IN TiAl INTERMETALLIC ALLOYS.....	6
3.1.1 Elastic Behavior of Fully Lamellar Gamma Titanium Aluminides	6
3.1.2 Effects of Microstructural Anisotropy on Fatigue Behavior of Gamma TiAl Alloys	6
3.1.3 Lamellar Colony Orientation Determination in Gamma Titanium Aluminides Using Orientation Imaging Microscopy (OIM)	6
3.1.4 Defects in 3-95M Wrought Gamma Titanium Aluminides	7
3.2 MODELING EFFORTS ANALYSIS OF STRESS CONDITIONS LEADING TO INITIATION.....	7
3.2.1 Modeling of Anisotropic Behavior in Lamellar TiAl.....	7
3.2.2 Crystal Plasticity Model for Lamellar TiAl	8
4.0 DAMAGE ACCUMULATION AND FAILURE OF Ti-MATRIX COMPOSITES (TMC)	9
4.1 CYCLIC CRACK PROPAGATION PARALLEL TO FIBERS IN A UNIDIRECTIONALLY REINFORCED METAL MATRIX COMPOSITE [C1] ¹	9
4.2 USER'S MANUAL FOR THE COMPACT FIBER TEST MACHINE [C2].....	9
4.3 TENSILE, CREEP, AND FATIGUE BEHAVIOR OF [0] ₈ TRIMARC/Ti-6-2-4-2	9
4.4 A POWER LAW CREEP MODEL FOR NEAT Ti-6Al-4V	10
5.0 DAMAGE ACCUMULATION AND FAILURE OF CERAMIC MATRIX COMPOSITES (CMC)	11
5.1 MECHANICAL AND THERMOPHYSICAL CHARACTERIZATION OF OXIDE/OXIDE NEXTEL™720/AS and NEXTEL™610/AS CMC	11
5.1.1 Monotonic Fracture Behavior of Double-Edge Notched Oxide/Oxide NexTEL™720/AS Composite [C3].....	11
5.1.2 Creep Rupture Behavior of Double-Edge Notched Oxide/Oxide NexTEL™720/AS Composite [C4].....	11
5.1.3 Damage Progression from Double-Edge Notched Oxide/Oxide NexTEL™720/AS Composite Under Creep Loading	11

¹ Notation in square brackets refer to manuscripts in compendium.

5.1.4	Effect of Heat Treatment on Mechanical Behavior of Oxide/Oxide Nextel™720/AS Composite.....	12
5.1.5	Characterization of Thermophysical Properties of Oxide/Oxide Nextel™720/AS Composite.....	12
5.1.6	In-Plane Shear Behavior of Oxide/Oxide Nextel™720/AS & Nextel™610/AS Composite.....	12
5.1.7	Fracture Behavior of Single-Edge Notched Oxide/Oxide Nextel™610/AS Composite Under Cyclic Loading [C5].....	13
5.1.8	Damage Progression from Single-Edge Notched Oxide/Oxide Nextel™610/AS Composite Using Ultrasonic C-scans [C6].....	13
5.1.9	Characterization of Notched Fracture Behavior of Nextel™610/AS Oxide/Oxide Composite at 23 and 950°C Under Multiple Loading Conditions	13
5.2	MODELING AND MECHANICAL DESIGN ANALYSIS OF OXIDE/OXIDE NEXTEL™720/AS CMC	14
5.2.1	Development of Finite Element User Material Subroutine for Oxide/Oxide Nextel™720/AS Composite Deformation.....	14
5.2.2	Analysis of Local Stresses in Notched Oxide/Oxide Nextel™720/AS Composite.....	14
5.2.3	Elasticity, Creep, and Damage Model for Oxide/Oxide Nextel™720/AS Composite.....	14
5.2.4	Heat Transfer and Stress Analysis of CMC Combustor Conceptual Design	15
5.3	PRELIMINARY OBSERVATIONS OF THE MONOTONIC TENSILE BEHAVIOR OF MI SiC/SiC CMC	15
6.0	HIGH CYCLE FATIGUE AND FATIGUE CRACK GROWTH IN AEROSPACE MATERIALS.....	16
6.1	FRETTING FATIGUE	16
6.1.1	Fretting Fatigue of Ti-6Al-4V Under Flat-on-Flat Contact With Blending Radii	16
6.1.2	Characterization of Fretting Fatigue Crack Nucleation Life of Ti-6Al-4V in a Flat-on-Flat Contact [C7].....	16
6.1.3	Effect of Specimen Thickness on Fretting Fatigue Behavior	17
6.1.4	SEM Characterization of Pre-Fretted Ti-6Al-4V Fatigue Specimens	17
6.2	CHARACTERIZATION OF FOD IMPACT SITES ON TI-6AL-4V UNDER HIGH CYCLE FATIGUE [C8]	18
6.3	EVOLUTION AND EFFECTS OF DAMAGE IN Ti-6Al-4V UNDER HIGH CYCLE FATIGUE	19
6.4	HCF SYSTEM ENHANCEMENTS	19
6.5	CPLM FOR Ti ALLOYS	19
6.6	FRACTOGRAPHIC OBSERVATIONS ON THE NATURE OF STRESS RATIO EFFECT IN FATIGUE	20
7.0	DEVELOPMENT OF EXPERIMENTAL PROCEDURES, METHODOLOGIES, AND LABORATORY ENHANCEMENTS	21
7.1	LABORATORY TEST CONTROL AND DATA MANAGEMENT	21

7.1.1	WinMATE 2000 Development Support.....	21
7.1.2	Improvement in Load Frame Alignment Equipment and Procedures.....	21
7.1.3	Upgrade Of Laboratory Test Automation Hardware and Instrumentation	22
7.1.4	Design and Implementation of a Network for Laboratory Data Transfer	22
7.1.5	Data Archival and Status of Keyserver®.....	22
7.2	APPARATUS AND INSTRUMENTATION.....	23
7.2.1	Infrared Damage Detection System (IDDS)	23
7.2.2	Short-Gage-Length LVDT Extensometer Development.....	23
7.2.3	Design of a High-Resolution Displacement Calibrator.....	23
7.2.4	Improvements to Direct Current Potential Difference Crack Detection System	24
7.2.5	Improvements in Acoustic Emission (AE) Detection of Damage in MMC During Mechanical Testing	24
7.2.6	Design of Shear Wave Ultrasonic NDE Techniques for Detecting Fatigue Cracks During Fretting Tests	24
7.2.7	Blade Root Fretting Fatigue Apparatus Design.....	24
8.0	REFERENCES.....	25
	Appendix A: Compendium of Manuscripts	26
	List of Symbols, Abbreviations, and Acronyms	155

FOREWORD

The work described in this report was performed at the Ceramic Development & Materials Behavior Branch in the Metals, Ceramics & Nondestructive Evaluation Division of the Materials & Manufacturing Directorate, Air Force Research Laboratory (AFRL/MLLN) under Contract No. F33615-98-C-5214, "Life Prediction Methodologies for Aerospace Materials." The contract is administered under the direction of AFRL by Lt. Brett Conner. The program is being conducted by the Structural Integrity Division, University of Dayton Research Institute, Dayton, Ohio with Dr. Noel E. Ashbaugh and Mr. Robert J. Andrews acting as the Principal Investigator and Program Manager, respectively. This report is an interim report on the progress of the 5-year contract effort.

In the second year of the contract, the investigations were developed and directed by Drs., Robert Brockman, Geoffrey Frank, Victoria Kramb, and Kezhong Li and Messrs. Dennis Buchanan, George Hartman, David Maxwell, W. John Porter, and David Stubbs and Mrs. Alisha Hutson. Mrs. Jacqui Hawkins was responsible for coordinating the input and typing of this document. This interim report covers the work performed during the period of 25 May 1999 to 24 May 2000.

SECTION 1.0

EXECUTIVE SUMMARY

1.1 g TiAl-BASE ALUMINIDES

As our understanding of the mechanical behavior of gamma titanium aluminides continues to mature, the transitioning of these materials from the laboratory to application in United States Air Force (USAF) systems still must overcome a few significant hurdles. For example, a general lack of experience in applying materials with such limited ductility and damage tolerance is apparent in the design community. Also, life prediction methodologies and models still require significant further refinement to compel designers into including these types of materials in their systems. The focus of our work over the last year was to improve our understanding of the mechanical behavior with emphasis on fatigue properties and to incorporate these advancements into robust models and improved life prediction techniques that will increase the likelihood of widespread application.

Significant progress was made in a number of areas over the past year including: 1) increased understanding of the effect of material defects, i.e. inclusions and grain size variances, on tensile and fatigue behavior, specifically initiation, in wrought material, 2) significant use of analytical tools, such as orientation imaging microscopy (OIM), to aid in determining microstructural situations favorable for initiation of fatigue cracks, and 3) continued refinement of models to predict elastic and plastic behavior of fully lamellar microstructures under static loading.

1.2 Ti-MATRIX COMPOSITES

In the effort to assess the performance of titanium-matrix composites (TMC) under service conditions, the following tests and analyses were conducted. An effective ligament model was developed that successfully correlated crack-growth-rate behaviors parallel to the fibers in a unidirectional fiber composite to growth rates of the neat matrix. The damage tolerance and life prediction of unidirectional TMC to off-axis loads can be evaluated with this model.

Tensile, creep, and fatigue tests were conducted on a unidirectional TMC to evaluate the evolution of damage under variety of conditions. Acoustic emission signals were obtained from the specimens during the tests to assess damage. The results are being used to develop an improved life prediction model for the TMC.

Data must be obtained and robust models of the constitutive behaviors of the TMC components must be used to predict the mechanical behavior of a TMC under various loading conditions. A phenomenological model for the constitutive behavior of the matrix has been developed to predict the time-dependent response of a TMC under tensile, creep, and fatigue conditions. The model will be applied to a variety of available data sets to assess its viability. Also, a test system used to obtain the tensile stress-strain response of fibers and wire has been described.

1.3 CERAMIC MATRIX COMPOSITES

Ceramic matrix composites (CMC) are currently being evaluated as replacement materials in high temperature environments such as gas turbine engines. Many of the applications including

exhaust wash structures, exhaust nozzle flaps and seals and combustor liners require holes, fillets, and attachment points in the design of these structures. Fracture behavior and damage progression in NextelTM720/AS and NextelTM610/AS were studied on middle hole specimens (MH(T)), single edge hole specimens (SE(T)), semicircular double-notched specimens (DEH(T)) and double-notched (DE(T)) geometries. As-received, heat-treated, load and unload, fast fracture, and sustained load (creep) experiments were conducted on notched specimens to determine how damage initiates and progresses at notch tips. Thorough SEM investigation of notched specimens subjected to the different mechanical and thermal loading conditions revealed that only under sustained load (creep) conditions was there any evidence of damage progression from the notch tips. Results of the in-plane tensile tests on ±45° tow orientation showed that for both NextelTM610/AS and NextelTM720/AS at 23°C, shear deformation was highly nonlinear.

In support of the ER Combustor program baseline thermal and physical properties of the as-received NextelTM720/AS were measured by Thermophysical Properties Research Laboratory (TPRL) over the anticipated range of combustor operating temperatures, ≤ 1000°C. The thermal and mechanical properties were essential for comparison of the NextelTM720/AS material with other candidate material systems for the combustor application. These properties are also necessary for the development of finite element models.

In addition to the elasticity models of NextelTM720/AS, creep and damage models of the CMC system have been developed. The one-dimensional creep model has been validated with experimental creep results and is being extended to three dimensions for analysis of notched specimen geometries. Steady state heat transfer and stress analysis calculations have been completed, using the thermophysical properties of the CMC, to investigate the feasibility of using the NextelTM720/AS for the combustor application.

Initial room temperature tensile tests on melt infiltrated (MI) Sylramic/BN/SiC composite exhibited poor ultimate strength results and provided evidence of oxidized fibers and of large regions of matrix porosity.

1.4 OTHER AEROSPACE MATERIALS

Ti-6Al-4V and some other alloys used in fabricating engine components are being revisited to assess their behavior under conditions that simulate engine operation. Among the types of loading conditions being investigated are fretting fatigue, as observed in turbine engine blade attachments, and foreign object damage (FOD). The ongoing effort to characterize fretting fatigue phenomena focussed on the effects of applied clamping stress, time required for detrimental fretting fatigue damage, and applied shear stress. Applied clamping stress was identified as a parameter influencing the time to fretting fatigue crack nucleation – a parameter critical to component life prediction.

Extensive characterizations of laboratory simulated fretting fatigue and FOD damage were conducted using scanning electron microscopy for in-house studies and in conjunction with an off-site investigation conducted under the High Cycle Fatigue (HCF) initiative. The observations of fretting fatigue scars revealed lower observable wear than that reported for service components. Investigation of simulated FOD damage revealed no correlation between fatigue life and either FOD depth along simulated airfoil leading edges or material loss at the FOD surface. These results are being used to define criteria by which detrimental damage may be identified.

An investigation of the effect of compressive mean stress on fatigue behavior was conducted within the elastic compressive regime to identify damage mechanisms related to compressive mean stress loading, often observed in components fabricated with shot peening. This work indicated the compressive mean stress contributed less than 30 percent to fatigue damage and provided data to extend the Goodman diagram to stress ratios lower than -1.

Several investigations focussed on the development of laboratory capability and methodologies for future studies. Crack propagation load measurement (CPLM) capabilities were enhanced and expanded, and verification of the CPLM technique for different load histories and threshold behaviors was continued. For the HCF laboratory, existing test systems were improved and preparations for two new test systems were begun. Finally, a fractographic technique to investigate the effect of stress ratio on small crack growth rates using fatigue striations was developed.

1.5 DEVELOPMENT OF EXPERIMENTAL PROCEDURES, METHODOLOGIES, AND LABORATORY ENHANCEMENTS

State-of-the-art experimental capability is critical for sophisticated studies of fundamental material properties and behavior. Providing cutting-edge capability within a reasonable budget requires the ability to efficiently maintain existing assets, to identify new technologies and realistically evaluate their potential, and to integrate both existing and new technologies with emerging techniques to obtain new types of data.

The university has attacked this challenge on two fronts. First, we have made a concerted effort to maintain and enhance the general laboratory infrastructure. Second, we have designed, fabricated, and tested a number of specific new technologies aimed at improving the tools available to AFRL/MLLMN laboratory researchers. Infrastructure improvements range from greatly enhanced test automation software and laboratory connectivity to better methods of aligning load frames for precision testing. Specific new technologies include infrared damage detection and ultra-precise calibration equipment. Details of the university's efforts in keeping the AFRL/MLLMN laboratories at the forefront of material characterization research are contained in section 7.

SECTION 2.0

INTRODUCTION

2.1 BACKGROUND

The U.S. Air Force (USAF) has various programs in place directed towards the advancement of new gas turbine engines and aerospace vehicle technology and the support of current gas turbine engines. These programs include Integrated High Performance Turbine Engine Technology (IHPTET), Titanium Matrix Composite Turbine Engine Component Consortium (TMCTECC), National Turbine Engine Durability (NTED), Engine Rotor Life Extension (ERLE), etc. The primary goals are: (1) improved performance, i.e., maintain properties at higher service temperatures, and (2) reduction in weight, i.e., use of lightweight materials with high-temperature capability. Advanced materials such as gamma titanium aluminide (γ -TiAl) alloys, high-temperature intermetallics, TMC, and CMC are leading candidates to satisfy these needs for various engine components. In addition, the need to extend the life of a wide range of current aerospace components has resulted in programs such as the HCF initiative, Aging Aircraft, and Propulsion Life Extension (anticipated). These programs are directed towards conventional materials, such as aluminum alloys, Ni-base superalloys and titanium (Ti) alloys (near α and $\alpha+\beta$). To apply the advanced materials effectively or to consider further applications of conventional materials that have experienced service conditions, a thorough understanding of the material behavior must be obtained and a methodology of life prediction for these materials must be developed or refined.

2.2 PROGRAM OBJECTIVES

The primary objectives of this program are to:

- (a) evaluate the performance of advanced and conventional materials under simulated service conditions
- (b) develop and/or adapt experimental techniques for characterization of deformation, damage evolution, and failure of advanced and conventional materials under typical service conditions
- (c) develop an understanding of the mechanisms leading to deformation, damage accumulation, and failure of advanced and conventional materials under a variety of test conditions including simulated mission cycles
- (d) develop physically-based deformation and life prediction models necessary to ensure in-service reliability and maintainability of advanced and conventional materials subjected to aerospace usage loading conditions
- (e) transition the new technology to USAF suppliers and customers
- (f) use and update the data for various aerospace materials in the current archival system and enhance the materials data archival procedure

2.3 REPORT ORGANIZATION

This second interim report presents the research conducted on the material behavior and modeling of aerospace materials within the Behavior/Life Prediction Section (MLLMN) of the Metals Branch (MLLM) in the Metals, Ceramics & Nondestructive Evaluation Division of the

Materials and Manufacturing Directorate at Wright-Patterson Air Force Base, OH. This effort was conducted over the period from 25 May 1999 to 24 May 2000. The investigations that have been completed and were in progress during the second year of the contract will be discussed in this report.

In sections 3, 4, 5, and 6, the material properties and damage assessment for γ -TiAl, TMC, CMC, and other engine materials, respectively, are discussed. The development of experimental procedures and test techniques, methodologies, and laboratory enhancements are presented in section 7. Extended discussions of the work-in-progress are presented to provide as much information as possible about the current investigations. Copies of the manuscripts which have been written on the completed efforts are provided in the Compendium for the convenience of readers who wish to have more detailed information of the investigations readily available.

SECTION 3.0

DAMAGE TOLERANCE STUDIES OF γ TiAl-BASE TITANIUM ALUMINIDE

3.1 MECHANISMS OF FATIGUE CRACK INITIATION IN TiAl INTERMETALLIC ALLOYS

3.1.1 Elastic Behavior of Fully Lamellar Gamma Titanium Aluminides

Gamma titanium aluminide (γ -TiAl) alloys are being considered for application in rotating components of gas turbine engines. While the elastic properties of gamma and alpha-2 single-phase materials have been thoroughly investigated, the elastic response of fully lamellar, two-phase materials have not received the same amount of attention. Detailed reports on the elastic property information of two-phase gamma alloys are scarce. Also, colony-level properties are required for development of accurate models in these material systems. In an effort to determine colony-level properties, samples with gage sections composed of specifically oriented individual lamellar grains were tested in tension to determine the elastic behavior of this two-phase structure. Preliminary attempts at modeling the elastic behavior of this material have shown good agreement with the experimental results. Efforts at modeling the elasto-plastic behavior of the large grain specimens are currently underway.

3.1.2 Effects of Microstructural Anisotropy on Fatigue Behavior of Gamma TiAl Alloys

The notch sensitivity of a fully-lamellar γ -TiAl alloy to fatigue crack initiation and failure was investigated. Tests indicated a pronounced degradation in fatigue strength and an increase in data scattering for multiple-notched specimens as compared to smooth bars of the same geometry and material. Examination of the failure origins in the notched specimens found that crack initiation was dependent upon the orientation of the particular colony that cracked. The notches decreased the fatigue crack initiation stress and minimized the crack initiation period by promoting rapid mode I crack initiation in colonies oriented with the α_2 and γ interface at low angles ($<20^\circ$) to the notch plane. Extensive work on the determination of the notch-colony orientations, utilizing scanning electron microscopy (SEM) and OIM, further concluded that the initiation notch-colony angle was the smallest of the notched colonies.

3.1.3 Lamellar Colony Orientation Determination in Gamma Titanium Aluminides Using Orientation Imaging Microscopy (OIM)

The lamellar microstructure of gamma titanium aluminides is characterized by strong crystallographic anisotropy, resulting in anisotropic mechanical properties. OIM, which is based on SEM utilizing electron backscattered diffraction patterns, determines crystal orientation on a microstructural scale. The fatigue crack initiation and propagation mechanisms of this class of alloys are governed by microstructurally inhomogeneous plastic deformation. This process is strongly affected by the lamellar colony orientation relative to the loading axis. Suitable operating parameters of OIM have been determined to obtain lamellar lath orientation mapping and the colony orientation has been analyzed using OIM software. The results of the lamellar colony orientation have also been used to calculate the lath spacing associated with SEM results; lath spacing is a microstructural parameter known to have a major effect on the mechanical properties.

3.1.4 Defects in 3-95M Wrought Gamma Titanium Aluminides

The IHPTET Phase 3 requirements call for substantial use of γ -TiAl alloys in blade and disk applications. To aid designers in their understanding of these types of materials, the development of life prediction models for intermetallic materials is required. To develop robust models, mechanical property information generated through assorted experiments is needed. Our efforts focus primarily on determining the fatigue properties of these alloys and the mechanisms controlling this behavior. The materials of interest need to be fully characterized with respect to their chemical homogeneity and resulting microstructures, as well as their overall integrity (i.e., the presence of voids or inclusions). To accomplish this task, forgings slated for use in the IHPTET program and manufactured using the gamma alloy known as 3-95M (nominal chemistry: Ti-46.5Al-1.5Cr-2Nb-0.5Mo-0.125B-0.26C (at%)) were interrogated before an extensive testing program was initiated. X-ray radiography revealed elemental segregation associated with flow lines in the forgings and extensive porosity in the center of the forgings. The SEM investigation of the areas where elemental segregation was apparent revealed no appreciable microstructural variations and this phenomenon was deemed insignificant. Most of the porosity appeared to be associated with the original cast ingot, while a small percentage may have been strain induced during hot working. Upon further investigation using SEM, the microstructure of the high-density regions exhibited a grain boundary beta phase encircling small lamellar grains with finely spaced laths. Small, equiaxed gamma grains were found along the interfaces of the lamellar/grain boundary beta phases. The high density regions are thought to be remnants of the master alloy additions used during ingot production. Their presence indicates incomplete melting of the master alloys due to inadequate heat introduced during melting and/or insufficient residency time in the melt path. Overall, the characterization results have led to changes in future gamma titanium aluminide melting practices that, ideally, will allow for delivery of a reliable, low-defect content material.

3.2 MODELING EFFORTS ANALYSIS OF STRESS CONDITIONS LEADING TO INITIATION

3.2.1 Modeling of Anisotropic Behavior in Lamellar TiAl

Our efforts to understand the nature of crack initiation in γ -TiAl has focused on three-dimensional models of TiAl polycrystals that predict the local variation in stress and strain caused by anisotropy and differences in orientation among neighboring grains. The results are best represented in statistical form, depicting the cumulative distribution of stress levels within a sample of material. Recently, we have performed simulations using progressive model refinement to examine the convergence of the numerical solutions, since numerous singular points exist in these models at the multiple-phase interfaces. This study confirmed that, although pointwise stresses near singularities are sensitive to model refinement, cumulative probability statistics based on the amount of material volume at a given stress level are relatively well behaved. We also have studied models representing successively larger material samples (at constant refinement), to determine the sample size that must be included in the model to eliminate boundary effects. Calculations have been made, based on the elastic finite element results, to compare the Schmid resolved shear stress within individual lamellar colonies with the actual interlamellar shear stress. These results explicitly separate the effect of grain orientation from that of stress variations caused by stress concentrations and by orientation differences in adjacent material grains.

3.2.2 Crystal Plasticity Model for Lamellar TiAl

The initial development of a crystal plasticity model for fully lamellar γ -TiAl has been completed. This model has been used to analyze polycrystal models like those used in the elastic calculations above; we believe these are the first three-dimensional polycrystal simulations of this material. Predictions of polycrystal stress-strain curves, starting with constituent properties of the γ (TiAl) and α_2 (Ti_3Al) phases, are in reasonable agreement with experimental measurements. The plasticity solutions reveal that localized yielding occurs at extremely small macroscopic strains, further affecting the localized stress variations arising from orientation differences from grain to grain. Data from the crystal plasticity solutions has been used to assemble stress statistics, similar to those from the elastic models, and analogous information about localized plastic strains. Further work with the plasticity model will involve more sophisticated representation of the hardening behavior and development of more detailed models of the mutual constraint between material phases within the lamellar microstructure.

SECTION 4.0

DAMAGE ACCUMULATION AND FAILURE OF Ti-MATRIX COMPOSITES (TMC)

4.1 CYCLIC CRACK PROPAGATION PARALLEL TO FIBERS IN A UNIDIRECTIONALLY REINFORCED METAL MATRIX COMPOSITE [C1]

The crack growth parallel to fibers in unidirectionally reinforced SCS-6/TIMETAL®21S was studied at room temperature using multiple geometries and stress ratios. Baseline characterization of neat (fiberless) TIMETAL®21S was also conducted. Closure levels were determined from the load-crack mouth opening displacement responses measured during crack growth. The crack growth behavior was geometry independent confirming the applicability of linear elastic fracture mechanics. The composite exhibited high closure levels of K_c/K_{max} up to 0.8. Similar to the neat TIMETAL®21S response, the use of effective ΔK based on closure correction enabled correlation of the crack growth behavior of the composite up to $R=0.8$. The conventional net-section based prediction of the $[90]_4$ composite response overestimated the crack growth rate at medium to low ΔK . An effective ligament method was proposed to incorporate the nonplanar fracture, and successfully used to correlate the crack growth rate behavior of the $[90]_4$ composite to that of the neat matrix. The apparent fracture toughness of the composite was also successfully predicted using the proposed model.

4.2 USER'S MANUAL FOR THE COMPACT FIBER TEST MACHINE [C2]

Due to the many investigations concerning the behavior of TMC, an inexpensive but effective test system was developed to evaluate the tensile stress-strain behavior of the various types of fibers used in the TMC. The manual outlines the procedures used to conduct tension tests on single fiber specimens. Individuals need not have extensive knowledge of fiber testing procedures to understand and use the manual. However, prior experience may allow the operator to improve on some of the techniques discussed in this manual.

In addition, the manual contains a description of the test system, a method to extract *in situ* fibers from the processed TMC that did not apparently degrade the fiber strength, and a procedure to evaluate the tensile behavior of ductile wire.

4.3 TENSILE, CREEP, AND FATIGUE BEHAVIOR OF $[0]_8$ TRIMARC1/Ti-6-2-4-2

A program in support of an Air Force sponsored SBIR Phase II program with Accurate Automation Corporation was conducted to evaluate the behavior of a TMC. Tensile, creep, and fatigue tests were conducted on $[0]_8$ Trimarc1/Ti-6Al-2Sn-4Zr-2Mo. All specimens were monitored to obtain acoustic emission (AE) signals during each test to assess damage evolution. Additional information on the AE system and sensors used in this program are described in section 7.2.5 of this report. One of the objectives of these tests was to evaluate the evolution of damage as a function of a given test type as well as a function of the various test conditions within a test type.

The test specimens were machined from two HIP TMC panels that were made by a powder-tape process by ARC. The fiber volume of the panels was between 35 and 36 percent. An

examination of the cross section of a specimen machined from the middle of one of the panels indicated that fiber spacing was fairly regular and no fibers were touching.

Dogbone specimens were used for the tests. The gage section was 17.8 mm long, 1.5 mm nominal thickness, and 6.0 mm wide for the tensile specimens or 7.5 mm wide for the creep and fatigue specimens. Tensile tests were conducted at room temperature and 371°C (700°F). Creep tests were conducted at 371°C (700°F) and at various stress levels. Fatigue tests were conducted at stress ratios of 0.05 and 0.5 at both room temperature and 371°C (700°F) and at various stress levels.

The AE signals were obtained from two pairs of sensors. Each sensor of one pair was placed in direct contact with each end of the specimen. These sensors were primarily activated by longitudinal waves created by an AE event. Each sensor of the second pair was placed in direct contact to one end of a 0.50 mm diameter ceramic rod. The other end of each rod was touching the surface of the specimen on either side of the hot zone for the elevated temperature tests and in the same locations of the specimen for the room temperature tests. As a result of the very small physical contact region between the rod and the specimen surface, the waves transmitted by the rods to the sensors were primarily activated by Rayleigh or flexural waves created on the specimen surface by an AE event.

4.4 A POWER LAW CREEP MODEL FOR NEAT Ti-6-4

A conventional type creep model for the titanium matrix in SCS6/Ti-6-4 had been investigated for characterizing the creep behavior of neat Ti-6-4 over a range of temperatures and stresses. The model was based upon a product between a function of stress and temperature and an exponential decay in time for the primary creep response summed with a product between a second function in stress and temperature and a linear function in time for the secondary (steady) creep behavior. The tensile creep data were generally fit very well over the range of temperatures (370 to 538°C) and stress levels (0 to 485 MPa) with this model. However, the model was under predicting the short-time relaxation behavior. Since the model was also under predicting the initial creep rate behavior, a third term, also having an exponential decay in time, was added to the model to provide a better fit to the initial creep rate data. Currently, this model is being implemented in several codes used for the prediction of stress and strain behavior of the neat matrix under relaxation and fatigue conditions and of a TMC under sustained load.

SECTION 5.0

DAMAGE ACCUMULATION AND FAILURE OF CERAMIC MATRIX COMPOSITES (CMC)

5.1 MECHANICAL AND THERMOPHYSICAL CHARACTERIZATION OF OXIDE/OXIDE NEXTEL™720/AS CMC AND NEXTEL™610/AS CMC

5.1.1 Monotonic Fracture Behavior of Double-Edge Notched Oxide/Oxide Nextel™720/AS Composite [C3]

An investigation on the effects of notches on the fracture strength and damage at room and elevated temperature was initiated on Nextel™720/AS. Two double-edge notched geometries were studied, semicircular and sharp (saw-cut) notches with notch tip radii 1.88 mm and 0.1 mm, respectively. Strain gages, extensometry, and fractured samples were used to characterize the damage zone in the vicinity of the notches. Nextel™720/AS exhibited notch insensitive behavior for a range of tip radii and temperatures. Only at temperatures $\geq 1100^{\circ}\text{C}$ did the Nextel™720/AS CMC show any observable notch sensitivity that was characterized by a 15 percent decrease in net-section failure strength. Finite element predictions of stress-strain behavior at the notch tip showed good agreement with the measured strain gage data.

5.1.2 Creep Rupture Behavior of Double-Edge Notched Oxide/Oxide Nextel™720/AS Composite [C4]

Unnotched and double-edge notched Nextel™720/AS specimens were tested under tensile and sustained load (creep) conditions at 1100°C . Two notch tip geometries were evaluated with elastic stress concentration factors $K_t = \sigma_{\text{tip}}/\sigma_{\text{nom}} = 2.3$ and 7.2 with notch tip radii, 1.88 and 0.1 mm, respectively. The Nextel™720/AS exhibited a 15 percent decrease in net-section failure strength under tensile loading and 40 percent reduction in rupture strength for a life of 100 hours. The decrease in tensile and rupture strength was independent of the initial stress concentration at the notch tip. The results from this study showed that design of durable CMC components with notches should account for the increased notch sensitivity under sustained load conditions.

5.1.3 Damage Progression from Double-Edge Notched Oxide/Oxide Nextel™720/AS Composite Under Creep Loading

Damage progression from double-edge notches in the oxide/oxide composite Nextel™720/AS was investigated using destructive evaluation of failed and multiple interrupted test specimens. The double-edge notched specimens, with notch tip radii of 0.1 mm, were tested at 1100°C under monotonic and sustained load conditions, in lab air. Results of the study showed that thermal exposure at 1100°C , with zero applied stress produced no significant observable changes in the matrix crack morphology of the composite from the as-received condition. Similarly, an as-received specimen that was rapidly loaded to 100 MPa at 1100°C , followed by immediate unloading showed no observable damage in the notch tip region. After sustained loads however, matrix cracking and fiber breakage were observed near the notch tips. The extent of the observed damage was < 0.6 mm beyond the notch tip, which is less than the width of an individual fiber tow.

For creep rupture specimens, the damage observed on the fracture surfaces showed that longitudinal fibers extended beyond the fracture plane to a length of up to 4 mm near the notch tip. In the center portion of the specimen the fracture profile was relatively flat with little fiber extension (<1 mm). The flat fracture profile in the center portion of the notched specimens compared closely to the entire fracture profile of the unnotched specimen. The observed damage progression suggests that for double-notched specimens, damage within the first fiber tow effectively redistributed the notch tip stress concentration, resulting in a nearly uniform stress condition away from the notches. The observed creep damage away from the notches was therefore similar to that in the unnotched composite.

5.1.4 Effect of Heat Treatment on the Mechanical Behavior of Oxide/Oxide Nextel™720/AS Composite

Unnotched and double-edge notched Nextel™720/AS specimens were heat-treated at 1100°C in laboratory air for 100 hours. Tension tests of as-received and heat-treated specimens were conducted at room temperature. The test results showed that heat treatment at 1100°C for 100 hours reduced the room temperature strength and strain to failure by approximately 50 percent for both the unnotched and notched geometries. The elastic modulus of the composite remained unchanged by the thermal aging. The results from this study were in agreement with data previously collected.

5.1.5 Characterization of Thermophysical Properties of Oxide/Oxide Nextel™720/AS Composite

The University of Dayton Research Institute issued a purchase order to the Thermophysical Properties Research Laboratory (TPRL) for thermal conductivity and coefficient of thermal expansion (CTE) measurements on the as-received Nextel™720/AS composite. The thermal conductivity and CTE properties were measured for both in-plane and through-thickness orientations for temperatures of 23 to 1100°C at 100°C increments. Both the in-plane and through-thickness data showed that the thermal conductivity were relatively constant over the range of test temperatures. The in-plane thermal conductivity was approximately 2.3 W/mK and was independent of the orientation in the plane of the plate. The through-thickness thermal conductivity was approximately 20 percent lower than the in-plane results. The CTE data for the in-plane and through-thickness orientations were almost identical. Both CTE data sets showed a moderate increase in CTE from 4.5 ppm/°C at room temperature to 6.0 ppm/°C at 1100°C.

5.1.6 In-Plane Shear Behavior of Oxide/Oxide Nextel™720/AS & Nextel™610/AS Composite

The in-plane shear behavior of Nextel™610/AS and Nextel™720/AS oxide/oxide composites was investigated at 23 and 950°C in lab air. Tensile tests were conducted on specimens with fiber reinforcement oriented at [±45°] to the loading axis. Strain gages were used to measure deformation in the direction of the loading axis and transverse to the loading axis. The tensile tests at 23°C were conducted on specimens 12.6, 25.4, and 38.1 mm wide in order to examine the effect of specimen width on the in-plane shear behavior. No effect of specimen width was observed. Results of the in-plane shear tests at 23°C showed that the Nextel™610/AS and Nextel™720/AS shear stress-shear strain response was nonlinear with a gradual failure of the composite under displacement control. The Nextel™610/AS shear stress-shear strain behavior at 950°C was approximately linear with a brittle failure mode. The fracture surface profiles of the failed specimens showed that during failure at 23°C, matrix disintegration allowed entire fiber tows to be pulled from the matrix, resulting in a fibrous fracture surface. The slow fiber pullout was

consistent with the nonlinear shear deformation behavior. At 950°C, fibers were failed at the fracture plane, consistent with the brittle failure mode.

5.1.7 Fracture Behavior of Single-Edge Notched Oxide/Oxide NextelTM610/AS Composite Under Cyclic Loading [C5]

The fracture behavior of NextelTM610/AS oxide/oxide composite was investigated at 23 and 950°C using a single-edge notched specimen geometry with a notch tip radius of 0.2 mm and clamped end conditions. Crack growth and damage progression was monitored during the tests using optical microscopy, ultrasonic C-scans, and crack mouth opening displacement (CMOD). NextelTM610/AS was found to be notch sensitive, with net section failure stresses below the unnotched ultimate tensile strength. The failure mode was nonbrittle with nonlinear net section-CMOD response prior to and after the peak load at 23 and 950°C. The effect of temperature on the notched strength was significant. Net section failure stress decreased 50 percent when temperature was increased from 23 to 950°C. Observations of damage progression indicated that the reduction in notch strength with temperature was associated with self-similar crack growth at 950°C. Ultrasonic C-scans were found to be an effective method of monitoring damage progression. Ultrasonic attenuation ahead of the notch tip was correlated with surface matrix cracks and exposed fiber lengths on the fracture surface.

5.1.8 Damage Progression from Single-Edge Notched Oxide/Oxide NextelTM610/AS Composite Using Ultrasonic C-scans [C6]

Ultrasonic C-scans were used to monitor the damage progression that developed during quasi-monotonic loading from notches with a notch tip radius of 0.2 mm in NextelTM610/AS oxide/oxide composite. Test specimens were monotonically loaded, removed from the test machine, then ultrasonically C-scanned using a through transmission, reflector plate method. The level of ultrasonic attenuation was monitored as a function of applied stress and correlated with the matrix cracking observed within the composite. Results of the study showed that the ultrasonic technique successfully monitored the progressive matrix cracking prior to the peak load in specimens tested at 23°C. Close to the peak load, fiber breakage occurred near the notch tip, which was not indicated by the ultrasonic C-scans. At 950°C, damage progressed from the notch as a single dominant crack. The ultrasonic attenuation in the C-scans correlated well with the crack length from the notch.

5.1.9 Characterization of Notched Fracture Behavior of NextelTM610/AS Oxide/Oxide Composite at 23 and 950°C Under Multiple Loading Conditions

Notched fracture behavior was studied in NextelTM610/AS oxide/oxide composite [Kramb, 1999]. The notched composites were tested under monotonic, cyclic and sustained tensile loading conditions in air at temperatures of 23 and 950°C. The results of the experimental tests were analyzed using linear elastic fracture mechanics and finite element modeling. The applicability of isotropic and orthotropic continuum material models to predict deformation behavior were examined.

Fracture tests showed that notch sensitivity was geometry and temperature dependent. At 23°C, open center hole specimens were notch insensitive. In contrast, edge notched fracture specimens were notch sensitive. At 950°C, failure stress decreased by 50 percent and 33 percent for the edge notched and open center hole geometries, respectively. Unnotched [$\pm 45^\circ$] tension tests conducted at 23 and 950°C showed that, the in-plane shear response was

temperature dependent. The observed changes in shear behavior correlated with the changes in notched load-deformation behavior with temperature.

Destructive and nondestructive evaluation of tested specimens showed that, at 23°C, damage progression was characterized by distributed matrix cracking within 90° fiber tows, above and below the notch plane. Longitudinal fiber breakage did not occur until close to the peak stress. At 950°C, damage progression in edge notched specimens was characterized by matrix cracking over a smaller region, resulting in limited stress redistribution and fiber breakage at a lower applied stress. At 950°C, open center hole specimens failed abruptly with no prior crack growth.

Using a finite element model of the notched specimens, applicability of isotropic and orthotropic continuum models to predict deformation was assessed. Comparisons between the predicted deformation and the measured deformation showed that at 23°C deformation response was linear elastic in the fiber directions and nonlinear away from the fiber directions.

5.2 MODELING AND MECHANICAL DESIGN ANALYSIS OF OXIDE/OXIDE NEXTEL™720/AS CMC

5.2.1 Development of Finite Element User Material Subroutine for Oxide/Oxide Nextel™720/AS Composite Deformation

A User Material (UMAT) subroutine for the Nextel™720/AS oxide/oxide composite material was developed and implemented with the finite element code ABAQUS. The homogeneous model was based on the monotonic tensile stress-strain and monotonic shear stress-shear strain response of the composite. The model was verified by comparison with strain gage data from notched specimens. In experiments with semicircular notches, strain gages were mounted at the perimeter of the notch in the loading direction and at a 45° angle to the loading direction. The deformation predictions from the model were in excellent agreement with the experimental results.

5.2.2 Analysis of Local Stresses in Notched Oxide/Oxide Nextel™720/AS Composite

In connection with the development of constitutive models for static loading and creep of Nextel™720/AS oxide/oxide composite, analytical studies were performed to evaluate whether a material model that does not represent the weave pattern explicitly could reproduce the extremely localized behavior observed in experiments. To this end detailed analyses (ca 10^6 finite elements) of a notched composite test specimen have been conducted to define the rate of decay of stresses near the notch. In experiments with very sharply notched coupons, notch tip radius = 1.88 mm, damage caused by the stress concentration was limited to an area of one or two fiber tows wide. The same localized response has been successfully modeled with a homogeneous model. Thus, demonstrating that the models under development for damage and creep might be applied correctly without representing the detailed geometry of the weave in a finite element model.

5.2.3 Elasticity, Creep, and Damage Model for Oxide/Oxide Nextel™720/AS Composite

An accurate steady-state creep model for the Nextel™720/AS oxide/oxide composite has been developed and validated by comparison with experimental creep measurements. Progressive fiber damage during loading and creep was predicted using a model which links fiber damage rate to the instantaneous strain rate, using properties derived directly from Weibull statistics for

fiber failure. Local stress analysis of the weave, which was necessary to distinguish the relative amounts of stress carried in the fibers and matrix, was based on a Mori-Tanaka model. The accuracy of the creep model has been verified through several blind predictions, all of which were within a factor of two of the measured creep rate. This one-dimensional model presently is being extended to three-dimensions for use in finite element calculations on notched specimens and other irregular geometries.

5.2.4 Heat Transfer and Stress Analysis of Oxide/Oxide Nextel™720/AS Composite Combustor Conceptual Design

Several heat transfer and stress simulations of conceptual designs for the ultra-compact turbine engine combustors have been evaluated using Nextel™720/AS oxide/oxide material properties.

Steady-state heat transfer and stress calculations have been performed to investigate the feasibility of using an oxide/oxide CMC in high-g combustor applications. Potential areas of concern included the required surface temperatures and thermal stresses induced by temperature variations in the combustor shell. Of particular interest were the thickness temperature gradients caused by forced convection cooling of the combustor wall and the longitudinal thermal gradients caused by varying heat loads and flow conditions.

Stress analyses have been performed of designs using single and multiple materials and of one-piece and segmented combustor shells. Although the simulations were highly idealized, several valuable conclusions have emerged. The most serious stress problems occurred near the inlet to the high-g chamber where a significant thermal gradient existed or in the cavity proper. Within the cavity, stress problems typically involved bending stresses caused by the thickness temperature gradient. In the inlet (or outlet) region, where the radiative heat load dropped off sharply, a significant thermal gradient always existed although its orientation (thickness or longitudinal) depended upon the shell geometry. Additional concepts involving the use of hybrid or functionally graded materials are being investigated as well.

5.3 PRELIMINARY OBSERVATIONS OF THE MONOTONIC TENSILE BEHAVIOR OF MI SiC/SiC CMC

The monotonic tensile stress-strain behavior of melt infiltrated (MI) Sylramic/BN/SiC ceramic matrix composite was investigated at room temperature in laboratory air. Four specimens were selected from three different panels. The measured ultimate strengths of specimens from two of the three plates were 25-50 percent lower than were reported in the literature. The third panel strength was approximately 10 percent lower than expected. The elastic modulus results were in agreement with those reported in the literature. The fracture surface and composite microstructure were examined using an optical and an SEM. The optical microscope images showed large regions of matrix porosity and a relatively flat fracture surface. The SEM images showed good fiber distribution however evidence of severely oxidized fibers in the panels was apparent that exhibited poor tensile strengths.

SECTION 6.0

HIGH CYCLE FATIGUE AND FATIGUE CRACK GROWTH IN AEROSPACE MATERIALS

6.1 FRETTING FATIGUE

6.1.1 Fretting Fatigue of Ti-6Al-4V Under Flat-on-Flat Contact With Blending Radii

A study was conducted to investigate fretting fatigue damage of Ti-6Al-4V against Ti-6Al-4V under flat-on-flat contact with blending radii at room temperature. Both the location of and the time required to nucleate fretting fatigue cracks were investigated for two static average clamping stress values that are representative of those estimated for turbine engine blade attachments. The axial fatigue limit for a 10^7 cycle life was determined at 300 Hz and $R = 0.5$ for average clamping stresses of 140 and 420 MPa. Then, feasibility of *in situ* fretting fatigue crack detection using a shear wave ultrasonic technique was evaluated. Finally, the effect of fretting fatigue on uniaxial fatigue life was quantified by interrupting fretting fatigue tests, and conducting uniaxial residual fatigue life tests. Metallography, fractography, and spectral analysis were used to characterize the level of fretting damage. Experimental observations were supported with finite element analysis of a simplified two-dimensional geometry for the loading conditions under investigation.

Fretting fatigue limits for a 10^7 cycle life under the clamping stress conditions used were 330 MPa for the lower clamping stress and 250 MPa for the higher clamping stress and are 60 percent and 70 percent, respectively, lower than the uniaxial fatigue limit for this material. Using shear wave ultrasonics, cracks with a surface length of approximately 2 mm were detected on 10 mm wide specimens in tests conducted at the higher clamping stress. Fretting fatigue tests interrupted at 1 million cycles indicated significant fretting damage and reduction in residual uniaxial fatigue life for half of the specimens subjected to the higher clamping stress. Little observable damage and no reduction in residual uniaxial fatigue life were identified for the lower clamping stress.

Stress distribution trends from the finite element analysis supported experimental findings. Relative slip values determined from the analysis were lower than expected based on values reported in the literature. Results of the analysis were used to calculate the inherent bending moment in the experimental apparatus, which was determined to be small.

6.1.2 Characterization of Fretting Fatigue Crack Nucleation Life of Ti-6Al-4V in a Flat-on-Flat Contact [C7]

The effects of several parameters on fretting fatigue behavior in Ti-6Al-4V at room temperature were evaluated as part of an ongoing study. A flat-on-flat contact with blending radii was employed to simulate the geometry used in dovetail blade attachments. This investigation involved two phases of mechanical testing. The first involved interrupted fretting tests followed by residual strength uniaxial fatigue tests. Two average clamping stresses, 140 MPa and 420 MPa, were investigated. For each average clamping stress, three specimens were tested to failure using the step loading technique, to determine the limit stress for 10^7 cycles for each condition. The resulting fatigue limits from the step load tests were ~260 MPa for the 420 MPa clamping stress condition, and ~350 MPa for the 140 MPa clamping stress condition. In addition, three specimens for each clamping stress were tested to 10 percent of fretting fatigue

life using the limit stresses identified with the step load tests to identify the level of damage accumulation at 10 percent of life. The SEM inspection of the fretted regions revealed almost no damage to the specimens subjected to 140 MPa clamping stress. However, cracking and considerable wear to specimens subjected to the 420 MPa clamping stress was identified. Finally, three specimens for each clamping stress were tested using a shear wave ultrasonic procedure to attempt crack detection *in situ*. The two specimens that were stopped prior to specimen fracture had large cracks, which were undetectable with the shear wave apparatus until very late in life. All tests were conducted at $R = 0.5$.

The second phase employed specimens of varying thickness: 2 and 4 mm, under a range of clamping loads to evaluate changes in the fretting fatigue limit stress as a function of average applied shear stress at the contact. Tests were conducted at both $R = 0.1$ and $R = 0.5$. The SEM inspection revealed differences in cracking behavior, as identified in the first phase of mechanical testing for this investigation. No trends were observed with the average applied shear stress versus various average applied clamping stress.

6.1.3 Effect of Specimen Thickness on Fretting Fatigue Behavior

The applicability of laboratory fretting fatigue results to the modeling of behavior in dovetail components is debatable because of differences between the geometries in lab and service applications. Lab samples are usually thin specimens with fretting imposed on either one or both faces of the specimen, while service components such as dovetail blade attachments are relatively thick with appreciable distance between adjacent contacts. The University has developed a study to investigate the effect of lab specimen thickness on fretting fatigue behavior in an effort to link lab results and real component behavior, and to provide information on the effect of imposed shear force on fretting fatigue. The tests for this study have been completed for two of the three specimen thicknesses: 2, and 4 mm. The tests for the 1 mm thickness are ongoing. Finite element analysis to assist in explaining the test results is completed for the 2 mm thickness, and for selected conditions for the 1 and 4 mm thicknesses. Additional analysis is ongoing.

6.1.4 SEM Characterization Of Pre-Fretted Ti-6Al-4V Fatigue Specimens

SEM images were taken of four specimens supplied under the HCF program. All specimens were subjected to fretting fatigue damage with two normal stresses over two ranges of applied fretting cycles at $13\mu\text{m}$ (0.5 mil) relative displacement, as described in Table 1. None of the fretted surfaces were subjected to surface modifications such as shot peening. Overall, the fretting damage observed was minimal. The wear damage was nearly undetectable, and no cracks were detected throughout. The primary damage mechanism appeared to be removal or deformation of the surface layer left by the chemical milling process, with no third body particles present. Wear features characteristic of each of the four samples are shown in Figure 1. In this image, the material microstructure is seen clearly in the chemically milled region (right half), while the surface layer seems either to have been compressed or worn away in the fretted region (left half). In general, the level of wear was somewhat worse for higher normal stresses, and better for lower normal stresses than is indicated here. The dark smudges observed in the fretted region are most likely due to oxidation of the surface, which would imply wear.

TABLE 1: Specimen Test Conditions

Specimen Number	Normal Stress (ksi)	Number of Cycles	Relative Displacement (mils)
75-9	35.0	400,000	0.5
94-11	65.0	40,000	0.5
75-10	65.0	400,000	0.5
79-12	35.0	40,000	0.5

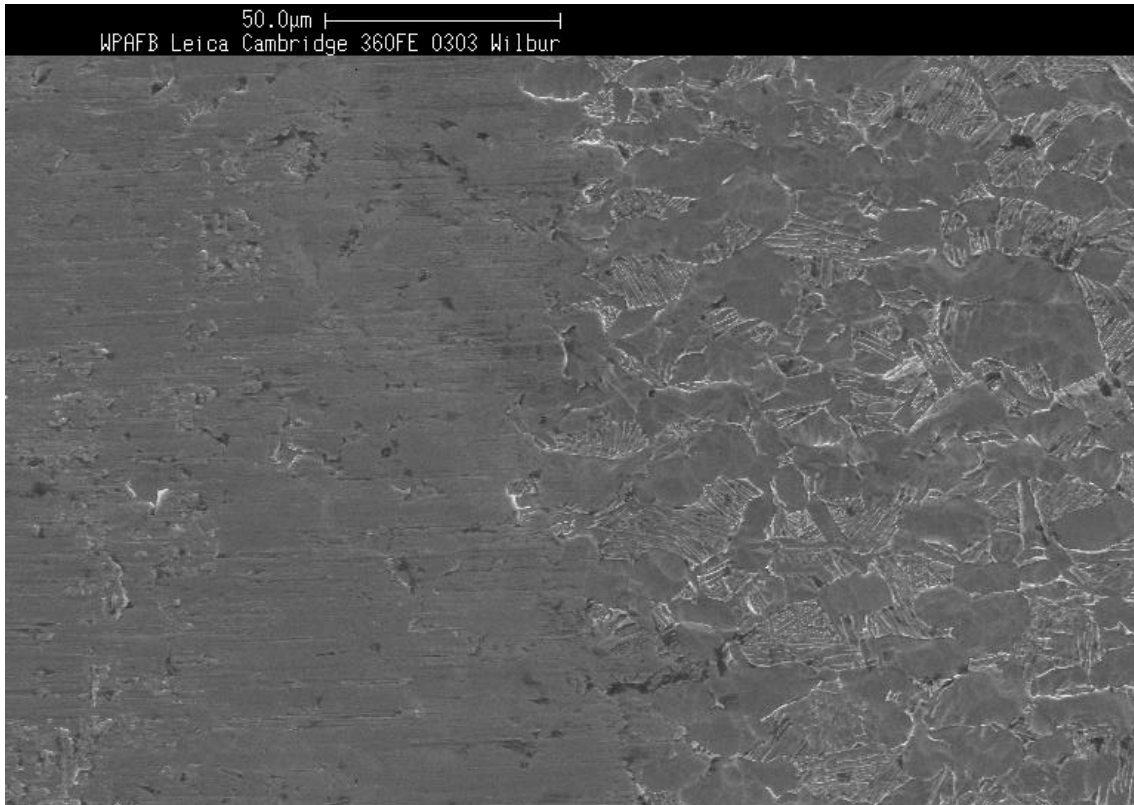


Figure 1. Fretted Region from 94-11. Unfretted surface is shown in the right half; the fretted surface is shown in the left half.

6.2 CHARACTERIZATION OF FOD IMPACT SITES ON Ti-6Al-4V UNDER HIGH CYCLE FATIGUE [C8]

Damage sites were characterized in simulated engine blades of Ti-6Al-4V that were subjected to ballistic foreign object impact damage. Diamond cross-sectioned tension (DCT) axial fatigue samples, with either a 0.381 mm (0.015 in) or 0.127 mm (0.005 in) leading-edge (LE) radius, were impacted with 1 mm (0.040 in) diameter glass spheres at a velocity of 305 m/s (1000 f/s) and at an angle of incidence of either 0° or 30°. Subsequent fatigue testing showed fatigue strength degradation as a result of the edge damage. Scanning electron microscopy showed a variety of damage features on the fractured notches. The characterized features included the notch depth, material loss at the notch, material shear, material folding over the LE, and embedded glass from the shattered bead. The fatigue strength of the damaged specimens at 10⁷ cycles was determined using a step loading procedure. Fracture initiation occurred generally at the deepest section of the notch region. However, the depth of the fractured notch

alone has no direct effect on the fatigue strength. The amount of material loss at the notch surface also had no apparent effect on the fatigue strength. Neither surface cracks, nor embedded glass fragments could be correlated with fatigue strength, in spite of the fact that cracks initiated at these features in most samples.

6.3 EVOLUTION AND EFFECTS OF DAMAGE IN Ti-6Al-4V UNDER HIGH CYCLE FATIGUE

An investigation was undertaken to evaluate the effects of mean stress on the HCF limit stress under uniaxial loading. Tests were conducted at a frequency of 70 Hz for a fatigue life of 10^7 cycles using a step loading technique and for the regime $R < -1$ to determine the effect of negative mean stress on the material behavior. Due to material behavior, the lowest mean stress that was investigated corresponded to $R = -4$. For lower mean stresses, the minimum applied cyclic stress would be lower than the monotonic compressive yield stress of the material. While numerous models could provide approximate fits to the data in the constant life High diagram for positive mean stresses, none of them captured the trends of the data at $R < -1$. The Jasper equation [Jasper, 1923], based on a constant range of stored energy density, was found to represent the positive mean stress data quite well. The equation was modified to account for stored energy density at negative mean stresses. The best fit to the data implied that compressive strain energy density contributed less than 30 percent to the fatigue process as the strain energy density under tensile stresses contributed.

6.4 HCF SYSTEM ENHANCEMENTS

Improvements to the HCF systems in the MLLMN laboratory were made in four areas. First, considerable effort was expended to upgrade the older DOS-based software to a LabView interface. Most of this work was completed on the 2 kHz test system although some progress was made on software for the large Unholtz-Dickie and C-20 systems as well.

Second, most of the components for a second small Unholtz-Dickie system were obtained and prepared for assembly. This design was chosen for replication since it has shown good performance in the region required for general HCF testing. The new system will be assembled using an improved set of instrumentation and electronics. Operation of this system will, in part, help to work out bugs in the new hardware in preparation for a general standardization of the equipment in the HCF laboratory.

Third, a large number of minor modifications were made to various systems to improve performance and add capability. Areas of improvement include system alignment, low-frequency load control, and soft-turn-on HCF cycles.

Fourth, physical plant planning and preparations were initiated to accept a new 20 kHz test system being developed at the UDRI. Preparations included evaluation of noise abatement options, relocation of existing equipment to provide the required floor space, utility installation (electrical service, etc.), and decisions concerning control system location.

6.5 CPLM FOR Ti ALLOYS

Methodologies for CPLM were improved to include additional solutions for direct current potential difference (DCPD) and certain test control feature enhancements. In addition, we have expanded the number of systems capable of running CPLM-type tests from two to four. The four systems are currently being used to study several titanium and titanium-aluminide

alloys and will be used for work with superalloys as work on the Engine Rotor Life Extension (ERLE) program ramps up. A large number of tests have been performed using this methodology to investigate its ability to predict load interaction effects on crack growth as well as certain threshold crack growth rate concepts.

6.6 FRACTOGRAPHIC OBSERVATIONS ON THE NATURE OF STRESS RATIO EFFECT IN FATIGUE

In an effort to investigate the effects of stress ratio on fatigue crack growth rates in small cracks, fractographic investigations of samples subjected to a three-step loading spectrum were undertaken. The spectra contained three blocks of fatigue cycles with three specific stress ratios ($R=0.64, 0.69,$ and 0.73). Each high-R block was separated by a band of marker cycles ($R=0.1$) to aid in determination of crack growth rates in each case. The results indicated that crack growth rates in small cracks were significantly effected by the applied stress ratio. The differences in crack growth rates were not attributable to closure effects. The differences also greatly diminished and eventually disappeared with increasing stress intensity. The effects of environment on stress ratio effects on crack growth rates in an aluminum alloy were also investigated. Growth rates in vacuum were substantially lower than those obtained in air. Also, no effect of stress ratio on growth rates was apparent in vacuum, unlike the case of small cracks tested in laboratory air.

SECTION 7.0

DEVELOPMENT OF EXPERIMENTAL PROCEDURES, METHODOLOGIES, AND LABORATORY ENHANCEMENTS

A number of new capabilities were added to the AFRL/MLLMN laboratories during FY00. These new capabilities fall into one of two categories:

- 1) infrastructure improvements related to overall laboratory test control and data management
- 2) specific types of apparatus or instrumentation that have been developed or enhanced

The capabilities added in these two categories are discussed in the paragraphs below. As one might expect, some crossovers exist between the categories and appropriate discussion is included to address these crossovers where they are important.

7.1 LABORATORY TEST CONTROL AND DATA MANAGEMENT

The AFRL/MLLMN laboratories are of sufficient size that a coordinated system of implementing new test technologies and methodology enhancements as well as managing the data collected from tests is required. The following paragraphs describe work performed to improve, extend, and/or replace this infrastructure.

7.1.1 WinMATE Development Support

The existing software for test control and data acquisition in the AFRL/MLLMN laboratories is, for the most part, based on the older MS-DOS operating system. The University initiated an effort to convert the DOS-based code to a Microsoft Windows-based system. While the bulk of the software development effort was performed as part of an SBIR program, some effort was expended on the on-site contract to support this initiative. Specifically, numerical solutions for DCPD versus crack length were obtained to develop a cohesive and comprehensive solution library. In addition, on-site staff performed evaluation of the emerging Windows-based software modules.

7.1.2 Improvement in Load Frame Alignment Equipment and Procedures

Several improvements were implemented in StraightArrow®, the load frame alignment hardware and software package developed by the UDRI and used in the AFRL/MLLMN laboratories. A new specimen was designed and fabricated to solve several shortcomings of commercially available alignment specimens. Analysis showed that a square cross section has the best overall bending sensitivity when compared to circular and rectangular cross sections. An aluminum alloy, 7075-T6, was chosen as the specimen material. The combination of low modulus and high yield strength of 7075-T6 made possible an alignment specimen that could reach 500 $\mu\epsilon$ at a load of 3.6 kN and required almost 50 kN to reach yield strength. The high conductivity of 7075-T6 provided the heat dissipation capacity needed to use larger strain gage excitation voltages. Larger excitation voltages increased strain sensitivity without increasing electronic noise in the system.

7.1.3 Upgrade Of Laboratory Test Automation Hardware and Instrumentation

As noted above, an SBIR effort and work on the on-site contract are both contributing to development of a Windows-based upgrade to the existing test automation software package in the AFRL/MLLMN laboratories. This software also requires upgrades to the test automation hardware in the laboratories – primarily in two areas.

First, the existing microcomputers associated with each test station were reaching the end of their useful lifespan both in terms of their component failure rate and their computational power. The University of Dayton has identified the critical requirements for new computers that will meet the needs of the new automation software and has purchased eight systems through government procurement channels. These systems have been integrated into selected laboratory test systems and have demonstrated excellent performance and reliability.

Second, the university has selected a comprehensive set of commercial interface hardware (adaptor boards) to connect the microcomputers to the test station instrumentation. The selected interface hardware was designed to have a 10 to 15 year life span before it becomes obsolete. In addition to the commercial interface boards, we have designed and constructed appropriate cabling and breakout boxes to allow easy operator access to all system signals. These components will be standardized for all laboratory systems to reduce operator training time and errors during test setup.

7.1.4 Design and Implementation of a Network for Laboratory Data Transfer

As part of the overall upgrade to the AFRL/MLLMN laboratory computer systems, the university has designed and obtained approval for the use of physically isolated networks (PINs) within the laboratory. A PIN was designed to meet the security needs of the USAF by being completely physically isolated from other data management systems including other intranets and the Internet. The PIN also met the research needs of the laboratory by allowing test control computers to operate in a real-time mode without the need for local security monitoring over the network.

The University has implemented one PIN within the AFRL/MLLMN laboratories for demonstration purposes. After obtaining appropriate approval, planning PINs for additional laboratory modules has begun as hardware and software become available. The performance of the demonstration PIN has met our expectations and will provide greatly enhanced efficiency and capability in managing data as well as in monitoring ongoing tests.

7.1.5 Data Archival and Status of Keyserver®

The Data Archive is a central computer on which test data generated by RG 2.3 is stored and indexed. Its purpose is to prevent the loss of valuable test data and provide independent user access within RG 2.3. Few fundamental changes have been implemented during FY00; however, a large volume of test data was added to the archive for both fibers and coupons.

Software and hardware support for the server has been maintained by government computer support (MLOC) in coordination with the needs of RG 2.3. The transfer of computer software and hardware administration responsibilities took place during FY00, prompted by changes in USAF computer administration policy requiring all system administrators to hold secret level security clearances. The UDRI still supports local administration of file access privileges and works with MLOC on global system administration. The Keyserver® system, which was put in

place in 1996 to provide hands-off control of commercial software licenses, has also been maintained.

7.2 APPARATUS AND INSTRUMENTATION

The AFRL/MLLMN laboratories have a long tradition of developing state-of-the-art instrumentation designed to provide critical information on material behavior under various test conditions. The following paragraphs describe work performed in FY00 by the University of Dayton to continue in this tradition of innovation and creativity.

7.2.1 Infrared Damage Detection System (IDDS)

An infrared camera, frame grabber, computer, and software module were combined to produce a system that can detect extremely localized damage in a specimen under fatigue cycling. The system detects changes in infrared emissions due to temperature changes, surface emissivity changes, cavity radiation, or other phenomena. The detection is fully integrated with a waveform generator so that infrared "snapshots" can be made at different points in the loading cycle at loading frequencies up to about 50 Hz. The system has been used on titanium alloys to detect cracks with total surface lengths of less than 20 μm .

7.2.2 Short-Gage-Length LVDT Extensometer Development

The university has previously designed, fabricated, and tested a 12 mm gage length linear variable differential transformer (LVDT) extensometer for elevated temperature use. This extensometer showed an order of magnitude better stability as compared with commercial strain-gage-based extensometers under similar test conditions. Within the last year, the need for a shorter gage length extensometer has become apparent. Thus, a 4 mm gage length version of the LVDT extensometer was designed and fabricated. This unit showed the same sensitivity as the original 12 mm gage length unit but, as anticipated, was somewhat more difficult to physically mount on the specimen. Nevertheless, the new unit has been successfully used to test single grain regions of titanium alloys.

7.2.3 Design of a High-Resolution Displacement Calibrator

The LVDT extensometers described above have excellent sensitivity being able to resolve displacements as small as 50 nm. Their stability was such that the 50 nm resolution could be effectively used in material testing. A calibration device capable of accurately imposing displacements of at least as small as 25 nm would be required to fully utilize this extremely fine displacement resolution. The best mechanical calibration devices typically have resolutions on the order of 500 nm not including backlash.

Based on these considerations a calibration device was designed to deal with full scale displacement calibrations from 500 nm up to about 100 μm with a resolution of approximately 5 nm. The device is based on a solid-state magnetostrictive actuator coupled with a flexing end plate. This arrangement limited the total motion, however, extremely fine control of displacement would be achieved. The actual calibrator displacement was measured using an integrated HeNe laser interferometer device. The interferometer is considered an *a priori* traceable standard by NIST and, thus, periodic outside calibration of the unit is not required.

Most of the components have been ordered and received and we anticipate fabricating and testing the calibrator during the next fiscal year.

7.2.4 Improvements to Direct Current Potential Difference Crack Detection (DCPD) Systems

DCPD systems have been used in the AFRL/MLLMN laboratories for some 20 years or more to detect and measure cracks and crack propagation. The basic DCPD tasks of imposing a constant current and measuring small DC voltages have remained the same. However, the technology available to perform these tasks has changed substantially. The latest enhancements included a new, ultra-high resolution A/D converter, multiple channels of measurement, and improved software. The 26-bit A/D converter was originally designed for military inertial guidance systems and could measure DC voltages to one part in 67 million – a significant increase over the earlier 18-bit systems. Multiple channels of measurement allowed the operator to average multiple readings for a single crack, use one channel to normalize readings and reduce thermal drift, or monitor multiple cracks simultaneously. The improved control and data acquisition software allowed the operator to configure the system for a wide variety of test types.

7.2.5 Improvements in the Acoustic Emission (AE) Detection of Damage in MMC During Mechanical Testing

Improvements were made in existing AFRL/MLLMN AE technology including enhanced data processing, improved data acquisition hardware, and more consistent test protocols. Several data processing modules were written to convert binary data to ASCII format, filter the AE data, analyze the data, and view the AE events from each of the four sensors. The different modules were combined into one Windows-based program for ease of use. A number of enhancements were also made to the AE data acquisition hardware. A function generator was installed to correlate AE events between two separate AE systems across 24-hour periods. A load-slope circuit was implemented to indicate whether an event occurred during increasing or decreasing load. Finally, the test procedure was optimized and written instructions were produced. A test process sheet was developed and used for all of the tests to record the settings of the AE systems, mechanical test and specimen parameters, and significant changes during the testing.

7.2.6 Design of Shear Wave Ultrasonic NDE Techniques for Detecting Fatigue Cracks During Fretting Fatigue Tests

Fatigue cracks initiated under fretting conditions [Hutson, 2000] were detected using shear wave ultrasonic techniques. The 10 MHz ultrasonic shear waves were induced in the specimen and transmitted to the fretting interface via routes that included multiple surface reflections. The ultrasonic energy reflected from the fretting interface was monitored and recorded. Analysis of this reflected energy represented cracks formed at the interface with characteristic dimensions on the order of 250 μm . This analysis also revealed that careful time-alignment of the ultrasonic signals from sequential readings was critical due to the strain induced by the applied load.

7.2.7 Blade Root Fretting Fatigue Apparatus Design

A fatigue fretting test apparatus was designed and constructed that simulates a single tooth firtree structure commonly used to join blades to a rotating structure such as a disk. The relative motion of the blade and disk at the firtree joint can cause crack initiation in service due to fretting fatigue. A limited amount of testing was performed on Ti-6Al-4V alloy using the fretting fixture to evaluate its ability to simulate service conditions and produce reliable test results.

SECTION 8.0

REFERENCES

Hutson, A.L., "Fretting Fatigue of Ti-6-4 Under a Flat-on-Flat Contact with Blending Radii," University of Dayton Master Degree Thesis, August 2000.

Jasper, T.M., "The Value of the Energy Relation in the Testing of Ferrous Metals at Varying Ranges of Stress and at Intermediate and High Temperatures," Philosophical Magazine, Series 6, Vol 46, October 1923, pp. 609-627.

Kramb, V.A., "Notched Fracture Behavior of a Woven Oxide/Oxide Ceramic Matrix Composite," Ph.D. Dissertation, University of Dayton, Department of Materials Engineering, August 1999.

APPENDIX A
COMPENDIUM OF MANUSCRIPTS

LIST OF MANUSCRIPTS

C1: John, R., Lackey, A.F., and Ashbaugh, N.E., "Cyclic Crack Propagation Parallel to Fibers in a Unidirectionally Reinforced Metal Matrix Composite," submitted to Composite Science and Technology, May 2000.....	29
C2: Garner, D.I., Sieverding, M., and Johansen, K., "User's Manual for the Compact Fiber Test Machine," UDRI-TR-XXXX, February 2000.....	51
C3: Buchanan, D.J., John, R., and Zawada, L.P., "Notched Fracture Behavior of Oxide/Oxide Nextel™720/AS Composite," Proceedings American Ceramics Society 2000 Conference and Exposition, Cocoa Beach, FL, 23-28 January 2000.....	75
C4: John, R., Buchanan, D.J., and Zawada, L.P., "Creep Deformation and Rupture Behavior of a Notched Oxide/Oxide Nextel™720/AS Composite," proceedings of American Ceramics Society 2000 Conference and Exposition, Cocoa Beach, FL, 23-28 January 2000.....	83
C5: Kramb, V.A., John, R., and Zawada, L.P., "Fracture Behavior of an Oxide/Oxide Ceramic Matrix Composite," J. American Ceramic Society, vol. 82, no. 11, 1999, pp. 3087-3096.....	89
C6: Kramb, V.A., and John, R., "Damage Progression from Notches in an Oxide/Oxide Ceramic Matrix Composite Using Ultrasonic C-Scans," submitted to Composites Science and Technology, May 2000.....	113
C7: Hutson, A.L., Nicholas, T., and Stubbs, D., "Characterization of Fretting Fatigue Crack Nucleation Life of Ti-6Al-4V in a Flat-on-Flat Contact," Proceedings of the National Conference on High Cycle Fatigue, Chandler, AZ, US Air Force, Mar. 2000.....	135
C8: Martinez, C.M., Birkbeck, J.C., Eylon, D., Ruschau, J.J., Thompsom, S.R., Porter, W.J., and Nicholas, T., "Characterization of FOD Impact Sites on Ti-6Al-4V Simulated Airfoils," to be published in the Proceedings of the 5th National Turbine Engine High Cycle Fatigue Conference, Chandler, AZ, March 7-9, 2000.....	147

This page intentionally left blank.

Composites Science and Technology, Submitted, September 2000.

Cyclic Crack Propagation Parallel to Fibers in a Unidirectionally Reinforced Metal Matrix Composite

Reji John¹, Andrew F. Lackey^{*} and Noel. E. Ashbaugh^{*}

Materials and Manufacturing Directorate,

Air Force Research Laboratory (AFRL/MLLMN),

Wright Patterson Air Force Base, OH 45433-7817, U.S.A.

* University of Dayton Research Institute, Dayton, OH 45469-0128, U.S.A.

Abstract

The crack growth parallel to fibers in unidirectionally reinforced SCS-6/TIMETAL®21S was studied at room temperature using multiple geometries and stress ratios. Baseline characterization of neat (fiberless) TIMETAL®21S was also conducted. Closure levels were determined from the load-crack mouth opening displacement responses measured during crack growth. The crack growth behavior was geometry independent confirming the applicability of linear elastic fracture mechanics. The composite exhibited high closure levels of K_{cl}/K_{max} up to 0.8. Similar to the neat TIMETAL®21S response, the use of effective ΔK based on closure correction enabled correlation of the crack growth behavior of the composite up to $R=0.8$. The conventional net-section based prediction of the [90]₄ composite response overestimated the crack growth rate at medium to low ΔK . An effective ligament method was proposed to incorporate the non-planar fracture, and successfully used to correlate the crack growth rate behavior of the [90]₄ composite to that of the neat matrix. The apparent fracture toughness of the composite was also successfully predicted using the proposed model.

Keywords

A. Metal-matrix composites (MMCs), B. Crack Growth, B. Fatigue, B. Fracture, C. Damage tolerance

¹ Corresponding author

1. Introduction

Unidirectionally reinforced metal matrix composites (MMC) are targeted for use in many aerospace applications which require high specific strength and stiffness at elevated temperatures [1,2]. Such applications include blings and disks. The primary weakness of a component made of unidirectionally reinforced MMC is its susceptibility to transverse loads. The strength of the component in the transverse direction is significantly lower than that in the longitudinal direction under monotonic, sustained and fatigue loading conditions [1-17]. During service the transverse loads are typically cyclic, resulting in crack growth parallel to fibers from damage initiators such as flaws and holes. Available experimental results on B₄C/Ti-6Al-4V [5], SiC/Ti-6Al-4V [6], SCS-6/Ti-24Al-11Nb [7], SCS-6/Ti-15V-3Cr-3Al-3Sn [8] and SCS-8/6061-Al-Mg-Si [9] indicate that the resistance to crack growth parallel to fibers is significantly lower than that of the fiberless matrix. The crack growth rate in the composite was about an order of magnitude faster than that in the neat matrix and the crack growth occurred in the narrowest matrix ligament between the fibers [5-9].

Mahulikar et al. [5] showed that using applied strain energy release rate range (ΔG_a) instead of applied stress intensity factor range (ΔK_a) enables the collapse of the crack growth curve obtained from different fiber orientations into a single curve. No attempt was made to relate the transverse crack growth behavior with that of the neat matrix. Based on data from different geometries, John et al. [7,15] concluded that linear elastic fracture mechanics (LEFM) is applicable to describe the crack growth parallel to fibers in SCS-6/Ti-24Al-11Nb and SCS-6/TIMETAL®21S. In addition, the load versus crack mouth opening displacement (CMOD) measurements showed that closure loads in the composite were as high as 40% of the maximum load [7,9,15]. These high closure loads indicate that the effective stress ratio at the crack tip in the composite could be significantly different from that of the applied (far-field) stress ratio. Hence, the prediction of crack growth behavior of the composite would also require the characterization of the closure-corrected crack growth behavior of the neat matrix. John et al. [15] and Walls et al. [8] were unsuccessful in using a net-section based correction to relate the crack growth behavior in the composite to that in the neat matrix. Closure effects from debonded fibers on the fracture surface [8,15], limited fatigue resistance from the fiber/matrix interface [8] and non-planar fracture surface [15] were suggested as possible reasons for the lack of correlation of the area-corrected composite response to that of the neat matrix. Hence, an understanding of the stress ratio, closure, and non-planar fracture surface effects on the crack growth parallel to fibers is required for development of life prediction models. This paper discusses the extensive characterization of the crack growth behavior of neat TIMETAL®21S and [90]₄ SCS-6/TIMETAL®21S using two geometries, multiple stress ratios and closure measurements. An approach, which accounts for the non-planar fracture surface, is proposed to correlate the crack growth parallel to fibers in SCS-6/TIMETAL®21S to that in neat TIMETAL®21S.

2. Experimental Procedure

2.1 Material

The composite consisted of a titanium alloy matrix (TIMETAL®21S²) reinforced unidirectionally with silicon carbide fibers (SCS-6TM³). The composite was fabricated by hot isostatic pressing (HIPing) alternating layers of woven fiber mat and matrix foil. The fibers were held in place using a Ti-Nb crossweave. The composite had four layers of fibers with the volume fraction of fibers, V_f , ranging from 0.32 to 0.36. The thickness of the composite specimens ranged from 0.86 to 0.99 mm. The radius (R_f) of the SCS-6 fibers was typically 70 μm and the center-to-center spacing (s) between the fibers was 0.197 mm, i.e., the fiber mat consisted of 129 fibers per inch. The baseline data was generated for the neat (fiberless) matrix using specimens from matrix panels which were fabricated by HIPing layers of matrix foils. The HIPing process used for the neat matrix was identical to that used for the composite. The thickness of neat TIMETAL®21S ranged from 0.2 to 3.0 mm. Following consolidation, the composite and the neat matrix were aged in vacuum for 8 hours at 621°C to stabilize the matrix.

2.2 Fatigue Crack Growth Testing

Two specimen geometries, namely, compact tension, C(T), and clamped single edge, CSE(T), were used during this study. The specimens were fabricated by abrasive water jet machining from the composite panels. The C(T) geometry was based on the ASTM [18] standard except for the thickness. The CSE(T) is a single edge cracked geometry with clamped ends [19]. The CSE(T) geometry enabled successful testing of thin matrix and composite specimens at high ΔK_a . In the CSE(T) specimens, the initial notch was cut using a diamond saw, and in the C(T) specimens, electrodischarge machining (EDM) was used to create the initial notch. All the initial notches were oriented along the direction of the fibers. The surfaces of the specimens were polished using a diamond paste to 3 μm finish for optical crack length measurements.

The fatigue crack tests were conducted using a fully automated servo-hydraulic test system. The tests were conducted in laboratory air at room temperature and at a frequency of 1.0 to 3.0 Hz. Neat TIMETAL®21S was tested at stress ratios of 0.1 and 0.5, and [90]₄ SCS-6/TIMETAL®21S at 0.1, 0.5 and 0.8. During all the tests, the crack mouth opening displacement (CMOD) was measured using an extensometer with quartz rods. The load versus CMOD response was recorded periodically to monitor changes in specimen compliance and closure levels. The initial linear portion of unloading response was used to calculate the current specimen compliance from which the crack length was calculated. The compliance crack length was thus continuously monitored for C(T) specimens. The direct current potential difference (DCPD) and compliance techniques were used to monitor the crack growth in the CSE(T) specimens. The surface crack lengths were measured periodically on both sides of the specimen using 20X travelling microscopes. The optical measurements were used to verify and correct the DCPD and compliance measurements, if required. Additional details of the specimen geometries and test procedure can be found in Ref. [15].

² Timetal®21S (Ti-15Mo-2.6Nb-3Al-0.2 Si) is manufactured by TIMET, Henderson, NV 89015.

³ SCS-6 is manufactured by Textron Specialty Materials, Lowell, MA 01851.

3. Results

3.1 Crack Growth Behavior of Neat TIMETAL®21S

The crack growth rate (da/dN) versus applied stress intensity factor range, ΔK_a , response of neat TIMETAL®21S at room temperature is shown in Fig. 1. The data obtained at $R=0.1$ show that the crack growth behavior is independent of test geometry. A typical load versus CMOD response is shown in Fig. 2 for a test conducted at $R=0.1$. The data typically exhibited nonlinear response suggesting the partial closure of cracks during unloading. Upper and lower windows were chosen to include the linear range of the initial unloading portion of the load-CMOD data. A straight line was fit to the unloading data between these windows, and the difference between the data and the straight line was plotted as the differential data in Fig. 2. The load at which the unloading data deviated from the straight line was defined as the closure load.

Figure 3 shows the ratio of the closure stress intensity factor, K_{cl} , to the maximum applied stress intensity factor, K_{max} , as a function K_{max} for the $R=0.1$ tests. K_{cl} / K_{max} is ≈ 0.28 throughout the crack growth range. The load versus CMOD response obtained during the $R=0.5$ test was linear throughout the test, confirming the absence of closure effect for tests with $K_{min} / K_{max} \geq 0.5$. As shown in Fig. 4, the closure corrected $R=0.1$ data correlated well with the $R=0.5$ data.

The closure-corrected R -independent matrix crack growth behavior can be adequately represented using Eqn. (1) as,

$$\log\left(\frac{da}{dN}\right) = C_1 \{\sinh [C_2 (\log (\Delta K_{eff})) + C_3)]\} + C_4 , \quad (1)$$

in which C_i = constants obtained by regression, da/dN = crack growth rate in m/cycle and ΔK_{eff} = effective stress intensity factor range in MPa \sqrt{m} . The constants in Eqn. (1) are: $C_1 = 0.7158$, $C_2 = 3.0207$, $C_3 = -1.1139$, and $C_4 = -7.0690$. Note that, in general $\Delta K_{eff} = K_{max} - K_{cl}$, and for the $R=0.5$ test, $K_{cl} = K_{min}$, where K_{min} is the minimum applied stress intensity factor. Equation (1) is shown as the solid line in Fig. 4, along with the trend line (dashed) for the raw $R=0.1$ data. In all subsequent graphs, Eqn. (1) will be used to represent the closure-corrected crack growth behavior of the neat matrix.

In the [90]₄ composite, the matrix ligament between the fibers is ≈ 0.09 mm. Hence, tests were conducted to determine the effect of thickness on the crack growth behavior. Figure 5 shows the closure-corrected data from specimens with thickness ranging from 0.2 to 3.0 mm along with the trend line given by Eqn. (1). The closure-corrected crack growth behavior of neat TIMETAL®21S is independent of thickness for the range 0.2 to 3.0 mm. Specimens with thickness < 0.2 mm were unavailable for testing.

3.2 Crack Growth Behavior of [90]₄ SCS-6/TIMETAL®21S

The crack growth rate versus ΔK_a response of [90]₄ SCS-6/TIMETAL®21S at R=0.1 is shown in Fig. 6. The data from C(T) specimen correlated well with that from the CSE(T) specimen. These data also correlate well with the data from the center-crack geometry, M(T) from Hermann and Hillberry [20]. The excellent correlation between the data from geometries confirms the potential applicability of linear elastic fracture mechanics (LEFM) to describe the crack growth parallel to fibers. Similar results were also reported for crack growth parallel to fibers in SCS-6/Ti-24Al-11Nb by John et al. [7,21]. The load versus CMOD response data from the C(T) and CSE(T) geometries were nonlinear indicating the presence of closure effects. Hence, tests were also conducted at R = 0.5 and 0.8 using the C(T) and CSE(T) geometries. These data are shown in Fig. 7, in which there is clear evidence of the layering corresponding to the stress ratio, i.e., for the same ΔK_a , da/dN increases with increase in R. The load versus CMOD response obtained during these tests was analyzed as discussed earlier to obtain the ratio K_{cl}/K_{max} as a function of K_{max} as shown in Fig. 8. The data shown in Fig. 8 are from tests conducted at R=0.1 and 0.5. K_{cl}/K_{max} for the [90]₄ composite varies from ≈ 0.15 to ≈ 0.8 in contrast to near-constant 0.28 for the neat TIMETAL®21S. The data for the composite are clearly geometry and specimen dependent, and no single trend was observed. Hence, the data from each test was closure-corrected individually. Tests conducted at R=0.8 did not exhibit closure consistent with the maximum value K_{cl}/K_{max} observed in Fig. 8. The closure-corrected data from R=0.1 and 0.5 tests correlated well with the raw data from R=0.8 test as shown in Fig. 9. The closure corrected stress intensity factor of the composite is defined as $\Delta K_{90,eff}$. Figures 3 and 8 show that K_{cl}/K_{max} for the composite is significantly different from that the neat matrix. However, Figs. 4 and 9 show that the principle of using closure based correction to correlate data from tests at different stress ratios ($0.1 \leq R \leq 0.8$) is valid for neat matrix and crack growth parallel to fibers in a unidirectionally reinforced composite.

Since the neat matrix and the [90]₄ composite exhibited closure effects, the corresponding closure-corrected curves are compared in Fig. 9. The crack growth rate in the [90]₄ composite is similar to that in the neat matrix at low ΔK (near-threshold), and is almost 10X faster than in the neat matrix at high ΔK . In Fig. 9, ΔK for the [90] composite was calculated using the far-field stress (or load) and the overall dimensions of the specimen similar to earlier investigations [5,7,8,9,12,13,15]. Figure 10 shows the fracture surface of the failed composite highlighting the propagation path along the matrix ligament between the fibers. Since the crack growth is restricted to the matrix, and the fiber/matrix interface is not expected to offer any resistance to the crack growth behavior, we can expect the crack growth response of the composite to be related to the crack growth response of the neat matrix [7,15]. The correlation between the crack growth parallel to fibers in [0] composite and that in the neat matrix is discussed next.

4. Correlation of Crack Growth Behavior of SCS-6/TIMETAL®21S

4.1 Net-Section Method

A direct method to relate $\Delta K_{90,eff}$ of the composite to ΔK_{eff} is based on the net section model shown in Fig. 11. Using load equilibrium and assuming uniform stress distribution in the ligament, we obtain,

$$\Delta\sigma_{\text{lig}} = \Delta\sigma_{90} \frac{B_p}{B_{\text{lig,net}}} = \frac{\Delta\sigma_{90}}{\left(1 - \frac{2R_f}{B_p}\right)} . \quad (2)$$

where $B_{\text{lig,net}} = B_p - 2R_f$, R_f = radius of fiber, B_p = average ply thickness = B/n , B = thickness of composite specimen, n = number of plies in the composite, $\Delta\sigma_{90}$ = far-field stress, and $\Delta\sigma_{\text{lig}}$ = uniform stress in the matrix ligament. This approach, i.e. Eqn.(2), was successfully used to predict the transverse creep-rupture and fatigue behavior of [0] composite by John et al. [10,16]. Using Eqn. (2), the stress intensity factor range in the matrix ligament, $\Delta K_{\text{lig,net}}$ can be related to $\Delta K_{90,\text{eff}}$ as,

$$\Delta K_{\text{lig,net}} = \frac{\Delta K_{90,\text{eff}}}{\left[1 - \frac{2R_f}{B_p}\right]} . \quad (3)$$

Using the net-section geometry shown in Fig. 11, the volume fraction of the fibers, V_f can be calculated as,

$$V_f = \frac{\pi R_f^2}{B_p s} , \quad (4)$$

where s = center-to-center fiber spacing in a ply. Substituting Eqn. (4) in Eqn. (3), we obtain,

$$\Delta K_{\text{lig,net}} = \frac{\Delta K_{90,\text{eff}}}{\left[1 - \sqrt{\frac{4V_f s}{\pi B_p}}\right]} . \quad (5)$$

Note that, in a square arrangement, $s = B_p$. Using Eqn. (3) or Eqn. (5), $\Delta K_{\text{lig,net}}$ was calculated from $\Delta K_{90,\text{eff}}$ and compared with the neat crack growth behavior in Fig. 12. Since $\Delta K_{\text{lig,net}}$ represents the average ΔK in the matrix ligament, it can be compared directly to the neat matrix trend line. The crack growth rate in the neat matrix curve is similar to that in the composite at high ΔK and $\approx 10\text{-}50X$ faster than in the composite at low ΔK , if the ΔK calculation in the composite is based on the net-section. Hence, the net-section approach, as discussed above, will lead to a safe design of the component.

An expression similar to Eqn. (5) was used by John et al. [15] and Walls et al. [8] in an attempt to correlate the crack growth parallel to fibers in SCS-6/TIMETAL®21S and SCS-6/Ti-15V-3Cr-3Al-3Sn, respectively, with that of the neat matrix. John et al. [15] had accounted for closure effects

while Walls et al. [8] did not account for closure effects. In addition, Note that Walls et al. [8] assumed a square arrangement of fibers in the composite, i.e. $s = B_p$.

4.2 Effective Ligament Method

Figure 12 shows that the direct net-section method, discussed above, was unable to correlate the composite crack growth behavior with that of the matrix. The net-section method was based on the following assumptions: (1) the fibers are arranged uniformly spaced in parallel plies, and (2) cracking occurs between the fibers along the narrowest ligament resulting in a planar fracture surface, i.e. perpendicular to the loading direction. In contrast, the cross-section (eg. A-A in Fig. 10) along the fracture reveals evidence of a staggered fiber arrangement as shown in Fig. 13. The staggered fiber arrangement resulted in matrix ligaments (fracture surfaces between the fibers) which are not always perpendicular to the loading direction. Hence, we propose the following method to account for the fracture surface regions which are not perpendicular to the loading direction.

Consider the fracture profile at a given crack length as shown in Fig. 13. Using a digitizing software, the actual ligament lengths were measured along the fracture surface as b_1, b_2, \dots, b_m . Hence the effective ligament thickness, $B_{\text{lig,eff}}$, can be obtained as

$$B_{\text{lig,eff}} = \frac{\sum_{i=1}^m b_i}{n}. \quad (6)$$

where n = number of plies. In the net-section method, as discussed in Eqn. (2), the ligament thickness was defined as $B_{\text{lig,net}} = B_p - 2R_f$. During this study, we sectioned a specimen from each geometry at various crack lengths, and measured $B_{\text{lig,eff}}$ as function of crack length. Using these measurements, the ratio $B_{\text{lig,eff}} / B_{\text{lig,net}}$ was determined as a function of $\Delta K_{\text{lig,net}}$ for the two specimens as shown in Fig. 14. Note that $B_{\text{lig,eff}} / B_{\text{lig,net}} = 1$ corresponds to a perfectly planar fracture surface. The measurements show that the effective ligament thickness could be 40% higher than the net-section ligament thickness at low $\Delta K_{\text{lig,net}}$. $B_{\text{lig,eff}} / B_{\text{lig,net}}$ approaches 1.0 with increasing $\Delta K_{\text{lig,net}}$.

If the angle between the effective fracture surface and the net-section (planar) fracture surface is defined as θ (see inset in Fig. 14), then we obtain,

$$\cos \theta = \frac{B_{\text{lig,net}}}{B_{\text{lig,eff}}}. \quad (7)$$

Thus, the resolved load acting perpendicular to the effective ligament thickness can be obtained as,

$$P_{\text{res}} = P \cos \theta, \quad (8)$$

where P = applied load. Thus, combining Eqns. (7) and (8), we obtain,

$$\frac{P_{\text{res}}}{B_{\text{lig,eff}}} = \frac{P}{B_{\text{lig,net}}} \cos^2 \theta. \quad (9)$$

Hence, a resolved stress intensity factor range for the effective matrix ligament can be obtained as,

$$\Delta K_{\text{lig,res}} = \Delta K_{\text{lig,net}} \cos^2 \theta, \quad (10)$$

where $\Delta K_{\text{lig,net}}$ is defined by Eqn. (5).

Using the data from Fig. 14, the correction factor $\cos^2 \theta$ is plotted versus $\Delta K_{\text{lig,net}}$ in Fig. 15. The correction factor increases from ≈ 0.45 to ≈ 0.8 with increase in $\Delta K_{\text{lig,net}}$ from ≈ 10 to ≈ 70 MPa $\sqrt{\text{m}}$. Thus, $\approx 20\text{-}55\%$ reduction in the effective $\Delta K_{\text{lig,net}}$ can occur depending on the magnitude of $\Delta K_{\text{lig,net}}$. A polynomial was fit to the data in Fig. 15 and used to correct the $\Delta K_{\text{lig,net}}$ data in Fig. 12 to obtain $\Delta K_{\text{lig,res}}$. Figure 16 shows the excellent correlation between dadn- $\Delta K_{\text{lig,res}}$ data from the [90]₄ composite and the closure-corrected neat matrix trend line. The correction factor (Fig. 15) is based on the limited amount of measurements from 2 specimens. However, using the proposed correction factor, we were able to establish the correlation between the [90]₄ data and the neat matrix behavior across the entire crack growth regime.

5. Discussion

The thickness of neat TIMETAL®21S specimens tested during this study ranged from 0.2 to 3 mm. For this range of thickness, the crack growth behavior was independent of thickness (Fig. 5), when closure-corrected data were used. As discussed earlier, the thickness of the narrowest matrix ligament between the fibers is ≈ 0.1 mm, which is 50% lower than the lowest thickness tested. Potential differences, if any, can be expected to occur at high ΔK or near fracture because of the relatively large plastic zone size. Hence, we evaluated the ability to predict the fracture toughness of the [90]₄ composite, using the concepts proposed in the previously discussed net-section and effective ligament methods. Substitution of Eqn. (3) or Eqn. (5) into Eqn. (10) for a monotonic loading yields,

$$K_{90,\text{frac}} = \frac{K_{m,\text{frac}} \left[1 - \frac{2R_f}{B_p} \right]}{\cos^2 \theta} = \frac{K_{m,\text{frac}} \left[1 - \sqrt{\frac{4V_f s}{\pi B_p}} \right]}{\cos^2 \theta}, \quad (11)$$

where $K_{90,\text{frac}}$ = fracture toughness of the [90] composite, $K_{m,\text{frac}}$ = fracture toughness of the neat matrix on the effective ligament surface, and $\cos^2 \theta$ = correction factor near fracture (≈ 0.8). Using $K_{m,\text{frac}} \approx 80$ MPa $\sqrt{\text{m}}$ (see Fig. 4), $K_{90,\text{frac}}$ was predicted for the two geometries as shown in Table 1. The predictions correlate well with the measured fracture toughness. Hence, the crack growth behavior of matrix with thickness ≈ 0.1 mm could be assumed to be similar to that shown in Fig. 5.

This study did not account for the residual stresses generated in the composite during fabrication due to the thermal mismatch between fiber and the matrix [22]. Hall et al. [13] reported that the residual stresses decrease significantly with increase in applied cycles. In addition, the presence of residual stresses would affect the absolute K , i.e., effective K_{\max} and K_{\min} values, however, ΔK value would remain the same. Consequently, the presence of the residual stress will alter the effective stress ratio and will not alter the ΔK at the matrix crack tip. Thus, the use of R-independent response for the composite and the neat matrix during this study minimizes the influence of the residual stresses on the predictions in Figs. 12 and 16.

The good correlation in Fig. 16 also indicates that the interfacial bonding has a negligible effect on the fatigue crack growth parallel to fibers in this composite. In the proposed effective ligament, we neglected the load component parallel to the fracture surface ($=P \sin \theta$), i.e. the tearing mode or mode III type of loading. Since the resistance to mode III fracture can be expected to be very high, neglecting the mode III component is a reasonable assumption.

The data from the [90] composite and the effective ligament method of correlating the composite and matrix data show clearly that the staggered fiber arrangement results in significantly higher damage tolerance at low ΔK , i.e. in the near-threshold regime compared to the direct net-section model. Hence, the use of techniques such as metallic foils with grooves for the unidirectionally reinforced components should ensure that the fiber rows in successive plies are offset longitudinally as shown in Fig. 17.

Figure 15 showed that the correction factor increased from ≈ 0.45 to ≈ 0.8 with increase in $\Delta K_{\text{lig,net}}$. This trend could be attributed to the increase in plastic zone size ahead of the crack with increasing ΔK_{lig} . Figure 17 shows the ratio of the cyclic plastic zone size (r_p) to the fiber spacing (s) as function of the applied maximum stress intensity factor in the matrix ligament, $K_{\max,\text{lig}}$. The cyclic plastic zone size was calculated as $r_p = (1/[2\pi]) (K_{\max,\text{lig}} / \sigma_{\text{flow}})^2$, where $\sigma_{\text{flow}} = \text{flow stress of matrix} = 1100 \text{ MPa}$. When $K_{\max,\text{lig}} \geq 40 \text{ MPa}\sqrt{\text{m}}$ (i.e., $\Delta K_{\text{lig}} \geq 36 \text{ MPa}\sqrt{\text{m}}$ for $R=0.1$), the ratio r_p/s becomes ≥ 1 , indicating that the yield region at the crack front has attained a size that is comparable to a representative volume element. Hence, the local stress concentrations at the “fiber” holes no longer exist, allowing the crack fronts to propagate nearly perpendicular to the loading axis. Thus the correction factor ($=\cos^2\theta$) in Fig. 15 is closer to 1.0 at high ΔK .

6. Conclusions

Neat (fiberless) TIMETAL®21S exhibited marginal closure ($K_{\text{cl}} / K_{\max} \approx 0.28$). For neat TIMETAL®21S, the use of effective ΔK based on closure correction enabled correlation of the crack growth behavior up to $R=0.5$. The closure corrected crack growth behavior of TIMETAL®21S was identical for thickness ranging from 0.2 to 3.0 mm. Crack growth behavior of [90]₄ SCS-6/TIMETAL®21S was geometry independent, confirming the applicability of linear elastic fracture mechanics to describe the crack growth behavior. Contrary to the neat TIMETAL®21S, the

composite exhibited high closure levels of K_{cl}/K_{max} up to 0.8. Similar to the neat TIMETAL®21S response, the use of effective ΔK based on closure correction enabled correlation of the crack growth behavior of the composite up to $R=0.8$. The conventional net-section based prediction of the [90]₄ composite response overestimated the crack growth rate at medium to low ΔK . An effective ligament method was proposed to incorporate the non-planar fracture, and successfully used to correlate the crack growth rate behavior of the [90]₄ composite to that of the neat matrix. The good correlation indicates that the interfacial bonding has a negligible effect on the fatigue crack growth parallel to fibers in this composite. The apparent fracture toughness of the composite was also successfully predicted using the proposed model.

Acknowledgments

This research was conducted at the Materials and Manufacturing Directorate, Air Force Research Laboratory (AFRL/MLLMN), Wright-Patterson Air Force Base, OH, USA. A.F. Lackey and N.E. Ashbaugh were supported under an onsite contract number F33615-98-C-5214.

References

1. Larsen JM, Russ SM, Jones JW. An Evaluation of Fiber-Reinforced Titanium Matrix Composites for Advanced High-Temperature Aerospace Applications. *Metallurgical and Materials Transactions A*, 1995;26A(12):3211-3223.
2. Johnson WS, Larsen JM, Cox BN, editors. *Life Prediction Methodology for Titanium Matrix Composites*, ASTM STP 1253, American Society for Testing and Materials, Philadelphia, PA, 1996.
3. Castelli MG, Gayda J. *Reliability, Stress Analysis, and Failure Prevention*, DE-55, ASME, pp. 213, 1993.
4. Johnson WS, Lubowinski SJ, Highsmith AL. Mechanical Characterization of Unnotched SCS-6/Ti-15-3 Metal Matrix Composites at Room Temperature. In: Kennedy JM, Moeller H, Johnson WS, editors, *Thermal and Mechanical Behavior of Metal Matrix and Ceramic Matrix Composites*, ASTM STP 1080, American Society for Testing and Materials, Philadelphia, PA, 1990, p. 193-218.
5. Mahulikar DS, Park YH, Marcus HL. Environmental Influences on the Fracture and Fatigue Properties of Titanium Metal-Matrix Continuous Fiber Composites. In: Lewis JC and Sines G, editors. *Fracture Mechanics: Fourteenth Symposium - Volume II: Testing and Applications*, ASTM STP 791, American Society for Testing and Materials, Philadelphia, PA, 1983, p. II-579-II-597.
6. Park YH, Narayen D, Schmerling M, Marcus HL. Fatigue Crack Growth Behavior of Ti-6Al-4V Metal Matrix/Continuous SiC and B₄C/B Fibre Composites. *Journal of Materials Science*, 1984;19:2239-2245.
7. John R, Ashbaugh NE. Fatigue Crack Growth Parallel to Fibers in Unidirectional Metal Matrix Composites. In: Mall S, Nicholas, T, editors. *Elevated Temperature Crack Growth*, MD-Vol. 18, ASME, 1990, p. 149-153.
8. Walls DP, Bao G, Zok FW. Mode I Fatigue Cracking in a Fiber Reinforced Metal Matrix Composite. *Acta Metallurgica et Materialia*, 1993;41(7): 2061-2071.
9. Venkateswara Rao KT, Siu SC, Ritchie RO. Failure Mechanisms in SiC-Fiber Reinforced 6061 Aluminum Alloy Composites under Monotonic and Cyclic Loading. *Metallurgical Transactions A*, 1993;24A:721-734.
10. John R, Khobaib M, Smith PR. Prediction of Creep-Rupture Life of Unidirectional Titanium Matrix Composites Subjected to Transverse Loading. *Metallurgical and Materials Transactions A*, 1996;27A:3074-3080.
11. Buchanan DJ, John R, Goecke KE. Influence of Temperature and Stress Ratio on the Low-Cycle Fatigue Behavior of Trimarc-1/Ti-6Al-2Sn-4Zr-2Mo. In: Bucinell RB, editor, *Seventh Symposium on Composites: Fatigue and Fracture*, ASTM STP 1330, American Society for Testing and Materials, Philadelphia, PA, 1998, pp. 199-216.
12. Gambone ML. Fatigue and Fracture of Titanium Aluminides, WRDC-TR-89-4145, Air Force Research Laboratory (AFRL), Wright-Patterson Air Force Base, OH 45433, USA, 1990.
13. Hall JA, Peralta A, Hollars RL, Harmon D, Finefield MA, James MR, Marshall DB. Damage Tolerance Concepts for Titanium-Aluminide Composites, WL-TR-95-4089, Air Force Research Laboratory (AFRL), Wright-Patterson Air Force Base, OH 45433, USA, 1995.
14. Cotteril PJ, Bowen P. *Journal of Materials Science*, 1996;31:5897-5905.

15. John R, Lackey AF, Ashbaugh NE. Fatigue Crack Propagation Parallel to Fibers in Unidirectionally Reinforced SCS-6/TIMETAL®21S. *Scripta Materialia* 1996;35(6):711-716.
16. John R, Buchanan DJ, Larsen JM. Prediction of Transverse Fatigue Behavior of Unidirectionally Reinforced Metal Matrix Composites. *Scripta Materialia* 1998;39(11):1529-1536.
17. Castelli MG. Thermomechanical and Isothermal Fatigue Behavior of a [90]₈ Titanium Matrix Composite, NASA Contractor Report 191196, NASA Lewis Research Center, Cleveland, OH, USA, October 1993.
18. ASTM Annual Book of Standards, Section 3, Vol. 03.01, E647-95a, 1997, p. 557-593.
19. John R, Rigling B. Effect of Height to Width Ratio on K and CMOD Solutions For a Single Edge Cracked Geometry With Clamped Ends. *Engineering Fracture Mechanics*, 1998;60(2): 147-156.
20. Hermann D, Hillberry BM. Department of Mechanical Engineering, Purdue University, West Lafayette, Indiana, USA, Private Communication, 1995.
21. Blatt D, John R, Coker D. Stress Intensity Factor and Compliance Solutions for a Single Edge Notched Specimen with Clamped Ends. *Engineering Fracture Mechanics*, 1994;47(4):521-532.
22. Coker D, Ashbaugh NE, Nicholas T. Analysis of Thermomechanical Cyclic Behavior of Unidirectional Metal Matrix Composites. In: Sehitoglu, editor, *Thermomechanical Fatigue Behavior of Matereials*, ASTM STP 1186, American Society for Testing and Materials, Philadelphia, PA, 1993, p. 50-69.

Table 1. Measured and Predicted Fracture Toughness for [90]4 SCS-6/TIMETAL® 21S

Geometry	Stress Ratio	Thickness (mm)	Measured Matrix Fracture Toughness, $K_{m,frac}$ (MPa \sqrt{m})	Predicted [90] Composite Fracture Toughness, K_{frac} (Eqn. 11) (MPa \sqrt{m})	Measured [90] Composite Fracture Toughness, K_{frac} (MPa \sqrt{m})
CSE(T)	0.5	0.90	80	43	38
C(T)	0.1	0.93	80	40	40

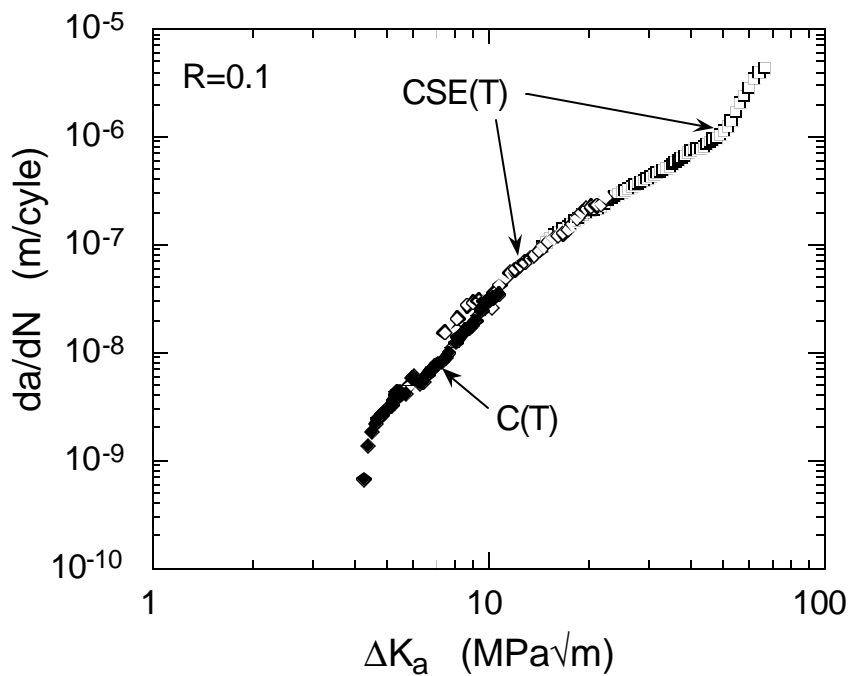


Figure 1. Crack growth behavior of neat TIMETAL®21S at 23°C and R=0.1. Thickness of specimens = 0.86 – 0.99 mm.

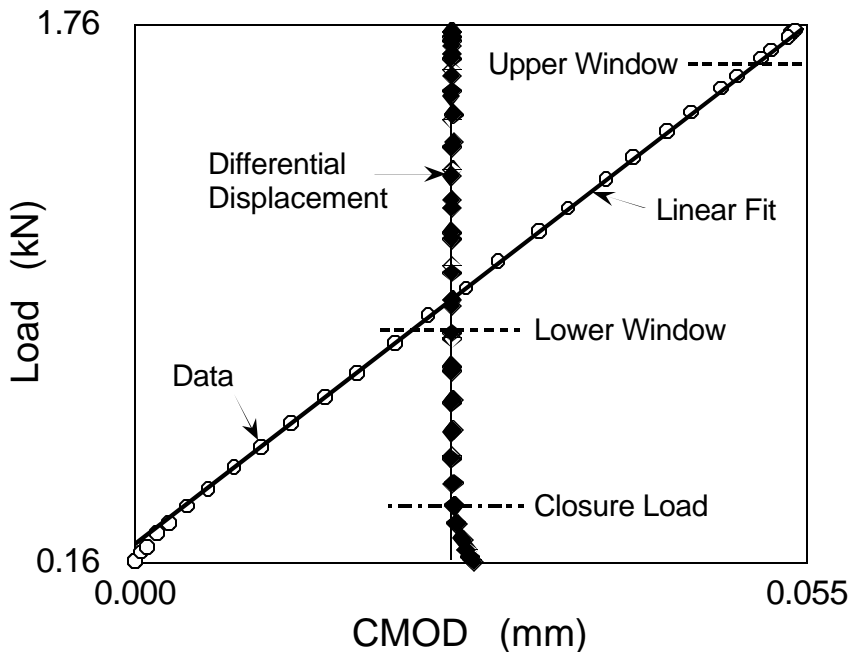


Figure 2. Typical load versus CMOD response of neat TIMETAL®21S at R=0.1. Only 3% of 1000 data points are shown.

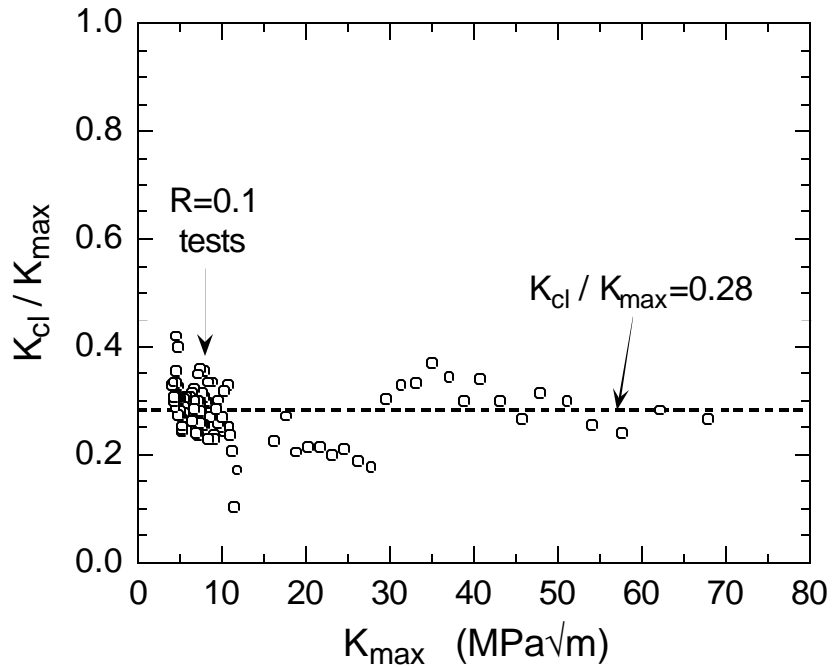


Figure 3. Ratio of closure stress intensity factor (K_{cl}) to maximum stress intensity factor (K_{max}) versus K_{max} for neat TIMETAL®21S.

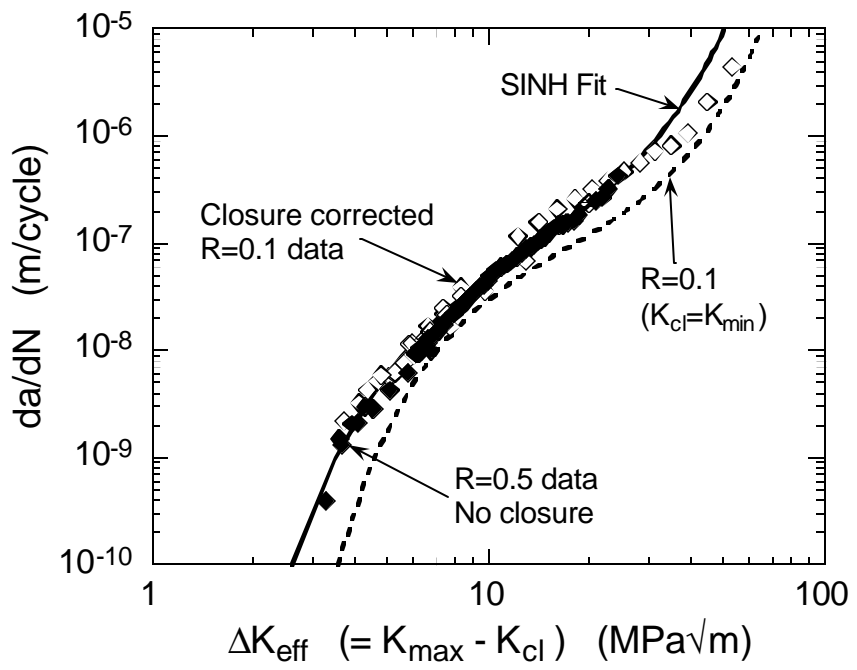


Figure 4. Closure corrected crack growth behavior of neat TIMETAL®21S.

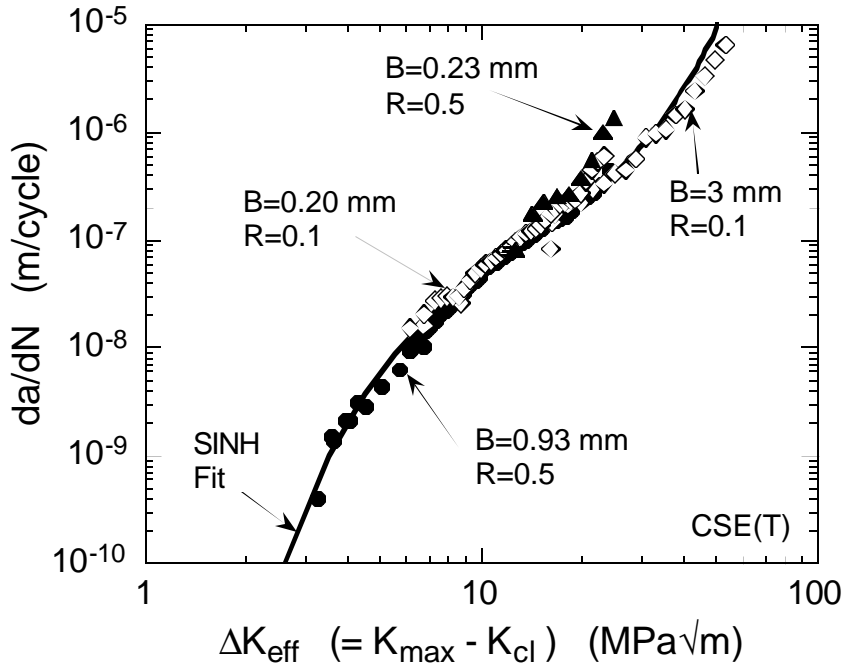


Figure 5. Effect of thickness (B) on crack growth behavior of neat TIMETAL®21S.

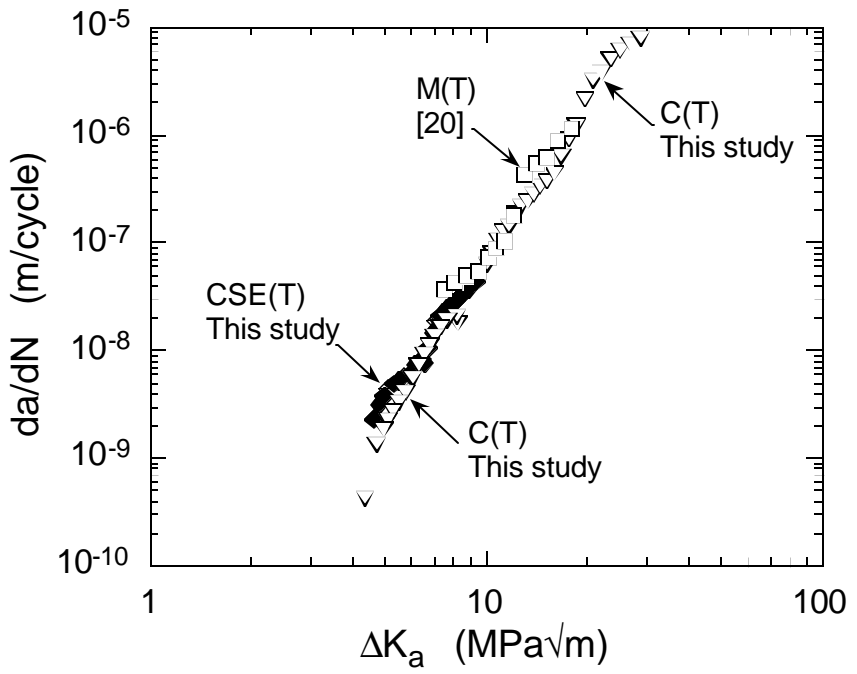


Figure 6. Crack growth behavior of [90]4 SCS-6/TIMETAL®21S for different geometries at R=0.1.

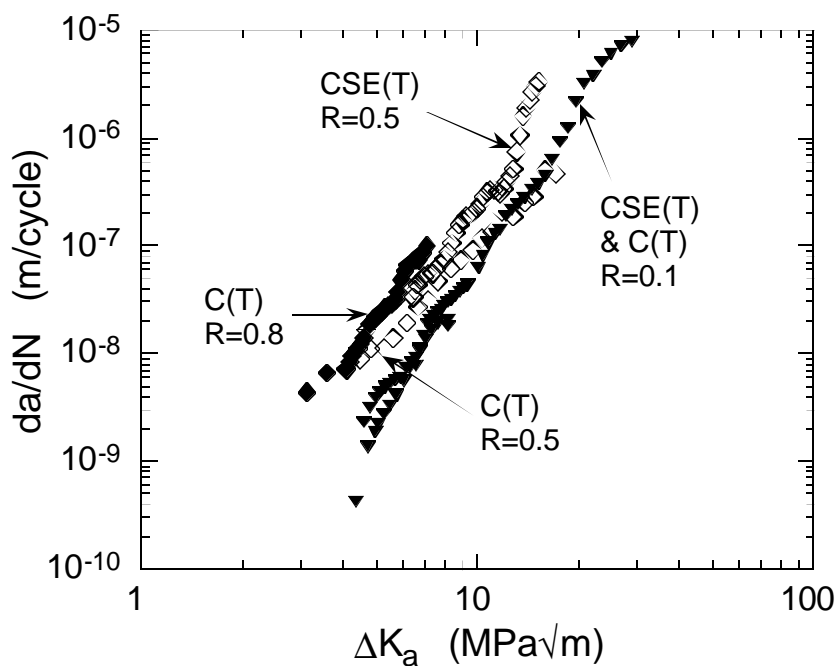


Figure 7. Effect of stress ratio (R) on crack growth behavior of [90]₄ SCS-6/TIMETAL®21S.

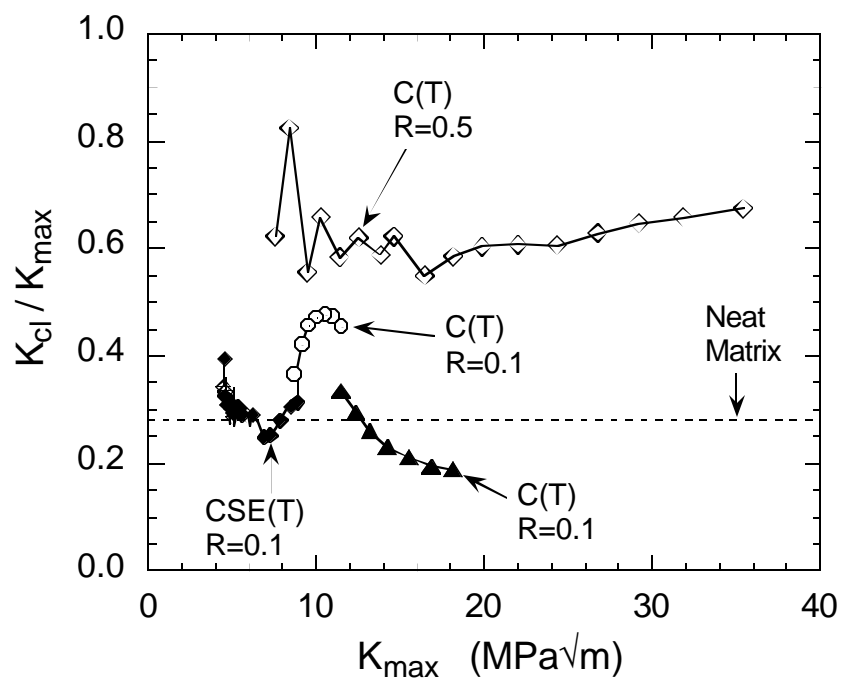


Figure 8. Ratio of closure stress intensity factor (K_{cl}) to maximum stress intensity factor (K_{max}) versus K_{max} for [90]₄ SCS-6/TIMETAL®21S.

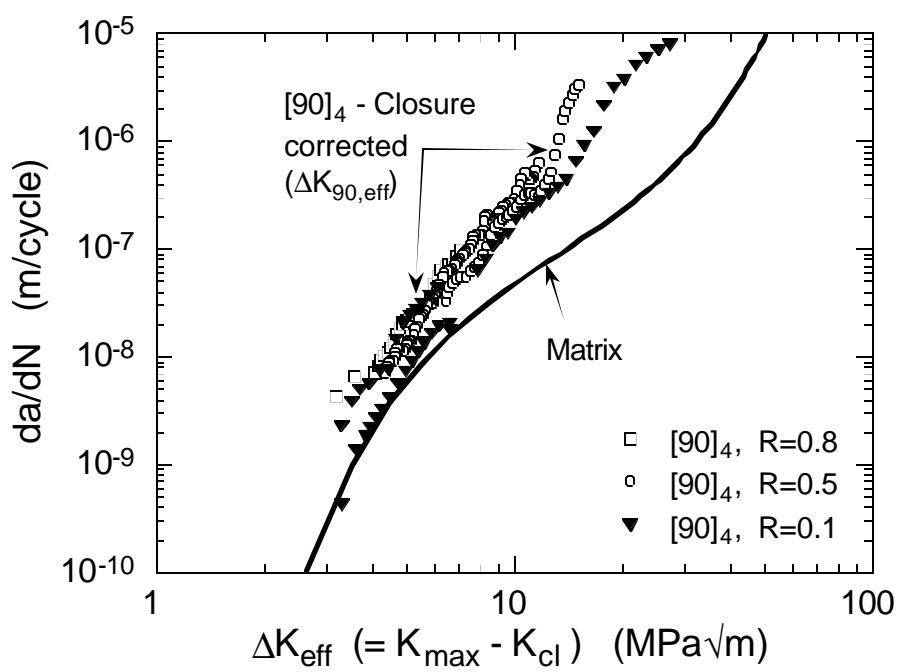


Figure 9. Closure corrected crack growth behavior of $[90]_4$ SCS-6/TIMETAL®21S.

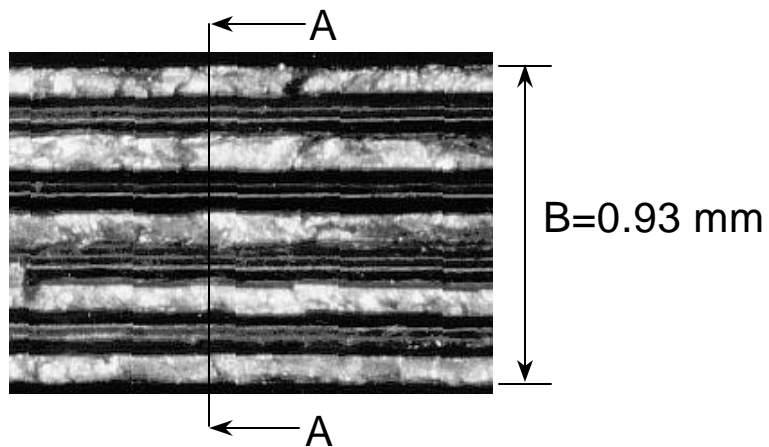


Figure 10. Fracture surface of $[90]_4$ SCS-6/TIMETAL®21S.

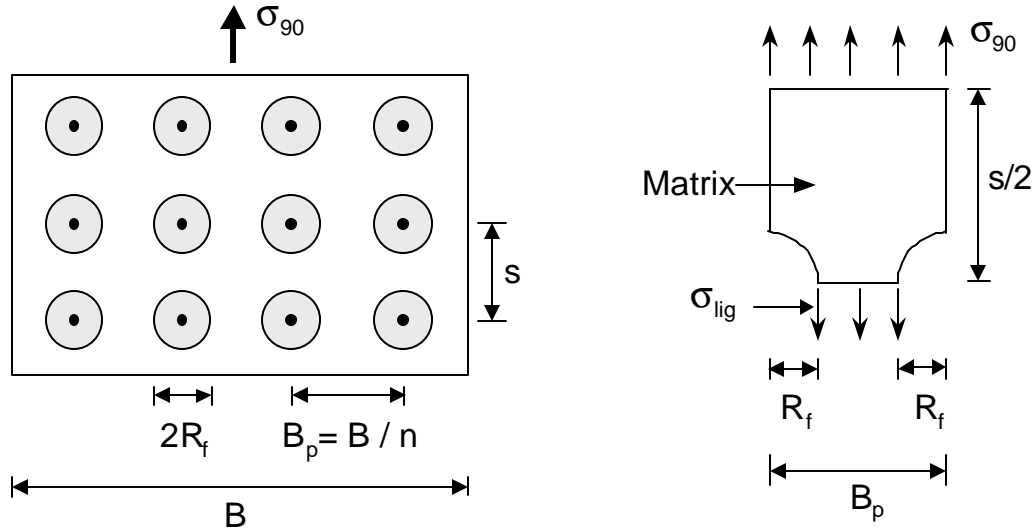


Figure 11. Schematic of [90] composite and the net section between the fibers. n = number of plies (=4 in this study).

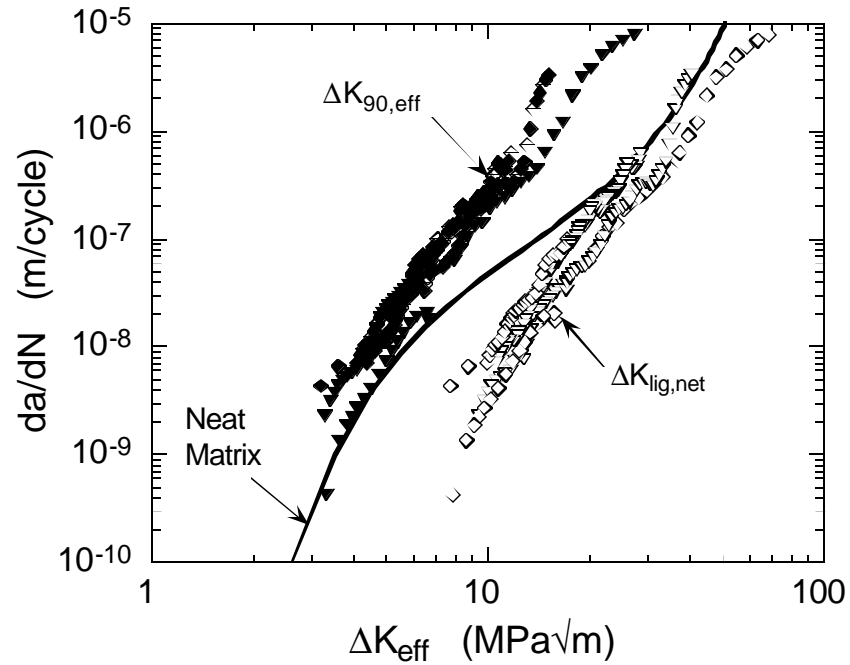


Figure 12. Net-section adjusted crack growth behavior of [90]₄ SCS-6/Timetal®21S. Solid and hollow symbols correspond to $\Delta K_{90,\text{eff}}$ and $\Delta K_{\text{lig},\text{net}}$, respectively.

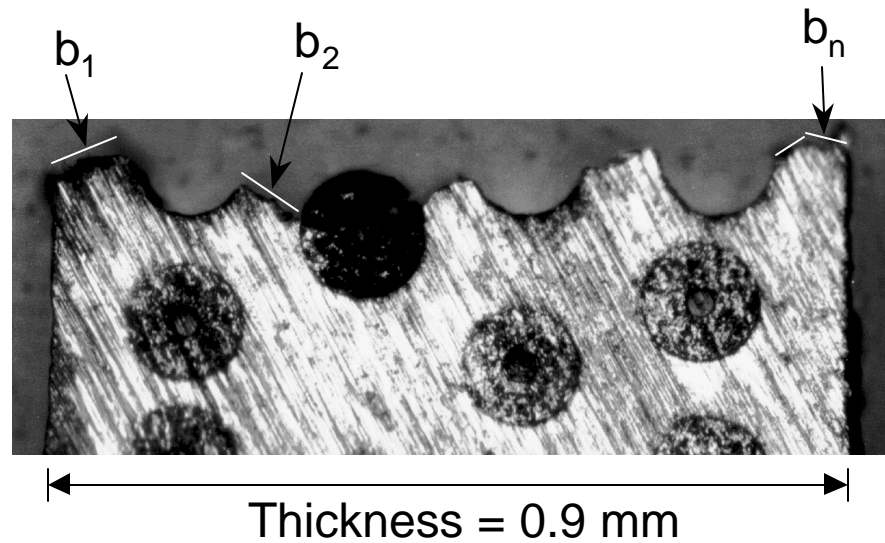


Figure 13. Typical fracture profile highlighting the non-planar fracture surface.

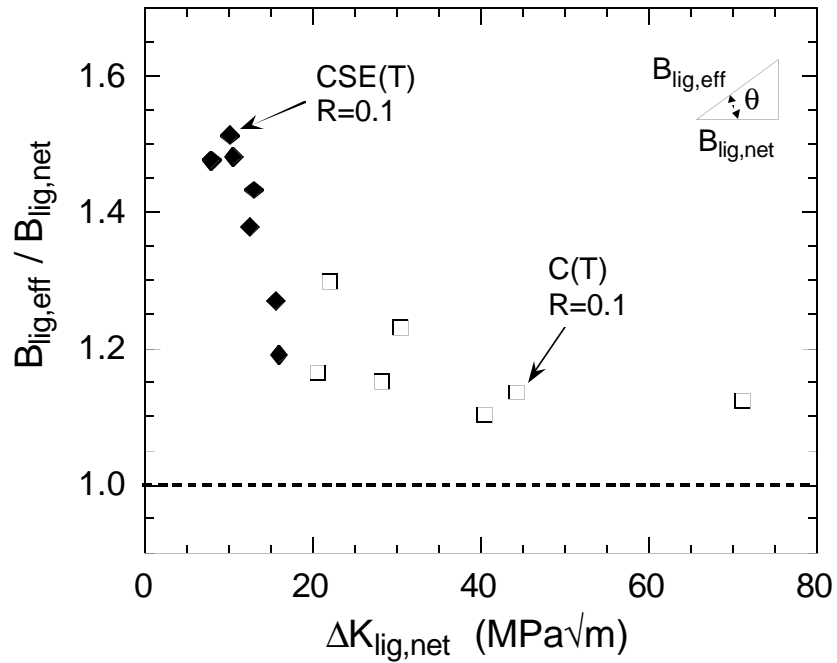


Figure 14. Ratio of effective ligament to narrowest ligament thickness, $B_{\text{lig},\text{eff}} / B_{\text{lig},\text{net}}$ versus $\Delta K_{\text{lig},\text{net}}$. Note that $B_{\text{lig},\text{net}} = B_{\text{lig},\text{eff}} \cos \theta$.

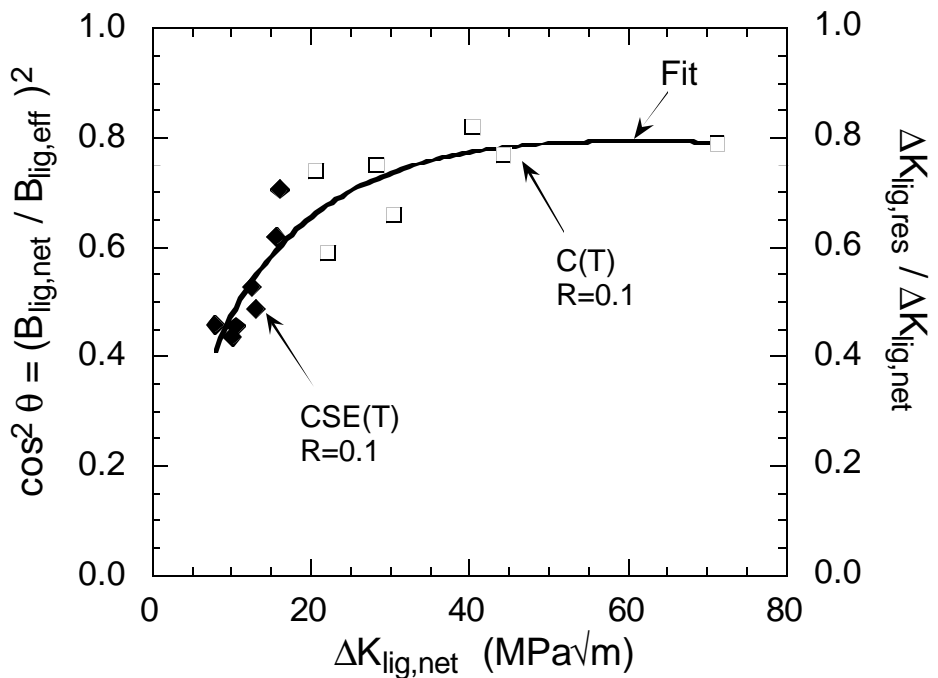


Figure 15. Correction factor for $\Delta K_{\text{lig,net}}$ due to the non-planar fracture surface.

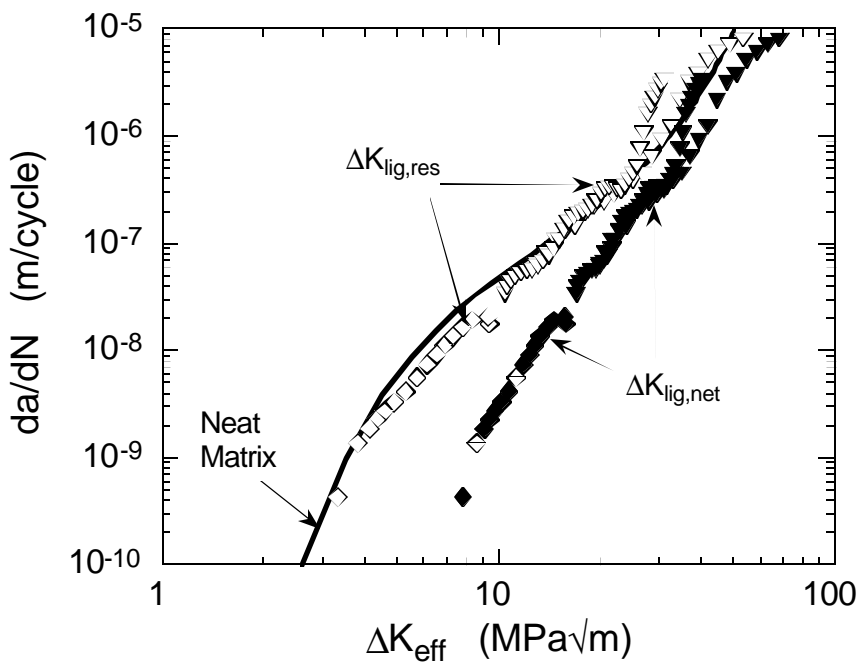


Figure 16. Correlation between closure-corrected crack growth behavior of [90]₄ SCS-6/TIMETAL®21S with that of neat TIMETAL®21S. $\Delta K_{\text{lig,net}}$ corresponds to the net-section method and $\Delta K_{\text{lig,res}}$ to the effective ligament method.

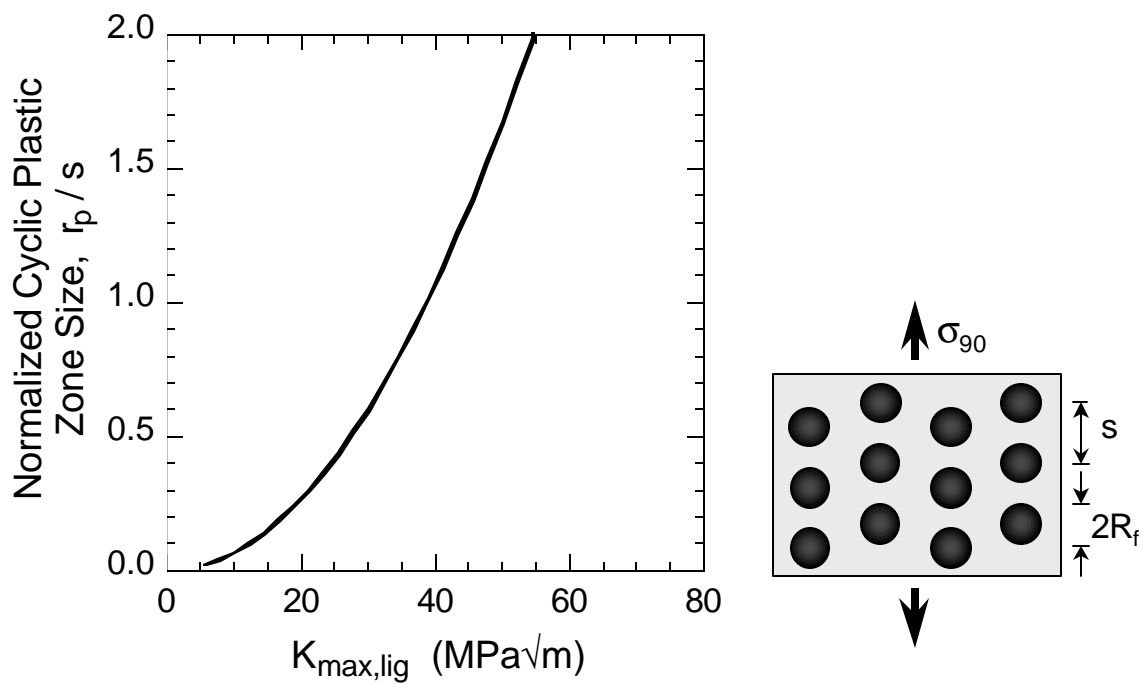


Figure 17. Relationship between plastic zone, fiber spacing and applied stress intensity factor in the matrix ligament in the [90]₄ composite.

**USER'S MANUAL FOR THE
COMPACT FIBER TEST MACHINE**

Deborah I. Garner and Michelle Sieverding

University of Dayton Research Institute
Dayton, Ohio 45469-0128

February 2000

Table of Contents

Section 1	Introduction	53
Section 2	Description and Capabilities of the Fiber Test Machine	54
Section 3	Preparation	56
Section 4	Fiber Testing	59
Section 5	Testing of Fibers Directly From a Composite Specimen	62
Section 6	Wire Testing	64
Section 7	Removing Metal Matrix From Fibers In a Composite Specimen by Etching	66
Section 8	Making the 10% Bromine/90% Methanol Solution	69
Section 9	Connecting LaserMike to the Computer After a Power Failure	71
Section 10	Calibrating the Load Cell and LaserMike	72
Section 11	Changing the Gage Length of the Compact Fiber Test Machine	73
Appendix A	MSDS for Bromine	74

Section 1

Introduction

This manual outlines the procedures necessary to conduct tension tests on single fiber specimens utilizing the compact fiber test machine. This manual is for use by individuals having little knowledge about the fiber test procedure. Experience by the operator may allow he or she to improve on some of the techniques discussed in this manual. The authors of this manual assume no liability for results generated from using the techniques described in this manual.

Section 2

Description and Capabilities of the Fiber Test Machine

Figure 1 illustrates the various components of the fiber test system. The LaserMike system has been excluded from the illustration to allow the gripping system on the machine to be seen. This system was designed in-house by George Hartman and Dennis Buchanan from the University of Dayton Research Institute and Paul Stibich formerly of the University of Dayton Research Institute. The system has room temperature testing capability only.

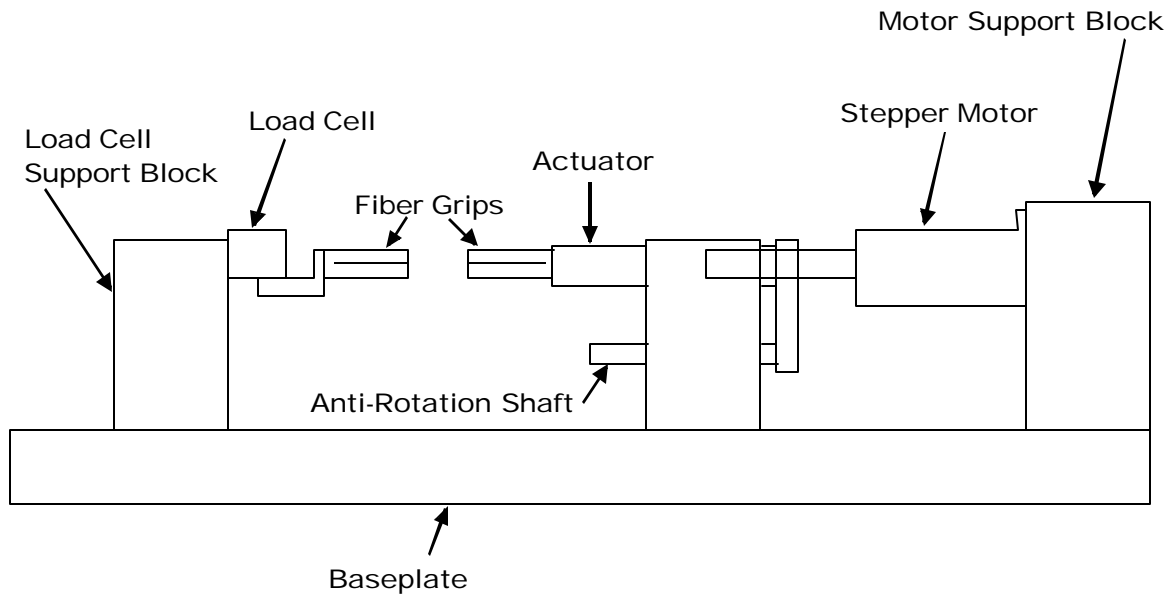


FIGURE 1: FIBER TEST SYSTEM ASSEMBLY

The test frame is comprised of baseplates and alignment blocks to house the various components of the system and provide absolute alignment of the test machine fixturing, such as the grips and stepper motor. The load cell (S.N. C19344) is attached to the load cell support block with a threaded insert. The load cell has a capacity of 100 pounds and is calibrated annually by the PME Group. The test machine must be disassembled before the load cell can be calibrated, and the grips must be aligned again after the calibration has been completed. The fiber grip on the left is attached to the load cell via a socket head cap screw and a machined alignment fixture. The fiber grip on the right is attached to the actuator and is housed in a wood's metal pot to allow alignment with the top grip. The fiber specimen is placed in the slots in the grips and centered with the centering blocks. The grips are then tightened by turning the socket head cap screws (4-40 x $\frac{3}{4}$) with a hex wrench. The actuator is attached to a screw-driven stepper motor (Model M063-FF-206E) which controls the movement of the actuator. The actuator is also attached to the actuator alignment block that also houses the anti-rotation shaft from which the displacement is measured with a linear variable displacement transducer (LVDT). As

the stepper motor moves the actuator at a rate specified in the test program by the operator, the LVDT's movement is entered into the test program electronically via cables.

The entire system is controlled by the computer with test parameters entered by the operator into the **MATE** software program. The software also collects the data and includes a package to analyze the test data immediately after every test. The test machine is very user-friendly and compact.

The LaserMike (Model 501-195S) which is not shown in Figure 1 is connected to the computer via cables and is used to measure the distance between the grips as well as the distance between the flags on the fiber test specimen during testing. It is housed on a baseplate, which has been leveled by two lifts. The test software converts the lasermike scans to strain during the test.

The fiber test system is used to test small diameter fibers and larger diameter wire. Before testing any material in the machine, consideration should be given to the loads needed to fail the intended test specimens. The load cell has only a one-hundred pound capacity. This level must never be exceeded.

Section 3

Preparation

A number of tasks must be done in preparation of tension testing of single filament fibers on the compact fiber test machine. It is assumed that the operator has been shown the various steps involved and has the basic knowledge of how to operate the equipment discussed in the following paragraphs.

3.1 *Diameter Measurement*

Get instructions on the number of fiber tests to be conducted from the project engineer. For groups of 50 or more fibers, measure the diameters of 30 fibers to obtain an average diameter value. For groups less than 50, please consult with the project engineer to receive instructions on the number of fibers that need to be measured to obtain an average diameter for that group of fibers. This value is important, as it is used to compute the ultimate strength during the tension test.

Use the Nikon system to measure the fibers. Until comfortable with handling and measuring the individual fibers, measure only one fiber at a time. Place the fiber on a surface that will allow clear visibility of the fiber. Select the proper magnification, turn on the measuring equipment, and measure the fiber in metric units. Measure and record both ends of each fiber. After a fiber is measured, place it in a safe location where it will not be measured again. Once the diameters of the various fibers have been measured and recorded, obtain an average value for that group by calculating the sum of the measurements and dividing that number by the total number of measurements which have been made. Keep the written measurements and the calculated average diameter with the fiber specimens. Give both back to the project engineer upon completion of testing.

3.2 *Foil Preparation*

Heavy aluminum foil (0.010-inch thick), when used to line both grips on the fiber tester, has significantly decreased slippage and breakage of the fiber in the gripped areas of the fiber specimen. Use this same foil to line the grips during testing. Prepare a large number of foils prior to each session, since each foil can be used only one time. The heavy aluminum foil is located in the same room as the fiber tester. Using a standard paper cutter, cut the foil into rectangular tabs measuring two inches in length by one inch in width. Using a single-edge razor blade, fold the foil in half over the blade. Insert the foil lined blade into the slotted grip with the open foil facing the operator. While holding the foil-lined blade with one hand, fold the excess foil up above the blade and down below the blade. Ensure that the blade remains firmly in the grip slots during this procedure.

3.3 *Flag Preparation*

Flags are hung from the fiber specimen during testing to measure displacement. The lasermike scans the distance between the two flags during the test, and that

information is recorded in the test file during testing. If the flags need to be replaced, make them with any wire with suitable thickness. Cut the wire approximately 1-1/2-inch in length. Bend one end of the wire into the shape of a candy cane and then flatten that same end with a hammer. An old flag can be used as an example of how the new flags should look.

3.4 Materials Needed

Certain materials are needed to perform tension testing on single filament fiber specimens. Gather the following materials prior to testing so as not to interfere with the process once it has been started. The materials include, but are not limited to, the following:

- log book
- glue stick
- measurement flags
- fiber test specimens
- pencil
- foil tabs
- tweezers
- glass slide
- razor blade
- hex wrenches

3.5 MATE Test Program

Make the appropriate directories on the computer hard drive before setting up the test specimen. Initialize the MATE program from your personal directory before setting up the test. Enter the MATE testing program by entering **MATE** at the prompt. Choose the **Monotonic Test Control/Data Analysis** for a **Tension Test**. Choose the box entitled **Mate Tension Test Control**. Choose **metric units**. Choose **Perform Tension Test**. Ignore any references made to the **Span** (on this test machine only) as a span is not used on this test machine. Then choose **Enter Test Parameters Interactively**. The program will prompt the operator for information and, unless stated otherwise, the following information should be entered:

Operator Name: (Operator's Name)

Test System ID: (Fiber Tester No. 1)

Load Transducer Serial Number: (C19344, unless changed)

Displacement Transducer Serial Number: (1629)

Specimen ID: (Changed Every Test, Example: SCS6-01, SCS6-02, SCS6-03)

Select **Round** when prompted to select specimen type.

Specimen Diameter: (Average Diameter in millimeters).

Material ID: (Fiber Material, Example: SCS-6, Ultra SiC, etc.)

Poisson's Ratio: (0.3)

Test Temp.: (23)

Test Environment: (Lab Air)

Load Range (Full Scale): (Top Left Indicator=1 kN; Top Right Indicator=0.2 kN)

Extensometer Range: (0.3 mm)

Strain Auto Zero (Y/N): (Y)

Stroke Range: (2.00 mm)

Choose **Compute Engineering Stress and Strain**

Choose **Crosshead Displacement (Stroke) Control**

Number of Breakpoints: (1)

Ramp Rate for Breakpoint #1: (0.33000E-01 mm/s)

Choose **Take Data Based on Time Intervals**

Data Time Interval: (2.50E-01 seconds)

Acquire Auxiliary Data (Y/N): (N)

Take Photos (Y/N): (N)

Active Log File Name: (Changed every test, Example: SCS601.Raw, SCS602.Raw, SCS603.Raw...)

Press the **Esc** key when prompted for various limits.

At this time, cursor to the **File Controls** box on the main menu and press **Enter**. Select **Save Parameters and Data for Restart**. Enter a restart file name which is related to the test series ending with **.RST** (Example: SCS6.RST). If the program is exited at any time, a restart file will be available, therefore eliminating the need to enter all of the test parameters already entered earlier.

Discuss the previous information with the project engineer if there are any questions or concerns. Remember to change the file name and specimen number for every test. If the file name is not changed, data from the previous test will be overwritten and lost. Choose file names carefully and be consistent with their use.

To exit the test program, select the box entitled **Exit to MATE Main Menu**. Press the **Esc** key. When prompted to quit at the top of the monitor, enter **Y** for yes. Again, ignore all references made to the span. Press the **Esc** key again. Enter **Y** when prompted to quit. This will return the operator back to the DOS prompt.

Section 4

Fiber Testing

Follow these instructions to set-up and run a fiber test. It is assumed that the operator has been shown these steps previously and has the basic knowledge of what each step entails. Caution must be exercised when handling the fiber test specimens. Accuracy in centering the specimen and careful handling of the fiber are imperative for a successful test. Make sure that all of the appropriate directories on the computer hard drive have been created and that the MATE program has been initialized and set up appropriately.

1. Coat the threads of new set screws with lubricant. Insert the set screws into the grips.
2. Flatten the foil tabs by gently sliding the razor blade over both tabs until all the wrinkles have been removed. Insert the foil tabs into both grips by using the razor blade. Fold the excess material across the outer surface of the grip. *The foil tabs can only be used for one test, so they must be replaced before starting the next test.*
3. Remove a fiber specimen with the tweezers. Use the tweezers to insert the specimen into the grips. Insert an equal length of fiber into both grips. If the fiber is too long, break one end by simply bending the fiber until it breaks. Center the specimen in the grips by using the gage blocks. While keeping the specimen and gage blocks firmly in the grips, gently turn the set screws in the grips until they are somewhat snug. Remove the gage blocks. Tighten the set screws until they are tight. Tightening the set screws is the hardest task simply because there are many variables between operators such as individual strength, ability to feel resistance, and level of experience. If the set screws are not tightened enough, the fiber will slip from the grips during the test. If the set screws are too tight, the fiber will break in or at the grip. Patience and experience are the two most important factors when dealing with this task. *Remember to hold the grip which extends from the load cell on the left-hand side of the test machine so that the grip does not turn while tightening the screws. Movement of the grip can damage the load cell and cause misalignment of the grips.* If slippage occurs during the test, stop the test program, loosen the set screws on both grips, and choose **Abort Test and Ramp to Zero**. Set up the test again, exerting more force during the tightening process or replacing the set screws if excessive wear seems to be the problem.
4. Place one flag on the fiber as close as possible without touching the right-side grip. Place the other flag approximately 0.25-inch from the left-side grip.
5. In the MATE program, cursor to the **Data Acquisition** box as seen on the monitor screen and press **Enter**. Cursor to **View Lasermike Output**. The number shown on the screen will have six digits (00.0000). If the flags have been placed too far apart, the reading shown is zero. A reading between 16.000 and 20.000 is desired. Move the flags around to obtain this number.

6. The lasermike reading must be relatively calm before the test can be conducted. This applies only to the two digits before the decimal and the two digits after the decimal. It is typical for the last two digits to drift, and the test can be run when these particular digits are drifting. If the reading does not settle down after a minute, ensure that nothing is touching the table and that air is not blowing close to the specimen. The lasermike and flags can detect the movement caused by walking, so tread lightly around the test area. Wait until the lasermike reading has stabilized.
7. Press the **Esc** key to exit the lasermike reading. Immediately choose **Perform Test** from the menu. This step starts the test immediately and displays the data on the screen. Wear safety glasses if standing near the test machine and watching the specimen. Fiber fragments can travel quite a distance upon failure and end up in eyes, hands, arms, and even legs.
8. After failure occurs, press any key on the keyboard to stop the data acquisition and the test machine.
9. Fiber fracture surfaces are kept from every test when a gage section failure has occurred. Examine the specimen after the test to determine which type of failure occurred. A gage section failure has occurred if a portion of the fiber is extending from both grips. A shattered failure has occurred if there are no large fiber pieces lying below the grips on the paper. A grip failure has occurred if there is a large fiber extending from one grip but no fiber can be found at the other grip. Also, a grip failure has occurred if there are large pieces of fiber lying on the paper below the grips. Record the type of failure in the log book.
10. Gage section failure fracture surfaces are preserved on the glass slide. The glass slide should be labeled with a Sharpie marker as **Group (???)**, **Date**, **Slide 1, In Order From Left to Right, 1 through (???)**. Smear a thin strip of glue from the glue stick right below the writing. Place the gripped ends of the fiber in the glue. **Keep the actual fracture surfaces from the fiber out of the glue toward the bottom of the slide.** Record the type of failure in the log book and how many fracture surfaces were saved for that particular specimen. By using the above steps, the engineer will know which fracture surfaces belong to which test, etc. Always put the fibers on the glass slide starting from left to right and keep them in order by test. Note: If a large number of grip failures are occurring, this is a sign that the set screws on the grips are too tight. Try replacing the set screws and using less force to tighten the set screws. If the problem is not cured by this action, consult with the project engineer to determine if the problem is of a mechanical nature or a material nature.
11. Press **Enter** on the keyboard and choose **Abort Test and Ramp to Zero** from the menu. This will ramp the grip back to the starting position. When completed, the program will prompt the operator for a file name for the raw data. Remember to change this file name **after every test** to avoid writing over previously acquired test data. If a test on specimen 01 has just been completed, it may be saved under a file name such as GRP1-01.Raw. If specimen 02 has been done, save it under a file name such as GRP1-02.Raw, etc.
12. Choose **Analyze Test Data** from the main menu. The raw data will then be displayed. When asked to choose the first data point, press **Enter** to choose the

current data point, as the program automatically selects the first data point. When asked to choose the last data point for the test, cursor to the very last data point at the top of the curve and press **Enter**. This does not change the raw data. It just simply makes it easier for the operator to analyze the data. When asked to choose the portion of the curve to expand so that a modulus can be calculated, press the **End** key, and the program will select the entire curve. When prompted to pick the first point to be used for the modulus calculation, cursor to the first data point in the linear portion of the curve and press **Enter**. When prompted to choose the last point to be used for the modulus calculation, cursor to the last data point in the linear portion of the curve and press **Enter**. The program automatically selects the ultimate and yield strengths of the test. So when prompted to select these values, simply press **Enter**. View the analyzed results. Record the ultimate strength and modulus values in the log book. Do not save this data unless the project engineer has specified to do so. If it is to be saved, ensure that the file name is different than the raw data file name, otherwise the raw data will be written over. ***The raw data file should never be modified, written over, or changed under any circumstance.*** Press the **Esc** key to get back to the main menu.

13. Cursor to the **Material and Specimen Parameters** box. Continue to press **Enter** until prompted for a specimen number. Change the number to correspond to the next test (Example: GRP1.02, GRP1.03, etc.).
14. Cursor to **Data Acquisition Controls** and choose **View Lasermike Reading**. Set up the next test and start the testing procedure all over again, following the same steps as previously followed for this procedure.

When the test series is complete, make a copy of the recorded measurements and data from the log book. Give the excess fiber specimens, failure surfaces, and the copied log book information to the project engineer. Inform the engineer of the exact location of the data files on the computer hard drive.

Section 5

Testing of Fibers Directly From A Composite Specimen

Periodically, an engineer will request that fiber tests be conducted on fibers from a composite specimen. Depending on the engineer, the specimen will have been partially etched for the operator. Etching is a chemical process that removes the metal matrix from the fibers. Procedures for this etching process can be found in Section 7 of this manual. If done correctly, several layers of fibers can be seen. If done incorrectly, the fibers will be without all metal matrix material, leaving them separated and out of order. The actual testing procedure for the fibers from a composite specimen is the same as outlined in Section 4 of this manual. However, measurement of the fibers and recording of the various fibers are very different than previously mentioned. Except for the steps discussed below, follow all other procedures for testing of fibers from a composite specimen.

5.1 *Diameter Measurement*

The measurement of fibers in an etched specimen is basically the same as outlined before, except care must be taken to measure the actual fiber and to not measure the matrix material that may still be attached to the fiber. If the matrix material is still attached to the fibers and no clear areas can be found, consult with the project engineer and inform them of the situation. The specimen may need to be etched further, or the project engineer may need to provide an accurate diameter to use for the area calculation. If the fibers can be seen clearly and are free of the matrix material, measure the fibers located at the top and bottom layers of the composite using the same procedure as discussed earlier in Section 3.1. Do not separate the fibers as it is most important that the fibers remain together until tested. If any problems arise during this procedure, consult with the project engineer.

5.2 *Tracking and Logging of Specimens in a Composite Specimen*

A composite specimen is composed of multiple layers of fibers. When an engineer requests this type of work, the engineer is interested in studying the effects of temperature on the fiber strength. The effects of temperature on the fiber strength may vary according to the location of the fiber in the composite specimen. Therefore, tracking and numbering the specimens according to their location in the composite specimen are imperative. The following procedure is to be used in conjunction with the previously detailed test procedure to conduct tests on fibers from an etched specimen. Good record keeping is imperative during this process.

1. Measure the diameter and calculate the average diameter for the representative group of fibers.

2. Prepare the log book for this series of tests, including the information for which side of the composite specimen the extraction process will begin and which layer will be extracted first.
3. Prepare the glass slide used to hold the fracture surfaces.
4. Line both grips with aluminum foil.
5. Determine which side of the specimen to start on first. Use the magnifying glass, and adjust the glass to where the fibers can be seen clearly. Again, make good notes, and record the location of where this process is beginning in the log book.
6. Normally, specimens are numbered according to their location in the composite specimen. If working on the top layer of fibers and testing the fibers located at the very edge, the specimen number will be **L1-01** (L1 indicates layer one; 01 indicates specimen one). This will continue as **L1-02, L1-03,...** as fibers two, three, and so on are extracted and tested from the top layer. Record these numbers in the log book, and use them in the test program as the specimen number before conducting the test. When reaching the second layer, the specimen numbers will be **L2-01, L2-02, L2-03, etc.** Use this numbering system for each layer, changing the layer number when needed. **Do not remove the fiber from the composite specimen until it is ready to be tested.**
7. The magnifying glass and two pairs of tweezers are required for the extraction process. Place the composite specimen under the magnifying glass where the top layer of fibers can be seen. If right-handed, start the extraction process at the far right of the specimen at the fiber closest to the edge of the top layer. If left-handed, start at the far left at the fiber closest to the edge in the top layer. This will be specimen **L1-01**. Gently place one tip of the tweezers under the loose portion of the fiber close to where it is still attached to the matrix at the top, while gently pressing on the remaining fibers in the top layer with another pair of tweezers. Gently slide the tip of the tweezers under the fiber, along its length, until the fiber is free of matrix material. If the fiber breaks during the extraction process, record **Fractured During Removal Process** in the log book next to the corresponding specimen number. All of the fibers and their location in the composite specimen must be accounted for, regardless of when or how they fracture. If it is obvious that a fiber is missing, simply record the specimen number in the log book, and record **Missing** next to that particular specimen number. If a fiber specimen is too short to be tested, note the specimen number in the log book, enter **Too Short to be Tested** next to the same specimen number, and place the short fiber in a container that will be given to the project engineer after the series is completed. After extracting the fiber (the specimen number should already be in the log book and test program), immediately conduct the test on the fiber. Preserve the fracture surfaces if they are available. A new glass slide should be used for each layer to avoid confusion. The slides should be identified with their respective layer. Continue this process for the entire composite specimen, completing the entire layer before going on to the next layer.

Section 6

Wire Testing

Wire testing and fiber testing are very similar in that they both use the fiber test machine, the same MATE testing program, most of the same test parameters, and almost the same set up procedure. One of the main differences between wire testing and fiber testing is that wire testing does not involve an average diameter measurement. The diameter to be used in the test program is the actual diameter of the wire that is to be tested. Therefore, measure every wire, and change the wire diameter in the test program for every test and retest. Another main difference is, if the project engineer needs a good modulus value for the wire matrix, the wire may need to be prestretched in order to remove some of the residual stresses caused by the bends in the wire. If the wire looks completely straight or a good modulus value is not important to the project engineer, ignore the prestretch instructions in Section 6.4.

6.1 Materials Needed

The following materials are required to perform wire testing on the compact fiber test machine:

- wire specimens
- log book
- pencil
- scissors
- hex wrench
- index cards
- tape
- tweezers
- measurement flags
- safety goggles (optional)

If the measurement flags are not available, see Section 3.3 for the directions needed to make them.

6.2 Wire Test Program and Test Parameters

Use the fiber testing set-up procedures outlined in Section 3.5 for program initialization and test parameters. The only exceptions to the test parameters are that the Load Range = 1 kN and the Data Time Interval = 0.02 second.

6.3 Wire Test Set-Up

Cut the wire with scissors to a length of approximately one-fourth inch less than the distance between the two grip screws of the fiber test machine. Try to straighten the wire as much as possible by hand. Measure the wire diameter in millimeters using the Nikon compound microscope. Measure three different areas of the wire, and use the average of those three measurements for the diameter. Insert the wire into the grips using the procedures outlined in Section 4.2.

6.4 Prestretch

Place the measurement flags on the specimen using the procedures detailed in Sections 4.3-4.5. Press the **Esc** key to exit the lasermike reading. Choose **Perform Test** to start the test. During the test, the computer graphs the data on the monitor with Strain (m/m) on the x-axis and Stress (MPa) on the y-axis. Continue the test until a minimum of 2% strain (0.02 m/m) is reached. Upon reaching the aforementioned value, press any key to stop the test. Remove the wire from the grips and press **Enter**. Choose **Abort Test and Ramp to Zero**. Refer to Section 6.7 for data analysis.

6.5 Testing

Place the flags on the wire specimen using the procedures outlined in Section 4.3-4.5. Press the **Esc** key to exit the lasermike reading. Choose **Perform Test** to start the test. Wear safety glasses if standing near and facing the test machine during the test. Continue the test until the wire fails or the maximum number of data scans is reached. When the wire fails, press any key to interrupt the test program. If the maximum number of data scans is reached before the wire fails, remove the wire from the grips and press **Enter**.

6.6 Fracture Surfaces

If the wire fails, remove the wire pieces without touching the fractured ends, and record the failure of the wire (gage, shattered, or grip) in the log book for that specimen. A gage section failure occurs when a portion of the wire extends out of both grips. A shattered failure occurs when no portion of the wire extends out of the grips. A grip failure occurs when a portion of the wire extends out of only one grip or when a large piece of wire is lying on the paper below the grip. If the project engineer has requested the wire ends (gage failure or all failures), tape the unfractured ends down on a small card (just large enough to fit the wires) with the two fractured ends facing each other (without contact). Label the card with the proper specimen identification number. Press **Enter** and choose **Abort Test and Ramp to Zero**.

6.7 Data Analysis

Save the raw data file, remembering to include a new file name for every test and retest. Do not write over any other files. If the file is a retest file, use the same file name as the first test except add the letter **A** at the end (or **B** if this is the third test for this wire, etc.). For example, if the file name for the first test is WIRE-01.Raw, the retest file name for that same wire will be WIRE-01A.Raw. Analyze the data using the procedure outlined in Section 4.12. Record the data that has been requested by the project engineer. In the most frequent case, only the ultimate strength, strain at failure, and the modulus values are needed. If this test was a prestretch, or if the maximum number of data scans was reached, record the failure as **Interrupted**. If a retest is required, measure the wire diameter again, and enter the new measurement under **Initialize** in the main menu. Also, change the specimen number. Insert the wire into the grips again and return to Section 6.5. If a retest is not needed, return to Section 6.3 to set up a new wire test. Remember to change the specimen number in the test program.

Section 7

Removing Metal Matrix From Fibers In a Composite Specimen by Etching

Chemical etching may be required to extract fibers from a composite specimen. Etching involves use of an extremely hazardous chemical Bromine that falls into the Class 4 category of **Fatal Upon Short Term Exposure**. An MSDS for bromine has been included in Appendix A. Bromine is used with Methanol and Tartaric Acid to remove the metal matrix from the fibers during etching. The following procedure is to be used as a guideline only by persons having been formally trained in the use of bromine. Bromine can be absorbed through the skin causing the tissue to be destroyed from the inside to the outside. It can also be inhaled causing fatal lung damage. The authors of this manual assume no responsibility for accidents that may happen while using this procedure. The operator assumes all responsibility while working with this chemical and must make every effort to ensure that the safety precautions are being followed, that effective training has been given, and that all instructions are fully understood prior to the use of this chemical.

Chemical etching is done in the Metallurgy Laboratory under the appropriate fume hood. Prior to starting this procedure, ensure that all the required safety equipment is ready. Wear the following safety equipment while working with this procedure: safety goggles, neoprene gloves, and a lab coat. Tie long hair back or place the long hair under the lab coat where it will not interfere or come in contact with any chemicals during this procedure. **Wear all safety attire before starting this procedure.** Also, ensure that the fume hood is turned on. Read this procedure in its entirety before proceeding to ensure that all the needed materials and tools are in place and that the procedure is fully understood.

7.1 Materials Needed

While wearing gloves and all other safety equipment described above, gather all of the following items into the fume hood where the work is to be completed:

- Specimen
- Test tube
- Marker
- 3 X 5" index card
- 50-mL beaker (optional)
- Spray bottle of methanol
- 10% bromine/90% methanol storage bottle
- Waste bottle for 10% bromine/90% methanol
- Large plastic beaker or graduated cylinder (needed later when etching has been completed)
- Paperclips
- 400-mL beaker
- Alligator clip
- Tongs or tweezers
- Bottle of 100% methanol
- Plastic funnel

Also, make sure bicarbonate and paper towels are nearby for clean-up or in case of a spill.

7.2 Set-up

1. Make a specimen holding aperture out of an alligator clip and some paperclips. It should form a hook that rests on top of the test tube opening which hangs the specimen into the bromine methanol solution.
2. Make a test tube holder by taping the top of a 400-mL beaker with 4 pieces of tape leaving a square hole slightly smaller than the test tube. This will hold the test tube perpendicular and steady.
3. Hang the specimen into the empty test tube. Fill the test tube with water to the point the specimen is to be submerged. Leave about a one-inch tab of the specimen uncovered if the fiber locations are to be tracked later. If the top and bottom of the specimen is not to be etched, place the test tube half full of the solution, leaving the top of one half completely out of the solution. Take the specimen out of the tube and mark the water level on the beaker. The hazardous mixture will be poured to this level. Pour out the water.

7.3 Procedure

1. If there is any moisture on the countertop, neutralize it with bicarbonate and clean it up with a paper towel. Assume that any moisture is hazardous.
2. Keep the fume hood window down as far as possible so that the fumes go out the hood as they are supposed to. Do not inhale bromine, get it on your skin or in your eyes, or have any contact with it whatsoever. Never attempt to work with bromine outside of the fume hood and never handle the chemical recklessly.
3. Place the test tube into the holder of the taped beaker. Use the bottle labeled **10% Bromine, 90% Methanol**. Pour the bromine/methanol/ tartaric acid solution in the test tube up to the marked line. Use a funnel when pouring to ensure that the solution goes into the test tube.
4. Complete a 3"x5" index card stating **10% Bromine/90% Methanol, today's date, point of contact with telephone number, and "Do Not Touch."** Put the index card in the beaker containing the test tube, and gently place the beaker in the rear corner of the fume hood with the other etchings. The bottle of solution should be placed back on the top shelf from where it was retrieved.
5. Hang the specimen into the solution overnight. Covering the top of the beaker with a 50-mL beaker will slow the evaporation of the soup but may want to be avoided as to not disrupt the specimen hanging aperture.
6. If the top and bottom of the specimen are not to be etched, closely monitor the progress of the etching at regular intervals. Do one end of the specimen at a time.
7. Retrieve the waste bottle specifically labeled **10% Bromine/90% Methanol Waste** from the storage cabinet and pour the excess solution into the waste bottle. When rinsing all tools used during this process with methanol, ensure that the excess goes into this waste bottle. **Never pour excess liquid down the sink and never put it into a waste bottle for some other chemical. Always use the specific waste bottle made for this solution.**

8. Pour methanol into beakers, funnel, etc. (runoff methanol should be dispensed into a beaker) to neutralize the bromine. Use only methanol for this entire procedure as other chemicals will react to the bromine creating a hazardous situation. Put all excess or used methanol in the waste bottle for the bromine solution.
9. Neutralize all moisture on the countertop with bicarbonate and wipe the area clean. It is a good idea to use methanol on the neoprene gloves prior to taking them off to ensure that no bromine is left on the gloves. Also, wash the gloves in the sink with soap and water while wearing them.
10. When the specimen has finished being etched, or when the solution has weakened considerably, get a plastic beaker or graduated cylinder tall enough to hold the specimen and pour enough methanol into the beaker to completely immerse the specimen. Using tongs or tweezers, remove the specimen from the bromine solution and place it in the beaker with the methanol. Place the beaker in the ultrasonic cleaner for approximately five minutes. Pour the excess methanol into the waste bottle for the bromine solution, rinse the beaker with water, and repeat the cleaning in methanol using the ultrasonic cleaner. Pour the used bromine/methanol solution into the bromine/methanol waste bottle.
11. Use the previously mentioned cleaning procedure upon completion. Clean up everything, and use bicarbonate if any moisture is on the counter.

Section 8

Making the 10% Bromine/ 90% Methanol Solution

This procedure is considered to be potentially hazardous and should be followed closely. It should be used only by individuals having received formal training on working with Class 4 chemicals. Again, the authors assume no responsibility for accidents or injuries that may be sustained while following this procedure. All of the work described in this procedure must be performed under the fume hood in the Metallurgy Laboratory. Safety goggles and neoprene gloves must be worn at all times. Latex gloves may be used beneath the neoprene gloves for increased safety. A standard rubber-like apron, located in the hood room in the laboratory, must be worn to protect against any reactions that may occur when pouring the bromine into the methanol. Also, it is strongly recommended that a face shield, which is also in this same room, be worn as face protection. The same safety precautions as stated in Section 7 of this manual should be applied and followed during this procedure. ***Safety precautions are more important during this procedure than any other section in this manual.***

8.1 Materials Needed

While wearing gloves and all other safety equipment described above, gather all of the following items into the fume hood where the work is to be completed:

- 100% bromine, (Kept under lock and key and can only be obtained by contacting the Metallurgy Laboratory Manager)
- Storage bottle for the 10% bromine/90% methanol solution
- Scoopula – for adding tartaric acid to the solution
- Large beaker to hold all of the items coming in contact with the bromine
- Waste bottle for the bromine/methanol solution
- Graduated cylinder which will hold at least 400 ml of solution
- Tartaric Acid
 - Plastic funnel
- Bottle of 100% methanol
 - Spray bottle of methanol
- Glass stirring rod

8.2 Procedure

1. Make sure all safety attire is on. Also, ensure that the fume hood is turned on. It should be kept on at all times.
2. Determine the amount of bromine/methanol that will make a solution of 10% bromine and 90% methanol. For example, if a total solution of 300 ml is desired, this will require 270 ml of methanol and 30 ml of bromine. After calculating the amount of solution to be made in ml, check the calculations to ensure that no mistakes were made. Mistakes can lead to having a much stronger or much weaker solution than is required; neither one of these situations should be allowed to occur.

3. While being as exact as possible, pour the methanol into the graduated cylinder to the 270 ml mark on the cylinder.
4. Pull the fume hood window down as far as possible while still providing protection so everything needed can be reached during this procedure. Remove the cap on the waste bottle for the bromine/methanol solution and the cap on the bottle which will be used to contain the bromine/methanol solution.
5. It is now time to work with the 100% bromine. Place the plastic funnel into the top of the graduated cylinder now containing the methanol. Slowly remove the cap on the 100% bromine bottle. As soon as the cap is removed, bromine, in the form of a dark brown or red poisonous gas, will be coming from the bottle. Slowly pour the correct amount of bromine into the methanol (30 ml or a total cylinder liquid of 300 ml). Do not pour the bromine quickly as the reaction between bromine and methanol causes heat to be formed. If the bromine is poured too quickly, the mixture could boil over and create a spill. Immediately place the cap back on the bottle of bromine tightly.
6. Tartaric acid is added as a buffer to the bromine/methanol solution. Use the scoopula to add the tartaric acid to the solution. Stir with the stirring rod to help the tartaric powder dissolve into the bromine/methanol solution. Add more tartaric acid until the solution is saturated (up to the point where tartaric acid no longer dissolves into the solution).
7. Pour the 10% bromine/90% methanol/tartaric acid solution now located in the graduated cylinder into the bromine/methanol solution bottle. Ensure that the cap has been put on the bromine/methanol solution bottle tightly.
8. Rinse the funnel and the graduated cylinder completely clean with the spray bottle of methanol, ensuring that all waste goes into the waste bromine/methanol bottle. Place the bromine/methanol solution back on the top shelf located at the top of the fume hood and put the 100% bromine back in the cabinet under lock and key. Rinse all of the items used with methanol (dispensing excess in waste bottle). Everything should be rinsed again in the sink with water to ensure that nothing is contaminated. Any moisture or liquid located on the fume hood countertop should be neutralized with bicarbonate.
9. Wash the neoprene gloves with soap and water while wearing them and dry them. Put away everything that was used and remove the protective gear.

Section 9

Connecting the LaserMike to the Computer After a Power Failure

When a power failure occurs, the connection between the lasermike and the computer is broken. When this occurs, the lasermike cannot read the distance between the two measurement flags a fiber specimen and must be reconnected to the computer with the following procedure.

1. Install a fiber specimen in the test machine. Place the flags on the fiber just as if a test is being conducted.
2. At the C:\ prompt, enter **CD KERMIT**.
3. Once in the Kermit directory, type **KERMIT**.
4. Type **C** at the MS-KERMIT>: prompt.
5. There will be a series of numbers shown on the monitor. Ignore these numbers and enter **!S500100**.
6. Press the **Alt** key and the **X** key simultaneously (ALT-X).
7. Type **QUIT** and press **RETURN**.

The lasermike should then display a reading between the two flags once the test program has been entered. Consult with the project engineer if the numbers are not correct or if the above procedure did not correct the problem.

Section 10

Calibrating the Load Cell And LaserMike

The load cell must be calibrated annually to ensure its accuracy. This is done by the PME group. They must be notified when it is time for the load cell to be calibrated. The test machine must be taken apart and the lasermike must be removed before the load cell calibration can be performed. The grips must be aligned and the test machine put back together after the load cell has been calibrated. Details of this procedure are too complex to put into a manual. Please see Debbie Garner or Ken Goecke for instructions pertaining to load cell calibration of the fiber tester.

The lasermike can be checked for accuracy by putting a precisely measured piece of steel in between the grips and changing the lasermike to scan at one location. David Maxwell has the steel pieces in his possession. The lasermike scan can be changed following the instructions given in Section 9. If the lasermike reading does not match the known dimensions of the steel pieces, the lab manager should be informed, and actions should be taken to calibrate the lasermike.

Section 11

Changing the Gage Length of the Compact Fiber Test Machine

It may sometimes be necessary to change the gage length of the fiber test machine to accommodate fibers of shorter length. Follow the directions listed below specifically and carefully.

1. Turn off the power to the stepper motor on the main console.
2. Go to the C:\ prompt on the computer.
3. At the C:\ prompt, enter **CD UTIL**.
4. Once in the Utilities directory, enter **STEPTEST**. After doing this, a series of lines will be shown with fluctuating numbers. Press any key to go to the next screen.
5. Unplug the cable from the LVDT at the end of the fiber test machine.
6. Turn the LVDT in the appropriate direction that will allow the gage length to become longer or shorter, whichever is needed. Do this in small steps initially to ensure that the actuator/grip assembly is indeed moving in the right direction.
7. Plug the cable back in to the LVDT.
8. Turn on the power to the stepper motor on the main console.
9. Enter **RZ** from the menu to begin the movement of the actuator/grip assembly. At this point, the gage blocks from which the gage length will be measured can be inserted between the grips to ensure that the grip is moving in the right direction. Once the grips have stopped moving, the series of lines with the fluctuating numbers screen will appear on the computer. Once again, press any key to go to the main menu.
10. If the grips did not move, repeat the above steps, turning the LVDT more. Again, take small steps until confident in the ability to perform this task.
11. If the grips moved, but moved in the wrong direction, repeat the above steps and turn the LVDT in the opposite direction from which it was turned before.
12. Repeat all the steps until the exact gage length desired has been achieved, ensuring that the cable is unplugged before turning the LVDT and ensuring that the main stepper motor power on the console is in the off position while turning the LVDT.
13. When finished, ensure that the cable has been plugged back in to the LVDT and that the main power switch on the console is in the on position. Enter **QU** to exit the steptest program.

This page intentionally left blank.

NOTCHED FRACTURE BEHAVIOR OF OXIDE/OXIDE NEXTELTM720/AS COMPOSITE

Dennis J. Buchanan*, Reji John and Larry P. Zawada

Materials and Manufacturing Directorate, Air Force Research Laboratory (AFRL/MLLN), Wright-Patterson Air Force Base, OH 45433-7817

* University of Dayton Research Institute, Dayton, OH 45419

Abstract

Oxide/oxide ceramic matrix composites (CMC) are currently being demonstrated in high-temperature aerospace applications where their beneficial resistance to oxidation is critical to a successful design. Many of these component applications require holes and notches for cooling and attachment points. An investigation on the effects of notches on the fracture strength and damage at room and elevated temperature was initiated. The oxide/oxide CMC studied during this investigation was NextelTM720/AS. The Alumina-Silica matrix was reinforced with an eight-harness satin weave (8HSW) mat of NextelTM720 fibers. Two double-edged notch-geometries were studied, semi-circular and sharp (saw-cut) notches. Strain gages, extensometry and fractured samples were used to characterize the damage zone in the vicinity of the notches. NextelTM720/AS composite exhibited notch insensitive behavior for a range of tip radii and temperatures. Only at temperatures $\geq 1100^{\circ}\text{C}$ did the NextelTM720/AS CMC show any observable notch sensitivity. Finite element predictions of stress-strain behavior at the notch tip showed good agreement with the measured strain gage data.

Introduction

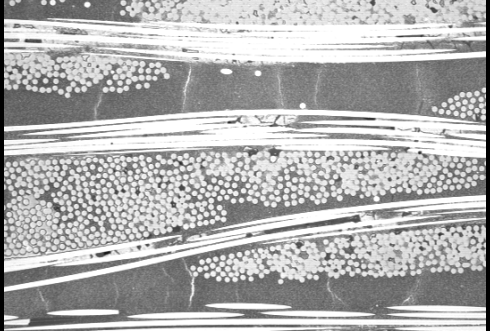
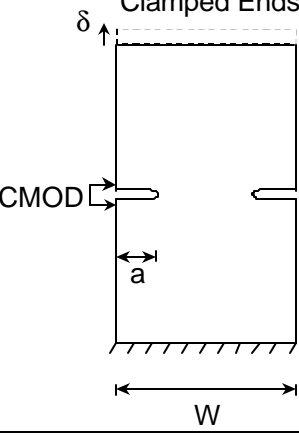
Ceramic matrix composites (CMC) are currently being demonstrated for high temperature aerospace applications. Many existing CMC materials suffer from oxidation problems at service temperature conditions. Oxide/oxide CMC have an inherent resistance to oxidation and therefore exhibit little or no degradation in mechanical properties at expected service temperatures. Many investigations [1-9] have shown that oxide/oxide CMC exhibit excellent tensile and fatigue properties at room and elevated temperatures. Tensile and fatigue strength of Nextel610/AS decreased by $\approx 15\text{-}20\%$ when tested at elevated temperatures around 1000°C [1,2,6,7]. Nextel610 fibers and Nextel610/AS CMC are susceptible to excessive creep deformation at temperatures $\geq 1000^{\circ}\text{C}$ [6,7,10,11]. In contrast, Nextel720 fibers exhibit significant creep resistance up to 1200°C [10,11]. Hence, oxide/oxide CMC with Nextel720 fibers are under consideration by the US Air Force for some applications with temperature requirements in the range of $1000\text{-}1200^{\circ}\text{C}$.

Recently, the notched fracture behavior of oxide/oxide CMC systems with Nextel610 and NextelTM720 fibers were studied [8,9,12,13]. Levi et al. [8] and Heathcote et al. [9] reported room temperature fracture results of NextelTM610/mullite-alumina and NextelTM720/mullite-alumina. Kramb et al. [12] reported the fracture behavior of NextelTM610/AS at room temperature and 950°C . John et al. [13] reported the fracture behavior of NextelTM720/AS at $23\text{-}1200^{\circ}\text{C}$ under tensile loading. This paper expands on the results reported in Ref. [13] to include prediction of the load-deformation response.

Material

The NextelTM720/AS CMC used in this investigation was manufactured by Engineered Ceramics, Inc, of San Diego, CA. The NextelTM720 fibers, which are produced by the 3M Company of St. Paul, MN

[14], are $\approx 12 \mu\text{m}$ in diameter. They are grouped together in tows and woven into a balanced eight-harness-satin weave (8HSW) cloth. Additional details about the manufacture of the panels can be found in Ref. [13].

 $200 \mu\text{m}$	
Figure 1. Microstructure of (0/90) 8HSW NextelTM720/AS microstructure highlighting the matrix cracks due to processing.	Figure 2. Schematic of the double notched geometry.

Experimental Procedure

The double-edge, notched-specimen geometry was used for the room and elevated temperature notched fracture tests. The typical dimensions of the specimens as shown in Fig. 2 were, width (W) = 15.0 mm, thickness (B) \approx 2.5 mm and length \approx 100 mm. The semicircular notch geometry, DEH(T), was made using a diamond coated grinding bit and the saw-cut notch geometry, DE(T), was made using a diamond saw.

The semicircular notch had a notch tip radius of 1.78 mm and the saw-cut notch had a notch tip radius of 0.11 mm. Both notch geometries were machined to the same length of \approx 1.875 mm which provided a normalized notch length of, $2a/W \approx 0.25$. The specimen notches were measured and photographed to document the condition of the notches prior to testing. The specimen ends were tabbed with fiberglass tabs to provide a flat uniform surface for the smooth grip surfaces and to minimize the possibility of grip failure. The specimens were mounted in a precisely aligned, rigid grip system [15] that minimized specimen bending and rotation. A clamshell style furnace was used with silicon-carbide heating elements under four-zone control for elevated temperature tests. Thermal profile maps on the specimen showed that the specimen was uniformly heated, $\pm 0.6\%$, over the entire gage section of the specimen. The fracture tests were conducted under displacement control at a rate of 0.005 mm/s generated by an 18-bit D/A function generator. During the tests, applied load and crack mouth opening displacement (CMOD) data were collected at elevated temperature and in addition, strain gage data were collected for selected room temperature tests. All the tests were conducted in laboratory air using a computer controlled servo-hydraulic test system [15,16].

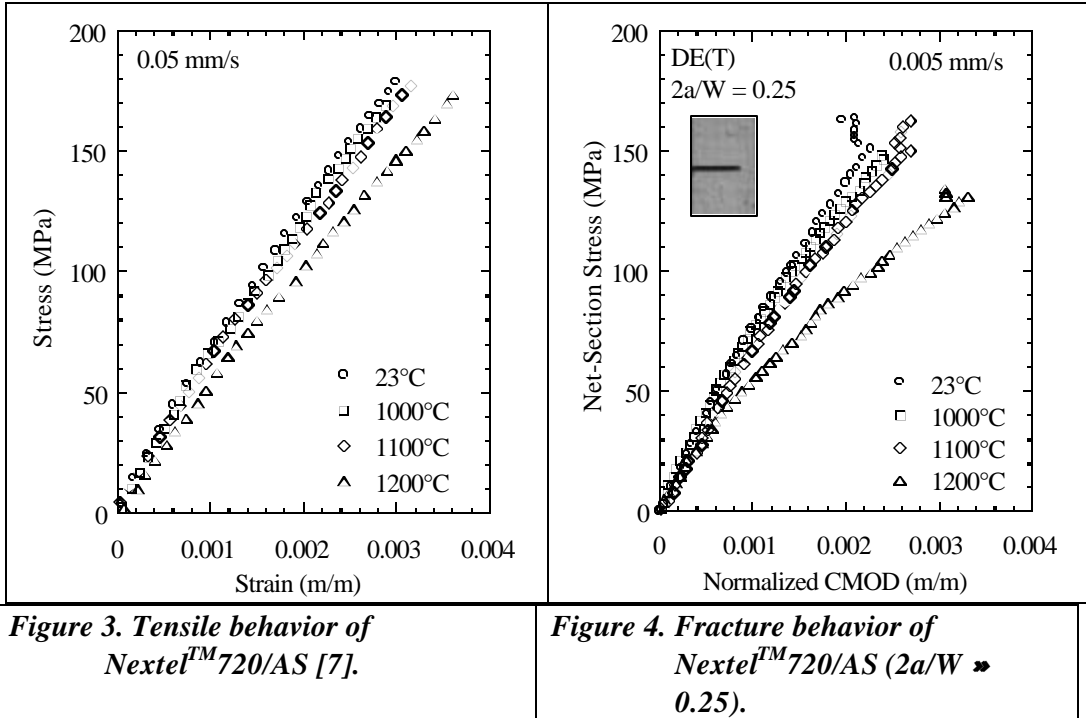


Figure 3. Tensile behavior of Nextel™720/AS [7].

Figure 4. Fracture behavior of Nextel™720/AS ($2a/W \approx 0.25$).

Experimental Results

Tensile and fracture tests were conducted at temperatures 23, 1000, 1100 and 1200°C as shown in Figs. 3 and 4 respectively. The tensile results show that the stress strain behavior does not change for temperatures of 1100°C and below. At 1200°C there was slightly more deformation compared to the lower temperature results but the ultimate strength was similar.

Fracture tests were conducted using the DE(T) geometry with a $2a/W \approx 0.25$ notch length. The fracture results, shown in Fig. 4, were similar to the tensile results where the deformation behavior did not change for temperatures of 1100°C and below. Figure 4 shows the net-section stress versus the normalized CMOD, where the normalized CMOD is the CMOD divided by the extensometer gage length. Again at 1200°C there was slightly more deformation compared to the lower temperature results and there was a noticeable 19% decrease in the ultimate net-section strength compared to the room temperature ultimate strength.

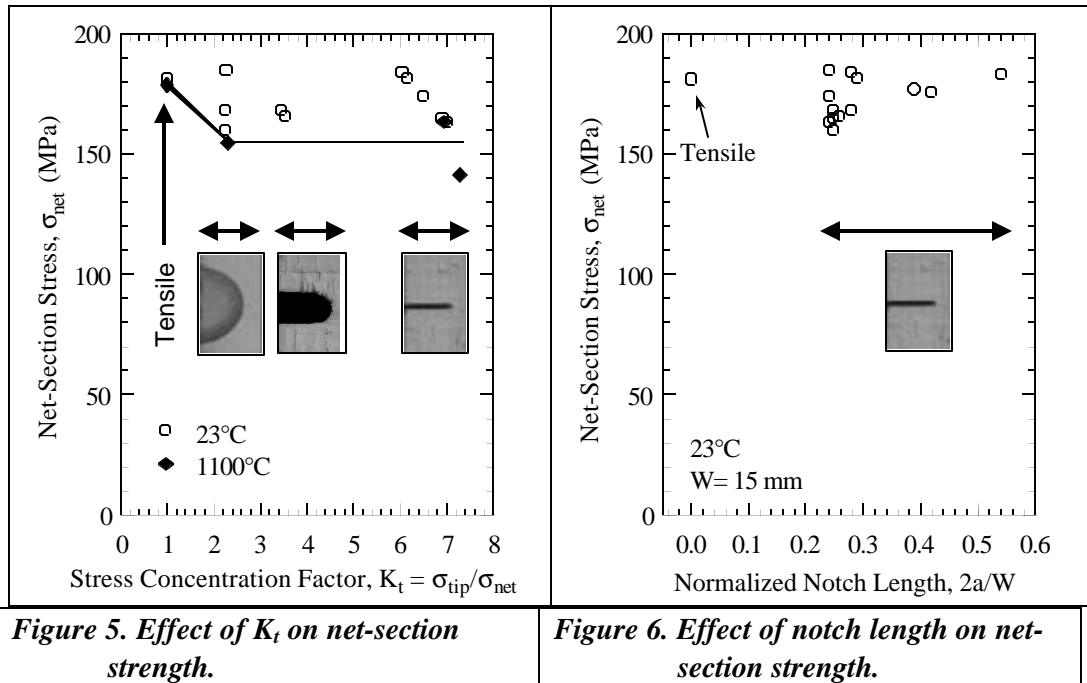
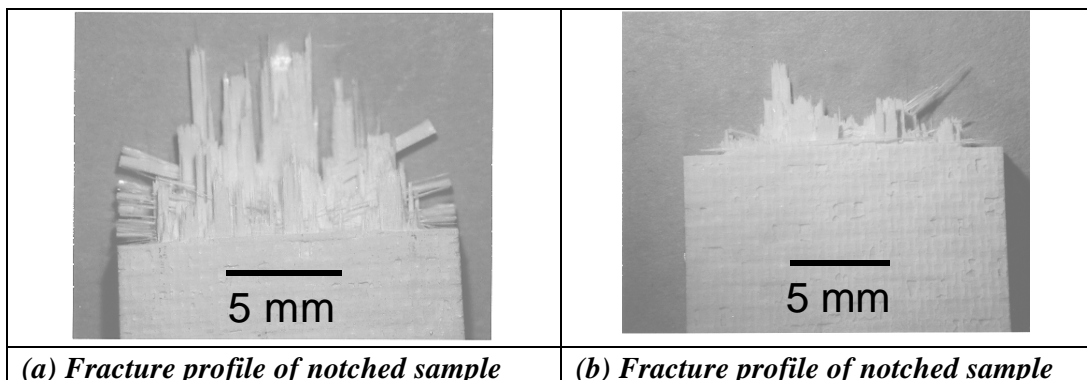


Figure 5. Effect of K_t on net-section strength.

Figure 6. Effect of notch length on net-section strength.

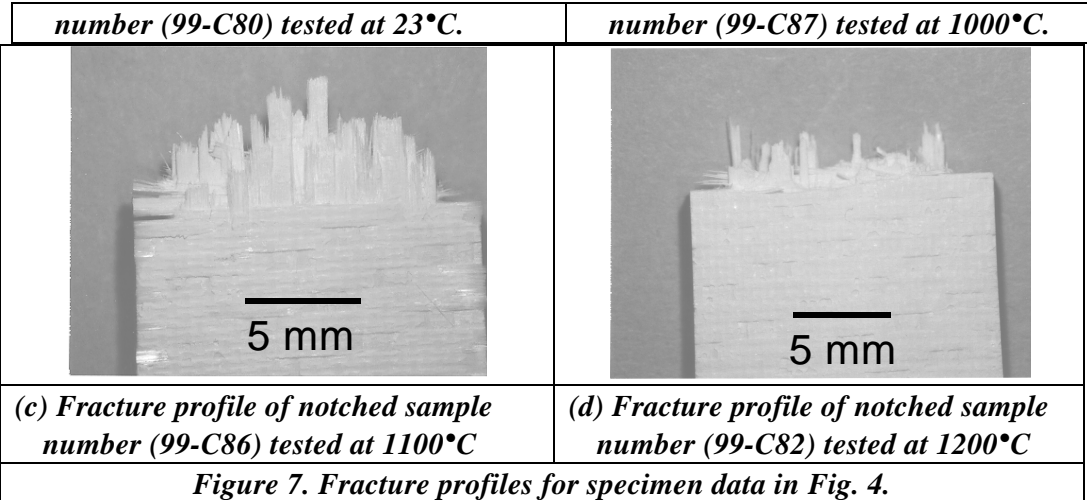
Figure 5 shows the effect of initial stress concentration factor ($K_t = \sigma_{tip}/\sigma_{net}$) on net-section failure strength for three notch-tip radii. Baseline ultimate strength from unnotched tensile data ($K_t = 1$) is also shown in Fig. 5. All notched specimens were tested with a common notch length of $a \approx 1.88$ mm ($2a/W \approx 0.25$), as shown in Fig. 2. The unnotched and notched specimens had a ligament width that was greater than the repeating pattern of the 8HSW, approximately 10 mm. The data shows that at 23°C the material is notch insensitive to the notch tip radii. At 1100°C, the material is slightly notch sensitive and exhibits about $\approx 15\%$ decrease in the net-section strength as compared to the unnotched tensile data. Figure 6 shows the effect of normalized notch length on the net-section failure strength at 23°C. The data in Fig. 6 shows that at 23°C the material is notch insensitive with respect to the notch length, for constant $W = 15$ mm.

Figures 7a-d show the fracture profiles for the specimens that were tested at temperatures 23, 1000, 1100 and 1200°C, respectively. The 23°C profile shows a significant amount of fiber pullout with the 90° fiber tows separated from the matrix material. The specimens tested at 1000°C and 1100°C showed less fiber pullout with the 90° fiber tows still attached to the matrix. The specimen tested at 1200°C had a relatively flat surface profile with minimal fiber pullout and was clearly different than the 23, 1000 and 1100°C test specimens.



(a) Fracture profile of notched sample

(b) Fracture profile of notched sample



Finite Element Analysis

During this study the finite element (FE) code ABAQUS [17] was used to predict the stress strain behavior around the notch in the DEH(T) geometry. For linear-elastic analysis Young's modulus for the two principal directions (E_1 , E_2), the shear modulus (G_{12}) and Poisson's ratio (ν_{12}) are required for modeling the orthotropic material behavior. Figure 8 shows the nonlinear shear stress versus shear strain data for the NextelTM720/AS material. Clearly, a linear elastic analysis approach would not accurately predict deformation around the notch with the nonlinear shear behavior shown in Fig 8. Tabulated axial stress-axial strain data, from Fig. 3, and tabulated shear stress-shear strain data, from Fig. 8, were input into the FE code and executed using an orthotropic nonlinear solution. This approach is similar to the work done by Kramb and John [18] and Heathcote et al. [9].

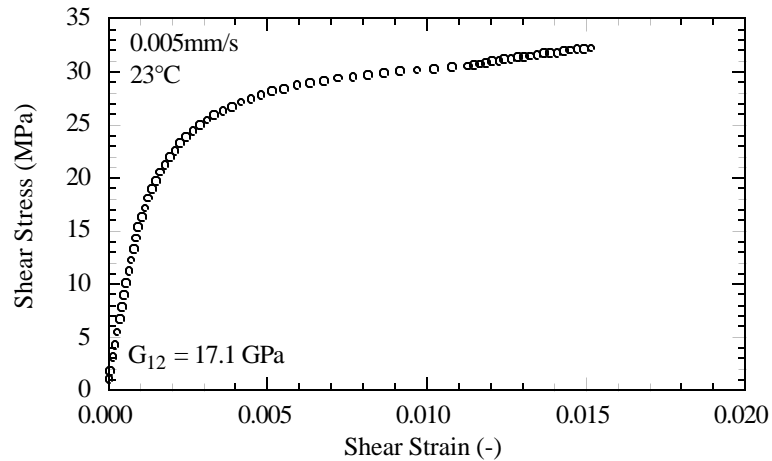


Figure 8. Shear Stress-Shear Strain behavior of NextelTM720/AS at Room Temperature.

Small strain gages, 0.8 mm x 0.8 mm in size, were placed within 1 mm of the notch edge at the 90° and 135° orientations, with respect to the horizontal axis, as shown in Fig. 9. Finite element predictions of stress-strain behavior at the notch tip in the DEH(T) geometry are shown in Fig. 9. The finite element predictions show good agreement with the measured strain gage data. The FE predictions captured the

near linear behavior of the 90° gage at the notch tip and the nonlinear behavior of the off-axis (135°) at the notch tip.

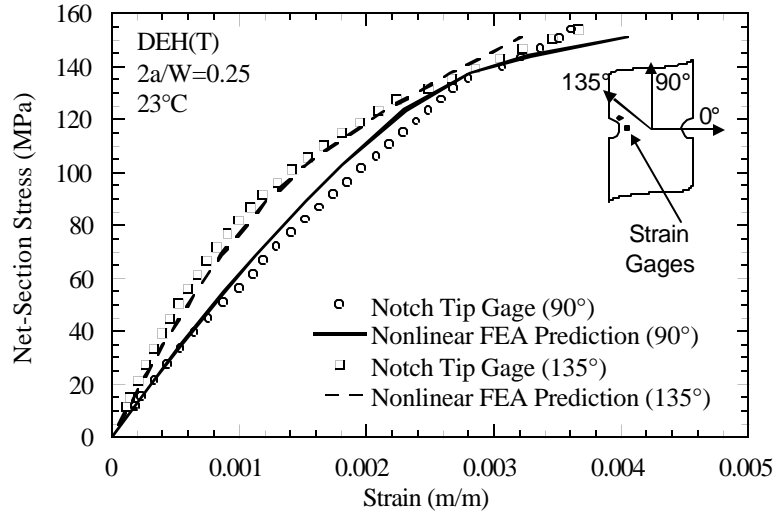


Figure 9. Finite element predictions of the stress strain behavior at the notch of the DEH(T) geometry under monotonic loading.

Summary

The fracture behavior of notched oxide/oxide CMC NextelTM720/AS was investigated at 23-1200°C. Specimens with semi-circular (DEH(T)) and saw-cut (DE(T)) double-edge notches were tested under monotonic loading in laboratory air at 23 to 1200°C. Only at temperatures $\geq 1100^{\circ}\text{C}$ did the NextelTM720/AS CMC show any observable notch sensitivity. Finite element predictions of stress strain behavior at the notch tip in the DEH(T) geometry showed good agreement with the measured strain gage data.

Acknowledgments

This research was conducted at the Materials and Manufacturing Directorate, Air Force Research Laboratory (AFRL/MLLN), Wright-Patterson Air Force Base, OH 45433-7817. Dennis Buchanan was supported under an onsite contract number F33615-98-C-5214. The authors gratefully acknowledge the assistance of Ms. Debbie Garner in conducting the experiments.

References

- [1] Zawada, L. P. and Lee, S. S., "Mechanical Behavior of CMCs For Flaps and Seals," *Proceedings of Advanced Research Projects Agency (ARPA) Advanced Ceramics Technology Insertion Program (ACTIP) Annual Review*, W.S. Coblenz, Ed., Washington, DC, August 1995.
- [2] Zawada, L. P. and Lee, S. S., "Evaluation of Four CMCs For Aerospace Turbine Engine Divergent Flaps and Seals," *Ceramic Engineering and Science Proceedings*, Vol. 16, No. 4, 1995, pp. 337-339.
- [3] Lundberg, R. and Eckerbom, L., "Design and Processing of All-Oxide Composites," *Ceramic Transactions*, Vol. 58, 1995, pp. 95-104.

- [4] Mouchon, E. and Colombar, Ph., "Oxide Ceramic Matrix/Oxide Fiber Woven Fabric Composites Exhibiting Dissipative Fracture Behavior," *Composites*, Vol. 26, 1995, pp. 175-182.
- [5] Lange, F. F., Tu, W. C, and Evans, A. G., "Processing of Damage-Tolerant, Oxidation- Resistant Ceramic Matrix Composites by a Precursor Infiltration and Pyrolysis Method," *Materials Science and Engineering*, Vol. A195, 1995, pp. 145-150.
- [6] Lee, S. S., Zawada, L. P., Hay, R. S. and Staehler, J., "High Temperature Mechanical Behavior and Characterization of an Oxide/Oxide Composite," *Journal of the American Ceramic Society*, Submitted for publication, October 1998.
- [7] Zawada, L. P., "Longitudinal and Transverse Tensile Behavior of Several Oxide/Oxide Composites," *Ceramic Engineering and Science Proceedings*, Vol. 19, No. 3, 1998, pp. 327-340.
- [8] Levi, C. G., Yang, J. Y., Dalglish, B. J., Zok, F. W. and Evans, A. G., "Processing and Performance of an All-Oxide Ceramic Composite," *Journal of the American Ceramic Society*, Vol 81, No. 8, 1998, pp. 2077-2086.
- [9] Heathcote, J. A, Gong, X. -Y, Yang, J., Ramamurty, U., and Zok, F. W., "In-Plane Mechanical Properties of an All-Oxide Ceramic Composite," *Journal of the American Ceramic Society*, Submitted for publication, 1998.
- [10] Wilson, D. M., Lieder, S. L., and Lueneburg, D.C., "Microstructure and High Temperature Properties of Nextel 720 Fibers," *Ceramic Engineering Science Proceedings*, Vol. 16, No. 5, 1995, pp. 1005-1014.
- [11] Yun, H. M. and DiCarlo, J. A., "Time/Temperature Dependent Tensile Strength of SiC and Al₂O₃-Based Fibers," *NASA Technical Memorandum 107370*, NASA Glenn Research Center, Cleveland, OH, USA, 1996.
- [12] Kramb, V. A., John, R., and Zawada, L. P., "Notched Fracture Behavior of an Oxide/Oxide Ceramic Matrix Composite," *Journal of the American Ceramic Society*, Vol. 82, No. 11, 1999, pp. 3087-3096.
- [13] John, R., Buchanan, D. J. and Zawada, L. P., "Notch-Sensitivity of a Woven Oxide/Oxide Ceramic Matrix Composite," *Environmental, Mechanical, and Thermal Properties and Performance of Continuous Fiber Ceramic Composite (CFCC) Materials and Components*, ASTM STP 1392, Michael G. Jenkins, Ed., American Society for Testing and Materials, West Conshohocken, PA, Submitted for publication, July 1999.
- [14] 3M Company Product Data Sheet, 3M Ceramic Fiber Products, 3M Center-Building 207-1W-11, St. Paul, MN 55144-1000.
- [15] Hartman, G. A. and Buchanan, D. J., "Methodologies for Thermal and Mechanical Testing of TMC Materials," *Characterisation of Fibre Reinforced Titanium Matrix Composites*, 77th Meeting of the AGARD Structures and Materials Panel, AGARD Report 796, Bordeaux, France, 27-28 September 1993.
- [16] Hartman, G. A. and Russ, S.M., "Techniques for Mechanical and Thermal Testing of Ti3Al/SCS-6 Metal Matrix Composites," *Metal Matrix Composites: Testing, Analysis, and Failure Modes*, ASTM STP 1032, W. S. Johnson, Ed., American Society for Testing and Materials, West Conshohocken, PA, 1989, pp. 43-53.
- [17] ABAQUS Version 5.8, Hibbit, Karlsson & Sorensen, Inc., 1080 Main Street, Pawtucket, RI 02860-4847, 1998.
- [18] Kramb, V. A. and John, R., "Off-Axis Response of NextelTM610/AS," *to be submitted for publication*, Jan. 2000.

This page intentionally left blank.

CREEP DEFORMATION AND RUPTURE BEHAVIOR OF A NOTCHED OXIDE/OXIDE NEXTEL™720/AS COMPOSITE

Reji John, Dennis J. Buchanan* and Larry P. Zawada

Materials and Manufacturing Directorate, Air Force Research Laboratory (AFRL/MLLN), Wright-Patterson Air Force Base, OH 45433-7817

* University of Dayton Research Institute, Dayton, OH 45419

ABSTRACT

Oxide/oxide ceramic matrix composites such as Nextel™720/Alumina-Silica(AS) are currently being demonstrated in high-temperature aerospace applications ($\geq 1000^{\circ}\text{C}$). Many of these components containing holes and notches will be subjected to long-term exposures. Hence, the knowledge of the effect of sustained (creep) loading on the deformation and rupture of notched Nextel720/AS was investigated. Unnotched and double-edge notched specimens were tested under tensile and sustained loading at 1100°C . Nextel™720/AS is slightly notch-sensitive ($\approx 15\%$) under tensile loading and significantly notch-sensitive ($\approx 40\%$) under sustained loading for 100+ hours.

INTRODUCTION

Ceramic matrix composites (CMC) consisting of an oxide matrix and oxide fibers with no engineered fiber-matrix interphase are currently being demonstrated for high temperature aerospace applications due to their inherent resistance to oxidation. Many investigations [1-11] have shown that Oxide/Oxide CMCs exhibit excellent tensile and fatigue properties at room and elevated temperatures. For example, tensile and fatigue strength of Nextel610/Alumina-Silica (Nextel610/AS) decreased only 15-20% when tested at elevated temperatures of $\approx 1000^{\circ}\text{C}$ in laboratory air [1-3,7,8]. Nextel610 fibers and Nextel610/AS are susceptible to excessive creep deformation at temperatures $\geq 1000^{\circ}\text{C}$ [7,8,12,13]. In contrast, Nextel720 fibers exhibit significant creep resistance up to 1200°C [12,13]. Hence, Oxide/Oxide CMC with Nextel720 fibers are under consideration by the US Air Force for some applications with temperature requirements in the range of $1000\text{-}1200^{\circ}\text{C}$. Current targeted aerospace turbine engine components such as combustors, combustor liners, and divergent flaps and seals contain bolted attachment points and cooling holes. Hence, component design using oxide/oxide CMCs will therefore require knowledge of the notched fracture behavior and damage progression under service loading conditions.

Recently, the notched fracture behavior of Oxide/Oxide CMC systems with Nextel610 and Nextel720 fibers has been studied [10,11,14]. Levi et al. [10] and Heathcote et al. [11] reported room temperature fracture results of Nextel610/AS and Nextel720/AS, while Kramb et al. [14] reported the fracture behavior of Nextel610/AS at room temperature and 950°C . John et al. [15] reported the fracture behavior of Nextel720/AS at temperatures $23\text{-}1200^{\circ}\text{C}$ under tensile loading and at 1100°C under sustained (creep) loading. This paper expands on the creep results reported in Ref. [15] to include additional results from specimens with semicircular and sharp notches.

MATERIAL

The Nextel720/AS CMC used in this investigation was produced by Engineered Ceramics, Inc, San Diego, California, USA. The Nextel720 fibers [16], consisted of fine grained ($<0.5 \mu\text{m}$) polycrystalline alpha alumina plus mullite. The composition of the fibers included 85% Al_2O_3 and 15%

SiO_2 with an average fiber diameter $\approx 10\text{-}12 \mu\text{m}$. The fiber architecture was a balanced eight harness satin weave (8HSW). The 12-ply composite plate had a fiber volume fraction, $V_f \approx 0.4$. Image analysis (Fig 1) revealed extensive microcracking throughout the matrix as a result of the shrinkage, which occurred during the pyrolysis processing. These microcracks were distributed throughout the composite with spacing $\approx 50\text{-}200 \mu\text{m}$ prior to machining and testing [15]. Additional details of the material can be found in Ref. [15].

EXPERIMENTAL PROCEDURE

The double-edge, notched-specimen geometry shown in Fig. 2, was used for all the notched fracture and creep tests. The specimen ends were rigidly clamped resulting in rotationally constrained end conditions. The overall dimensions of the specimens were: width (W) = 15.0 mm, thickness (B) $\approx 2.5 \text{ mm}$ and height (between clamped ends) $\approx 100 \text{ mm}$. The semicircular and narrow notches were made using a diamond coated grinding bit and diamond saws, respectively.

Figure 1. Microstructure of (0/90) woven Nextel720/AS.

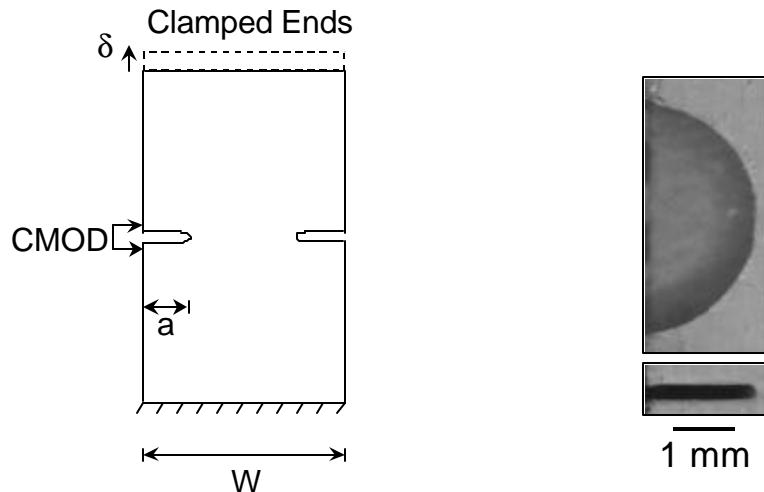
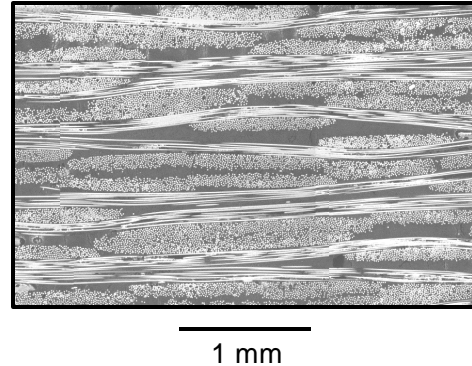


Figure 2. Schematic of the double edge notched geometry.

Figure 3. Photographs of notch geometries.

Typical notch geometries are shown in Fig. 3. The narrowest notch had notch root radius of 0.11 mm. All the data were generated using specimens with notch length to width ratio, $2a/W \approx 0.25$. During the creep tests, crack mouth opening displacement (CMOD) was measured using a high temperature extensometer with alumina rods. The fracture tests were conducted under load-line displacement control

at a rate ($\dot{\delta}$) of 0.005 mm/s. This loading rate corresponded to time to peak load of \approx 35 - 40 s. The loading portion during the creep tests was achieved under load control using a rate of 20 MPa/s. Unnotched creep rupture tests were conducted using dogbone specimens. All the tests were conducted in laboratory air using an automated, servo-hydraulic controlled, horizontal test system [15]. Details regarding the elevated temperature testing procedure can be found in Ref [15].

RESULTS AND DISCUSSION

The unnotched tensile [9] and creep behaviors of Nextel720/AS are shown in Figures 4 and 5, respectively.

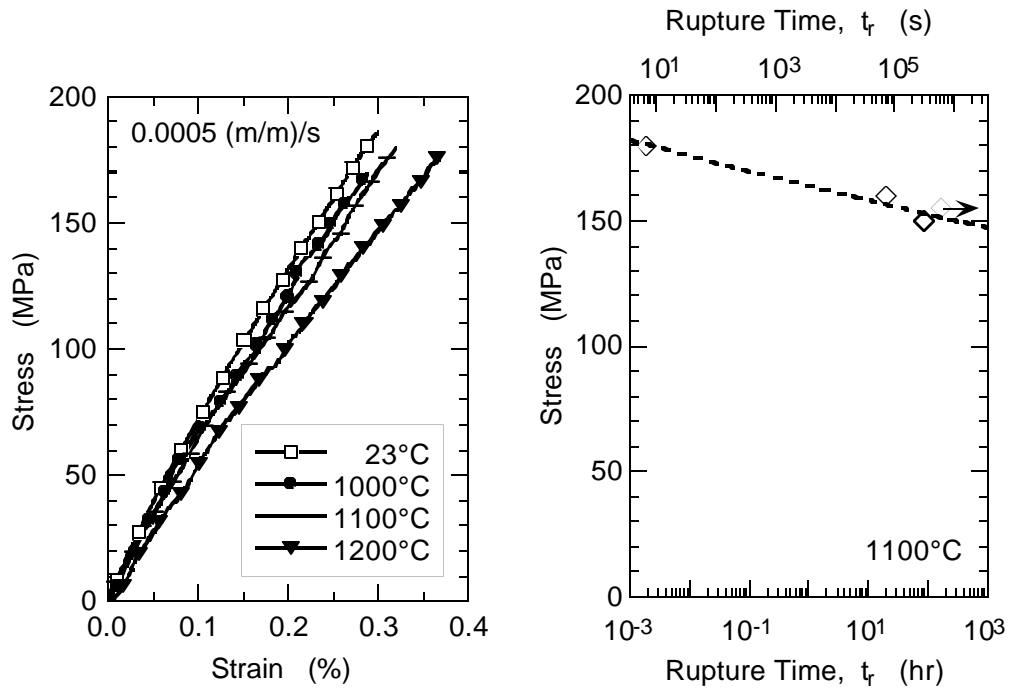


Figure 4. Tensile behavior of unnotched Nextel720/AS.

Figure 5. Creep behavior of unnotched Nextel720/AS.

Young's modulus (E) and the ultimate tensile strength (UTS) are relatively stable from 23 to 1200°C. UTS ranged from 170 to 186 MPa while E ranged from 75 GPa at 23°C to 57 GPa at 1200°C. At 1100°C, under sustained (creep) loading, the applied stress versus rupture time shows the familiar negative slope however the decrease of net-section stress is gradual. Based on the data in Fig. 5, we conclude that the unnotched creep strength of Nextel720/AS is \approx 145 MPa (\approx 80% of UTS) after 100+ hr loading at 1100°C. The high creep strength after 100 hrs of exposure at 1100°C highlights the thermal stability of the unnotched oxide/oxide composite.

Figure 6 shows the creep response of unnotched and notched Nextel720/AS. The stress levels for the notched specimens, i.e. DE(T) and DEH(T), correspond to the equivalent uniform net-section stress. Normalized CMOD (=CMOD/Gage Length) was used to compare the creep deformation of the notched specimens with that from an unnotched specimen. Typical gage length for CMOD measurements was \approx 9.68 mm.

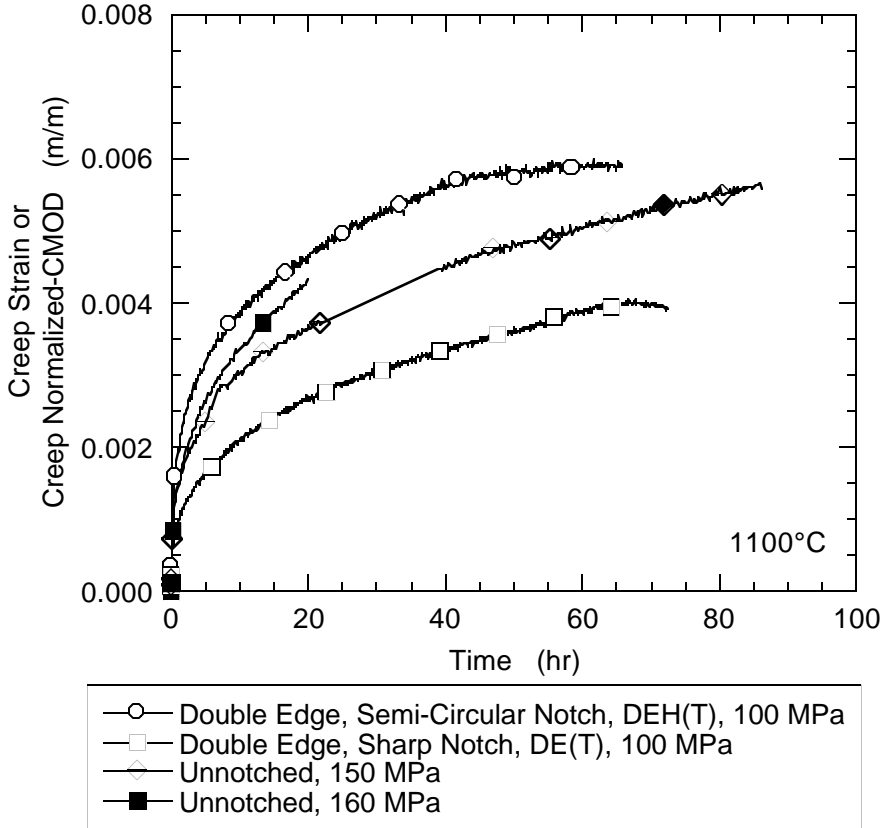


Figure 6. Creep response of unnotched and notched Nextel720/AS (1100°C).

Interestingly, the normalized CMOD is in the same range as the strain measurements from unnotched specimens, although the stress levels are significantly different. For example, the response of notched specimen with net-section stress of 100 MPa is similar to that of an unnotched specimen with stress of 150-160 MPa. This difference in stress levels implies increased notch-sensitivity under creep loading conditions. In contrast, fracture tests of Nextel720/AS by Buchanan et al. [16] exhibited only slight notch-sensitivity at 1100°C. Hence additional notched creep tests were conducted and compared with the unnotched creep rupture behavior as shown in Fig. 7.

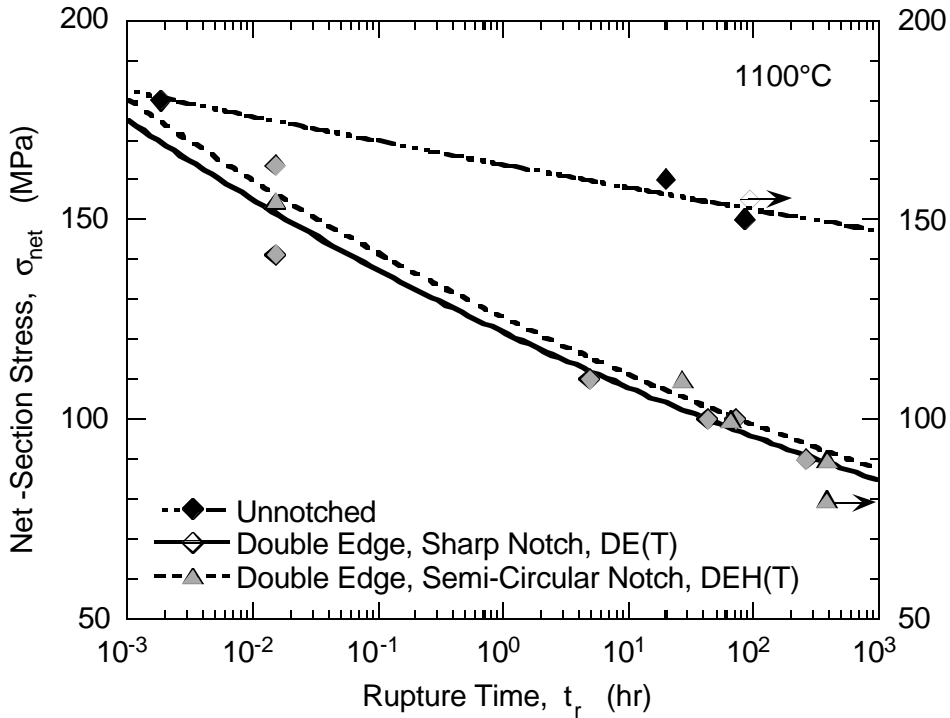


Figure 7. Notch effects on creep rupture behavior of Nextel720/AS (1100°C).

The unnotched tensile data are also shown in Fig. 7 corresponding to rupture time, $t_r \approx 6.7$ s. As discussed earlier, Nextel720/AS exhibited a slight notch-sensitivity under tensile loading at 1100°C, i.e. the notched strength is $\approx 15\%$ lower than the unnotched strength corresponding to $t_r = 55$ s [16]. At stress levels lower than the notched tensile strength, Nextel720/AS exhibited substantial deformation leading to failure under sustained (creep) loading. Figure 7 shows that for the same net-section stress, the rupture times for the notched specimens were significantly lower than that for the unnotched specimens. Hence, the notch-sensitivity of Nextel720/AS at 1100°C increases significantly with increase in exposure time. In addition, the creep-rupture behavior of the semi-circular notched specimens is similar to that of sharp notched specimens. Thus, the increase in notch-sensitivity is independent of the initial stress concentration at the notch tip. Fractographic studies are in progress to understand the damage mechanisms leading to the increased notch-sensitivity under creep loading.

SUMMARY

The creep behavior of a notched oxide/oxide CMC Nextel720/AS was investigated at 1100°C. The results show that Nextel720/AS is slightly notch-sensitive ($\approx 15\%$) tensile loading. The notch-sensitivity increased significantly (to $\approx 40\%$) under sustained (creep) loading. The increase in notch-sensitivity is independent of the initial stress concentration at the notch tip. The results from this study show that design of durable CMC components with holes should account for the increased notch-sensitivity under long-term exposure conditions.

ACKNOWLEDGMENTS

This research was conducted at the Materials and Manufacturing Directorate, Air Force Research Laboratory (AFRL/MLLN), Wright-Patterson Air Force Base, OH 45433-7817. Dennis

Buchanan was supported under an onsite contract number F33615-98-C-5214. The authors gratefully acknowledge the assistance of Ms. Debbie Garner in conducting the experiments.

REFERENCES

- [1] Zawada, L.P. and Lee, S.S., "Mechanical Behavior of CMCs For Flaps and Seals," *Proceedings of Advanced Research Projects Agency (ARPA) Advanced Ceramics Technology Insertion Program (ACTIP) Annual Review*, W.S. Coblenz, Ed., Washington, DC, August 1994.
- [2] Zawada, L.P. and Lee, S.S., "Mechanical Behavior of CMCs For Flaps and Seals," *Proceedings of Advanced Research Projects Agency (ARPA) Advanced Ceramics Technology Insertion Program (ACTIP) Annual Review*, W.S. Coblenz, Ed., Washington, DC, August 1995.
- [3] Zawada, L.P. and Lee, S.S., "Evaluation of Four CMCs For Aerospace Turbine Engine Divergent Flaps and Seals," *Ceramic Engineering and Science Proceedings*, Vol. 16, No. 4, 1995, pp. 337-339.
- [4] Lundberg, R. and Eckerbom, L., "Design and Processing of All-Oxide Composites," *Ceramic Transactions*, Vol. 58, 1995, pp. 95-104.
- [5] Mouchon, E. and Colombar, Ph., "Oxide Ceramic Matrix/Oxide Fiber Woven Fabric Composites Exhibiting Dissipative Fracture Behavior," *Composites*, Vol. 26, 1995, pp. 175-182.
- [6] Lange, F.F, Tu, W.C, and Evans, A.G., "Processing of Damage-Tolerant, Oxidation- Resistant Ceramic Matrix Composites by a Precursor Infiltration and Pyrolysis Method," *Materials Science and Engineering*, Vol. A195, 1995, pp. 145-150.
- [7] L. P., Zawada and S.S. Lee, "The Effect of Hold Times on the Fatigue Behavior of an Oxide/Oxide Ceramic Matrix Composite," *Thermal and Mechanical Test Methods and Behavior of Continuous-Fiber Ceramic Matrix Composites, ASTM STP 1309*, Michael G. Jenkins, Stephen T. Gonczy, Edgar Lara-Curcio, Noel E. Ashbaugh, and Larry P. Zawada, Eds., American Society for Testing and Materials, Philadelphia, PA, 1996.
- [8] Lee, S. S., Zawada, L. P., Hay, R. S. and Staehler, J., "High Temperature Mechanical Behavior and Characterization of an Oxide/Oxide Composite," *Journal of the American Ceramic Society*, Submitted for publication, October 1998.
- [9] Zawada, L.P., "Longitudinal and Transverse Tensile Behavior of Several Oxide/Oxide Composites," *Ceramic Engineering and Science Proceedings*, Vol. 19, No. 3, 1998, pp. 327-340.
- [10] Levi, C.G., Yang, J.Y., Dalgleish, B.J., Zok, F. W. and Evans, A.G., "Processing and Performance of an All-Oxide Ceramic Composite," *Journal of the American Ceramic Society*, Vol 81, No. 8, 1998, pp. 2077-2086.
- [11] Heathcote, J.A, Gong, X.-Y, Yang, J., Ramamurty, U., and Zok, F.W., "In-Plane Mechanical Properties of an All-Oxide Ceramic Composite," *Journal of the American Ceramic Society*, Submitted for publication, 1998.
- [12] Wilson, D.M., Lieder, S.L., and Lueneburg, D.C., "Microstructure and High Temperature Properties of Nextel 720 Fibers," *Ceramic Engineering Science Proceedings*, Vol. 16, No. 5, 1995, pp. 1005-1014.
- [13] Yun, H.M. and DiCarlo, J.A., "Time/Temperature Dependent Tensile Strength of SiC and Al₂O₃-Based Fibers," *NASA Technical Memorandum 107370*, NASA Glenn Research Center, Cleveland, OH, USA, 1996.
- [14] Kramb, V.A., John, R., and Zawada, L.P., "Notched Fracture Behavior of an Oxide/Oxide Ceramic Matrix Composite," *Journal of the American Ceramic Society*, Vol. 82, No. 11, 1999, pp. 3087-3096.
- [15] John, R., Buchanan, D. J., and Zawada, L.P., "Notch-Sensitivity of a Woven Oxide/Oxide Ceramic Matrix Composite," *Environmental, Mechanical, and Thermal Properties and Performance of Continuous Fiber Ceramic Composite (CFCC) Materials and Components, ASTM STP 1392*, Michael G. Jenkins, Ed., American Society for Testing and Materials, West Conshohocken, PA, Submitted for publication, July 1999.
- [16] Buchanan, D.J., John, R., and Zawada, L.P., "Notched Fracture Behavior of Oxide/Oxide Nextel720/AS Composite," *This publication*.

Notched Fracture Behavior of an Oxide/Oxide Ceramic Matrix Composite

Victoria A. Kramb¹, Reji John and Larry P. Zawada

Materials and Manufacturing Directorate (AFRL/MLLN)
Air Force Research Laboratory
Wright-Patterson Air Force Base
OH 45433-7817
USA

¹ University of Dayton Research Institute, Dayton, OH 45469-0128, USA.

Abstract

The fracture behavior of an oxide/oxide ceramic matrix composite, alumina/alumina-silica (Nextel610/AS), was investigated at 23 and 950°C using a single edge notched specimen geometry with clamped ends. Crack growth and damage progression was monitored during the tests using optical microscopy, ultrasonic C-scans, and crack mouth opening displacement. Nextel610/AS was found to be notch sensitive, with net section failure stresses below the unnotched ultimate tensile strength. The failure mode was nonbrittle with considerable nonlinear deformation prior to and after the peak load at 23 and 950°C. The effect of temperature on the notched strength was significant. Net section failure stress decreased 50% when temperature was increased from 23 to 950°C. Observations of damage progression indicated that the reduction in notch strength with temperature was associated with self similar crack growth at 950°C. Ultrasonic C-scans were found to be an effective method of monitoring damage progression. Ultrasonic attenuation ahead of the notch tip was correlated with surface matrix cracks and exposed fiber lengths on the fracture surface.

I Introduction

Ceramic matrix composites (CMC) consisting of an oxide matrix and oxide fibers with no engineered fiber-matrix interphase are currently under consideration for high temperature aerospace applications due to their inherent resistance to oxidation. The CMC produced by General Electric Aircraft Engines (GEAE) consisting of alumina fibers and an 87% alumina-13% silica matrix (Nextel610/AS) exhibits excellent room temperature fatigue and tensile strength (170 MPa and 205 MPa respectively) [1, 2]. When tested at 1000°C, fatigue and tensile strength decreased by only 15% [1, 2]. Current component designs, however, include stress concentration sites such as bolted attachment points and cooling holes. Local stresses in these regions often exceed the proportional limit of the composite, thus acting as crack and damage initiation sites. Component design using Nextel610/AS composites will therefore require knowledge of the notched fracture behavior and damage progression at room temperature and expected service temperatures.

Fracture studies of other CMC systems [3-9] have shown that damage mechanisms such as multiple matrix cracking, fiber bridging and fiber pullout act to redistribute stresses in the vicinity of a notch. John et al. [3], Cady et al. [4] and Mall et al. [5] showed that NicalonTM fiber reinforced glass matrix composites exhibit multiple matrix cracking around notches and holes resulting in notch insensitive behavior at room temperature. Fiber dominated CMC, including some C/C composites, show a nearly linear unnotched stress-strain response in the [0/90] orientation. However, increasing nonlinearity with increasing notch length was observed for edge notched specimens [8, 9]. For these composite systems, damage ahead of the notch was found to extend as a narrow zone normal to the notch plane. The damage zone effectively redistributed the stresses away from the notch tip, thus increasing fracture toughness at room temperature. Similar to other fiber dominated systems, the oxide/oxide CMC Nextel610/AS exhibits nearly linear unnotched stress-strain behavior [1, 2]. However, the notched behavior of Nextel610/AS has not been examined.

For CMC to be used effectively in aerospace applications with sites of stress concentration, the decrease in fracture toughness at elevated temperatures must be minimized. For most of the CMC systems studied thus far, the enhanced fracture toughness relies on the existence of a weak fiber/matrix interphase which allows fiber debonding and sliding during fracture. At elevated temperature, oxidation of the fiber/matrix interphase resulted in embrittlement of these composites as the matrix became tightly bonded to the fiber [3, 6]. Consequently, the fracture toughness at elevated temperature was significantly lower than that at room temperature [3, 7]. Oxidation occurring at the fiber/matrix interface and degradation of the fiber itself must therefore be prevented to maintain fracture toughness in these CMC systems. A different approach to enhanced CMC fracture toughness utilizes a very weak, porous matrix bonded to the fiber with no engineered interphase. Oxide based CMC are inherently oxidation resistant at elevated temperature and are expected to show damage tolerance when produced using a strong interface and weak matrix [1, 2, 10]. The limited experimental data available in the open literature on the notched fracture behavior of an oxide/oxide CMC is restricted to room temperature [11]. This paper discusses the results of a study of the notched fracture behavior and damage progression of an oxide/oxide composite (Nextel610/AS) at room temperature and 950°C.

II. Material

The Nextel610/AS CMC used in this investigation was produced by GEAE under the trade name Gen IV. The Nextel610 fibers, produced by the 3M Company [10], consist of fine grained (<0.5 μm) polycrystalline alpha alumina. These fibers were woven into an eight harness satin weave (8HSW) cloth. The resulting cloth consists of fibers primarily in the warp direction on one side of the ply and fill fibers on the other. The plies were warp aligned during lay-up, but alternating plies were rotated about the warp direction so that fill fibers were matched with fill fibers, warp fibers matched with warp fibers. This lay-up provides better nesting of the plies and minimizes panel warpage. The resulting panel contained primarily fill fibers on the exposed outer plies. The composite panel used in this study contained 12 plies. Sections of the Nextel610 cloth were prepped with alumina powder and a silica forming polymer before stacking. No coating was applied to the fibers before prepelling. The laminate was then warm molded to produce the green state ceramic tile. Sintering the green tile in air at 1000°C removed the organic binders and produced a porous alumina-silica matrix. The resulting composite contains sintered matrix which is bonded to the fibers with no naturally occurring or engineered interphase. The matrix contains approximately 87 wt.% alumina and 13 wt.% silica. Image analysis of polished cross sections (Fig. 1) showed that the fiber volume fraction was 33%. Extensive microcracking present throughout the matrix is a result of the shrinkage which occurs during the pyrolysis processing. These microcracks are distributed throughout the interior matrix as well as on the specimen surface.

III. Experimental Procedure

(1) Test Procedure

Unnotched tension tests were conducted using an automated, servo-controlled, hydraulic, horizontal test system [13, 14]. The tests were conducted under load-line displacement control at a rate ($\dot{\delta}$) of 0.05 mm/s. Specimen

endpoint displacement was increased monotonically to specimen failure. Tension tests were conducted at 23 and 1000°C. Further discussion of the unnotched tension test procedures and results are described elsewhere [2].

Fracture tests were conducted using an automated, servo-controlled, hydraulic, horizontal test system [13, 14]. The single edge notched specimen geometry with clamped ends, MSE(T) [15] shown in Fig. 2, was used for all the tests. The specimen ends were rigidly clamped resulting in rotationally constrained end conditions. The overall dimensions of the specimens were: width (W) = 19.0 mm or 25.4 mm, thickness (B) = 2.9 mm and height to width ratio (H/W) = 4.0. The notches were cut using a diamond saw to produce an initial notch height of 0.4 mm, and length (a_0) equal to 0.2 W for all specimens. Crack mouth opening displacement (CMOD) was measured continuously using a high resolution knife edge extensometer at room temperature and a high temperature extensometer with alumina rods at 950°C. Optical measurements of matrix crack extension were made on both sides of the specimen during testing.

(2) *Elevated Temperature Testing*

Heating of the test specimen was achieved with closed-loop controlled, 4 zone quartz lamps. The heated section of the specimen was approximately 3 inches in length centered on the specimen notch. Slotted windows in the center of the quartz lamps allowed for visual inspection of crack growth from the notch tip during testing. Further details of the test equipment have been described elsewhere [13, 14].

Various methods of thermocouple attachment were investigated. The method which produced the most repeatable temperature measurements with minimal damage to the specimen surface was chosen for use in testing. Platinum-10%Rhodium, S-type, beaded thermocouples were first wire tied to the specimen with the thermocouple bead in contact with the specimen surface. A small drop of Ceramabond™ (Ceramabond 503, Aremco Products, Inc., 23 Snowden Ave., Ossining, NY 10562) ceramic adhesive was then placed over the thermocouple bead and spread to cover the bead surface. The adhesive was cured for 30 minutes at 300°C resulting in a hard, adhesive, insulating cover for the thermocouple bead while assuring contact with the specimen surface during testing. The adhesive was white in color, matching the color of the Nextel610/AS specimen, which eliminated temperature errors due to differential radiant heat absorption. The Ceramabond™ was also easily removed from the specimen surface after testing.

A thermal map of the temperature distribution across the specimen length, width and thickness was obtained using a notched Nextel610/AS specimen with W = 25.4 mm and a_0 = 0.2 W . The temperature variation was $\leq \pm 2.9\%$ across the gage length, and $\leq \pm 1.0\%$ through the thickness. During testing, 6 thermocouples were attached to the top and 1 to the bottom surfaces. Four thermocouples controlled the quartz lamp output and 3 monitored temperature near the notch plane.

(3) *Fracture Test Parameters*

Fracture tests were conducted under load-line displacement control at a rate of 0.001 mm/s and 0.01 mm/s. During the tests conducted at 0.001 mm/s, load-line displacement was periodically held constant for crack length measurements. During this hold time, the specimen was also unloaded and reloaded to determine residual CMOD and changes in specimen compliance. The fracture test conducted at 0.01 mm/sec was loaded monotonically (without unloading loops or hold times) to specimen failure. Applied load, CMOD and load-line displacement (δ) were recorded continuously as a function of time during all tests. Whenever possible, specimens were unloaded and removed from the test machine after attaining the peak load for ultrasonic and optical evaluation. Mode I stress intensity factor (K_I), and elastic modulus (E), from specimen compliance (= CMOD/P), were calculated using isotropic expressions [15] given by Eqn. (1). Assuming crack length (a) equal to the saw-cut notch length, elastic modulus was calculated from the initial loading compliance below a far-field applied stress (σ_a) = 15 MPa. Applied stress was calculated as $\sigma_a = P/(BW)$ where P = applied load, and B and W are shown in Fig.2.

$$K_I = \sigma_a \sqrt{\pi a} F(a/W) \quad \text{and} \quad E = \frac{2\sigma_a a}{CMOD} G(a/W), \quad (1)$$

where $F(a/W)$ and $G(a/W)$ are given in [15].

(4) Damage Characterization

Ultrasonic C-scans of the test specimens were recorded before testing and during interrupted tests. The C-scans were obtained using a through transmission, reflector plate scanning technique described elsewhere [16, 17]. Each ultrasonic C-scan was calibrated, and referenced to a calibrated ultrasonic attenuation scale. During the C-scan, the ultrasonic signal passing through the specimen was acquired at regularly spaced x-y locations, digitized, and color coded. A 12.7 mm diameter, 10 MHz, 76 mm focused transducer produced by KB Aerotech was used to emit and receive the ultrasonic energy. The C-scan technique required immersion of the test specimen in water during the scan. After each C-scan, excess moisture was removed during a 1 hour bake out at 70°C. Zawada and Lee [2, 18] showed that water exposure did not result in a change in the mechanical behavior of Nextel610/AS.

Optical inspection of the notch tip region was performed on both sides of the specimen during testing. Due to the extensive preexisting matrix cracking on the specimen surface, the notch tip region appeared cracked before testing. Crack growth from the notch tip was identified as a clearly observable opening of a pre-existing surface crack (identified as the dominant crack), or the appearance of a new crack at the notch tip. Post test inspection of the crack growth and fracture surfaces was performed using optical and scanning electron microscopy (SEM). Specimens were sputter coated with gold/palladium before SEM imaging. Backscatter electron imaging was used to minimize charging effects and highlight microcracks. Destructive evaluation of interrupted test specimens was performed by sectioning and polishing using a diamond impregnated lapping film. Polishing the specimens with light pressure removed surface layers slowly enough to prevent damage to fibers within the underlying layers.

IV. Results and Discussion

(1) Notched Fracture Behavior

The experimental results of the notched fracture tests are shown in Figs. 3-5 and summarized in Table I. Each experimental condition listed in the table represents a single test result. For each fracture test, a low load (< 1.0 kN) check out cycle was used to determine the initial loading compliance. Elastic modulus calculated using Eqn. (1) and the initial loading compliance ranged from 69-71 GPa for all fracture tests (Table I). No dependence of elastic modulus on temperature was observed.

The load-CMOD response for room temperature fracture tests conducted on 19.0 mm and 25.4 mm wide specimens is shown in Fig. 3. Unloading the specimen from applied loads within the initial linear region resulted in no residual CMOD or loop hysteresis. Beyond the linear region, loading behavior was increasingly nonlinear and associated with increasing residual CMOD ($CMOD_{res}$) and measurable hysteresis in the unloading loops.

The onset of nonlinear loading behavior was determined by fitting a linear curve to the initial load/displacement data. Measured load deviation from the linear fit exceeding 5% was defined as the onset of nonlinear loading behavior. Fracture tests conducted at room temperature exhibited linear loading behavior up to an applied stress intensity factor (K_a) = 6 MPa \sqrt{m} , corresponding to an applied load, P = 2.8 kN for the 25.4 mm wide specimen. Unloading the specimen from K_a levels above 6 MPa \sqrt{m} resulted in measurable $CMOD_{res}$ and hysteresis in the load-CMOD loops. Residual CMOD and unloading loop hysteresis increased with applied load up to the peak load. After reaching the peak load, CMOD continued to increase under increasing load-line displacement, while the applied load remained nearly constant (Fig. 3).

The stress intensity factor (K_{peak}) based on the peak load and initial notch length was calculated to be 16.8 MPa \sqrt{m} and 15.5 MPa \sqrt{m} for the 19.0 mm and 25.4 mm wide specimens, respectively. The 19.0 mm wide specimen failed abruptly after reaching a $CMOD = 0.10$ mm. The 25.4 mm wide specimen reached the peak load when $CMOD =$

0.08 mm and was removed from the test frame when $\text{CMOD} = 0.10$ mm for ultrasonic and optical evaluations. Although the current data is limited, the fracture results indicate that within the range of specimen widths examined, the effect of width on K_{peak} at room temperature is minimal.

The load versus CMOD responses for fracture tests conducted at 23 and 950°C on 25.4 mm wide specimens are shown in Fig. 4. Unloading loops for the 23°C test were eliminated from Fig. 4 for clarity. Loading behavior at 950°C was linear to $K_a = 4 \text{ MPa}\sqrt{\text{m}}$ ($P = 1.7 \text{ kN}$) which is $\approx 33\%$ lower than that at 23°C. Similar to the 23°C fracture test, unloading the specimen from applied loads within the initial linear region at 950°C resulted in no CMOD_{res} or loop hysteresis. Increase in applied load beyond the linear region resulted in sudden decrease in specimen compliance.

Nonlinear loading behavior can be compared for the two fracture tests by examining the residual CMOD_{res} . Figure 5 shows the CMOD_{res} after unloading the specimen from a maximum load with corresponding maximum CMOD (CMOD_{max}). For the room temperature specimen, CMOD_{res} increased slowly as CMOD_{max} increased. Prior to the peak load, CMOD_{res} remained below 0.01 mm, corresponding to 13% of the CMOD_{max} at the peak load. This result is consistent with CMOD_{res} due primarily to distributed matrix cracking with minimal 0° fiber breakage. In contrast, the 950°C specimen showed a sudden rapid increase in CMOD_{res} prior to the peak load with values $\approx 5X$ higher than that at room temperature. The sudden rapid increase in CMOD_{res} indicates a change in damage mode, consistent with observations of dominant crack growth discussed later in section 3. The increase in CMOD_{res} and dominant crack growth at 950°C are consistent with the onset of 0° fiber breakage. However, additional interrupted tests are required to determine if 0° fiber breakage occurred prior to the peak load at 950°C.

As a result of the enhanced nonlinear deformation prior to the peak at 950°C, a decrease in peak load $\approx 50\%$, compared to that at 23°C, was observed. The decrease in peak load corresponded to a decrease in K_{peak} from 16 $\text{MPa}\sqrt{\text{m}}$ at 23°C to 7.9 $\text{MPa}\sqrt{\text{m}}$ at 950°C. The higher CMOD_{res} at 950°C, and decrease in notch strength, indicated a change in damage mechanism from 23°C.

(2) Effect of Loading Rate on 950 °C Fracture Behavior

The effect of loading rate and unloading loops on the fracture behavior at 950°C was examined by conducting an additional fast-rate monotonic fracture test. The load versus CMOD response for the slow and fast rate tests are shown in Fig. 4. The load-line displacement rate ($\dot{\delta}$) used during the fracture test with unloading loops was $\dot{\delta} = 0.001 \text{ mm / s}$, resulting in a total elapsed time to peak load (t_p) of 668 s. The test without unloading loops was conducted at a rate of $\dot{\delta} = 0.01 \text{ mm / s}$, resulting in $t_p = 15 \text{ s}$. As shown in Fig. 4, the overall load versus CMOD response was nearly the same for both tests, indicating that loading rate and unloading loops had no effect on the peak stress intensity factor or overall fracture behavior. However, a complete assessment of time at temperature effects on the notched behavior must be examined under sustained load conditions.

(3) Damage Accumulation

Ultrasonic Evaluation

Due to the extensive pre-existing matrix cracks present throughout the Nextel610/AS composite, characterization of damage accumulation based on surface matrix crack growth alone was determined to be inappropriate. A nondestructive ultrasonic C-scan technique [16, 17] was therefore adapted for use with the Nextel610/AS composite system [19]. Some of the Nextel610/AS specimens were scanned prior to testing. Due to the extensive pre-existing matrix cracks and porosity C-scans of the untested composite showed regions of varying

ultrasonic attenuation. These regions typically varied from 0-50% attenuation, with isolated regions of high porosity which attenuated the signal up to 75%. C-scans of specimens which had been loaded to sufficiently high stress, showed levels of ultrasonic attenuation near the notch tip region which exceeded 75%. Specimens which were tested and showed increased attenuation in the notch tip region showed no change in the level of ultrasonic attenuation of the undamaged regions far from the notch tip. Therefore, attenuation of the ultrasonic signal exceeding 75% was identified as that which indicated damage accumulation during testing. For clarity in this publication, the original color scale used for the C-scans, was mapped into the gray scale image shown in Fig. 8. With reference to the gray scale, white indicates that the ultrasonic signal through the specimen was attenuated less than 75%, gray shades indicate attenuation of 75-100%. Further discussion of the ultrasonic test technique and detailed color C-scan images can be found in Ref. [19].

The room temperature fracture tests were conducted with periodic unloading, but without interruption until clearly beyond the peak load. Optical inspection of the notch tip region during testing did not reveal the formation of either new matrix cracks or a dominant matrix crack. The lack of dominant matrix crack extension prior to the peak load correlated with the small CMOD_{res} after unloading (Fig. 5). Although CMOD_{res} increased more rapidly after the peak load, clear dominant surface crack growth was not observed. However, nonlinear loading behavior prior to and after the peak load indicated that a progressive damage mechanism was operative. Therefore, subsurface damage was examined using ultrasonic C-scans. The ultrasonic C-scan of the specimen after the peak load showed a region of enhanced ultrasonic attenuation approximately 10 mm in length and 10 mm in height (Fig. 6a). The extent of ultrasonic attenuation indicated that the damage progression from the notch tip at room temperature was distributed away from the notch plane, consistent with the absence of primary crack growth from the notch.

During the 950°C fracture test with periodic unloading, optical inspection of the notch tip region first identified the formation of a dominant matrix crack at an applied load of 3.0 kN. Unloading the specimen from this applied load resulted in the significant CMOD_{res} (Fig. 5). Increasing load-line displacement resulted in extension of the dominant crack as it grew and linked with other preexisting surface matrix cracks. When the test was stopped, the continuous matrix crack extension from the notch tip was equal to 9 mm (Fig. 6c). Fig. 6b shows the corresponding ultrasonic C-scan at the same point of unloading. The region of ultrasonic attenuation was 5 mm in height and extended 11 mm beyond the notch, slightly longer than the surface matrix crack extension. The dominant crack extension at 950°C was associated with a more narrow damage zone compared to that observed at room temperature.

Fracture surface profiles of the 23 and 950°C specimens are shown in Fig. 7. Note that the specimen in Fig. 7a corresponds to that in Fig. 6a, and the specimen in Fig. 7b was monotonically loaded to failure as shown in Fig. 4. The 23°C fracture specimen exhibited fiber bundles which extend 2-3 mm in either direction from the notch plane (Fig. 7a). In contrast, fibers extended a maximum of 1.0 mm from the crack plane of the fracture surface on the 950°C specimen (Fig. 7b). These relative fiber lengths are consistent with the C-scan attenuation regions which indicated a damage zone which was more concentrated in the notch plane at 950°C. For both temperatures, the height of the C-scan damage zone is approximately 2X larger than the maximum length of exposed fibers. This result can be attributed to matrix damage which extends beyond the point where fiber breakage occurs. Hence, fibers do not necessarily break at the end of the damage zone, and exposed fiber lengths on the fracture surface underestimate the extent of damage above and below the notch plane.

Observed Damage Modes

Micrographs of the room temperature specimen fracture surface are shown in Fig. 8. A cross-sectional view of the crack growth from the machined notch tip showed the primary failure plane advanced from the notch along 90° tows and matrix rich regions (Fig. 8a). The friable nature of the brittle matrix resulted in multiple distributed matrix cracking *within* the 90° tows. This damage mode, allowed the 90° fibers to be pulled away from the fracture surface at the notch tip and thus, cannot be seen in Fig. 8a. The 0° fiber tows extend from the failure plane as fiber bundles. Farther from the failure plane, the bundles separated into individual fibers with uncorrelated fiber failure locations.

Matrix cracking throughout the 90° fiber tows, resulted in long unbroken lengths of exposed 90° fibers and a peeling type failure mode. This damage mode led to disintegration of the 90° tows (Fig. 8b and 7a). Matrix

degradation *within* 90° tows was also observed above and below the primary failure plane. The distributed damage resulting from degradation of the matrix *within* 90° tows resulted in the enhanced ultrasonic attenuation away from the notch plane in the room temperature specimen [19, 20].

The observed damage indicated that crack growth from degraded 90° tows and pre-existing matrix cracks was dissipated in the crack plane by the 0° fiber tows as a whole. Near the primary crack plane, broken matrix remained attached to the fiber tows as shown in Fig. 8c. Away from the crack plane, matrix crack growth parallel to individual fibers further promoted energy dissipation. This mechanism of stress redistribution is in contrast to the debonding/sliding mechanism operating in CMC with an engineered interphase. The matrix remaining within the tow >1 mm away from the primary failure plane was effectively disintegrated as fibers broke during the final fast fracture. As a result of the matrix disintegration, no matrix sockets were observed on the fracture surfaces as are observed in CMC which exhibit a fiber/matrix sliding mechanism. The absence of sockets is similar to the observations of damage in an all oxide CMC by Levi, et al. [11]. As a result of matrix cracking and disintegration along 0° fibers, exposed fibers far from the primary crack plane are relatively smooth and nearly devoid of matrix (Fig. 8d). These damage mechanisms associated with extensive matrix cracking, result in redistribution of stresses at the notch tip, thus decreasing notch sensitivity and increasing fracture toughness at room temperature.

Observations of surface and subsurface damage occurring at 950°C were obtained from fracture surfaces and polished sections of two specimens. The fracture surface images were obtained from the specimen loaded monotonically to failure. The polished sections were obtained from the specimen shown in Fig. 6c, which was unloaded after reaching the peak load. Fig. 9a shows a cross-sectional view of the machined notch tip in the unloaded specimen. The micrograph shows that the primary failure plane grew from the notch within the matrix rich regions and 90° tows. The residual crack opening displacement (COD_{res}) within the 90° tows is clearly seen in the micrograph. The average 90° tow $COD_{res} \approx 40 \mu\text{m}$, which is comparable to the $CMOD_{res}$ after final unloading = 42 μm (Fig. 5). A cross-sectional view of the notch tip region of the failed specimen is shown in Fig. 9b. As observed on the unloaded specimen, crack growth within the 90° tows and matrix rich regions was restricted to a single plane. However, both micrographs in Fig. 9 show that the primary crack was initially deflected in the notch plane by matrix cracking along 0° tows. This initial crack deflection allowed 0° fiber failure to occur away from the crack plane. Unlike the room temperature specimen however, distributed matrix cracking *within* both the 0° and 90° tows was greatly reduced. Within the 0° tows, the lack of distributed matrix cracking along 0° fibers resulted in failure locations significantly closer to the crack plane than at 23°C. Within the 90° tows, individual fibers remained bonded to the matrix and were broken in the crack plane as the crack advanced (Fig. 9b and 7b). Thus, individual 90° fibers were not pulled away from the crack plane as was observed on the room temperature fracture surface. Similarly, polished sections of the unloaded specimen showed matrix degradation within 90° fiber tows was limited. Thus, the lack of distributed matrix cracking between fibers *within* the 0 and 90° tows at 950°C resulted in a change in damage mechanism from that observed at 23°C.

Further details of the 0° tow behavior at 950°C were obtained by closer examination of crack propagation from the notch tip. Figure 10 shows the notch tip region of the specimen in Fig. 6c after polishing the specimen surface to remove the top matrix layer and some of the 90° fibers. At 950°C, matrix cracking between fibers within the 0° tows was minimal, resulting in 0° fibers breaking as bundles. Broken 0° fibers were observed along the entire length of the surface crack. A comparison of Fig. 8c and 10 shows the differences in 0° fiber bundle behavior at 950°C and 23°C. At 23°C, multiple matrix cracking *within* fiber tows allowed individual fibers to fail independently. This damage mode resulted in fiber failure far from the primary crack plane and long exposed individual 0° fibers on the fracture surface. In contrast, at 950°C, energy dissipation through matrix cracking along individual 0° fibers *within* the tow did not occur. As a result, 0° fibers were broken as bundles near the crack plane as the crack propagated through the 0° tow.

The observed differences in matrix cracking behavior at 23 and 950°C may be related to changes in the alumina-silica matrix with temperature. Studies of crack growth in alumina ceramics containing glassy grain boundary phases showed that crack healing and blunting occurred at temperatures near 1000°C [22, 23]. In Nextel610/AS, stress redistribution occurred, at room temperature, through distributed matrix cracking. This damage mechanism relied on the friable nature of the weak matrix. At 950°C, crack healing and blunting would inhibit distributed matrix

cracking. The lack of distributed matrix cracking around the notch would result in increased notch sensitivity at 950°C. Further studies are currently underway to investigate these mechanisms.

The assessment of damage progression in Nextel610/AS discussed above, indicated there was a change in damage mode as temperature was increased from 23 to 950°C. The lack of distributed damage at 950°C resulted in a higher stress concentration at the notch tip than at room temperature, and the propagation of a single dominant crack. This change in damage mode, coupled with the decrease in fiber strength at 950°C ($\approx 15\%$) [21], resulted in significant decrease ($\approx 50\%$) in apparent fracture toughness.

The applicability of linear elastic fracture mechanics (LEFM) to characterize the notched behavior has not been established for the present CMC system. The large post-peak damage zone size indicated in the C-scans (Fig. 6) implies LEFM may not be applicable. Further interrupted testing is required to determine damage progression prior to the peak load. The damage zone size at the peak load can then be used to assess the applicability of LEFM. In addition, variation in K_{peak} with notch length and specimen size must be examined to determine the applicability of K_{peak} to predict failure. However, independent of LEFM, notch sensitivity of the Nextel610/AS system can be studied in terms of the net section strength (σ_n) as discussed in the next section.

(4) Comparison of Notched and Unnotched Behavior

Table I summarizes the results for the notched fracture tests and unnotched tensile tests [1, 2]. The elastic moduli of 73 GPa and 77 GPa at 23°C and 1000°C, respectively, were close to the average value of 70 GPa for the notched specimens. The unnotched tensile stress-strain response is shown in Fig. 11. At room temperature the tensile behavior was nearly linear to the ultimate failure stress (UTS) (Fig. 11). In contrast, the notched specimens exhibited nonlinear loading behavior prior to the peak stress, and non-brittle failure after reaching the peak load (Fig. 4). The unnotched tensile response at 1000°C was slightly nonlinear before abrupt failure at the ultimate stress (Fig. 11). This is in sharp contrast to the notched fracture behavior at 950°C which resulted in extensive nonlinear loading prior to and after reaching the peak load.

The net section failure strength (σ_n) of the notched specimens was significantly less than the UTS (Table I). At room temperature, the average σ_n was 138 MPa; 34% lower than the unnotched UTS of 208 MPa. At 950°C, σ_n was 62 MPa; 65% lower than the UTS at 1000°C of 176 MPa. Thus, notch sensitivity was exhibited at 23 and 950°C. The notched strength decreased $\approx 50\%$ as temperature was increased from 23 to 950°C. In contrast, the unnotched UTS decreased by only 15% as temperature was increased from 23 to 1000°C. Hence, the relative decrease in notch strength with increasing temperature was significantly greater than the corresponding decrease in unnotched tensile strength. The time to peak stress, $t_p \approx 9$ s in both tensile tests, was close to $t_p \approx 15$ s in the notched fracture test without unloading loops. A similar time to peak stress in the tension and fracture tests implies that the observed decrease in fracture toughness between 23°C and 950°C was not due to time at temperature.

The room temperature unnotched tensile specimen fracture surfaces showed that failure was associated with interply delamination and 0° fiber failure far from the fracture plane (Fig. 12a). The absence of a stress concentration in the unnotched specimen distributed the applied stress across the entire width and gage length allowing the composite plies to fail on different planes. Examination of the 0° fiber tows on the fracture surface showed that close to the ply failure plane matrix remained attached to the fibers (Fig. 12c). This is similar to the observed failure features near the crack plane of the notched specimen (Fig. 8c). Far from the ply failure plane, relatively smooth fiber surfaces nearly devoid of matrix were observed, similar to the notched specimen (Fig. 12c and Fig. 8d). The smooth appearance of fibers in both the notched and unnotched specimens is a direct result of matrix cracking and disintegration during fracture, not due to a debonding/sliding mechanism as occurs in CMC with an engineered interphase. Multiple matrix cracking within the 90° fiber tows in the unnotched specimen resulted in long exposed 90° fiber lengths, similar to the notched specimen (Fig. 12a and Fig. 8b). Although overall features of the fracture surfaces are similar in the notched and unnotched specimens, exposed 0° fiber lengths were considerably longer (2-3X) in the unnotched tension specimen.

Unnotched tensile failure at 1000°C resulted in a more localized fracture zone with 0° fiber breaks closer to the crack plane than at 23°C (Fig. 12b). Similar to the notched specimen at 950°C, matrix cracks within 90° tows were restricted to a single plane. Matrix remained bonded to the fibers resulting in 90° fiber failure within the crack plane (Fig. 9b and Fig. 12d). Although the failure locations of exposed 0° tows were close to the failure plane, fracture was not planar. This result indicated that propagation of pre-existing matrix cracks was initially deflected by the 0° tows. In contrast to the observed room temperature fracture behavior, close examination of the 0° fiber tows showed no evidence of the extensive matrix cracking within the tows. As a result of the change in matrix cracking behavior at 1000°C, most fibers failed as bundles rather than individual fibers. These observations showed that the elevated temperature fracture surfaces for notched and unnotched specimens exhibited similar features. Hence, the average length of exposed 0° fibers was also similar \approx 0.5 mm. Although the fracture surfaces of the notched and unnotched specimens exhibited similar features, the overall tensile behavior was dramatically different for the two test geometries. Apparently the lack of matrix cracking within fiber tows at temperatures near 1000°C increased notch sensitivity without greatly affecting unnotched tensile strength.

V. SUMMARY AND CONCLUSION

Fracture tests conducted at 23 and 950°C showed that the Nextel610/AS composite was notch sensitive. The net section strength of the notched specimens was \approx 65% and 35% of UTS at 23 and 950°C respectively. The net sections strength decreased 50% with an increase in temperature from 23 to 950°C. Fracture behavior was nonlinear prior to the peak load. The post-peak behavior was characterized by non-brittle failure with considerable retained load bearing capacity. Load-line displacement rate and unloading loops were found to have no effect on the fracture behavior at 950°C. Exposed fiber lengths on the fracture surface were reduced at elevated temperature with fiber bundle failure significantly closer to the primary crack plane than at room temperature. At room temperature individual fibers failed away from the matrix crack plane with distributed matrix cracking within the 0° and 90° fiber tows. A comparison between the notched fracture behavior and the unnotched tensile response of Nextel610/AS showed that the effect of temperature is significantly different.

Ultrasonic C-scans were shown to be an effective method of measuring the extent of damage accumulation. Post-peak room temperature test specimens showed no evidence of damage on the specimen surface, however, the attenuated zone indicated by the C-scan provided a measure of the extent and distribution of damage. Dominant matrix crack growth was observed on the specimen surface during testing at 950°C. The surface crack length correlated well with the length of the C-scan damage zone. C-scans indicated that, at 950°C, the height of the damage zone was approximately half that at 23°C. The reduction in damage zone height correlated with the reduction in exposed 0° fiber lengths on fracture surfaces.

Observations of damage on fracture surfaces and polished sections revealed a change in matrix crack behavior between 23 and 950°C. At 23°C, extensive matrix cracking *within* fiber tows allowed for stress redistributnion around the notch. Evidence of this damage mechanism was indicated by exposed 0° fiber lengths, matrix cracking between fibers, and the extent of ultrasonic C-scan attenuation. At 950°C, a change in failure mode to self-similar crack growth occurred. Examinations of exposed 0° fibers revealed at 950°C matrix cracking between fibers *within* the tows was greatly reduced resulting in a higher stress concentration in the notch tip area. Exposed 0° fiber lengths and the extent of ultrasonic C-scan attenuation verified that the damage zone was confined to the notch plane at 950°C. Crack growth beyond the peak load was characterized by fiber breakage. Although load-bearing capacity decreased slightly after the peak load, clearly fiber breakage in the crack wake did not immediately result in catastrophic failure at 950°C.

Acknowledgments: This research was conducted at the Materials and Manufacturing Directorate, Air Force Research Laboratory (AFRL/MLLN), Wright-Patterson Air Force Base, OH 45433-7817. V. A. Kramb was supported in part by the Dayton Area Graduate Studies Institute (DAGSI) and in part by AFOSR/AASERT Program (Contract No. F49620-95-1-0500). L. P. Zawada received partial financial support from Dr. W. S. Coblenz at DARPA under contract no: in-house and order number A565.

References

1. L. P., Zawada and S., S., Lee, "The Effect of Hold Times on the Fatigue Behavior of an Oxide/Oxide Ceramic Matrix Composite," *Thermal and Mechanical Test Methods and Behavior of Continuous-Fiber Ceramic Matrix Composites, ASTM STP 1309*, Michael G. Jenkins, Stephen T. Gonczy, Edgar Lara-Curzio, Noel E. Ashbaugh, and Larry P. Zawada, Eds., American Society for Testing and Materials, Philadelphia, PA, 1996.
2. Lee, S. S., Zawada, L. P., Hay, R. S. and Staehler, J., "High Temperature Mechanical Behavior and Characterization of an Oxide/Oxide Composite," submitted for publication *J. Am. Ceram. Soc.*, Oct. 1998.
3. R. John and N. E. Ashbaugh, "Fatigue Crack Growth in Ceramics and Ceramic Matrix Composites"; pp 28-50 in *Cyclic Deformation, Fracture and Nondestructive Evaluation of Advanced Materials, ASTM STP 1157*. Edited by M.R. Mitchell and O. Buck, American Society for Testing and Materials, Philadelphia, PA, 1992.
4. C. M. Cady, T. J. Mackin and A. G. Evans, "Silicon Carbide/Calcium Aluminosilicate: A Notch -Insensitive Ceramic-Matrix Composite," *J. Am. Ceram. Soc.*, **78** [1] 77-82 (1995).
5. S. Mall, D. E. Bullock and J. J. Pernot, "Tensile Fracture Behaviour of Fibre-Reinforced Ceramic-Matrix Composite with Hole," *Composites*, **25** [3] 273-242 (1994).
6. A. G. Evans, F. W. Zok, R. M. McMeeking and Z. Z. Du, "Models of High-Temperature, Environmentally Assisted Embrittlement in Ceramic-Matrix Composites," *J. Am. Ceram. Soc.*, **79** [9] 2345-52 (1996).
7. R. F. Allen, C. J. Beevers and P. Bowen, "Fracture and Fatigue of a Nicalon/CAS Continuous Fibre-Reinforced Glass-Ceramic Matrix Composite," *Composites*, **24** [2] 150-156 (1993).
8. F. E. Heredia, S. M. Spearing, T. J. Mackin, M. Y. He, A. G. Evans, P. Mosher, and P. Brondsted, "Notch Effects in Carbon Matrix Composites," *J. Am. Ceram. Soc.*, **77** [11] 2817-27 (1994).
9. K. R. Turner, J. S. Speck, and A. G. Evans, "Mechanisms of Deformation and Failure in Carbon-Matrix Composites Subject to Tensile and Shear Loading," *J. Am. Ceram. Soc.*, **78** [7] 1841-48 (1995).
10. W. C. Tu, F. F. Lange and A. G. Evans, "Concept for a Damage-Tolerant Ceramic Composite with "Strong" Interfaces," *J. Am. Ceram. Soc.*, **79** [2] 417-24 (1996).
11. C. G. Levi, J. Y. Yang, B. J. Dalgleish, F. W. Zok and A. G. Evans, "Processing and Performance of an All-Oxide Ceramic Composite," *J. Am. Ceram. Soc.*, **81** [8] 2077-86 (1998).
12. 3M Company Product Data Sheet, 3M Ceramic Fiber Products, 3M Center-Building 207-1W-11, St. Paul, MN 55144-1000.
13. G. A. Hartman and D. J. Buchanan, "Methodologies for Thermal and Mechanical Testing of TMC Materials," Characterization of Fibre Reinforced Titanium Matrix Composites, 77th Meeting of the AGARD Structures and Materials Panel, AGARD Report 796, Bordeaux, France, 27-28 September 1993.
14. G. A. Hartman S. M. Russ, "Techniques for Mechanical and Thermal Testing of Ti3Al/SCS-6 Metal Matrix Composites," *Metal Matrix Composites: Testing, Analysis, and Failure Modes, ASTM STP 1032*, Edited by W. S. Johnson, American Society for Testing and Materials, Philadelphia, PA, 1989.
15. R. John and B. Rigling, "Effect of Height to Width Ratio on K and CMOD Solutions For A Single Edge Cracked Geometry With Clamped Specimen Ends," *Eng. Frac. Mech.* **60** [2] 147-56 (1997).
16. D. A. Stubbs and G. S. Clemons, "Screening Metal Matrix Composites Using Ultrasonic Reflector Plate and X-ray Radiography Nondestructive Evaluation Techniques," in *Characterization of Titanium Matrix Composites, Vol. VII - Mechanical Behavior and Damage Tolerance of TMCs*, NASP Technical Memorandum 1199 (1995).
17. D. A. Stubbs and G. S. Clemons, "Guidelines for Standardizing the Gain of Ultrasonic Inspection Systems used to Acquire Ultrasonic Reflector Plate C-scans," in *Characterization of Titanium Matrix Composites, Vol. VII - Mechanical Behavior and Damage Tolerance of TMCs*, NASP Technical Memorandum 1199 (1995).
18. L. P. Zawada and S. S. Lee, "Evaluation of Four CMCs for Aerospace Turbine Engine Divergent Flaps and Seals," *Ceram. Eng. Sci. Proc.*, **16** [4] 337-39 (1995).
19. V. Kramb, R. John and D. Stubbs, to be submitted for publication, *Mat. Eval.*, (1999).
20. V.A. Kramb and R. John, "Room Temperature Fracture Behavior of an Oxide/Oxide CMC," to be submitted: *J. Comp. Sci. Tech.*, (1999).
21. D. M. Wilson, S. L. Lieder and D. C. Lueneburg, "Microstructure and High Temperature Properties of Nextel 720 Fibers," *Ceram. Eng. Sci. Proc.*, **16** [5] 1005-14 (1995).
22. K. Y. Donaldson, A Venkateswaran and D. P. H. Hasselman, "Observations on the Crack-Enhanced Creep-Fracture of a Polycrystalline Alumina with a Glassy Grain-Boundary Phase," *J. Mat. Sci.* **27** [16] 4501-10 (1991).
23. S. R. Choi and V. Tikare, "Crack Healing of Alumina with a Residual Glassy Phase: Strength, Fracture Toughness and Fatigue," *Mat. Sci. Eng.* **A171** 77-83 (1993).

Table I. Notched and Unnotched Test Results

Temperature (°C)	Width (mm)	$\bullet\dot{\delta}$ (mm/s)	Elastic Modulus (GPa)	Unnotched Peak Stress (MPa)	Notched Peak Net Section Stress (MPa)	Peak Stress Intensity Factor (MPa \sqrt{m})	Time to Peak Stress (s)
<u>Unnotched</u>							
23*	10.1	0.05	73	205			9.4
1000*	13.6	0.05	77	173			8.9
<u>Notched</u>							
23	19.0	0.001	69		151	16.8	736
23	25.4	0.001	71		124	15.5	665
950	25.4	0.001	71		62	7.9	668
950	25.4	0.01	70		62	7.9	15

* Reported values are an average from 3 tests conducted at 23°C and 2 tests at 1000°C

Figures

- Figure 1 Nextel610/AS composite polished section optical micrograph.
- Figure 2 Schematic of single edge notched specimen with clamped ends, MSE(T). $W = 19.0 \text{ & } 25.4 \text{ mm}$, $B = 2.9 \text{ mm}$ and $H/W = 4$.
- Figure 3 Load versus crack mouth opening displacement for load-line displacement controlled fracture tests at room temperature, $W = 19.0$ and 25.4 mm .
- Figure 4 Effect of temperature, loading rate and unloading loops on the load versus crack mouth opening displacement response for load-line displacement controlled fracture tests, $W = 25.4 \text{ mm}$.
- Figure 5 Effect of temperature on residual CMOD after unloading from a maximum load with corresponding CMOD_{\max} CMOD_{\max} at the peak load is also indicated on the plot.
- Figure 6 (a) Ultrasonic C-scan of entire gage section, room temperature specimen. (b) Ultrasonic C-scan of entire 950°C specimen gage section. The saw-cut notch region is indicated by the solid white bar in both C-scans. (c) Optical micrograph of 950°C fracture test specimen unloaded after peak load.
- Figure 7 Optical fracture surface profiles for specimens tested at (a) 23°C and (b) 950°C monotonically loaded to failure.
- Figure 8 Scanning electron micrographs of room temperature fracture surface. (a) cross-sectional view of machined notch tip (b) top view of fracture surface (15° tilt from normal) (c) 0° fibers near matrix crack plane (d) 0° fibers $\approx 1 \text{ mm}$ from primary crack plane.
- Figure 9 Cross-sectional view of machined notch tip region in 950°C specimens: (a) interrupted after the peak load (b) monotonically loaded to failure.
- Figure 10 Notch tip region of 950°C specimen shown in Fig. 6c, after removing the top matrix layer and some 90° fibers. Failed 0° fibers were identified along the length of the dominant crack.
- Figure 11 Tensile stress/strain response for unnotched Nextel610/AS at 23°C and 1000°C .
- Figure 12 Nextel610/AS unnotched tension fracture surfaces: (a) 23°C (b) 1000°C and details of matrix and 0° fiber behavior (c) 23°C (d) 1000°C .

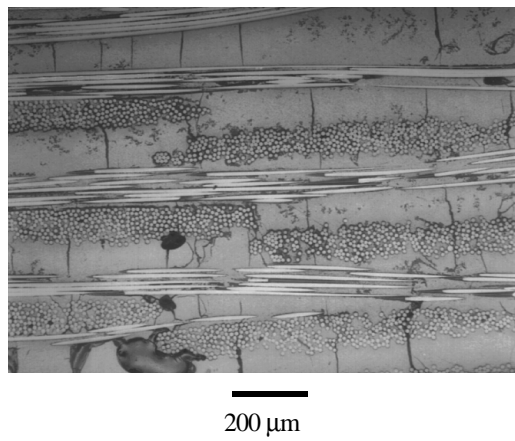


Figure 1. Nextel610/AS composite polished section optical micrograph.

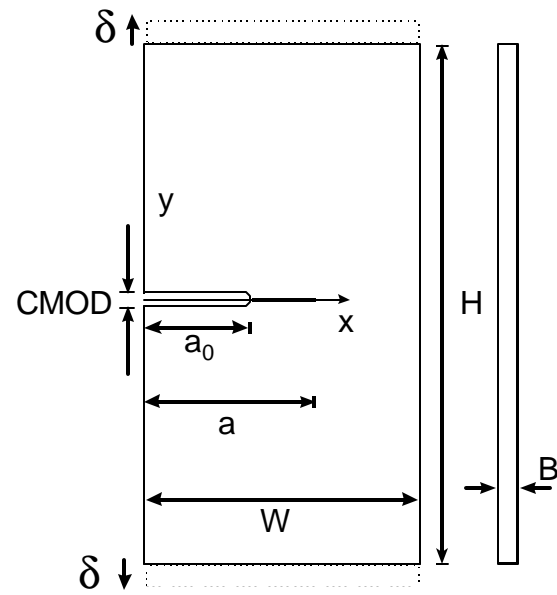


Figure 2. Schematic of single edge notched specimen with clamped ends, MSE(T). $W = 19.0 \text{ \& } 25.4 \text{ mm}$, $B = 2.9 \text{ mm}$ and $H/W = 4$.

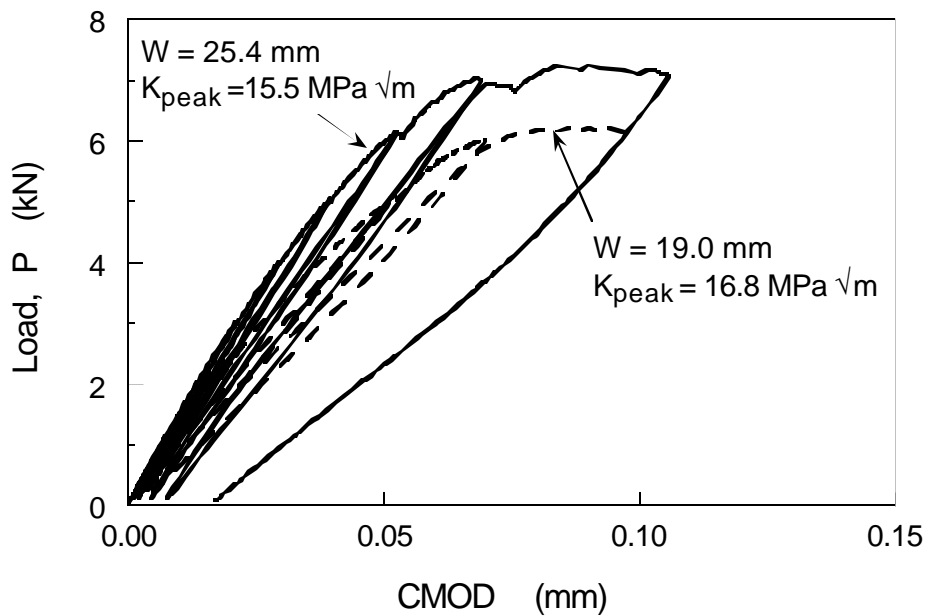


Figure 3. Load versus crack mouth opening displacement for load-line displacement controlled fracture tests at room temperature, $W = 19.0$ and 25.4 mm.

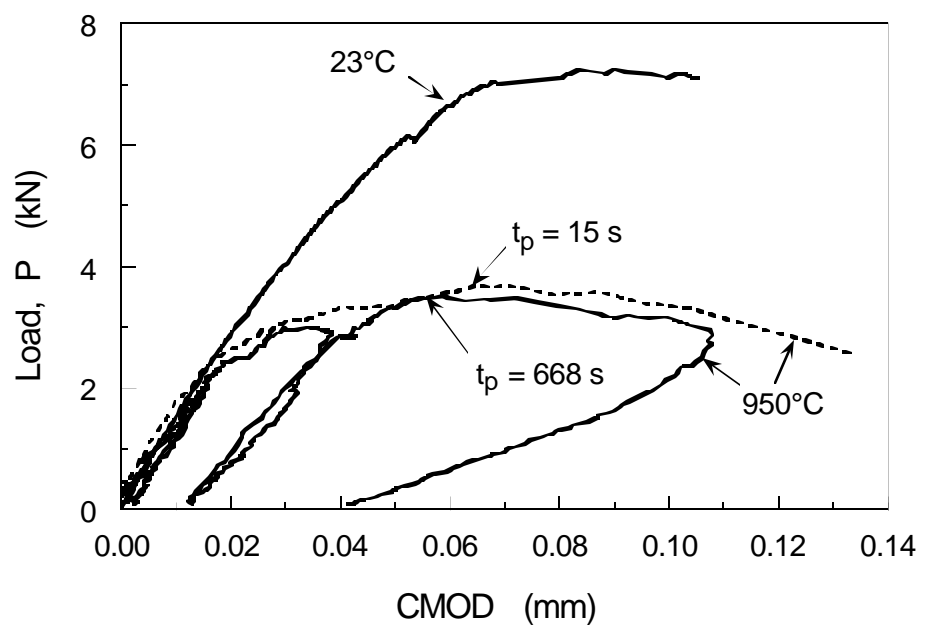


Figure 4. Effect of temperature, loading rate and unloading loops on the load versus crack mouth opening displacement response for load-line displacement controlled fracture tests, $W = 25.4\text{ mm}$.

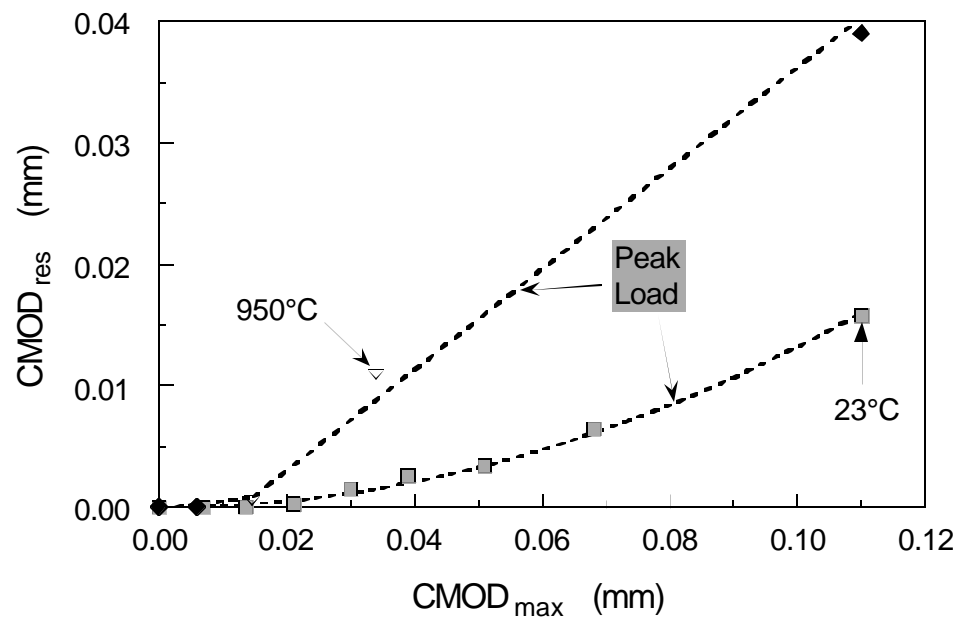


Figure 5. Effect of temperature on residual CMOD after unloading from a maximum load with corresponding $CMOD_{max}$ $CMOD_{max}$ at the peak load is also indicated on the plot.

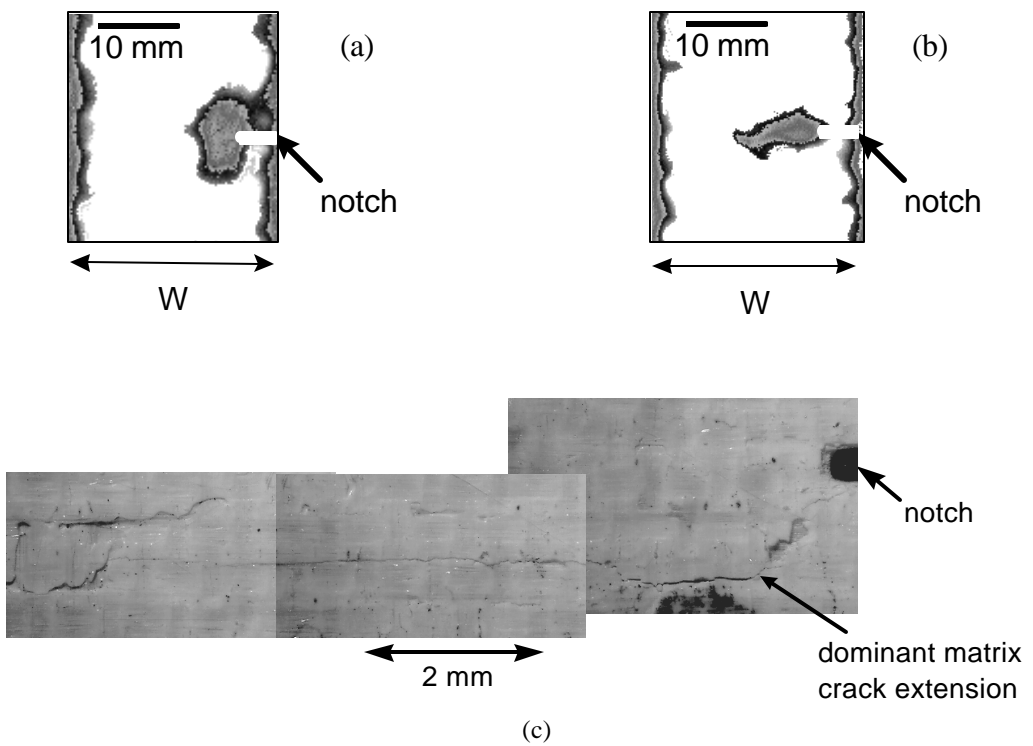
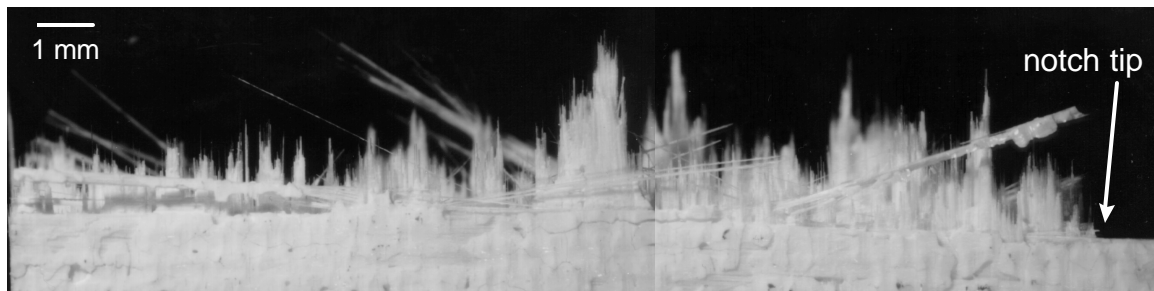
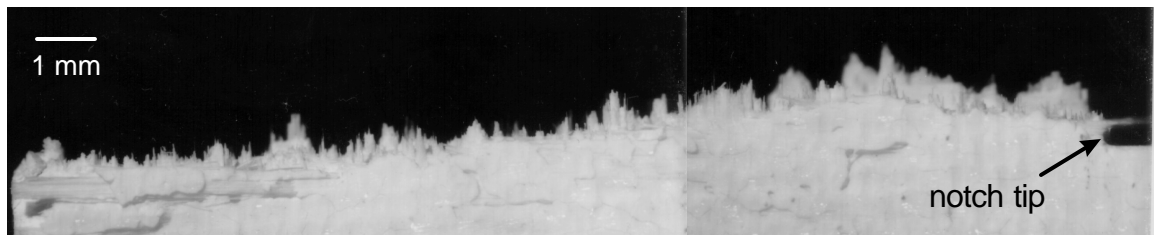


Figure 6. (a) Ultrasonic C-scan of entire gage section, room temperature specimen. (b) Ultrasonic C-scan of entire 950°C specimen gage section. The saw-cut notch region is indicated by the solid white bar in both C-scans. (c) Optical micrograph of 950°C fracture test specimen unloaded after peak load.



(a)



(b)

Figure 7. Optical fracture surface profiles for specimens tested at (a) 23°C and (b) 950°C monotonically loaded to failure.

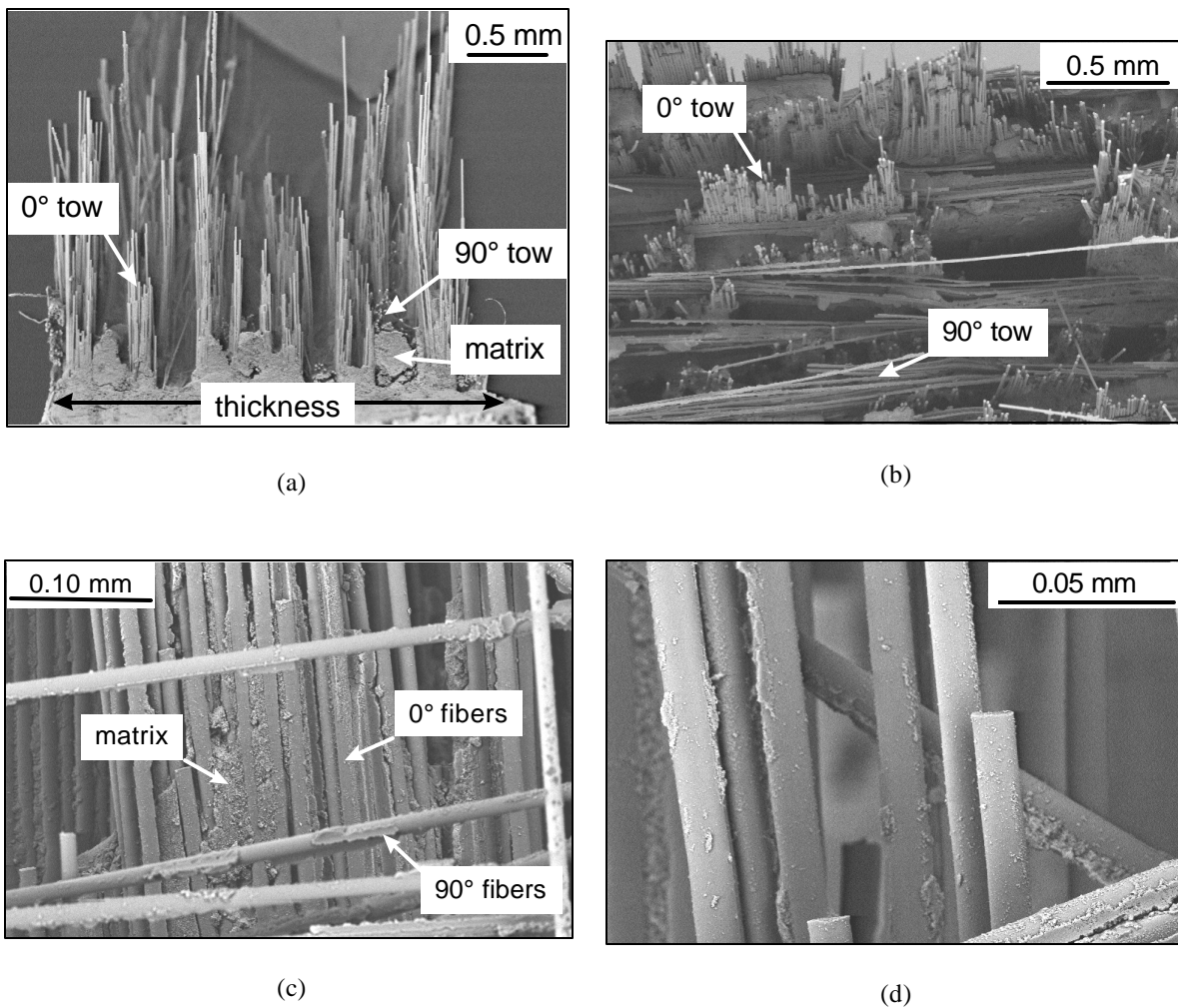


Figure 8. Scanning electron micrographs of room temperature fracture surface. (a) cross-sectional view of machined notch tip (b) top view of fracture surface (15° tilt from normal) (c) 0° fibers near primary crack plane (d) 0° fibers \approx 1 mm from primary crack plane.

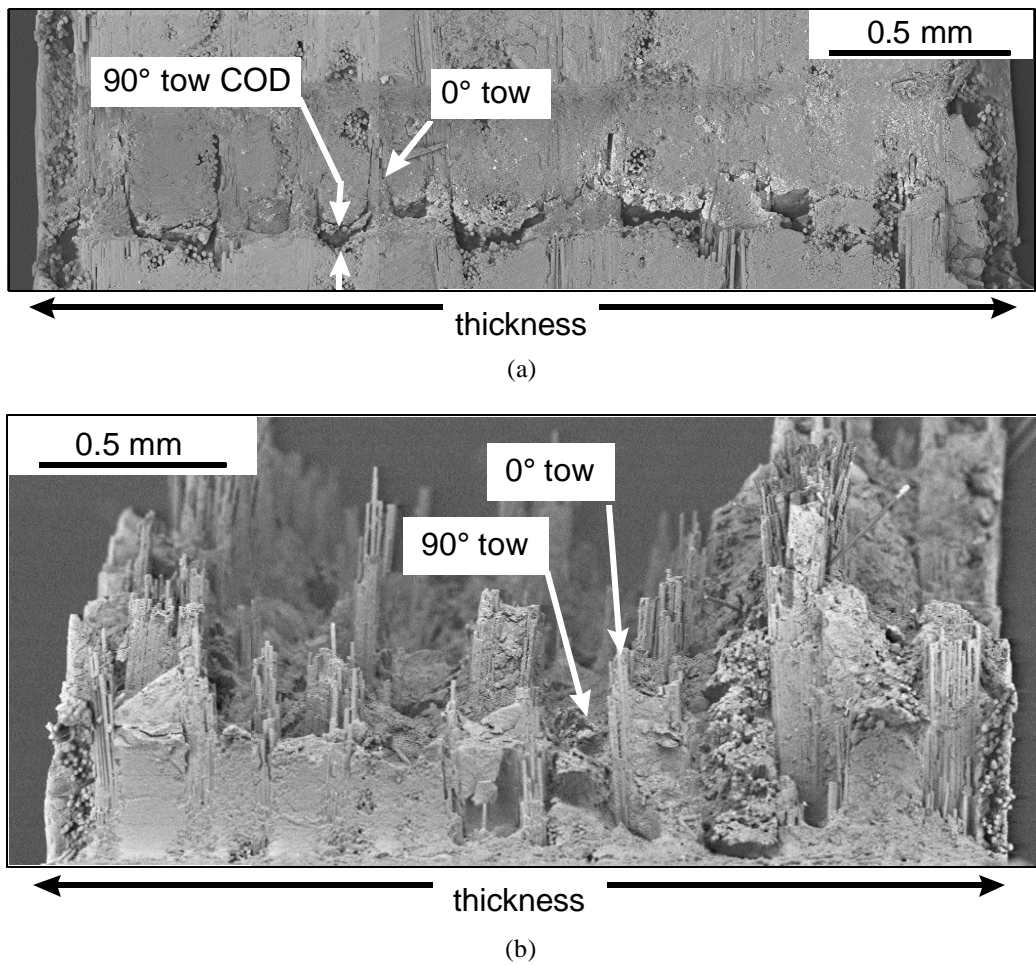


Figure 9. Cross-sectional view of machined notch tip region in 950°C specimens: (a) interrupted after the peak load (b) monotonically loaded to failure.

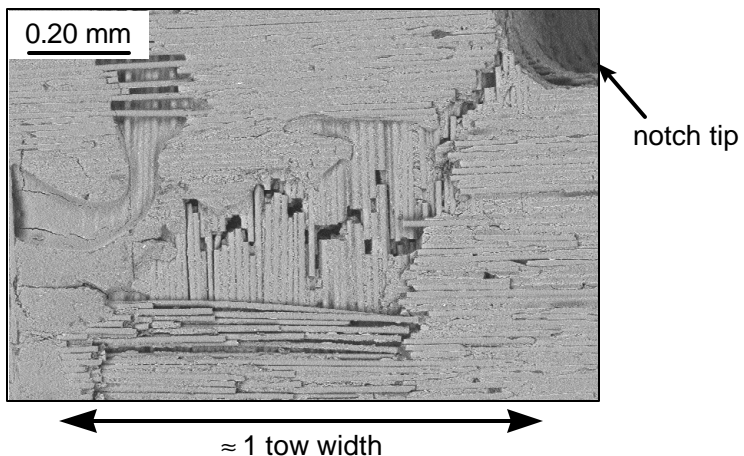


Figure 10. Notch tip region of 950°C specimen shown in Fig. 6c, after removing the top matrix layer and some 90° fibers. Failed 0° fibers were identified along the length of the dominant crack.

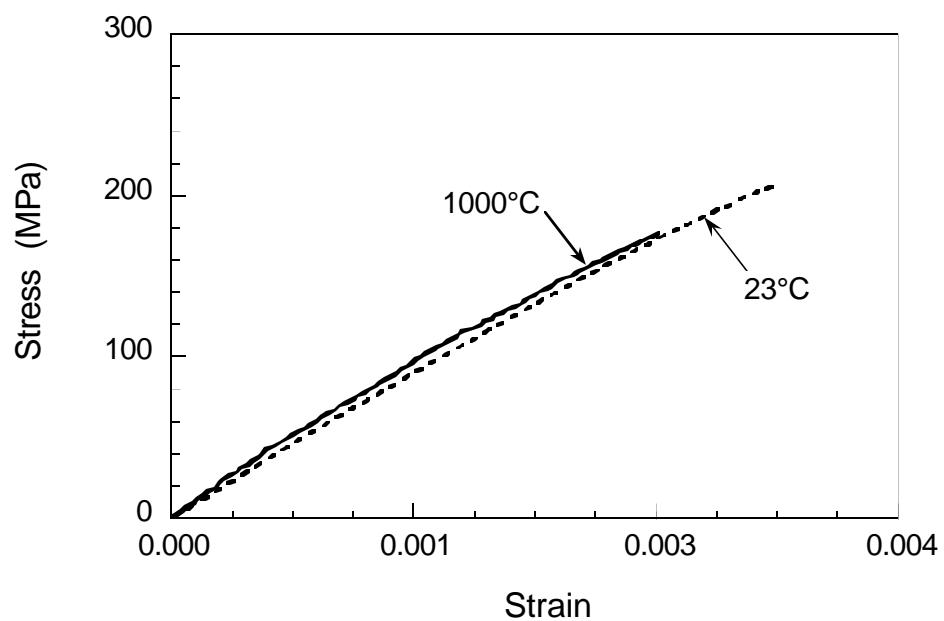
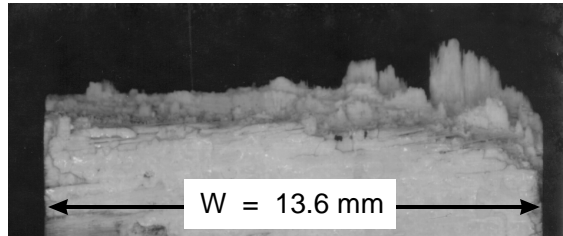


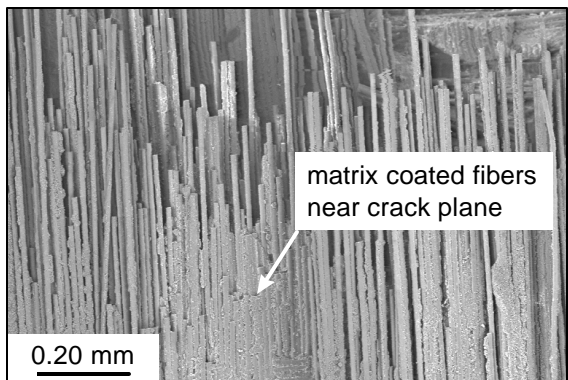
Figure 11. Tensile stress/strain response for unnotched Nextel610/AS at 23°C and 1000°C.



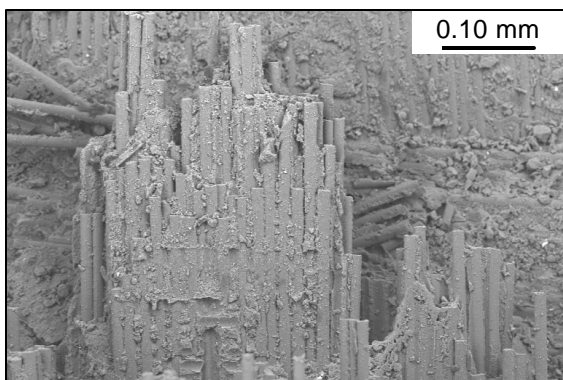
(a)



(b)



(c)



(d)

Figure 12. Nextel610/AS unnotched tension: fracture surfaces (a) 23°C (b) 1000°C and details of matrix and 0° fiber behavior (c) 23°C (d) 1000°C.

Submitted for publication: Composites Science and Technology, April 2000

Damage Progression from Notches in an Oxide/Oxide Ceramic Matrix Composite Using Ultrasonic C-scans

Victoria A. Kramb^{1,*}, Reji John and David A. Stubbs¹

Materials and Manufacturing Directorate (AFRL/MLLN)
Air Force Research Laboratory
Wright-Patterson Air Force Base
OH 45433-7817
USA

¹ University of Dayton Research Institute, 300 College Park, Dayton, OH 45469-0128, USA.

* Corresponding author

Abstract

The damage progression from notches during quasi-monotonic loading was investigated in an oxide/oxide ceramic matrix composite using ultrasonic C-scans. Test specimens were monotonically loaded, removed from the test machine, then ultrasonically C-scanned using a through transmission, reflector plate method. The level of ultrasonic attenuation was monitored as a function of applied stress and correlated with the damage observed within the composite. Results of the study showed that the ultrasonic technique successfully monitored the progressive matrix cracking prior to the peak load in specimens tested at 23°C. Close to the peak load, fiber breakage occurred near the notch tip, which was not indicated by the ultrasonic C-scans. At 950°C, damage progressed from the notch as a single dominant crack. The extent of enhanced ultrasonic attenuation in the C-scans correlated well with the crack length from the notch.

Keywords: ceramic composites, damage progression, nondestructive evaluation, notched fracture, oxide/oxide, ultrasound

Introduction

Ceramic matrix composites (CMC) consisting of an oxide matrix and oxide fibers with no engineered fiber-matrix interphase are currently under consideration for high temperature

aerospace applications due to their inherent resistance to oxidation. Oxide/oxide CMC produced with no fiber-matrix interphase utilize a weak, friable matrix which offers a low energy path crack path throughout the matrix [1-3]. In these CMC, nearly all the load is supported by the fibers. The nearly linear stress-strain behavior exhibited by these composites in the [0°/90°] orientation is typical of fiber dominated composites [3-7]. In contrast, the notched fracture behavior is highly nonlinear due to stress redistribution around the notch during loading [6-9]. Stress redistribution and damage around notches has been observed in CMC using x-ray [7], thermoelastic emission [6,7] and ultrasonic [8,9] techniques. Many nondestructive inspection methods typically used for monitoring damage progression are ineffective in oxide/oxide CMC because of the pre-existing porosity and matrix cracking which occurs during processing [4,5]. In spite of the highly cracked and porous condition of oxide/oxide CMC, previous studies have shown that there was no reduction in strength or mechanical behavior of oxide/oxide CMC after water exposure. Environmental stability in the presence of water makes ultrasonic inspection methods a viable approach for examining damage progression in oxide/oxide CMC. Damage progression in metal matrix composites (MMC) has been monitored using a through transmission, ultrasonic imagining technique referred to as reflector plate C-scanning [10,11]. In this paper, adaptation of the ultrasonic reflector plate C-scan technique to monitor damage progression from notches in oxide/oxide CMC will be described. The C-scan results will be correlated with observed damage mechanisms from monotonically loaded specimens.

Experimental Procedure

The Nextel610/AS CMC used in this investigation was produced by General Electric Aircraft Engines under the trade name Gen IV. The Nextel610 fibers, produced by the 3M Company [12], consisted of polycrystalline alpha alumina. The fibers were bundled into tows containing approximately 400 individual fibers, and woven into an eight harness satin weave (8HSW) cloth. The composite panel used in this study contained 12 plies. The matrix consisted of a porous alumina-silica (AS) matrix. Fiber volume fraction was 33%. Extensive microcracking was present throughout the matrix as a result of the shrinkage which occurred during the pyrolysis processing (Fig. 1). These microcracks are distributed throughout the interior matrix as well as on the specimen surface. The resulting composite contains sintered matrix which is bonded to the fibers with no naturally occurring or engineered interphase. Further details of the composite processing and microstructure are discussed in [4,5,9].

All mechanical testing was conducted on single edge notched specimens [13] in lab air, using a servo-controlled, hydraulic, horizontal test system [14,15]. The specimen ends were rigidly clamped using friction grips, thus resulting in rotationally constrained end conditions (Fig. 2). The fiber orientation relative to the loading axis was [0°/90°] for all edge notched specimens. During the room temperature tests, crack mouth opening displacement (CMOD) was measured using a high resolution, knife edge extensometer. At 950°C a high temperature extensometer, with quartz or alumina rods, was used to measure CMOD. The extensometer measured the displacements on the edge of the specimen, as shown in Fig. 2. Longitudinal strains ahead of the notch tip were measured using standard foil strain gages 0.8 mm in gage length and 1.6 mm in width. Typical gage locations are shown in Fig. 2.

Heating of the test specimen was achieved with closed-loop controlled, four zone quartz lamps. Slotted windows in the center of the quartz lamps allowed for visual inspection of the surface matrix crack during testing. Further details of the test equipment have been described elsewhere [14,15].

Fracture tests were conducted under load-line displacement control at a rate of 0.001 mm/s. After reaching the desired maximum load, test specimens were removed from the test machine for ultrasonic and optical evaluation. Applied load, CMOD, strain gage output and load-line displacement (δ) were recorded continuously as a function of time during all tests.

Ultrasonic C-scans of the specimens were recorded before and after testing. A schematic of the C-scan set-up is shown in Fig. 3. The C-scans were obtained using a through transmission, reflector plate scanning technique described elsewhere [10,11]. A 12.7 mm diameter, 10 MHz, 76 mm spherically focused transducer produced by KB Aerotech was used to emit and receive the ultrasonic energy. A Panametrics model 5052 pulser/receiver, LeCroy model TR 8828C 200 MHz digitizer, and a CalData 5 axis scanning system were used to acquire ultrasonic C-scan data. The data acquisition and scanning control was accomplished using in-house software.

During the C-scan, the amplitude of the ultrasonic energy passing through the specimen was recorded at regularly spaced x-y locations (0.1 mm increments) and digitized. The reflector plated ultrasonic C-scan technique records the ultrasound that passes through the specimen, reflects off a flat steel plate, and passes back through the specimen to the transducer. The amplitude of the ultrasonic signal returning to the transducer is very sensitive to physical changes

in the specimen. Using focused transducers provides good spatial resolution in the C-scan images. At each x-y location, the amplitude of the digitized ultrasonic signal was color coded to produce a planar (2 dimensional) color image of the amount of ultrasonic energy passing through the specimen. For the ultrasonic C-scans used in this study, white in the color bar, represents low attenuation of the ultrasonic energy passing through the specimen, or maximum amplitude. Red in the color bar represents high attenuation of the ultrasonic signal; the amplitude has decreased by > 48 dB. The color bar was referenced to a calibrated ultrasonic attenuation scale using a Ti-6-4 block of the same thickness as the specimen. Prior to each C-scan, the amplitude of the ultrasonic signal from the Ti-6-4 block was adjusted to be 90% of the full scale range of the digitizer. This procedure was used to compensate for slight differences in the set-up of the electronic equipment.

The reflector plate C-scan technique, required immersion of the test specimen in water during the scan. After each C-scan, excess moisture was removed during a 1 hour bake out at 70°C. Zawada and Lee [4,5] showed that water exposure did not result in a change in the mechanical behavior of Nextel610/AS.

Destructive evaluation of interrupted test specimens was performed on specimens which were monotonically loaded, unloaded and removed from the test frame. Sectioning and polishing of the specimen within the region of interest was performed to identify damage. Polishing using light pressure and water lubricant on a diamond impregnated lapping film successfully polished the surface without causing additional damage to underlying plies. Diamond grit size was decreased from 15 μm for the initial rough polish to 0.5 μm for final polishing. Sectioned and polished specimens were inspected optically and with scanning electron microscopy (SEM). Before SEM imaging, specimens were sputter coated with gold-palladium. Backscatter electron imaging was used to minimize charging effects and to highlight microcracks.

Results and Discussion

Edge Notched Fracture Test at 23°C

Typical load versus CMOD behavior of edge notched specimens at 23°C is shown in Fig. 4. Nonlinear load-CMOD behavior observed prior to and after the peak load indicated that some type of progressive damage was occurring during the test (Fig. 4(a)). However, longitudinal strains measured near the notch tip were much more linear until close to the peak load as shown in Fig. 4(b). Consistent with the linear longitudinal strain measurements, optical inspection of

the notch tip region during testing showed no new crack growth or change in the surface matrix crack pattern. Therefore, subsurface damage was suspected and searched for with ultrasonic C-scans and destructive evaluation of specimens loaded prior to and after reaching the peak stress.

The maximum loads chosen for the specimens that underwent destructive and nondestructive evaluation were based on the deformation behavior shown in Fig. 4(a) and 4(b). Three distinct types of deformation behavior were identified. Initial loading behavior, characterized by linear load-CMOD and load-longitudinal strain ahead of the notch occurred up to a net section stress (σ_n) \approx 50 MPa (region a in Fig. 4(b)). Intermediate loading behavior, characterized by nonlinear load-CMOD and linear load-longitudinal strain was exhibited for $50 < \sigma_n < 120$ MPa (region b in Fig. 4(b)). Final loading, corresponding to $\sigma_n > 120$ MPa, resulted in nonlinearity in the longitudinal strains ahead of the notch tip (region c in Fig. 4(b)). Therefore, damage progression from the notch was characterized using three specimens monotonically loaded to a predetermined level, unloaded, and C-scanned. Following the C-scans, the specimens were sectioned, polished, and the observed damage documented. An untested specimen was also examined to determine the baseline condition of the as received material (specimen #1). Specimen #2 was loaded to $\sigma_n = 88$ MPa to examine damage which resulted in nonlinearity in the load-CMOD behavior. Specimen #3 was loaded up to $\sigma_n = 140$ MPa to examine damage which resulted in nonlinearity in the measured longitudinal strains ahead of the notch tip. Post peak damage was examined on specimen #4 which was loaded beyond the peak net section stress ($\sigma_{n, peak}$) = 150 MPa.

Ultrasonic C-scans of specimens #1-4 are shown in Fig. 5 with the calibrated ultrasonic color bar. Due to the extensive pre-existing matrix cracks and porosity, C-scans of the untested composite showed varying levels of attenuation. These regions typically exhibited 0-50% attenuation (Fig. 5(a)), with isolated regions of high porosity exhibiting up to 75% attenuation. C-scans of specimens which had been loaded to sufficiently high stress, showed levels of ultrasonic attenuation near the notch tip which exceeded 75%. Specimens which were monotonically loaded and showed increased ultrasonic attenuation in the notch tip region showed no change in the level of ultrasonic attenuation of the undamaged regions far from the notch tip. Therefore, attenuation of the ultrasonic signal exceeding 75% was identified as that which indicated damage accumulation during testing. With reference to the color bar in Fig. 5(a), white

indicates full scale signal transmission through the specimen, red indicates ≈ -48 dB signal transmission ($\approx 0.4\%$ of the full scale transmission).

The C-scans showed an increase in the ultrasonic attenuation around the notch tip region with an increase in the level of applied load. Specimen #2, loaded just beyond the load-CMOD linear region (Fig. 5(b)), showed slightly more attenuation than the pretest condition (Fig. 5(a)). Applied loads which result in nonlinearity in the longitudinal strains resulted in extensive attenuation ahead of the notch (Fig. 5(c)). As shown in Fig. 5(d), continued loading beyond the peak load resulted in further growth of the attenuated region away from the notch tip.

Damage in the notch tip region was examined by destructive evaluation of the C-scanned specimens using the sectioning procedure shown schematically in Fig. 6. First, excess material far from the C-scan damage zone was removed above and below the notch plane. Second the specimen was sectioned perpendicular to the notch in the loading direction, just behind the notch tip. The specimens were polished along this through-thickness cross-section so that a view of the damage ahead of the notch tip was obtained. The top surface matrix was removed on the faces of some specimens, so that 0° fibers within the top surface ply could be observed.

The polished sections shown in Fig. 7 were obtained from the corresponding C-scanned specimens in Fig. 5. The cross sectional view in the micrographs is, as shown schematically in Fig. 6, the through-thickness view just ahead of the notch tip. Fig. 7(a) shows a micrograph of the notch tip region of an as notched, untested specimen. Pre-existing matrix cracks were seen throughout the notch tip region, similar to other regions of the composite away from the notch. A comparison of the untested notch tip region with that of the specimen loaded to $\sigma_n = 88$ MPa shows that the preexisting matrix cracks acted as initiation sites for matrix cracking within the 90° tows. For the specimen in Fig. 7(b) ($\sigma_n = 88$ MPa), the extent of matrix cracking within the 90° tows correlated with the area of higher attenuation in the C-scan (≈ 2 mm). Consistent with the limited matrix cracking, all 0° fibers observed on the polished sections were intact, i.e. no tensile fiber breakage was observed. The notch tip region of the specimen loaded to $\sigma_n = 140$ MPa, showed considerably more matrix degradation in the notch tip region (Fig. 7(c)). Similar to the specimen loaded to $\sigma_n = 88$ MPa (Fig. 7(b)), the height of the matrix damage zone correlated well with the height of the enhanced attenuation region in the C-scan (≈ 7.4 mm). Figure 7(d) shows that within the specimen loaded beyond the peak, matrix cracking and

distributed damage was widespread and correlated well with the area of high attenuation in the C-scan. Therefore, based on the results of the destructive evaluation, distributed damage resulting from degradation of the matrix *within* 90° tows resulted in the enhanced ultrasonic attenuation away from the notch plane in the room temperature specimens.

As applied stress was increased during the fracture test, damage progressed from matrix cracking to longitudinal fiber breakage. A few isolated 0° fiber breaks were observed within the specimen loaded to $\sigma_n = 140$ MPa. The fiber breaks occurred close to the notch plane, and were confined to a few tows. Due to the statistical distribution of fiber strengths, and the high stresses near the notch tip, weaker fibers will break prior to the peak load. Fiber breakage is consistent with the observed nonlinearity in the longitudinal strains measured in the notch tip gage at this applied stress. For the post-peak specimen, extensive matrix cracking between the 0° fibers was also observed (Fig. 8). The matrix cracking between 0° fibers, allowed the 0° fibers within the tow to fail independently. As shown in Fig. 8(b), 0° fiber breaks were distributed approximately 1 mm above and below the notch plane. Further polishing of the specimen also showed that 0° fiber breakage had only extended beyond the notch tip to first tow (≈ 1 mm). Thus, longitudinal fiber breakage within the first tow resulted in a nonlinear damage zone ≈ 1 mm from the notch tip at the peak load. A nonlinear damage zone ≈ 1 mm ahead of the notch tip is consistent with the width of the notch tip strain gage. Thus, nonlinear strains measured in the notch tip strain gage for $\sigma_n > 140$ MPa are consistent with longitudinal fiber breakage. The onset of nonlinearity in the longitudinal strains 2 mm from the notch tip (gage #2, Fig. 4(b)), did not occur until after the peak load. Therefore, the region of nonlinear longitudinal strains did not exceed 2 mm from the notch tip. These results imply that, prior to the peak load, distributed fiber breakage may occur within the first tow adjacent to the notch. However, fiber breakage beyond the first tow results in specimen failure.

The region of higher attenuation in the C-scan was also compared to the length of 0° fibers, which extended from fracture surfaces of failed specimens [8]. C-scans of post peak fracture specimens suggested a damage zone approximately ≈ 6 mm in height. Examination of fracture surface profiles showed that maximum 0° fiber pullout lengths were $\approx 2\text{-}3$ mm. Fiber pullout lengths were consistently smaller than that suggested by the C-scans. This result indicates that fiber breakage does not occur at the end of the damage zone.

Edge Notched Fracture Test at 950°C

The load-CMOD response for the edge notched fracture test at 950°C, is shown in Fig. 9. Similar to the fracture behavior at 23°C, nonlinear loading behavior was observed prior to and after the peak load. At 950°C however, linear loading was exhibited up to only $\sigma_n = 30$ MPa. Similarly, at 950°C $\sigma_{n,peak} = 62$ MPa, a reduction of 50% from the value at 23°C. The reduction in peak stress indicated a change in damage mode with temperature.

During mechanical loading at 950°C, optical inspection of the notch tip region revealed a dominant matrix crack at an applied load of 3.0 kN. Increasing load-line displacement, resulted in extension of the dominant crack as it grew and linked with other preexisting surface matrix cracks. When the test was stopped, the continuous matrix crack extension from the notch tip, measured on the specimen surface, was equal to 9 mm (Fig. 10(b)). Fig. 10(a) shows the corresponding ultrasonic C-scan at the same point of unloading. The region of enhanced ultrasonic attenuation ahead of the notch tip was ≈ 5 mm in height and 11 mm in length. A comparison of the surface crack length with the attenuated region suggested that the damage zone extended beyond the surface crack tip. A comparison of the C-scan in Fig. 10(a) to the C-scan in Fig. 5(d) showed that the crack extension at 950°C was associated with a damage zone that was much more confined to the notch plane at 950°C than at 23°C.

Surface and subsurface damage at 950°C was examined from polished sections of the specimen shown in Fig. 10(b). Damage along the surface crack length was examined by further sectioning the specimen at distances of 0.5, 4, 9 and 14 mm ahead of the machined notch tip. Immediately ahead of the notch tip (0.5 mm), a single crack was clearly identified which penetrated the 90° and 0° tows across the thickness of the specimen (Fig. 11). The large residual crack opening displacement (COD ≈ 40 mm) and matrix cracking along 0° tows likely caused the enhanced ultrasonic attenuation at 950°C. The matrix cracking and 0° fiber breakage extended ≈ 2 mm above and below the notch plane, consistent with the height of the C-scan damage zone.

Polished sections at 5 and 9 mm from the notch tip similarly revealed a clearly defined crack plane with 0° fiber breakage. The residual COD decreased with increasing length from the notch tip. The length of the C-scan damage zone correlated with the extent of 0° broken fibers observed in the polished cross sections. However, a few 0° fiber breaks were identified up to 14 mm ahead of the notch tip (Fig. 12). At 14 mm ahead of the notch tip, no clearly defined crack

plane was identified, and the 0° fiber breaks at 950°C were not associated with extensive matrix cracking along the fibers.

A comparison of Figs. 8 and 11 shows the differences in 0° fiber bundle behavior at 950°C and 23°C. At 23°C, multiple matrix cracking *within* fiber tows allowed individual load bearing fibers to fail independently. This damage mode resulted in fiber failure far from the primary crack plane. In contrast, at 950°C, energy dissipation through matrix cracking along individual 0° fibers *within* the tow did not occur. As a result, 0° fibers were broken as bundles near the crack plane as the crack propagated through the 0° tow (Fig. 11). Within the 0° tows, the lack of matrix cracking along 0° fibers resulted in failure locations significantly closer to the crack plane than at 23°C. Within the 90° tows, individual fibers remained bonded to the matrix and were broken in the crack plane as the crack advanced (Fig. 11). The growth of a single, through thickness crack from the notch at 950°C, resulted in a damage zone which was more confined to the notch plane, than at 23°C. Polished sections showed matrix degradation within 90° fiber tows was limited. Thus, the lack of distributed matrix cracking between fibers *within* the 0° and 90° tows at 950°C resulted in a change in damage mechanism from that observed at 23°C.

Summary and Conclusion

The results of the destructive and nondestructive evaluation showed that the damage mechanisms and crack growth behavior in Nextel610/AS CMC were temperature dependent. Observations of damage during fracture tests showed that dominant crack growth from the notch tip did not occur at 23°C. Ultrasonic and destructive evaluation of interrupted test specimens showed that nonlinearity in the load-CMOD response was due to distributed matrix cracking within the 90° tows. Although distributed matrix cracking was extensive, longitudinal strains remained linear, until just prior to the peak load for edge notched specimens. Destructive evaluation showed that, the onset of nonlinear longitudinal strains correlated with longitudinal fiber breakage. Ultrasonic C-scans were effective in monitoring the extent of matrix cracking, but were not indicative of longitudinal fiber breakage. At 950°C, damage progression of edge notched specimens was characterized by growth of a dominant crack from the notch tip. Destructive evaluation of tested specimens showed that the crack growth was associated with minimal matrix cracking within 90° fiber tows and 0° fiber breakage. Ultrasonic C-scans of the

950°C fracture specimen correlated well with both the length of the continuous surface matrix crack, and the extent of the matrix cracking away from the crack plane. At both 23 and 950°C, the extent of matrix cracking extended beyond the 0° fiber failure locations. Thus, good correlation between the ultrasonic C-scans and extent of matrix cracking indicated C-scans can be used effectively to monitor damage progression from notches in oxide/oxide CMC.

Acknowledgments: This research was conducted at the Materials and Manufacturing Directorate, Air Force Research Laboratory (AFRL/MLLN), Wright-Patterson Air Force Base, OH 45433-7817. The NDE facilities were provided by the NDE Branch of AFRL (AFRL/MLLP). V. A. Kramb was supported in part by the Dayton Area Graduate Studies Institute (DAGSI) and in part by AFOSR/AASERT Program (Contract No. F49620-95-1-0500).

References

1. Lu TJ, Crack branching in all-oxide ceramic composites. *J Am Ceram Soc* 1996;79(1): 266-74.
2. Tu WC, Lange FF, Evans AG, Concept for a damage-tolerant ceramic composite with "strong" interfaces. *J Am Ceram Soc* 1996;79(2): 417-24.
3. Levi CG, Yang JY, Dalgleish BJ, Zok FW, Evans AG, Processing and performance of an all-oxide ceramic composite, *J Am Ceram Soc* 1998;81(8): 2077-86.
4. Lee SS, Zawada LP, Hay RS, Staehler J. High temperature mechanical behavior and characterization of an oxide/oxide composite. submitted for publication *J Am Ceram Soc*.
5. Zawada LP, Lee SS. Evaluation of four CMCs for aerospace turbine engine divergent flaps and seals. *Ceram Eng Sci Proc* 1995;16(4): 337-39.
6. Heredia FE, Spearing SM, Mackin TJ, He MY, Evans AG. Notch effects in carbon matrix composites. *J Am Ceram Soc* 1994;77(11): 2817-27.
7. Mackin TJ, Purcell TE, He MY, Evans AG. Notch sensitivity and stress redistribution in three ceramic-matrix composites 1995;78(7): 1719-28.
8. Kramb VA, John R, Zawada LP. Notched fracture behavior of an oxide/oxide ceramic matrix composite. *J Am Ceram Soc* 1999;82(11): 3087-96.
9. Kramb VA. Notched fracture behavior of an oxide/oxide ceramic matrix composite. PhD Thesis, University of Dayton, Department of Materials Engineering, 1999.
10. Stubbs DA, Clemons GS. Screening metal matrix composites using ultrasonic reflector plate and x-ray radiography nondestructive evaluation techniques. In: Characterization of Titanium Matrix Composites, Vol. VII - Mechanical Behavior and Damage Tolerance of TMCs, NASP Technical Memorandum 1199, 1995.
11. Stubbs DA, Clemons GS. Guidelines for standardizing the gain of ultrasonic inspection systems used to acquire ultrasonic reflector plate C-scans. In: Characterization of titanium matrix composites, mechanical behavior and damage tolerance of TMCs, Vol VII, - NASP Technical Memorandum 1199, 1995.
12. 3M Company Product Data Sheet, 3M Ceramic Fibers Products, 3M Center-Building 207-1W-11, St. Paul, MN 55144-1000.
13. John R, and Rigling B. Effect of height to width ratio on K and CMOD solutions for a single edge cracked geometry with clamped specimen ends. *Eng Frac Mech* 1997;60 (2): 147-56.
14. Hartman GA, Buchanan DJ. Methodologies for thermal and mechanical testing of TMC materials. In: Characterization of fibre reinforced titanium matrix composites. 77th Meeting of the AGARD Structures and Materials Panel, AGARD Report 796, Bordeaux, France, 27-28 September 1993.
15. Hartman DA, Russ SM. Techniques for mechanical and thermal testing of Ti3Al/SCS-6 metal matrix composites. In: Johnson WS, editor. Metal matrix composites: testing, analysis, and failure modes, ASTM STP 1032, American Society for Testing and Materials, Philadelphia, PA, 1989.

Figure Captions

Figure 1. Nextel610/AS composite polished cross section optical micrograph.

Figure 2. Schematic of (a) single edge notched specimen geometry, $W = 12.6$ mm at 23°C , 25.4 mm at 950°C , $B = 2.9$ mm and $H/W = 4$. (b) Strain gage locations for edge notched fracture tests. The lines within the gages indicate the direction of strain measurement.

Figure 3. Schematic of the ultrasonic C-scan set-up (a) reflector plate scanning technique (b) equipment schematic.

Figure 4. Typical loading behavior for an edge notched specimen, $W = 12.6$ mm, $a/W = 0.2$. (a) Load-CMOD response (b) load-longitudinal strain ahead of the notch.

Figure 5. Ultrasonic C-scans of edge notched fracture specimens after varying levels of maximum applied load. (a) Pretest condition (b) Pre-peak loading at $\sigma_n = 88$ MPa, (c) Pre-peak loading at $\sigma_n = 140$ MPa, (d) Post-peak loading $\sigma_n, \text{peak} = 150$ MPa.

Figure 6. Schematic edge notched test specimen showing material removed for destructive evaluation of C-scan damage zone.

Figure 7 SEM micrographs of the notch tip region for (a) an untested, as saw-cut, edge notched specimen, (b) after an applied net section stress $\sigma_n = 88$ MPa, (c) after $\sigma_n = 140$ MPa (d) after $\sigma_n, \text{peak} = 150$ MPa.

Figure 8. Higher magnification micrographs of post peak fracture specimen (Fig. 7(d), $\sigma_n = 140$ MPa) (a) cross-section view of notch tip region (b) higher magnification of selected region on left with 0° fiber breaks.

Figure 9. Typical load-CMOD response for an edge notched specimen, $W = 25.4$ mm, $a/W = 0.2$, 950°C .

Figure 10. (a) C-scan of entire gage section, and (b) optical micrograph of the edge notched specimen after reaching the peak load. $W = 25.4$ mm, $a_0/W = 0.2$, 950°C .

Figure 11. Polished cross section of the unfailed edge notched specimen, tested at 950°C . Cross section 0.5 mm ahead of the notch tip.

Figure 12. Polished cross section 14 mm ahead of the notch tip, 950°C .

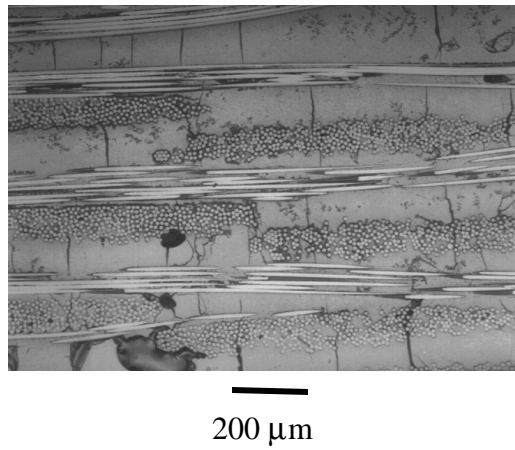


Figure 1. Nextel610/AS composite polished cross section optical micrograph.

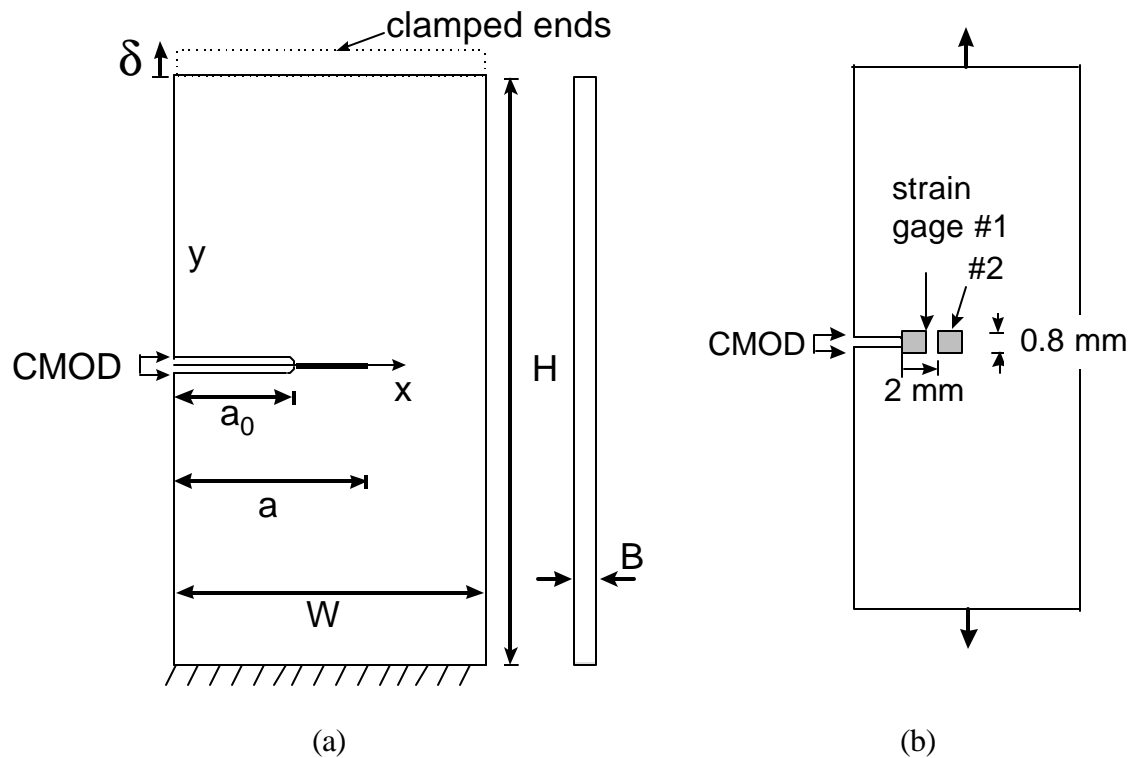
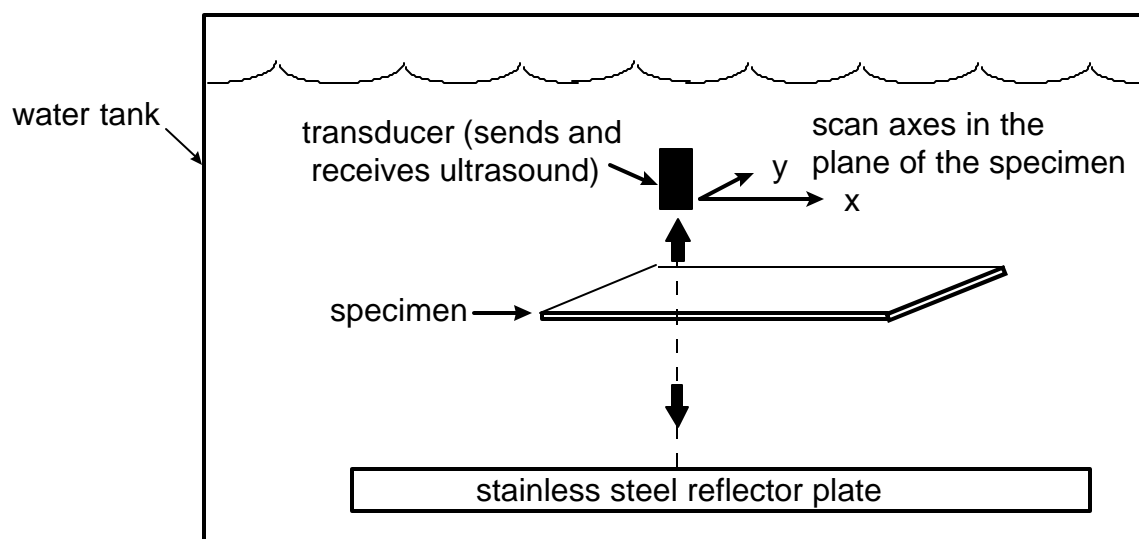
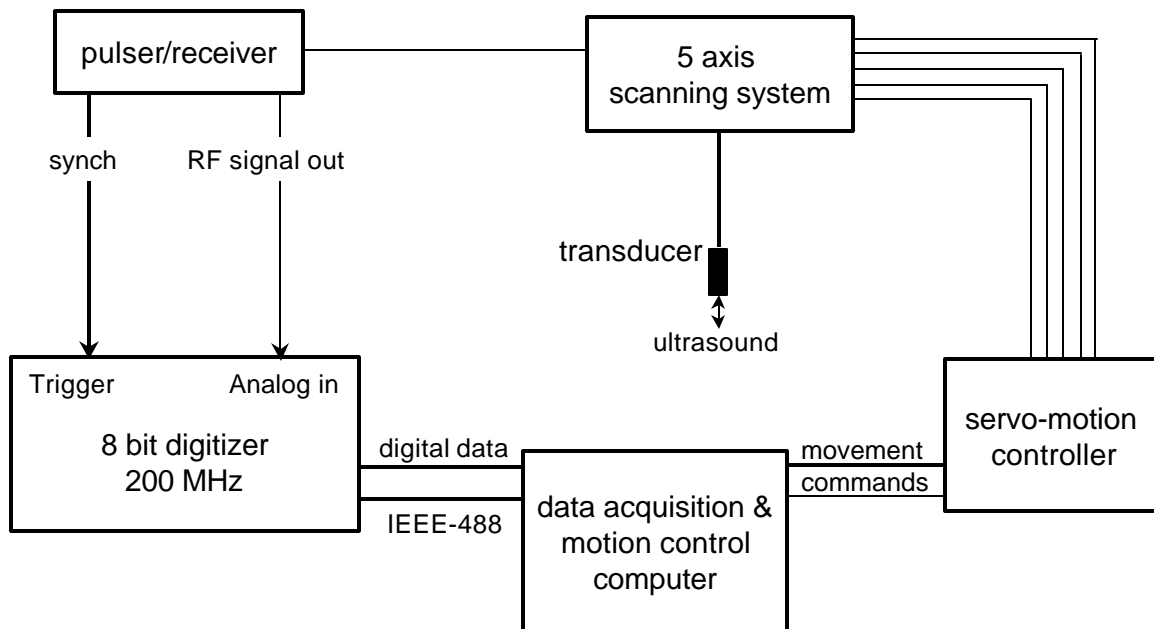


Figure 2. Schematic of (a) single edge notched specimen geometry, $W = 12.6$ mm at 23°C , 25.4 mm at 950°C , $B = 2.9$ mm and $H/W = 4$. (b) Strain gage locations for edge notched fracture tests. The lines within the gages indicate the direction of strain measurement.

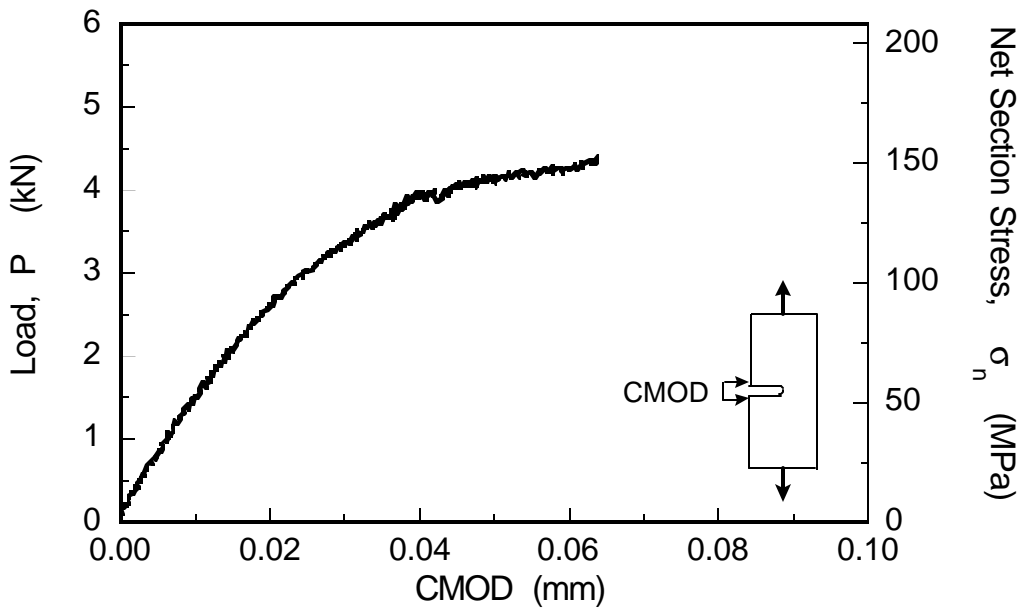


(a)

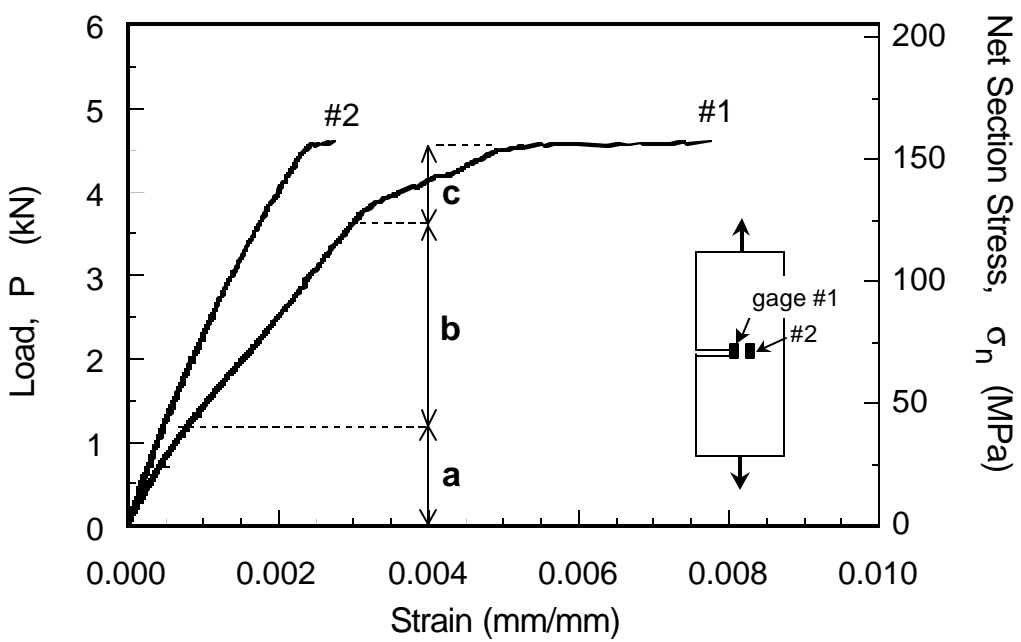


(b)

Figure 3 Schematic of the ultrasonic C-scan set-up (a) reflector plate scanning technique (b) equipment schematic



(a)



(b)

Figure 4 Typical loading behavior for an edge notched specimen, $W = 12.6$ mm, $a/W = 0.2$. (a) Load-CMOD response (b) load-longitudinal strain ahead of the notch.

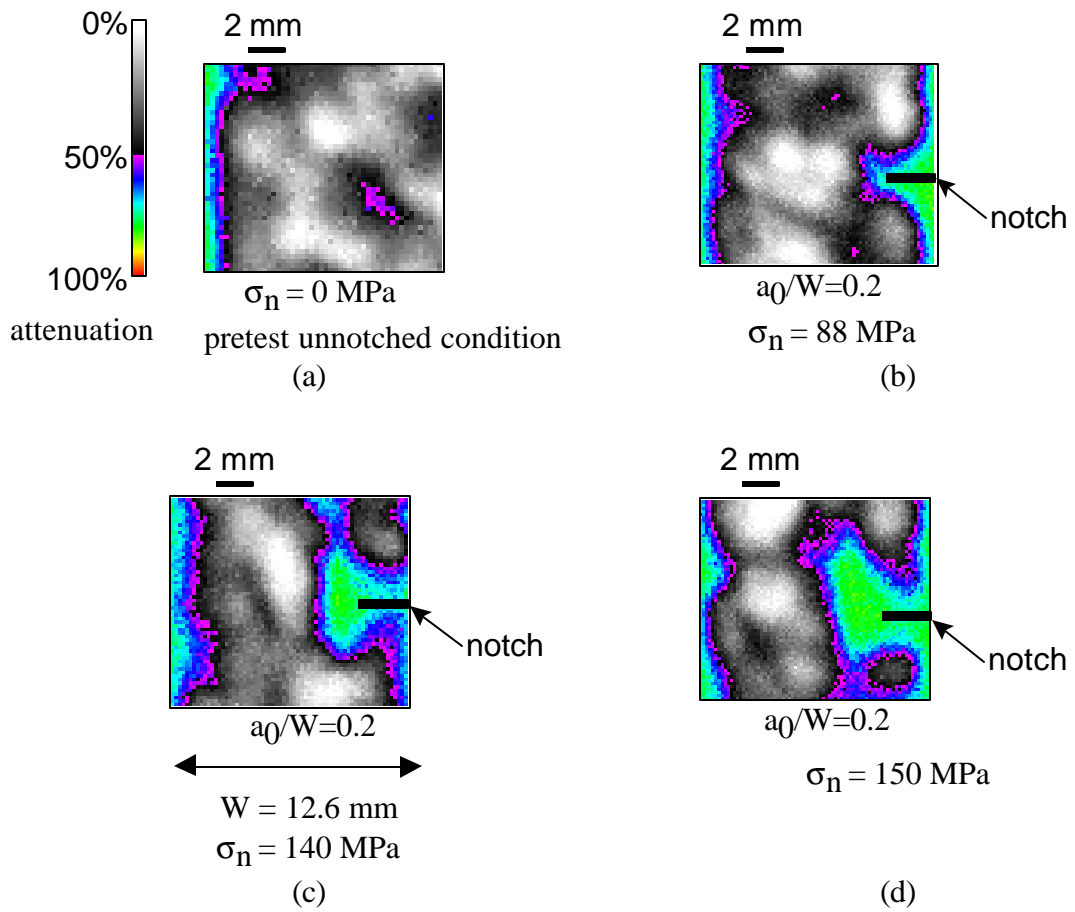


Figure 5. Ultrasonic C-scans of edge notched fracture specimens after varying levels of maximum applied load. (a) Pretest condition (b) Pre-peak loading at $\sigma_n = 88 \text{ MPa}$, (c) Pre-peak loading at $\sigma_n = 140 \text{ MPa}$, (d) Post-peak loading $\sigma_n, \text{peak} = 150 \text{ MPa}$.

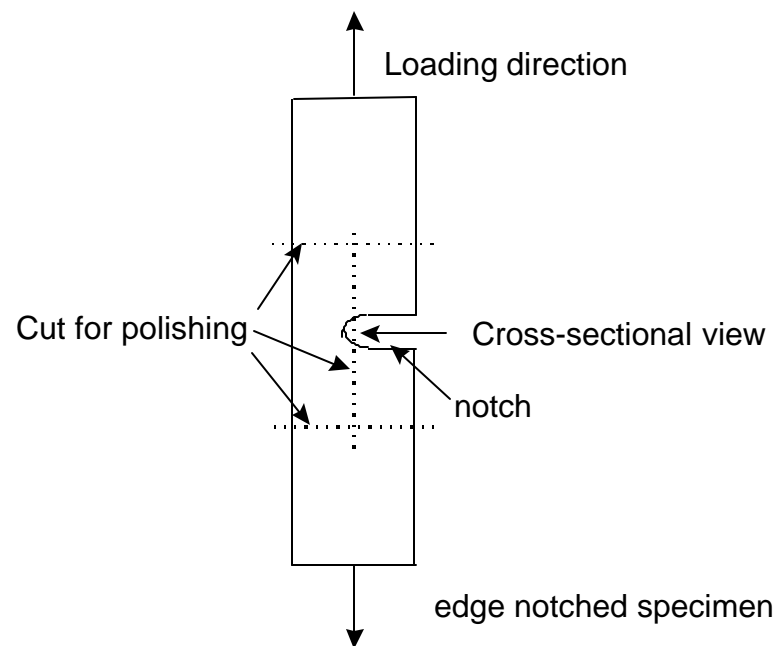


Figure 6. Schematic edge notched test specimen showing material removed for destructive evaluation of C-scan damage zone.

specimen thickness = B

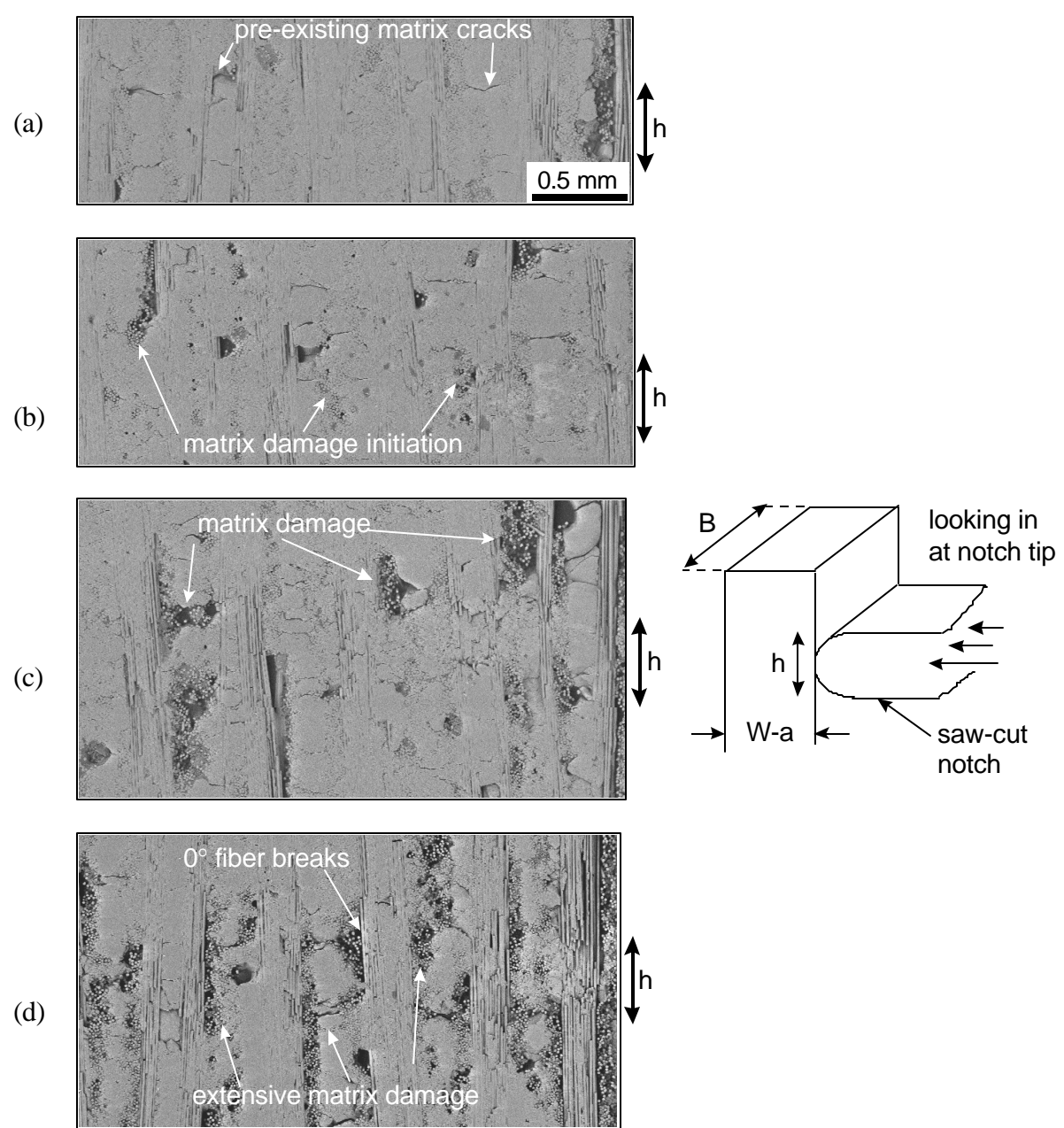


Figure 7 SEM micrographs of the notch tip region for (a) an untested, as saw-cut, edge notched specimen, (b) after an applied net section stress $\sigma_n = 88$ MPa, (c) after $\sigma_n = 140$ MPa (d) after σ_n , peak = 150 MPa.

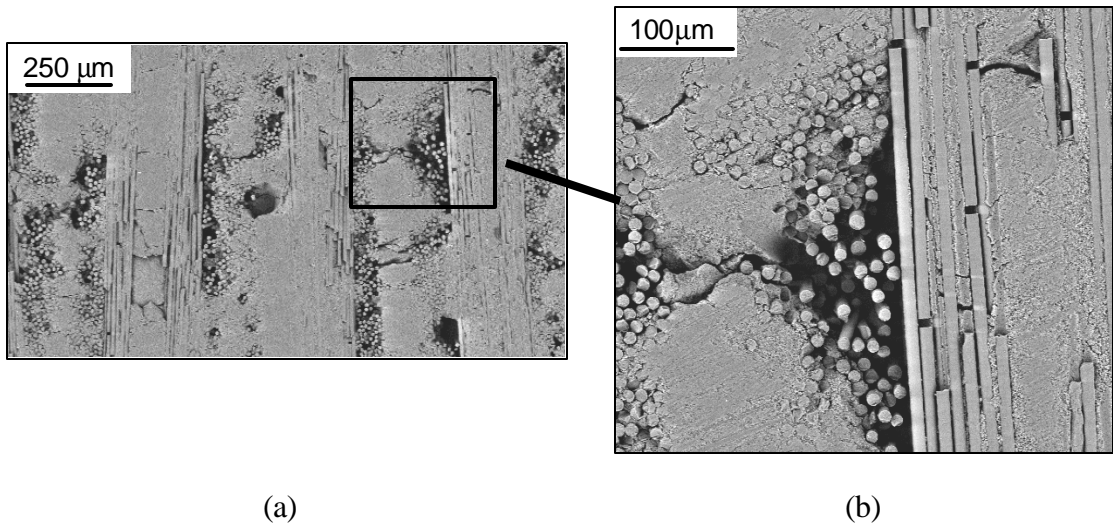


Figure 8. Higher magnification micrographs of post peak fracture specimen (Fig. 7(d), $\sigma_n = 150$ MPa) (a) cross-section view of notch tip region (b) higher magnification of selected region on left with 0° fiber breaks.

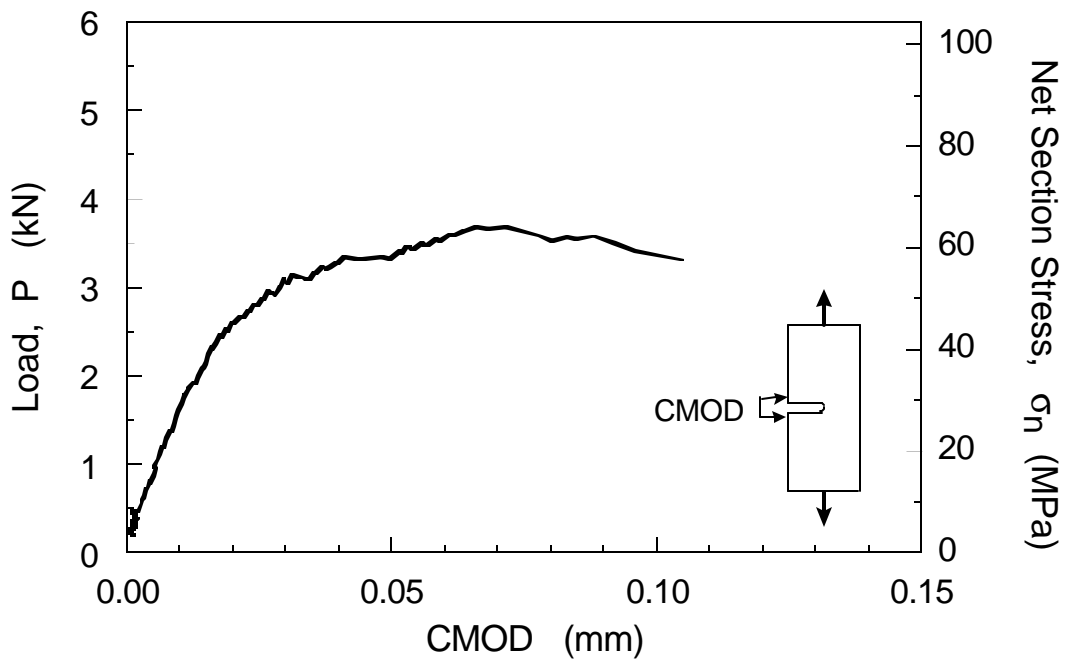


Figure 9. Typical load-CMOD response for an edge notched specimen, $W = 25.4$ mm, $a/W = 0.2$, 950°C .

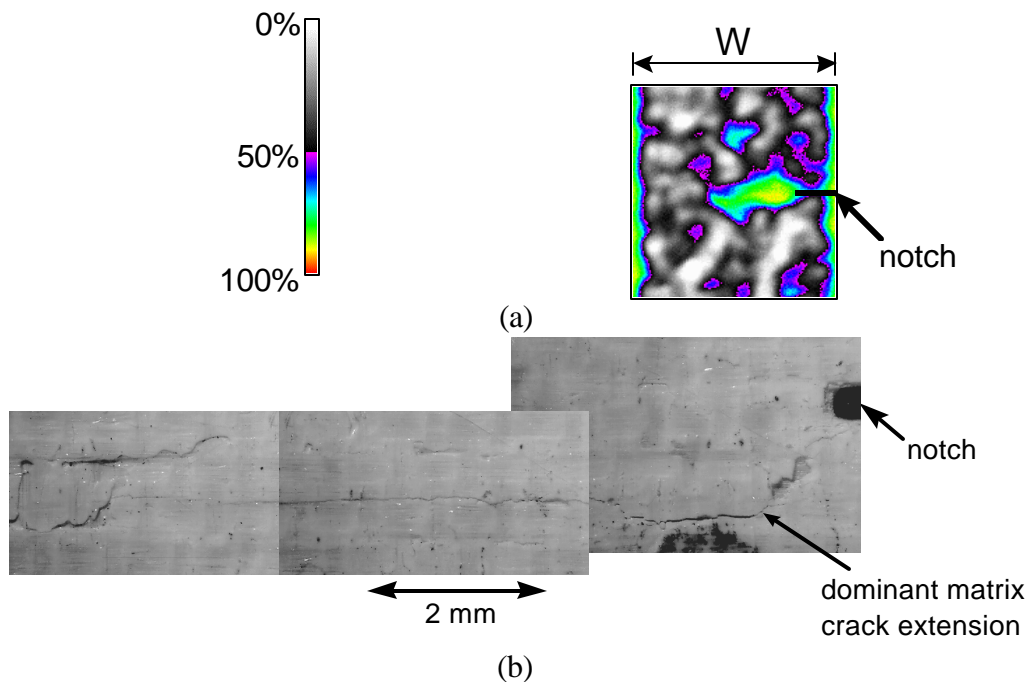


Figure 10. (a) C-scan of entire gage section, and (b) optical micrograph of the edge notched specimen after reaching the peak load. $W = 25.4$ mm, $a_0/W = 0.2$, 950°C .

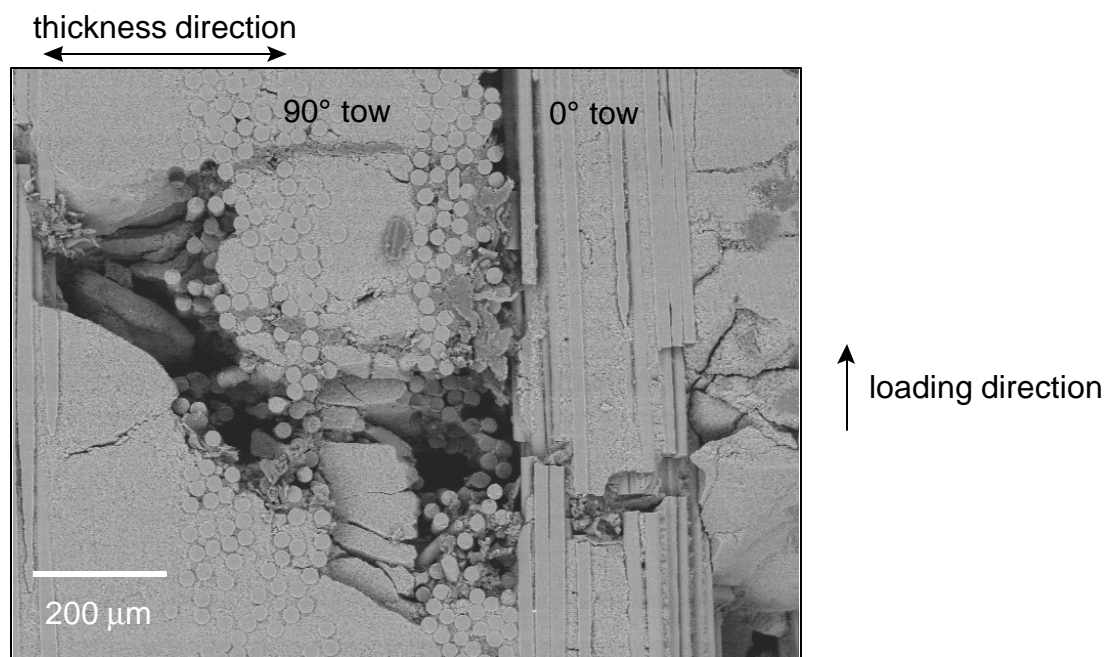


Figure 11. Polished cross section of the unloaded edge notched specimen, tested at 950°C . Cross section 0.5 mm ahead of the notch tip.

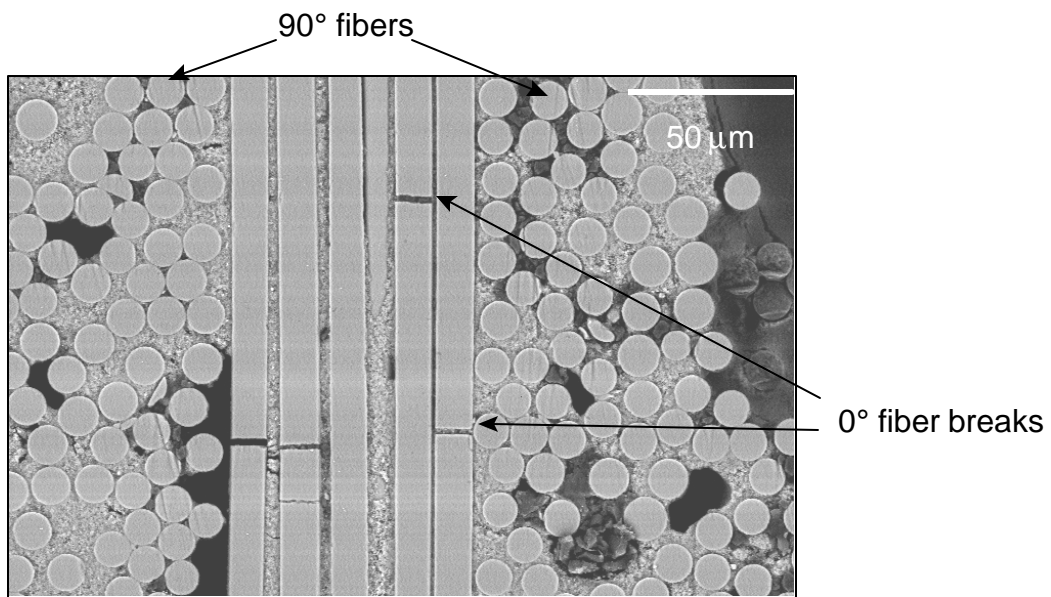


Figure 12. Polished cross section 14 mm ahead of the notch tip, 950°C.

Characterization of Fretting Fatigue Crack Nucleation Life of Ti-6Al-4V in a Flat-on-Flat Contact

Mrs. Alisha Hutson* and Mr. Dave Stubbs

Advanced Materials Characterization Group, Structural Integrity Division
University of Dayton Research Institute, Dayton, OH 45469-0128, USA.

Dr. Ted Nicholas

Air Force Research Laboratory (AFRL/MLLN), Materials & Manufacturing Directorate; Wright-Patterson Air Force Base, OH 45433-7817, USA.

INTRODUCTION

Fretting fatigue damage is caused by localized recurring relative motion in the contact region between two components under load, and can result in premature crack initiation and failure. Such damage has been indicated as the cause of many premature disk and blade failures in turbine engines and, as a result, has been the focus of numerous studies over the years [1-9]. These studies commonly incorporate idealized geometries for ease of testing and comparison of results with available closed form analytical solutions for stress distributions. Neither the simplified geometries nor the analytical models produced from the closed form stress solutions are directly applicable to real hardware. The types of contacts and loading conditions used in experiments are rarely seen in service components, and the analytical models used are generally based on the assumption of contact with a half-space. Overall, good agreement between analytical models and experiments is achieved, even though the specimens used in the experiments are not representative of a half-space. However, only limited progress has been made in the development of accurate life prediction models for complex components based on the results of these efforts [10].

The following summarizes work to date on two separate studies: an evaluation of fretting fatigue damage on fatigue life, and the investigation of the effect of specimen thickness on fretting fatigue behavior. Both studies are designed to answer questions specific to the dovetail blade attachment geometry found in gas turbine engines. The former study is designed to evaluate fretting fatigue crack nucleation mechanisms. The latter study is designed to provide experimental evidence to evaluate the applicability of analytical models based on stress distributions within a half-space to hardware that is not representative of a half-space. In addition to acquiring data on fatigue life and fatigue limits, SEM inspection of fretted and fracture surfaces was used to qualitatively analyze fretting damage and to evaluate failure mechanisms.

TESTING APPARATUS

The fretting fatigue apparatus used in both studies was designed to closely simulate the primary loading conditions under which fretting damage occurs in turbine engine blade attachment areas. A typical fretting fatigue apparatus, as shown in Figure 1, transfers only part of the load applied to the specimen through the fretting pads. The remainder of the load is transferred to the specimen beyond the fretting pads. This arrangement permits the investigation of the lower range of shear stresses, and facilitates residual strength testing after the application of a predetermined amount of fretting damage. The apparatus employed for the present studies, which will be referred to as the AFRL apparatus, allows all of the load applied to the specimen to be transferred through the fretting pads into the grip, leaving the ends of the specimen stress free, as would be expected in the extremities of the dovetail section of a fan blade. Such an arrangement ensures no gross slip for valid tests, and allows for the investigation of a higher range of average shear stresses. In the standard fretting fatigue apparatus, the average shear

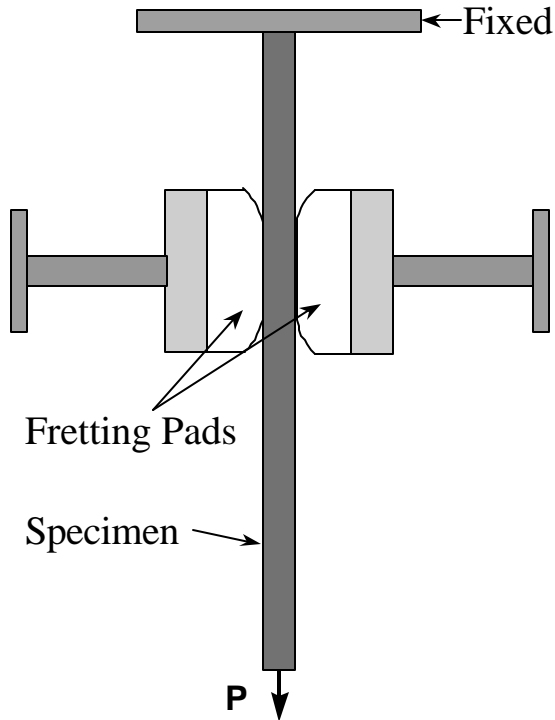


Figure 1. Schematic of a standard fretting fatigue apparatus.

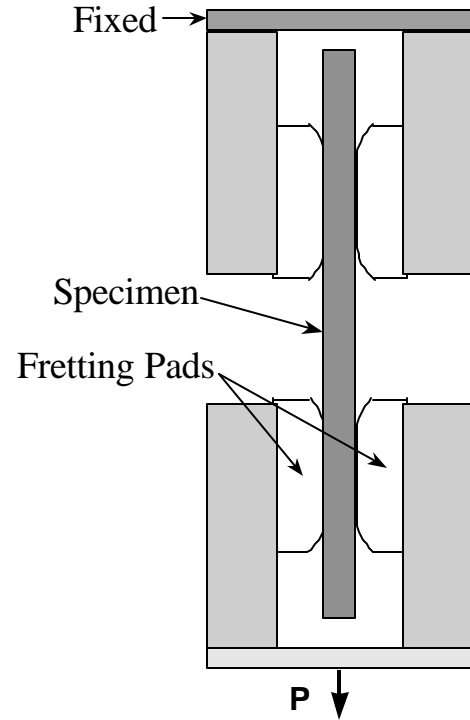


Figure 2. Schematic of the AFRL fretting fatigue gripping system.

stress may be modified by changing the applied normal load, the pad geometry, the location and/or compliance of the fixture holding the pad, or the load applied to the specimen. In the AFRL apparatus the average shear stress may be changed through changes in the specimen geometry or the applied specimen load. Changing the normal load in the AFRL apparatus may change the shear stress distribution, but not the average since the entire specimen load is already being transferred through the pads.

In the studies presented below, variations were made in normal load (N), contact radius (R), contact length (l), and specimen thickness (t). Figure 3 indicates the nomenclature used throughout both studies in reference to each of these parameters. In each test, the goal was to evaluate a fatigue limit stress for ten million cycles through the use of the step loading technique being used throughout the High Cycle Fatigue program. Normal loads were imposed with instrumented bolts. Axial loads were applied via an electromagnetic shaker system. Fretting pads were replaced for each test to facilitate control of surface conditions. Since the test configuration employs identical gripping at both ends of the specimen, two nominally identical fretting fatigue tests per specimen were produced. Additional details on the test apparatus can be found in [11].

All tests were conducted at constant frequency of either 300 or 400 Hz in lab air at room temperature. The PRDA V plate stock, which refers to the forged AMS4928 microstructure with TE01 heat treatment that has been used for the bulk of the High Cycle Fatigue Program testing, was used throughout the two current studies. All specimens and fretting pads were low stress ground to an # 8 surface finish.

EFFECT OF FRETTING FATIGUE DAMAGE ON FATIGUE STRENGTH

The purposes of this study were to evaluate the effect of prior fretting fatigue damage on fatigue strength, to analyze fretting fatigue damage using optical and SEM techniques, and to identify fretting fatigue failure mechanisms. To achieve these goals four series of tests were run, each at varying percentages of total life. Two pad lengths, 12.7 and 25.4 mm, were incorporated with an intermediate normal load of 26 kN to produce the upper and lower limits of normal stress typically observed in the dovetail blade attachment. A contact radius of 3.2 mm and a stress ratio of $R=0.5$ were selected because they more closely represent the engine hardware in question.

First, nine 100%-of-life tests were run using the step load technique, to produce an average fatigue strength with information on the repeatability of each condition. Next, the 1% and 10%-of-life specimens were run with three tests for each condition. In these tests, each specimen was run at the average fatigue strength determined for the respective geometry conditions in the 100%-of-life tests, for 100,000 and 1 million cycles, respectively (which is 1% & 10% of the estimated 10 million cycle fatigue life). Then each test was stopped after the designated number of cycles, and inspected in the SEM. Finally, tests were conducted to an undesignated number of cycles using a shear wave ultrasonic technique to detect fretting fatigue cracks *in situ*. These tests will be referred to as N_{det} . When cracks were detected, the test was stopped, the sample removed, inspected, & subjected to heat tinting. Then the sample was replaced against the same set of pads in the original position, and run to failure, resulting in a measure of the fatigue crack nucleation & propagation lives as well as their respective percentages of the total specimen life.

The results of the 100%-of-life tests are shown in Figure 4, along with the “effect of thickness” data. The data of immediate interest is the $R=0.5$ data for the thin samples. At 140 MPa average normal stress, the average fatigue strength is ~350

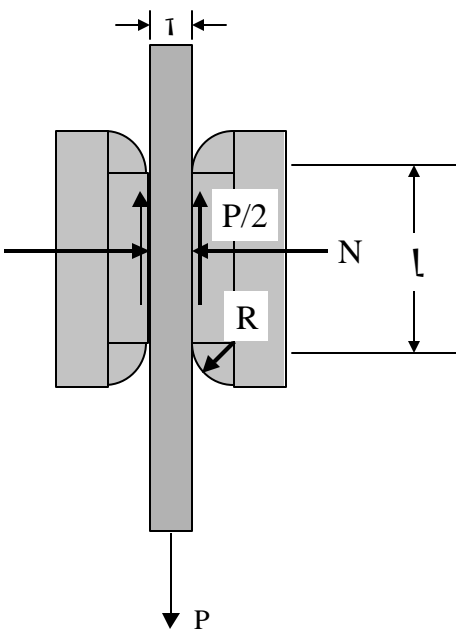


Figure 3. AFRL test nomenclature.

estimated 10 million cycle fatigue life). Then each test was stopped after the designated number of cycles, and inspected in the SEM. Finally, tests were conducted to an undesignated number of cycles

	large pad	small pad
Cycles of Fretting	140 MPa Normal stress	420 MPa Normal stress
100,000	3 tests	3 tests
1,000,000	3 tests	3 tests
N	2 tests	2 tests
Step load to failure	3 tests	6 tests

Table 1. Test matrix for effect of fatigue damage on fatigue strength.

MPa; at 420 MPa, the average fatigue strength is ~ 260 MPa. Note that the thin sample data for $R = 0.1$, and for $R = 0.5$ that isn't at either 140 MPa or 420 MPa is from “effect of thickness” matrix to be discussed later. Overall, the $R = 0.5$ data in Figure 4 indicate some trend with applied normal stress. However, the scatter indicated by the repeated tests at 140 MPa & 420 MPa makes it difficult to draw firm conclusions. The 1% & 10%-of-life tests were run at a constant axial stress of 350 MPa for the 140 MPa normal stress, and 260 MPa for the 420 MPa normal stress. Based on the data above, specimens run at these stresses with the respective normal stresses should have lives on the order of 10 million cycles. Thus, a sample run to 100,000 cycles is at 1% of life, and a sample run to 1 million cycles is at 10% of life. The specimens exposed to these fractions of life will be subjected to residual strength fatigue testing, to quantify any reduction in fatigue strength brought on by damage accumulation.

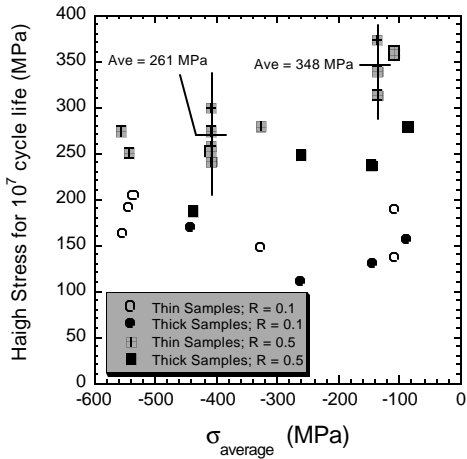


Figure 4. 100%-of-life test results, including some “effect of thickness” for comparison.

crack nucleation in the specimen. An example of such a signal is shown in Figure 6. The peak at $33\mu\text{s}$ is the reflection off the edge of contact from the fretting pad that is present when the normal load is applied. Since cracks are identified by changes in the overall ultrasonic waveform, the presence of such peaks was not relevant. Specific changes in peaks at or near the edge of contact in this test, such as those indicated

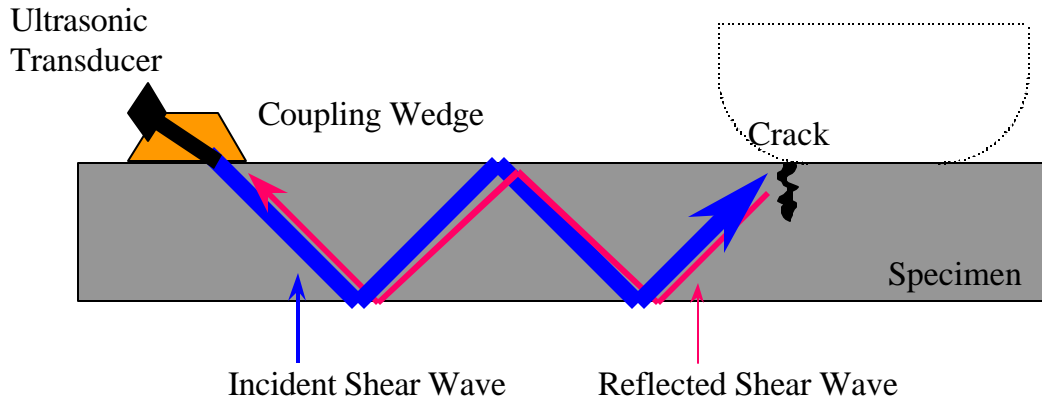


Figure 5. Ultrasonic crack detection using shear waves.

by the solid line in Figure 6 between 28 and $29\mu\text{s}$, and at 30 , 31 , and $33\mu\text{s}$, were sufficient to identify potential crack nucleation.

Cracks were successfully detected on both of the samples tested under 420 MPa normal stress. The picture shown in Figure 7 documents the primary crack observed when the sample was inspected in the SEM. This crack was ~ 2.3 mm long at the time of inspection and extends far beyond the left edge of the photo. The picture in Figure 8 shows the corresponding fracture surface after the sample was failed. The dark region of the fracture surface indicates the crack front at the time the test was stopped at $7,020,000$ cycles. (The dark region around the fracture surface is background only.) Final fracture occurred at $7,350,000$ cycles. Some interesting features of this specimen are present on the fracture surface. First, the 2.3mm long crack observed on the surface only penetrates the specimen $\sim 800 \mu\text{m}$ at its maximum. Second, the primary crack nucleation site seems to be less than $500 \mu\text{m}$ from the sample edge. A closer inspection along the region delineating the observed 2.3 mm crack would probably reveal many subsequent nucleation sites produced by the influence of local stresses, as has been noted in a previous investigation by the authors [12]. The second test conducted under the 420 MPa normal stress condition was stopped based on ultrasonic waveform changes at $6,125,000$ cycles, at which time a crack 2.6 mm long was identified. Final failure occurred at $6,227,000$ cycles. In both tests more than one crack was

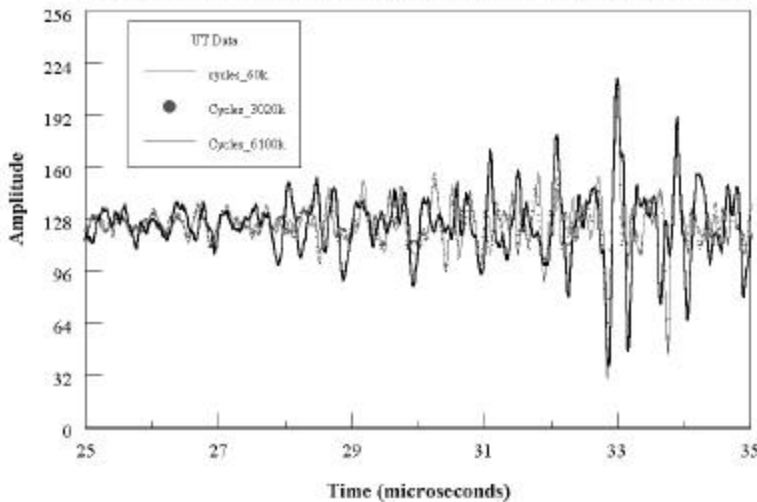


Figure 6. Ultrasonic shear wave detection of fretting fatigue cracks in Ti-6Al-4V.

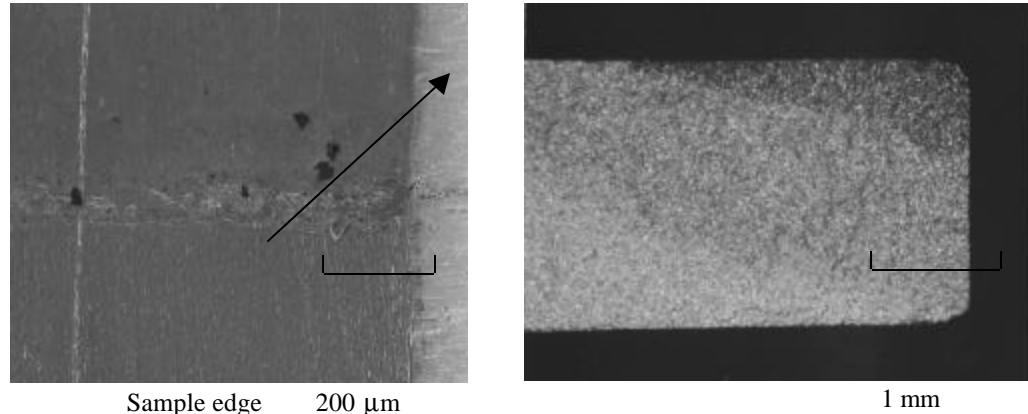


Figure 7. Crack detected using shear waves Figure 8. Fracture surface of a specimen for 420 MPa normal stress. Fatigue loading with successful shear wave crack detection. axis is vertical.

None of the attempts to detect cracks on samples subjected to the 140 MPa normal stress were successful. Overall, nothing was observed in the shear wave signal, which was acquired digitally every 500,000 cycles, over the life of the specimen. Then within ~200,000 cycles of the last observation, the specimen would nucleate cracks and fail. The total cycles to failure for the two tests were 14,630,000 cycles and 3,100,000 cycles. Thus, the specimens subjected to the higher normal stress presented cracking much earlier in the total specimen life and showed less scatter in the number of cycles to failure than the specimens subjected to the lower normal stress. In the samples subjected to high normal stress more than 90% of life was spent in crack propagation compared to less than 4% in samples subjected to lower normal stress.

A comparison of the fretting features observed on the surface at various percentages of life for 140 MPa normal stress is presented in Figures 9, 10, and 11. No photos were taken at the 1%-of-life damage level because the damage couldn't be located on any of the three specimens tested. Thus, Figure 9 represents damage at the 10%-of-life level, Figure 10 represents damage at the N_{det} damage level, and Figure 11 represents damage on the unfailed end of a 100%-of-life sample. All of the photos taken of samples at the 140 MPa normal stress were done so with the SEM back-scatter option, which enhances differences in microstructure and chemical composition. Thus, regions with elevated oxygen levels, such as wear products appear darker than the surrounding material. In all cases at the lower normal stress no

identified upon inspection. The first specimen contained two additional cracks (~900 and 350 μm) on the same end of the specimen as the dominant crack, but on the opposite side. The second contained three additional cracks (~500, 340, and 250 μm), of which the largest was located in the opposite end of the specimen from the dominant crack.

secondary cracking was observed, except for tiny ($<20 \mu\text{m}$) cracks that were contained within the wear debris.

Damage levels at the 420 MPa normal stress were more pronounced and occurred much earlier in life. Figure 12 represents damage at the 1%-of-life level, Figure 13 represents damage at the 10%-of-life level, and Figure 14 represents damage on the unfailed end of a 100%-of-life sample. Damage at 1%-of-life was clearly visible without use of the back-scatter option. At 10% of life, cracks on the order of 1 mm characterized all of the samples inspected. By the time



Figure 9. 10%-of-life damage for 140 MPa normal stress. Fatigue loading axis is vertical.

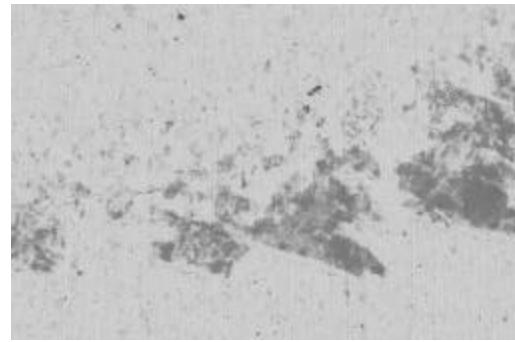


Figure 10. N_{det} damage for 140 MPa normal stress. ($N = 14,630,000$ cycles)

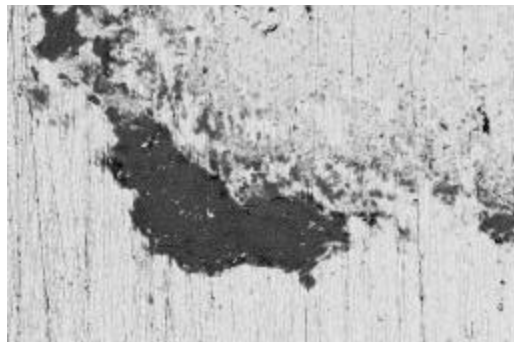


Figure 11. 100%-of-life damage for 140 MPa normal stress. Fatigue loading axis is vertical. ($N_f \sim 144$ million cycles.)

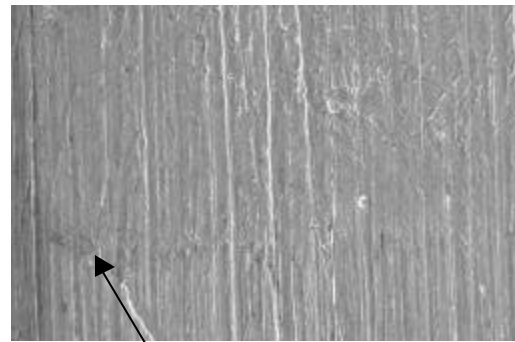


Figure 12. 1%-of-life damage for 420 MPa normal stress.



Figure 13. 10%-of-life damage for 420 MPa normal stress. (~1.1 mm crack)

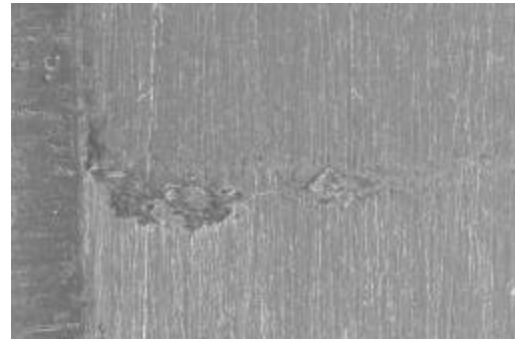


Figure 14. 100%-of-life damage for 420 MPa normal stress. (380 mm crack)

cracks of sufficient size were present to be detected with the shear wave ultrasonic equipment, multiple cracks were present ranging from 150 μm to 2.6 mm. In one case, cracks were present in both grips simultaneously. In all N_{det} cases, more than one crack was present on the end with the largest crack. (See Figure 7 for representative damage) The unfailed ends of the 100%-of-life samples were often characterized by cracks of significant size and considerable wear damage, which seems to come after the crack nucleates and not before. The comparison of the damage resulting from the two applied normal stresses seems to indicate that a more highly stressed contact might lend itself better to damage tolerant design, since a much larger percentage of total life is spent propagating damage that is detectable by current NDE technology.

One sample, on which secondary cracking was observed, was sectioned to see what crack orientation occurred compared to what has been observed in other fretting geometries from other test rigs. On the specimen shown in Figure 15, a 1 mm crack was sectioned to $\sim 600 \mu\text{m}$ from the specimen edge. The depth of the crack at the section location was $\sim 500 \mu\text{m}$. As shown in Figure 16, cracks nucleate at 45 degrees to the loading axis, as reported by other researchers [8], and within 5-10 μm , turn perpendicular to the loading axis. Both propagating and non-propagating cracks are observed. In this case, very little material was removed from this part of the specimen face during the crack nucleation process.

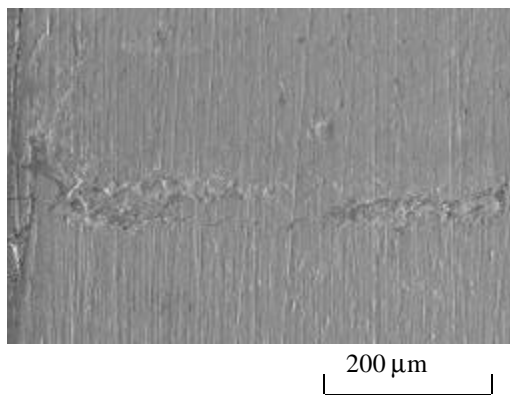


Figure 15. Secondary fretting crack nucleated at 420 MPa normal stress.

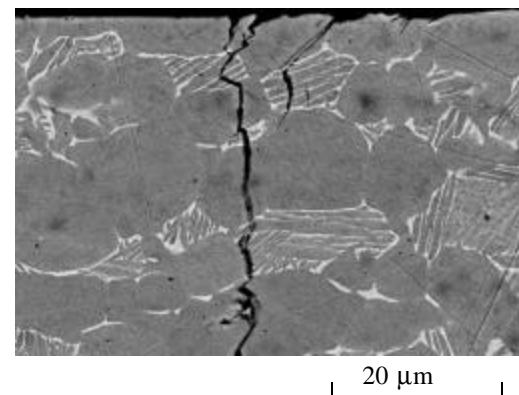


Figure 16. Cross-section of secondary fretting crack $\sim 600 \mu\text{m}$ from the specimen edge.

EFFECT OF SPECIMEN THICKNESS ON FRETTING FATIGUE BEHAVIOR

Normal Load	Contact Area			
	65 mm^2	120 mm^2	190 mm^2	245 mm^2
35 kN	t = 2 & t = 4 R = 0.1	t = 2 R = 0.1	t = 4 R = 0.1	t = 2 R = 0.1
	t = 2 & t = 4 R = 0.5	t = 2 R = 0.5	t = 2 & t = 4 R = 0.5	t = 2 R = 0.5
	t = 2 & t = 4 R = 0.1	t = 2 & t = 4 R = 0.1	t = 2 & t = 4 R = 0.1	t = 2 & t = 4 R = 0.1
	t = 2 & t = 4 R = 0.5	t = 2 R = 0.5	t = 2 & t = 4 R = 0.5	t = 2 R = 0.5
21 kN	t = 2 & t = 4 R = 0.1	t = 2 & t = 4 R = 0.1	t = 2 & t = 4 R = 0.1	t = 2 & t = 4 R = 0.1
	t = 2 & t = 4 R = 0.5	t = 2 R = 0.5	t = 2 & t = 4 R = 0.5	t = 2 R = 0.5

Table 2. "Effect of thickness" test matrix.

The purpose of this part of the investigation was to evaluate the effects of variation in average shear and normal stress on the fretting fatigue limit stress. Two each of the following parameters were selected for comparison: pad length (12.7 and 25.4 mm), contact radius (3.4 and 0.5 mm), which produced four different contact areas. Additionally two different normal loads (21 and 35 kN) were used. A total of eight normal stresses resulted, as shown in Table 2. Additionally, three values of specimen thickness (1, 2, and 4 mm) were selected

for the test matrix. By varying specimen thickness for a given contact geometry, the applied shear load and therefore, the shear stress is varied for a nominally constant value of applied stress. Specimen resonance problems has prevented any successful tests on the 1 mm thick samples. In addition, there was not sufficient time to complete tests for all of the thicker samples. Tests were conducted at stress ratios of either 0.1 or 0.5, as shown in the table. The information in Table 2 represents test conditions which were completed for each specimen thickness.

Results for this study, presented previously in Figure 4, are replotted in Figures 17, and 18. Figure 17 shows the fretting fatigue limit stresses (for 10^7 cycles) normalized with the undamaged fatigue strength (600 MPa for R=0.1, 825 MPa for R=0.5) as a function of the average applied normal stress. In the case of R=0.1, no effect of thickness is noted, and the overall trend with normal stress is relatively flat. For the case of R=0.5, the thicker samples show a slightly lower fatigue strength than the corresponding thin samples, but the difference is not statistically significant. All cases show a 55% to 80% reduction in fatigue strength compared with the undamaged fatigue strength. The same general conclusion (no effect of thickness; dramatic reduction in fatigue strength) may be reached from inspection of the plot in Figure 18, where the same data is plotted against the average shear stress, which is linearly proportional to the fatigue limit stress. Figure 4 shows the data from Figure 17 on an expanded scale with the actual limit stresses on the vertical axis.

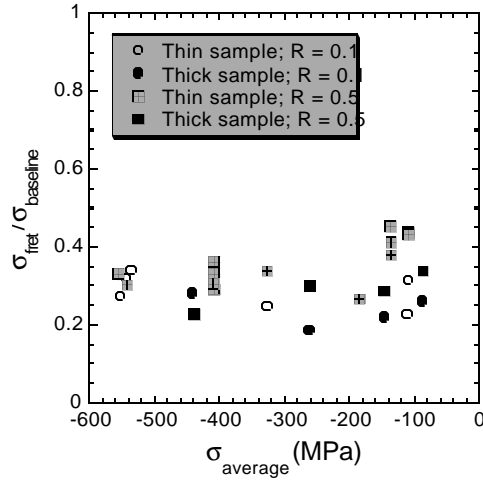


Figure 17. Comparison of normalized limit stresses for thick and thin samples vs. average applied normal stress.

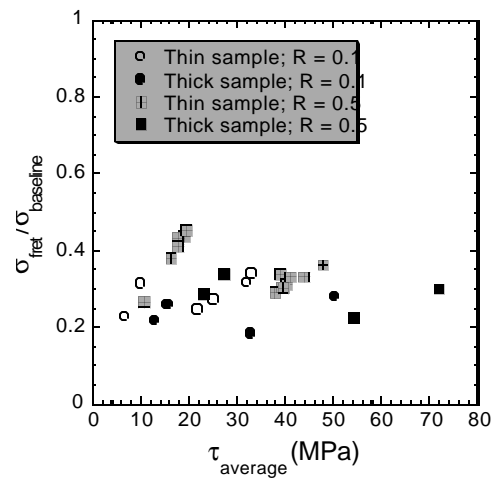


Figure 18. Normalized limit stresses for thick and thin samples vs. average applied shear stress.

While significant differences in observed cracking behavior were noted earlier between specimens subjected to 140 MPa & 420 MPa normal stress, the test data from Figures 4 and 17 do not provide an explanation for these differences. The slight trend observed with variations in normal stress could provide some indication of the different mechanisms responsible for the variations in mechanical behavior, which may become more evident through comparison of average applied shear stresses. Photos presented in Figures 19 and 20 were taken of the unfailed end of 100%-of-life samples at the 140 MPa normal stress for both the 2 and 4 mm thick specimens. The average applied shear stress was ~ 20 MPa, and no secondary cracking was observed. By comparison, Figures 21 and 22 contain similar photos taken for specimens subjected to a normal stress of ~500 MPa. The shear stresses ranged from 30 to 50 MPa, and significant secondary cracking was observed. Again, the marked difference in cracking behavior between low and high applied normal stress is observed; however, the reduction is strength relative to specimens subjected to uniaxial fatigue is nearly the same for all four conditions, ranging between 55% and 80%. Thus, although the cracking mode is influenced by stress level to a large degree, average applied shear stress does not appear to provide an explanation for the differences in mechanical behavior.

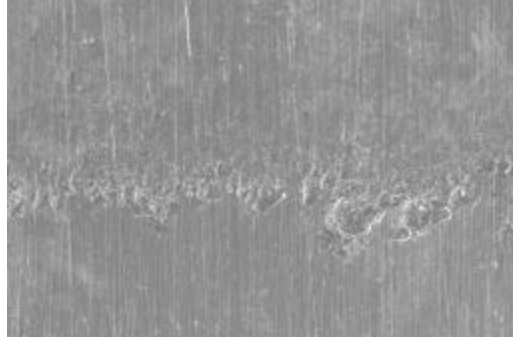


Figure 19. 2mm sample at 100%-of-life for 140 MPa normal stress. Fatigue loading axis is vertical.

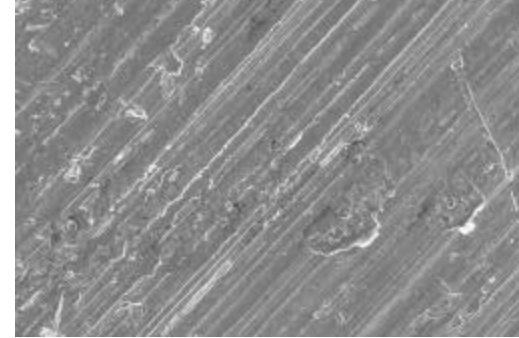


Figure 20. 4mm sample at 100%-of-life for 140 MPa normal stress. Fatigue loading axis is vertical.

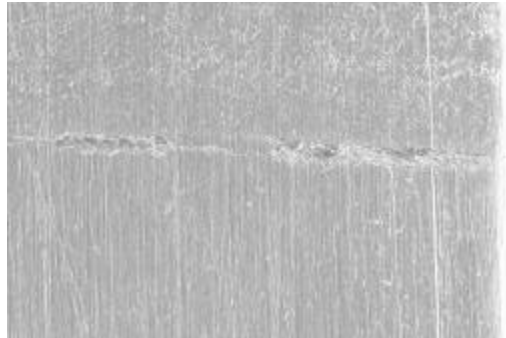


Figure 21. 2mm sample at 100%-of-life for 420 MPa normal stress. Fatigue loading axis is vertical.

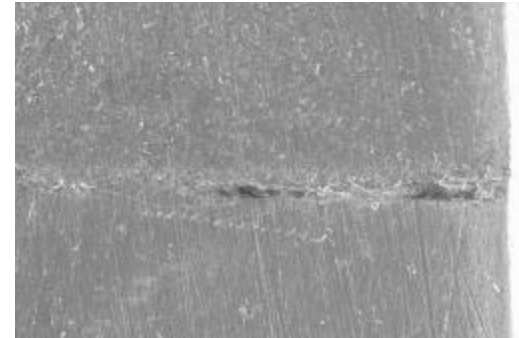


Figure 22. 4mm sample at 100%-of-life for 420 MPa normal stress. Fatigue loading axis is vertical.

SUMMARY

- Crack detection using Shear Wave is possible for 420 MPa, but not for 140 MPa normal stress.
- Different cracking behavior was observed for the different stress levels, but the debit in fatigue limit stress is insensitive to magnitudes of (average) shear or normal stresses.
- Crack nucleation behavior in the AFRL fretting fatigue apparatus is similar to other geometries.
- Fretting fatigue results in severe (55-80%) debit in 10^7 cycle fatigue limit stress under range of conditions investigated.

ACKNOWLEDGEMENTS

This research was conducted at the Materials Directorate, Air Force Research Laboratory (AFRL/MLLN), Wright-Patterson Air Force Base, OH, USA. A. Hutson was supported under on-site contract number F33615-98-C-5214.

REFERENCES

1. Ruiz, C., Boddington, P. H. B., and Chen, K. C., "An Investigation of Fatigue and Fretting in a Dovetail Joint," *Experimental Mechanics*, vol. 24, 1984, pp. 208-217.
2. Bryggman, U. and Söderberg, S., "Contact Conditions and Surface Degradation Mechanisms in Low Amplitude Fretting", *Wear*, vol. 125, 1988, pp. 39-52.
3. Del Puglia, A., Pratesi, F., and Zonfrillo, G., "Experimental Procedure and Parameters Involved in Fretting Fatigue Tests," *Fretting Fatigue, ESIS 18*, R.B. Waterhouse and T.C. Lindley, Eds., Mechanical Engineering Publications, London, 1994, pp. 219-238.
4. Fellows, L. J., Nowell, D., and Hills, D. A., "On the Initiation of Fretting Fatigue Cracks," *Wear*, vol. 205, 1996, pp. 120-129.
5. Fourny, S., Kapsa, P., and Vincent, L., "Quantification of Fretting Damage," *Wear*, vol. 200, 1996, pp. 186-205.
6. Vingsbo, O. and Schon, J., "Gross Slip Criteria in Fretting," *Wear*, vol. 162-164, 1993, pp. 347-356.
7. Zhou, Z. R. and Vincent, L., "Mixed Fretting Regime," *Wear*, vol. 181-183, 1995, pp. 551-536.
8. Adibnazari, S. and Hoeppner, D.W., "The Role of Normal Pressure in Modeling Fretting Fatigue," *Fretting Fatigue, ESIS 18*, R.B. Waterhouse and T.C. Lindley, Eds., Mechanical Engineering Publications, London, 1994, pp. 125-133.
9. Waterhouse, R.B., "Effect of Material and Surface Conditions on Fretting Fatigue," *Fretting Fatigue, ESIS 18*, R.B. Waterhouse and T.C. Lindley, Eds., Mechanical Engineering Publications, London, 1994, pp. 339-349.
10. Szolwinski, M.P., Harish, G., McVeigh, P.A., and Farris, T.N., "Experimental Study of Fretting Crack Nucleation in Aerospace Alloys with Emphasis on Life Prediction," *Fretting Fatigue: Current Technologies and Practices*, ASTM STP 1367, D.W. Hoeppner, V. Chandrasekaran, and C.B. Elliot, Eds., American Society for Testing and Materials, West Conshohocken, PA, 1999, pp. 267 - 281.
11. Hutson, A. and Nicholas, T., "Fretting Fatigue of Ti-6Al-4V Under Flat-on-Flat Contact", *International Journal of Fatigue*, Vol 21, No 7, pp. 663 – 670, 1999.
12. Hutson, A. and Nicholas, T., "Fretting Fatigue Behavior of Ti-6Al-4V against Ti-6Al-4V under Flat-on-Flat Contact with Blending Radii," *Fretting Fatigue: Current Technologies and Practices*, ASTM STP 1367, D.W. Hoeppner, V. Chandrasekaran, and C.B. Elliot, Eds., American Society for Testing and Materials, West Conshohocken, PA, 1999, pp. 308 - 321.

This page intentionally left blank.

Characterization of FOD Impact Sites on Ti-6Al-4V Simulated Airfoils¹

CAPT. CHRISTINE MARTINEZ¹, MS. JANINE C. BIRKBECK^{2,3}, DR. DANIEL EYLYON³, MR. JOHN J. RUSCHAU², MR. STEVEN R. THOMPSON⁴, MR. W. JOHN PORTER², and DR. THEODORE NICHOLAS⁴

¹Wright-Patterson Air Force Base and a graduate student at the University of Dayton, Graduate Materials Engineering, Dayton OH 45469-0240

²University of Dayton Research Institute, Dayton, Oh 45469

³University of Dayton, Graduate Materials Engineering, Dayton OH 45469-0240

⁴US Air Force Research Laboratory, Materials and Manufacturing Directorate, Wright-Patterson AFB, OH 45433

Abstract

Damage sites in Ti-6Al-4V simulated engine blades subjected to ballistic foreign object impact damage were characterized. Diamond cross-sectioned tension (DCT) axial fatigue samples, with either a 0.381 mm (0.015") or 0.127 mm (0.005") leading-edge (LE) radius, were impacted with 1 mm (0.040") diameter glass spheres at a velocity of 305 m/s (1000 f/s) and at an angle of incidence of either 0° or 30°. Subsequent fatigue testing showed fatigue strength degradation as a result of the edge-damage. Scanning electron microscopy showed a variety of damage features on the fractured notches. The features characterized include the notch depth, material loss at the notch, material shear, material folding over the LE, and embedded glass from the shattered bead. Fracture initiation occurred generally at the deepest section of the notch region. However, the depth of the broken notch alone has no direct effect on the fatigue strength. The amount of material loss at the notch surface also had no apparent effect on the fatigue strength. Neither surface cracks, nor embedded glass fragments could be correlated with fatigue strength, in spite of the fact that cracks initiated at these features in most samples.

Introduction

One of the greatest concerns for military and commercial engines is damage caused by the ingestion of foreign debris, often referred to as foreign object damage (FOD)¹. It results in nicks and dents in the leading edge of blades, which can affect their life. Current serviceability limit for the F110-GE-129 engine first stage compressor blade is 0.762 mm (0.030"). If the depth is above this serviceable limit, the damaged area is blended out by filing. If the damage depth exceeds the maximum repairable limit, 3.048 mm (0.120"), the engine is pulled out of the aircraft for blade replacement.² The damage depths found in this study ranged from 0.068 to 0.427 mm (0.0027" - 0.016") which is much lower than the maximum serviceable limits for engines in operation today. One item of interest is whether FOD as small as noted above provides a significant fatigue strength debit of simulated engine blade specimens. In addition, determination of whether damage depth is a good representative of the actual fatigue related damage inflicted on the leading edge is a concern.

A study characterizing the damage sites is currently underway in order to understand the effects of FOD on high cycle fatigue strength of engine blades. Characteristic material, geometries representing the leading edge of engine blades and 'realistic' impact conditions

¹ This material is based upon work supported in part under US Air Force Research Laboratory Contract Numbers F33615-94-C-5601, F33615-98-C-5214, F33615-97-C-5274

were selected for this work. Much of the previous impact work has been done on traditional fatigue specimens or rectangular cross-section bars without leading edge geometry.

The goal of this research is to quantify the various measurable damage parameters and to study if they play a role in controlling the fatigue strength in Ti-6Al-4V simulated blades.

Materials and Procedures

Samples were machined from a forged and solution treated Ti-6Al-4V plate processed in a similar manner to actual engine blades. The plate was forged from bar stock, produced in accordance with AMS 4928³. Two diamond-cross section specimen geometries typical of compressor airfoil leading edges were machined representing a “sharp” edge specimen with a 0.127 mm (0.00”) leading edge (LE) radius and a “blunt” edge specimen with a 0.381 mm (0.015”) LE, as shown in Figure 1⁴.

A single-stage compressed-gas gun was used to ballistically impact the samples at the Impact Physics Group of the University of Dayton Research Institute (UDRI). Each specimen was impacted with 1 mm (0.040”) diameter glass beads to simulate sand and grit impacts experienced in the field. The beads were shot at 0° and 30° incident angles, Figure 1, at 305 m/s (1000 ft/s) typical to fan and compressor blade FOD impacts. Samples were shot once on each leading edge on different planes, representing two potential crack initiation sites per sample, as shown in Figure 1. Both notches on a given sample had the same angle of incidence.

Samples were subjected to tension-tension axial fatigue at 350 Hz. Fatigue testing was performed at the US Air Force Research Laboratory, Materials Directorate. The two stress ratios chosen for this study are R = 0.1 and 0.5 (ratio of minimum to maximum stress) representing the idle and peak loading conditions for in service blades⁶. A step loading procedure was chosen⁴. Prior to fatigue testing, several samples were characterized by a Scanning Electron Microscope (SEM) for initial FOD impact damage and will be discussed later. Testing was performed under ambient temperature and humidity conditions.

The sample group consisted of 26 specimens with two notches per sample. The samples were separated into four batches designated by the testing conditions of stress ratio and leading edge radius. Each batch contained samples with both 0° and 30° shots, Table 1.

The damage features characterized included the notch depth, material loss on the notch surface, material shear, material folding over the LE, and embedded glass from the shattered bead. The notches were photographed at a variety of views: normal to the leading edge, in the direction of impact, profile of the leading edge, and profile of the notch edge. In addition, the broken samples were tilted 30° along the length of the LE to view the notch/fracture interface. This view provided insight into the crack initiation location. Figure 2 illustrates the views photographed for sample 3-19 which is a 0° impact on a blunt LE.

Table 1: Sample pool

Batch	Leading Edge Radius	Stress Ratio	# of 0° samples	# of 30° samples
1	0.005”	0.1	2	6
2	0.005”	0.5	2	3
3	0.015”	0.1	2	4
4	0.015”	0.5	2	5

Results and Discussion

The notch depth was measured by rotating the SEM stage to achieve a profile view of the notch, as shown in Figure 3. Figure 4 shows a comparison of the depth of the failed notch (where initiation occurred) and the unfailed notches (where failure did not occur) for each specimen impacted at 0°. The light bars represent the broken notches and the shaded bars represent the unbroken notches. The y-axis shows the notch depth and the x-axis lists the sample ID for each set of notches. In almost all of the cases where failure initiated at the notch, it failed from the deeper of the two notches. The 0° impacts failed at the deeper notch 65% of the time, and 85% of the 30° impacts. However, the notch depth of the failed notch alone has no direct effect on the fatigue strength as shown in Figure 5 of normalized fatigue strength as a function of notch depth. The average normalized fatigue strength, σ_{norm} , or fatigue strength for each sample, σ_{sample} , was normalized using the fatigue strength of un-notched smooth bar specimens, σ_{smooth} . The average fatigue strength of the smooth bar, used for normalizing, is 568 MPa at R=0.1 and 660 MPa at R=0.5.

Another feature observed is the loss of material (LOM) from the surface of the notch, which was found on 65% of the broken notches and 20% of the unbroken notches. This feature was observed and characterized by visual estimation using the SEM. Loss of material is categorized into four levels: 0%, 25%, 50%, and 75%. An example of this is shown in Figure 6 where the two notches are from the same specimen. Figure 6a illustrates a notch with no material loss and a smooth surface. This is a 30° impact, where the bead seems to have "dented" the leading edge. On the other hand, Figure 6b (also a 30° impact) shows a rough and jagged notch where there is a significant amount of material loss. Crack initiation occurred at this notch.

In Figure 7, an attempt was made to correlate the loss of material for the failed notches to the average normalized fatigue strength. Loss of material for 30° impacts shows highly scattered and inconsistent results indicating that LOM alone has no clear effect on fatigue strength. This is not the case however, for the material loss of 0° impacts. There is a general trend such that the larger the material loss, the lower the fatigue strength. Unfortunately, only two out of eight 0° impacts actually hit head-on to the LE, the remaining six missed the edge slightly and created a non-normal impact, an example of which is shown in Figure 8a. Additional 0° impacted samples need to be tested to confirm this trend. In addition, the identified amount of LOM is not a measured value providing that there may be some error in the LOM estimation. An example of this variability is illustrated Figure 8.

Even though the amount of LOM may not have an effect on fatigue strength debit, the result of such damage can produce sharp edges and micro-folds on the surface of the notch. Figure 9 illustrates the fracture surface for sample 3-19, with estimated 75% LOM. In addition to LOM, the notch contained embedded glass from the shattered bead. The crack did not initiate at the embedded glass, but at a slight fold in the LOM section of the notch denoted by the circle. The depth of this notch was 0.273 mm (0.0107") and the fatigue strength debit of this sample was 49%.

Other damage features found that were apparent in the impacts include material shear on the notch region (Figure 10a & b), material folding over the LE (Figure 10c), and embedded glass from the shattered bead (Figure 10d). None of these features alone appeared to have an actual effect on the fatigue strength. On the other hand, shearing and folds did contribute to crack initiation sites for some of the samples. Figure 11 illustrates the fracture of sample 3-4, which had a notch depth of 0.182-mm (0.0071") and a fatigue strength debit of 64%. The pre-fracture condition of the notch indicates a material shear (or tearing) indicated by the circle in Figure 11a. The post-fracture condition of the notch shows that the fracture initiated somewhere behind the material shear, Figure 11b & c.

Previous research shows that fatigue failures of samples ballistically damaged with larger steel balls at similar velocities failed at the edge (rim) of the FOD notch⁵. Data in this research found that failure generally occurred on the region of the notch center or closer to the edge (indicated by the 0.25-0.50 region in Figure 12). Regardless of the condition (notch depth, LOM, shearing, or embedded glass) of the notch, failure occurred at or near the center of the notch for 30° impacts. There is no clear correlation for 0° impacts, partially due to the data scatter of a limited number of data points, Figure 13. This finding may be due to the larger impact of a ball size/mass that was used and the resulting damage. In addition, Ti-6Al-4V flat specimens used in previous research were impacted onto the flat surface of a larger fatigue specimen as opposed to this investigation in which thin samples were impacted on the edge, the latter being more representative of an actual airfoil edge.

Precision micro-sectioning was performed on a limited number of FOD samples, shown in Figure 14. These particular photos were taken at the mid-plane of a fractured sample with a 53% fatigue strength debit and a notch depth of 0.21-mm (0.0083"). Evident from each photo is a band of deformed grains along the periphery of the FOD crater, typically 60-100 µm. While there was no evidence of subsurface cracking in any of the samples examined in the direction of eventual crack growth, multiple shear bands roughly parallel the FOD crater were observed in nearly all of the micro-sectioned samples. The fact that these bands are oriented parallel to the applied loading direction (perpendicular to eventual fatigue cracking) indicates that their presence may have little influence on the fatigue life.

Conclusions

High-cycle fatigue testing showed fatigue strength degradation as a result of the edge-damage. SEM photographs features characterized on the samples include: the notch depth, material loss on the notch surface, material shear, material folding over the LE, and embedded glass from the shattered beads. Fracture initiation occurred generally at the deeper section of the notch. However, the notch depth of the broken notch had no direct effect on the fatigue strength. Loss of material for 30° impacts showed highly scattered and inconsistent results indicating that LOM alone has no effect on the fatigue strength. The data of the 0° impacts, on the other hand, did show a general trend where the larger the material loss, the lower the fatigue strength. Unfortunately additional testing of 0° impacts needs to be conducted to verify this trend. Even though the amount of LOM may not have a measured effect on fatigue strength debit, the result of such a damage can produce sharp edges and micro-folds on the surface of the notch, which provides suitable sites for crack initiation. The same is true for material shear and folds but not for embedded glass. Regardless of the condition (notch depth, LOM, shearing, or embedded glass) of the notch, failure occurred at or near the center of the notch for 30° impacts, but there is no clear correlation for 0° impacts, partially due to the data scatter of a limited number of data points. Precision micro-sectioning showed shear bands which are oriented parallel to the applied loading direction (perpendicular to eventual fatigue cracking). The role of these shear bands on fatigue strength is believed benign, but is being researched further.

References

1. Nicholas, T. "Critical Issues in High Cycle Fatigue," International Journal of Fatigue: 21st Vol.", February 1999, pp 221-231.
2. Personal communication from TSgt David Harrington, 20th Fighter Wing FOD Prevention NCO, Shaw AFB, to Capt. Christine Martinez, Air Force Institute of Technology. February 14, 2000.

3. Bellows, R., et al., "Step Test, Stress Ratio and Surface Effects on the High Cycle Fatigue Behavior of Ti-6Al-4V". Proceedings of the 4th National Turbine Engine High Cycle Fatigue Conference . Monterrey, CA, February 99.
4. Ruschau, J., Nicholas, T., and Thompson, S. "Influence of Foreign Object Damage (FOD) on the Fatigue Strength of Simulated Ti-6Al-4V Airfoils". Submitted to the International Journal of Mechanical Science.
5. Peters, J. Roder, Boyce Thompson and Ritchie, "Role of Foreign Object Damage on Thresholds for High-Cycle Fatigue in Ti-6Al-4V," Metallurgical and Metals Transaction A, 1999 (submitted for publication)
6. Personal communication from Dr. Richard Bellows, Allied Signal Engines, to William Porter, UDRI. October 7, 1997.

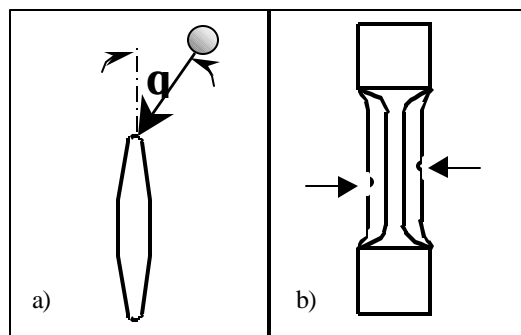


Figure 1: Ballistic Impact

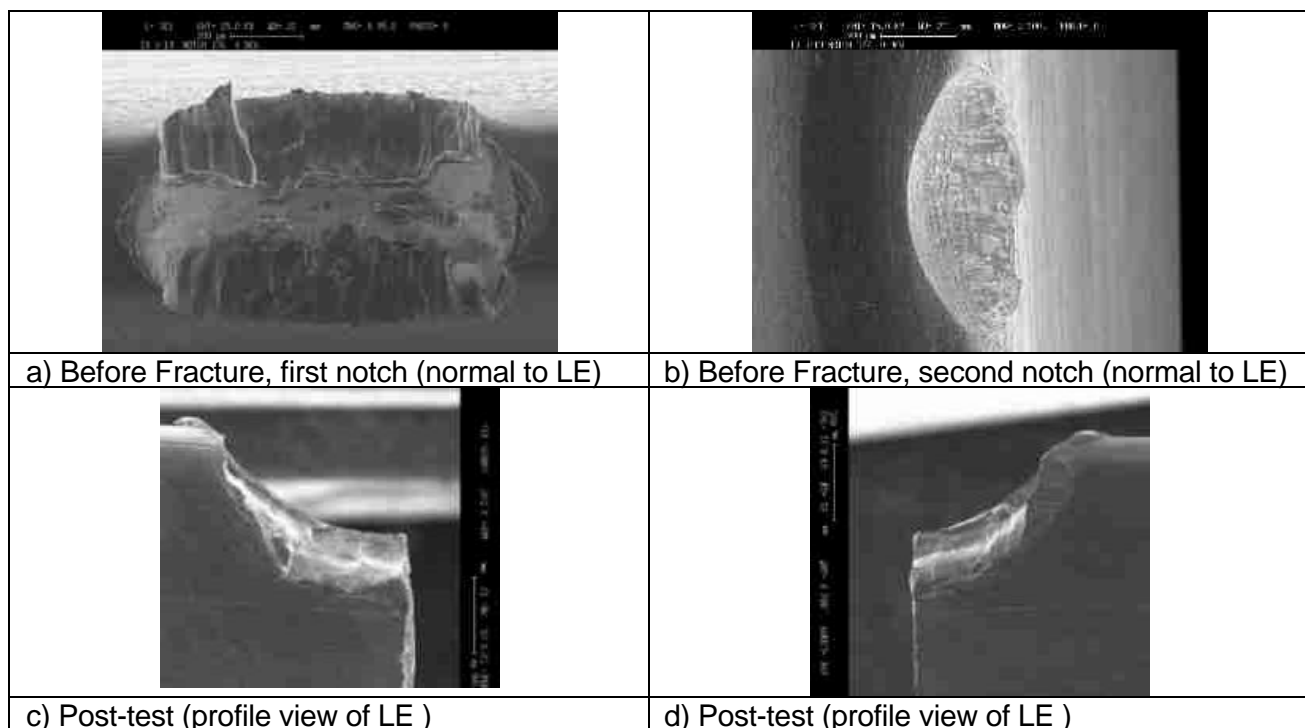


Figure 2: SEM Pictures of Sample 3-19

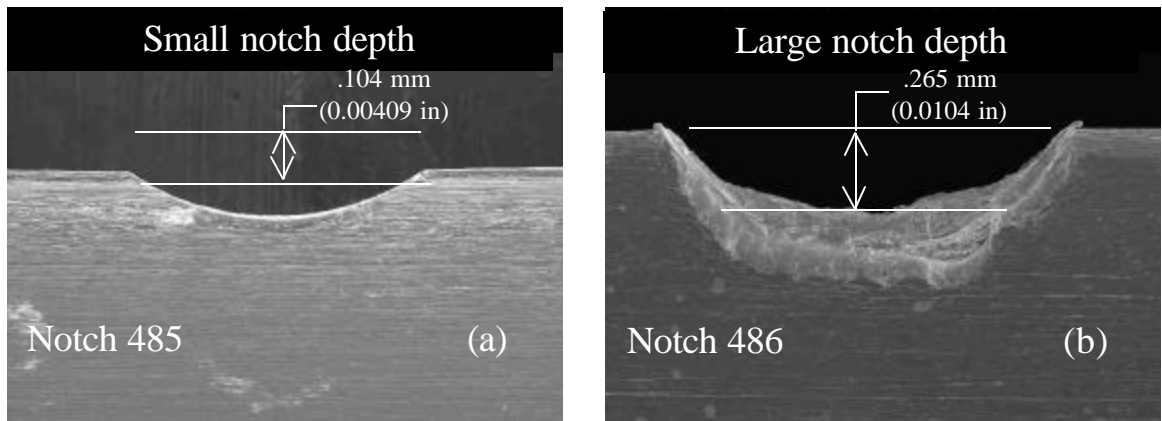


Figure 3: Characteristic Notch Depth (sample 4-21 @ 100X)

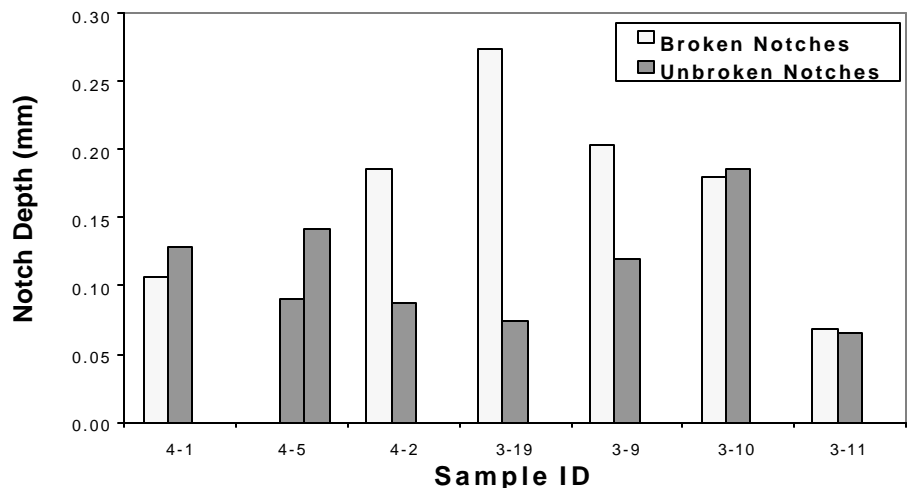


Figure 4: Depth of Broken Notches vs. Depth of Unbroken Notches for 0° impacts

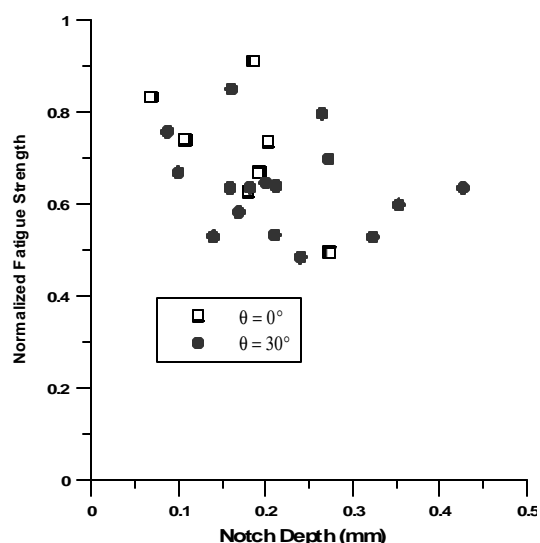


Figure 5: Comparison of notch depth and the fatigue strength

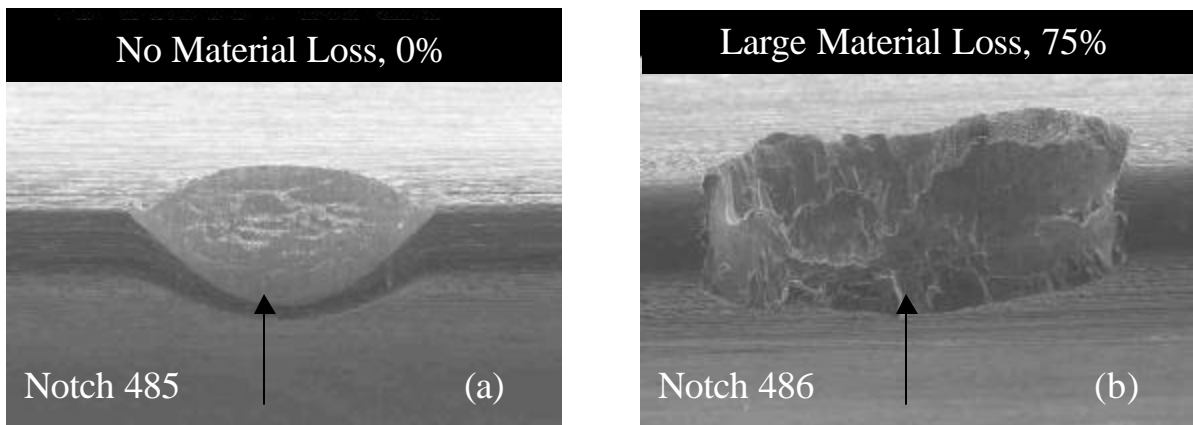


Figure 6: Loss of Material (sample 4-21 @ 100X)

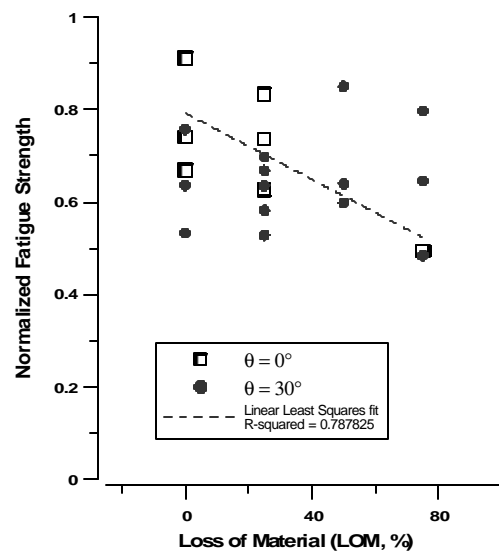


Figure 7: Comparison of materials loss and the fatigue strength

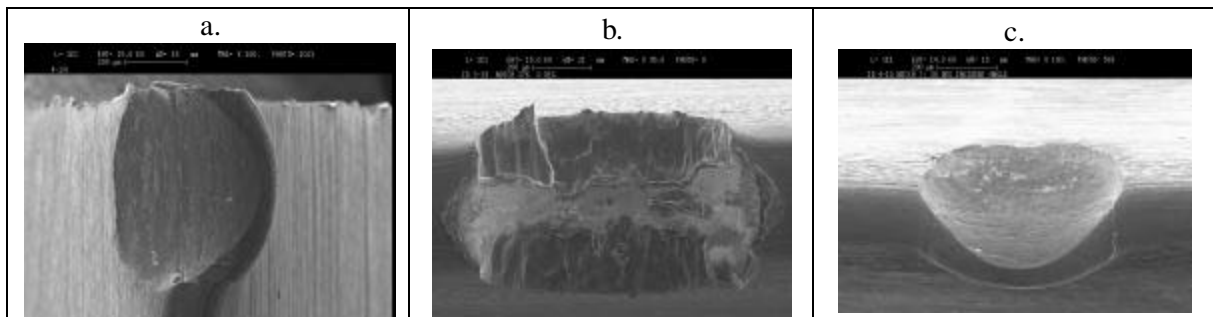


Figure 8: Ballistic Shots: a) 0° , sharp LE; b) 0° , blunt LE; c) 30° , blunt LE (all photos @ 100X)

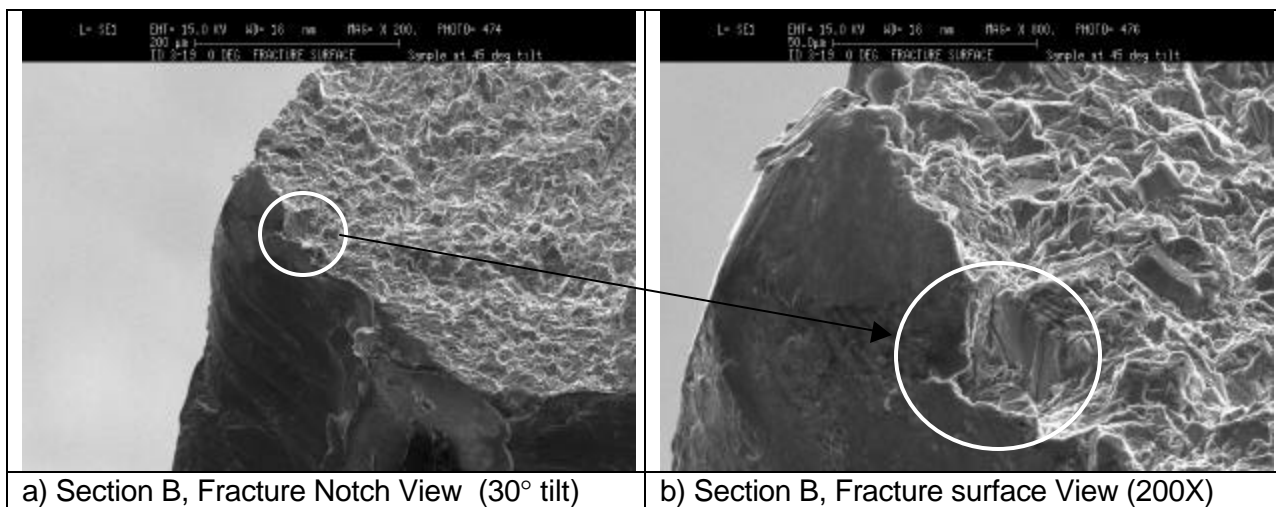


Figure 9: Fracture initiation of Sample 3-19

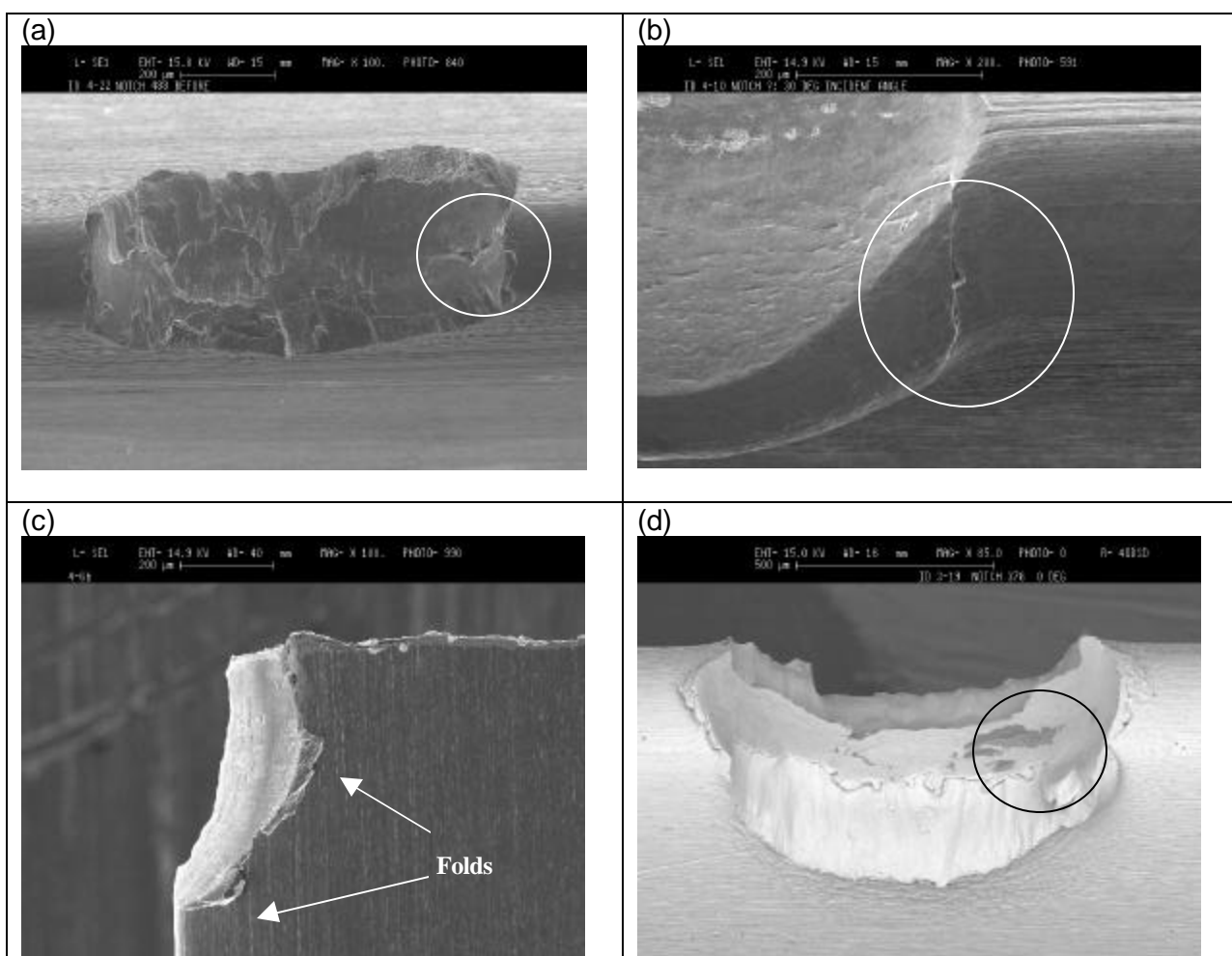


Figure 10: Other damage features: a) material shear; b) material shear; c) material fold; d) embedded glass, backscatter detector mode

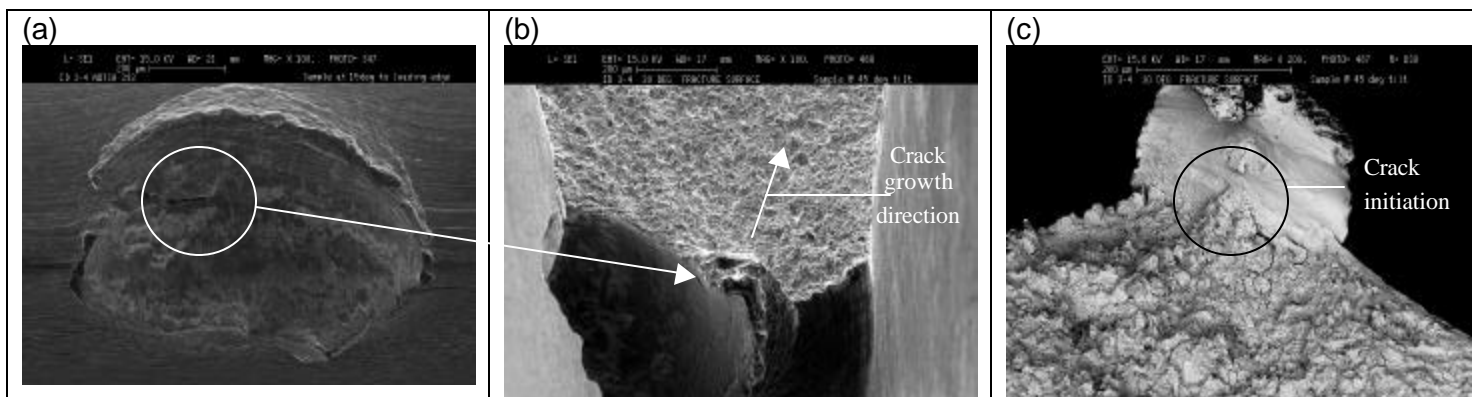


Figure 11: Shearing: a) Before fracture picture of sample 3-4, material shear parallel to LE b) After fracture photo; c) After fracture photo behind material shear

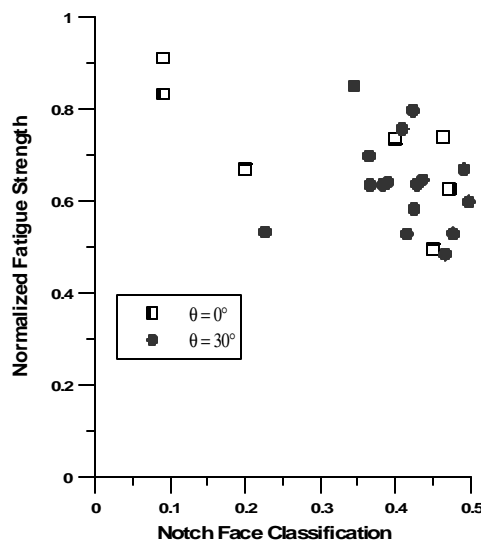


Figure 12: Crack Initiation Location photograph

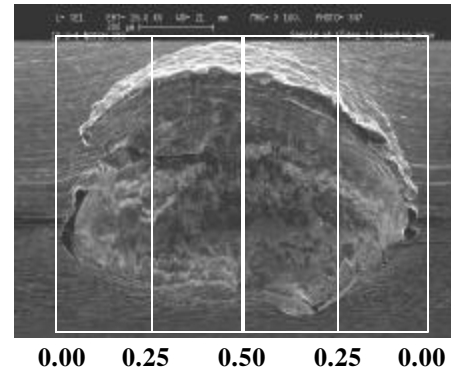


Figure 13: Crack Initiation Location

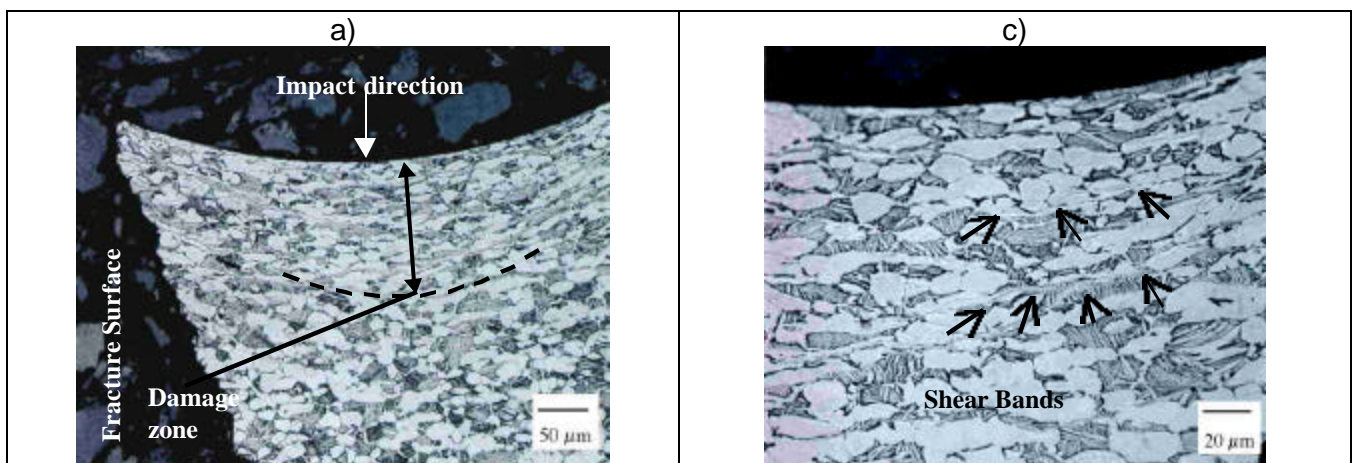


Figure 14: Precision Micro-sectioning of sample 3-13

LIST OF SYMBOLS, ABBREVIATIONS, AND ACRONYMS

<u>ABBREVIATION</u>	<u>DEFINITION</u>
γ -TiAl	Gamma Titanium Aluminide
AE	Acoustic Emission
CMC	Ceramic Matrix Composites
CMOD	Crack Mouth Opening Displacement
CPLM	Crack Propagation Load Measurement
CTE	Coefficient Thermal Expansion
DCDP	Direct Current Potential Difference
DCT	Diamond Cross-Sectioned Tension
DE(T)	Double-notched Tension Specimen
DEH(T)	Semicircular Double-notched Tension Specimen
ERLE	Engine Rotor Life Extension
FOD	Foreign Object Damage
FY	Fiscal Year
HCF	High Cycle Fatigue
IHPTE	Integrated High Performance Turbine Engine Technology
LE	Leading Edge
LVDT	Linear Variable Differential Transformer
MH(T)	Middle Hole Tension Specimen
MI	Melt Infiltrated
MLLM	Metals Branch
MLLMN	Behavior/Life Prediction Section
MLOC	Government Computer Support
NTED	National Turbine Engine Durability
OIM	Orientation Imaging Microscopy
PIN	Physically Isolated Networks
SE(T)	Single Edge Hole Tension Specimen
SEM	Scanning Electron Microscopy
Ti	Titanium
TMC	Titanium Matrix Composites
TMCTECC	Titanium Matrix Composite Turbine Engine Component Consortium
TPRL	Thermophysical Properties Research Laboratory
USAF	United States Air Force
UMAT	User Material